

NOVEL MULTIFUNCTIONAL LIGANDS AND THEIR APPLICATION IN

ALZHEIMER'S DISEASE

by

Maria A. Telpoukhovskaia

B.S., Yale University, 2007

A THESIS SUBMITTED IN PARTIAL FULFILLMENT OF

THE REQUIREMENTS FOR THE DEGREE OF

DOCTOR OF PHILOSOPHY

in

THE FACULTY OF GRADUATE AND POSTDOCTORAL STUDIES

(Chemistry)

THE UNIVERSITY OF BRITISH COLUMBIA

(Vancouver)

April 2014

© Maria A. Telpoukhovskaia, 2014

Abstract

Alzheimer's disease (AD) is a fatal, neurodegenerative disorder that is the most common cause of dementia currently affecting over 35 million people. Metal ions Cu(II), Zn(II), and Fe(III) have a dual deleterious role in Alzheimer's disease through acceleration of aggregation that leads to increased toxicity of the amyloid protein, and participation in catalytic cycles generating reactive species. The therapeutic effect of metal chelating agents is currently explored in clinical studies, as there are currently no drugs for this disease. This thesis investigates the 3-hydroxy-4-pyridinone family of chelating ligands, with attention given to its multifunctional activities. The main goal is to demonstrate that metal and amyloid-binding functionalities are compatible within this scaffold, while other functionalities are retained. Novel chelating agents 1-(benzo[d]oxazol-2-ylmethyl)-3-hydroxy-2-methylpyridin-4(1H)-one (**Hmbo2p**), 1-(benzo[d]thiazol-2-ylmethyl)-3-hydroxy-2-methylpyridin-4(1H)-one (**Hmbt2p**), 1-(2-aminobenzo[d]thiazol-6-yl)-3-hydroxy-2-methylpyridin-4(1H)-one (**Habt6p**), 1-(4-(benzo[d]oxazol-2-yl)phenyl)-3-hydroxy-2-methylpyridin-4(1H)-one (**Hpbo2p**), and 1-(4-(benzo[d]thiazol-2-yl)phenyl)-3-hydroxy-2-methylpyridin-4(1H)-one (**Hpbt2p**) were designed, synthesised, and structural characterised. The metal binding of **Hmbo2p** to Cu(II), Zn(II), and Fe(III) was confirmed with titration studies, while the solid state structures of **Hmbt2p** were characterised using X-ray crystallography. Amyloid binding functionalities of **Hmbo2p** were confirmed with microscopy, fluorescence, and binding studies. Moreover, the radical quenching ability of **Hmbo2p** was established in the absence and presence of Cu(II) by absorbance and fluorescence studies. As well, compounds **Hmbo2p**, **Hmbt2p**, and **Habt6p** were found to be relatively toxic in a mouse endothelial neuronal cell line, while **Hpbt2p** was visualised to permeate into the cell line. Finally, by installing a carbamoyl functionality, novel compounds 2-methyl-4-oxo-1-phenyl-1,4-

dihydropyridin-3-yl dimethylcarbamate (**Cppp**), 4-(3-hydroxy-2-methyl-4-oxopyridin-1(4H)-yl)phenyl dimethylcarbamate (**Chpp**), and 4-(((2-methyl-4-oxo-1-phenyl-1,4-dihydropyridin-3-yl)oxy)methyl)phenyl dimethylcarbamate (**Cbppp**) were synthesised for the purpose of adding an acetylcholinesterase (AChE) inhibitory functionality. The metal chelation site was masked on **Cppp** and **Cbppp**; all three inhibited *eel*AChE reversibly *in vitro*. The work presented herein demonstrates for the first time that incorporation of benzoxazole group into the hydroxypyridinone scaffold imbues it with amyloid-binding functionality while retaining the metal chelating ability. This insertion and concomitant increase of lipophilicity leads to morphological changes of amyloid protein upon incubation, and potentially results in increased toxicity and cell permeability. Finally, masking the hydroxyl group with a carbamate functionality on the scaffold leads to generation of reversible enzyme inhibitors.

Preface

The majority of Chapter 1 was published - Telpoukhovskaia, M. A., Orvig, C. “Werner coordination chemistry and neurodegeneration.” *Chem. Soc. Rev.* **2013**, *42*, 1836-1846. The manuscript was written by me and edited by Dr. Chris Orvig.

Those parts of Chapter 2, Chapter 3, and Chapter 4 pertaining to compounds abbreviated as **Hmbo2p**, **Hmbt2p**, and **Habt6p** (including their metal complexes) were published - Telpoukhovskaia, M. A., Rodríguez-Rodríguez, C., Cawthray, J. F., Scott, L. E., Page, B. D. G., Alí-Torres, J., Sodupe, M., Bailey, G. A., Patrick, B. O., Orvig, C. “3-Hydroxy-4-pyridinone derivatives as metal ion and amyloid binding agents.” *Metallomics* **2014**, *6*, 249-262. A portion of this article is also reproduced in Chapter 6. Dr. Lauren Scott (a Ph.D. graduate of the group) is credited with the original design and synthesis of **Hmbt2p**, and **Habt6p**, which was done with the aid of undergraduate student working under her supervision, Dr. Brent Page. I was responsible for the design and synthesis of **Hmbo2p**, and the improvement of synthesis of **Habt6p** and purification and complete characterisation of all three compounds. I ran the samples on the Bruker AV-300 spectrometer, while the Bruker AV-400 and -600 were operated by Dr. Maria Ezhova, Zorana Danilovic, and Helen Huang-Hobbs (the staff of the NMR facility). I performed the low-resolution mass analyses, while high-resolution mass spectra and elemental analyses were done by David Wong, Derek Smith, and Marshall Lapawa (the staff of MS/EA facility). X-ray crystallography studies were done by the crystallographer Dr. Brian Patrick. I was responsible for design and performance of all studies from the manuscript that are described in this thesis; Gwen Bailey, a summer undergraduate student, helped me with antioxidant studies, and Dr. Jacqueline Cawthray taught me how to set up and analyse titration studies. As

well, Dr. Cawthray operated the TEM microscope in analysing the samples that I prepared under her guidance. Jessie Chen and Dr. Elena Polishchuk taught me how to do cell studies and set up the initial cytotoxicity assay. The parts of the manuscript used for this thesis were written by me and edited by Dr. Chris Orvig.

Those parts of Chapter 2 and Chapter 4 pertaining to compounds abbreviated as **Hpb02p** and **Hpb12p** will be submitted for publication - Telpoukhovskaia, M. A., Rodríguez-Rodríguez, C., Cawthray, J. F., Scott, L. E., Page, B. D. G., Patrick, B. O., Orvig, C. “Amyloid interaction and cell permeability studies of 3-hydroxy-4-pyridinone derivatives.” Dr. Lauren Scott (a Ph.D. graduate of the group) is credited with the original design and synthesis of **Hpb12p**, which was done with the aid of undergraduate student working under her supervision, Dr. Brent Page. I was responsible for the design and synthesis of **Hpb02p**, as well as purification and complete characterisation of the two compounds. I ran the samples on the Bruker AV-300 spectrometer, while the Bruker AV-600 was operated by Dr. Maria Ezhova, Zorana Danilovic, and Helen Huang-Hobbs (the staff of the NMR facility). I performed the low-resolution mass analyses, while high-resolution mass spectra and elemental analyses were done by David Wong, Derek Smith, and Marshall Lapawahe (staff of MS/EA facility). X-ray crystallography studies were done by the crystallographer Dr. Brian Patrick. I was responsible for design and performance of all studies that are described in this thesis; Dr. Jacqueline Cawthray took images of the cells with a microscope of the samples that I prepared.

Those parts of Chapter 3 and Chapter 4 pertaining to compounds abbreviated as **Cu(ppp)₂**, **Zn(ppp)₂**, **Fe(ppp)₃**, **Cu(zapp)₂**, **Zn(zapp)₂**, **Fe(zapp)₃**, **Cu(bt2p)₂**, **Zn(bt2p)₂**, and **Fe(bt2p)₃**

were published – Telpoukhovskaia, M. A., Rodríguez-Rodríguez, C., Scott, L. E., Patrick, B. O., Orvig, C. “Synthesis, characterization, and cytotoxicity studies of Cu(II), Zn(II), and Fe(III) complexes of N-derivatized 3-hydroxy-4-pyridinones.” *J. Inorg. Biochem.* **2014**, DOI: 10.1016/j.jinorgbio.2013.12.003. Dr. Lauren Scott (a Ph.D. graduate of the group) is credited with the synthesis of **Hbt2p**, **Cu(ppp)₂**, **Cu(zapp)₂** and **Cu(bt2p)₂**, and it was the compounds prepared by her that I used in the assays included here; the work that she did was done with the aid of undergraduate student working under her supervision, Dr. Brent Page. I was responsible for the synthesis, purification and complete characterisation of all the other compounds. I performed the NMR studies and low-resolution mass analyses, while high-resolution mass spectra and elemental analyses were done by David Wong, Derek Smith, and Marshall Lapawa (the staff of MS/EA facility). X-ray crystallography studies were done by the crystallographer Dr. Brian Patrick. I was responsible for design and performance of all studies from the manuscript that are described in this thesis; Dr. Cristina Rodríguez-Rodríguez taught me and helped me with growing single crystals of metal complexes. The manuscript was written by me and edited by Dr. Chris Orvig.

Those parts of Chapter 5 pertaining to compounds abbreviated as **Hppp** and **Cppp** were published – Telpoukhovskaia, M. A., Patrick, B. O., Rodríguez-Rodríguez, C., Orvig, C. “Exploring the multifunctionality of thioflavin- and deferiprone-based molecules as acetylcholinesterase inhibitors for potential application in Alzheimer's disease.” *Mol. BioSyst.* **2013**, *9*, 792-805. I designed, synthesized, and characterized the compounds, and designed and conducted the *in vitro* experiments. For kinetic studies, the compounds were analysed with the aid of Dr. Cristina Rodríguez-Rodríguez. I performed the NMR studies and the low-resolution

mass analyses, while high-resolution mass spectra and elemental analyses were done by the staff of MS/EA facility David Wong, Derek Smith, and Marshall Lapawa. X-ray crystallography studies were done by the crystallographer Dr. Brian Patrick. The parts of the manuscript used in this thesis were written by me and edited by Dr. Cristina Rodríguez-Rodríguez and Dr. Chris Orvig.

Those parts of Chapter 5 pertaining to compounds abbreviated as **Chpp**, **Cchpp**, and **Cbppp** will be submitted as a manuscript – Telpoukhovskaia, M. A., Patrick, B. O., Rodríguez-Rodríguez, C., Orvig, C. “Further explorations of hydroxypyridinones as inhibitors of acetylcholinesterase: virtual library screening, computational, and *in vitro* studies.” I designed, synthesized, and characterised the compounds, and designed and conducted the *in vitro* experiments. I performed the NMR studies and the low-resolution mass analyses, while high-resolution mass spectra and elemental analyses were done by the staff of MS/EA facility David Wong, Derek Smith, and Marshall Lapawa. X-ray crystallography studies were done by the crystallographer Dr. Brian Patrick, with the exception of the data for **Hhpp** and **Chpp** that I analysed with his help. The HPLC instrument for **Cbppp** analysis was operated by Caterina Ramogida.

Material from Telpoukhovskaia, M. A., Rodríguez-Rodríguez, C., Cawthray, J. F., Scott, L. E., Page, B. D. G., Alí-Torres, J., Sodupe, M., Bailey, G. A., Patrick, B. O., Orvig, C. “3-Hydroxy-4-pyridinone derivatives as metal ion and amyloid binding agents.” *Metallomics* **2014**, *6*, 249-262; Telpoukhovskaia, M. A., Patrick, B. O., Rodríguez-Rodríguez, C., Orvig, C. “Exploring the multifunctionality of thioflavin- and deferiprone-based molecules as acetylcholinesterase inhibitors for potential application in Alzheimer's disease.” *Mol. BioSyst.* **2013**, *9*, 792-805; and

Telpoukhovskaia, M. A., Orvig, C. “Werner coordination chemistry and neurodegeneration.” *Chem. Soc. Rev.* **2013**, *42*, 1836-1846 was reproduced by permission of The Royal Society of Chemistry.

Material was reprinted from *Journal of Inorganic Biochemistry*, DOI:

10.1016/j.jinorgbio.2013.12.003, Telpoukhovskaia, M. A., Rodríguez-Rodríguez, C., Scott, L. E., Patrick, B. O., Orvig, C., “Synthesis, characterization, and cytotoxicity studies of Cu(II), Zn(II), and Fe(III) complexes of *N*-derivatized 3-hydroxy-4-pyridinones,” Copyright (2014), with permission from Elsevier [License number 3314891045632].

Table of Contents

Abstract	ii
Preface	iv
Table of Contents	ix
List of Tables	xv
List of Figures	xvii
List of Schemes	xxv
List of Abbreviations	xxvi
Acknowledgements	xxxv
Dedication	xxxvii
Chapter 1: Introduction	1
1.1 Contributions of inorganic chemistry to medicine.....	1
1.2 Introduction to the role of inorganic chemistry in neurodegenerative diseases.....	2
1.3 Overview of metal ion roles in neurodegenerative diseases	4
1.3.1 Alzheimer’s disease (AD).....	4
1.3.2 Parkinson’s disease (PD)	5
1.3.3 Prion diseases (PrD).....	5
1.4 Metal ions binding to proteins implicated in neurodegenerative diseases (NDs).....	5
1.4.1 Amyloid precursor protein (APP).....	7
1.4.2 Amyloid β ($A\beta$).....	9
1.4.3 α -Synuclein (α -syn)	13
1.4.4 Prion protein (PrP)	14
1.4.5 Metalloprotein summary and outlook.....	15

1.5	Metal binding therapy	16
1.5.1	Alzheimer's disease	16
1.5.1.1	Ligands based on aromatic nitrogens.....	18
1.5.1.2	Oxygen-based ligands.....	21
1.5.1.3	Other ligand scaffolds	24
1.5.2	Parkinson's and prion diseases	25
1.5.3	Chelating ligands summary and outlook.....	25
1.5.4	Conclusions.....	27
1.6	Focus on HPOs	28
1.7	Drug design considerations – multifunctional scaffold	30
1.8	Thesis goal and overview.....	32
Chapter 2: Synthesis and characterisation of next generation pro-ligands		33
2.1	Introduction.....	33
2.2	Experimental.....	36
2.2.1	Materials and methods	36
2.2.2	Instrumentation	37
2.2.3	Synthesis and characterisation	38
2.3	Results and discussion	43
2.4	Conclusions.....	50
Chapter 3: Metal binding studies with biorelevant metal ions in solution and solid states..		52
3.1	Introduction.....	52
3.2	Experimental.....	53
3.2.1	Materials and methods	53

3.2.2	Instrumentation	53
3.2.3	Synthesis and characterisation	55
3.2.4	Binding affinities	63
3.2.5	Stability.....	64
3.3	Results and discussion	65
3.3.1	Metal complex preparation and characterisation	65
3.3.2	Binding affinities	75
3.3.3	Stability.....	78
3.4	Conclusions.....	84
Chapter 4: <i>In vitro</i> characterisation of pro-ligands: antioxidant activity, amyloid binding, and cell studies.....		86
4.1	Introduction.....	86
4.2	Experimental.....	88
4.2.1	Materials and methods	88
4.2.2	Instrumentation	88
4.2.3	Trolox-equivalent antioxidant capacity (TEAC) assay.....	89
4.2.4	Amyloid- β aggregation studies	89
4.2.5	Binding to A β ₁₋₄₀ fibrils	90
4.2.6	Cytotoxicity.....	92
4.2.7	Cell permeability.....	93
4.3	Results and discussion	94
4.3.1	Trolox-equivalent antioxidant capacity (TEAC) assay.....	94
4.3.2	Amyloid- β aggregation studies.....	96

4.3.3	Binding to A β ₁₋₄₀ fibrils	98
4.3.4	Cytotoxicity.....	100
4.3.5	Modelling BBB penetration.....	104
4.4	Conclusions.....	106
Chapter 5: Hydroxypyridinones as acetylcholinesterase inhibitors		108
5.1	Introduction.....	108
5.2	Experimental.....	110
5.2.1	Materials and methods	110
5.2.2	Instrumentation	110
5.2.3	Synthesis and characterisation	111
5.2.4	Enzymatic activity - inhibition.....	118
5.2.5	Acetylcholinesterase inhibition kinetics	120
5.2.6	Prodrug metal ion binding activity and activation <i>in vitro</i>	121
5.3	Results and discussion	122
5.3.1	First generation study.....	122
5.3.1.1	Synthesis and characterisation	122
5.3.1.2	Acetylcholinesterase inhibition.....	123
5.3.1.3	Kinetic studies.....	124
5.3.1.4	Prodrug metal binding activity and activation <i>in vitro</i>	128
5.3.1.5	Conclusions.....	129
5.3.2	Second generation compounds	129
5.3.2.1	Synthesis and characterisation	130
5.3.2.2	Acetylcholinesterase inhibition.....	133

5.3.2.3	Kinetic studies.....	134
5.3.2.4	Prodrug activation.....	134
5.3.2.5	Conclusions.....	136
5.4	Conclusions.....	136
Chapter 6: Conclusions and future work		137
6.1	General comments	137
6.2	Conclusions from this body of work.....	139
6.2.1	Multifunctional HPO scaffold.....	139
6.2.2	Enzyme activity	139
6.3	Future work.....	140
6.3.1	A β interaction	140
6.3.2	BBB permeability studies	140
6.3.3	Cytotoxicity.....	141
Bibliography		142
Appendices.....		153
Appendix A – Crystallographic data		153
A.1	Novel pro-ligands and their precursors.....	153
A.2	Metal complexes	158
A.3	Acetylcholinesterase inhibitors and their precursors.....	162
Appendix B – Compound characterisation.....		166
B.1	Novel pro-ligands and their precursors.....	166
B.2	Metal complexes	173
B.3	Carbamated compounds.....	176

Appendix C – Additional data 180

List of Tables

Table 1.1 Coordination of biorelevant metal ions to metalloproteins implicated in neurodegenerative diseases. Table reproduced by permission of The Royal Society of Chemistry.....	10
Table 1.2 Stability constants for chelating ligands in this section. Table reproduced by permission of The Royal Society of Chemistry.....	22
Table 2.1 Lipinski's rules parameters and log BB calculated values for Hmbo2p, Hmbt2p, Habt6p, Hpbo2p, and Hpbt2p. Modified table reproduced by permission of The Royal Society of Chemistry.....	49
Table 3.1 Selected IR bands and their assignments. ¹⁰⁸ Symbols denote the following: * obscured by an adjacent peak, ν stretching, δ_{as} asymmetric in plane bend. Table used with permission from Elsevier.	68
Table 3.2 Stability constants for Hmbo2p with Cu(II), Zn(II), and Fe(III) in 0.1 M KCl H ₂ O at 25 °C, with standard deviation given in parentheses. Table reproduced by permission of The Royal Society of Chemistry.....	77
Table 4.1 EC ₅₀ values with their respective 95% confidence intervals, as calculated by GraphPad Prism for cisplatin, Hmbo2p, Hmbt2p, Habt6p, Hppp, Hzapp, and Hbt2p. Notes: a. first part of study, b. second part of study.....	101
Table 5.1 IC ₅₀ values for <i>eel</i> AChE activity <i>in vitro</i> for Hppp, Chph, Ccphp, Cbppp, and C-pcresol.	134
Table A.1 Crystal and refinement data for Bnma and Bnzapp. Table reproduced by permission of The Royal Society of Chemistry.	153

Table A.2 Crystal and refinement data for Hmbo2p, Hmbt2p, and Habt6p. Table reproduced by permission of The Royal Society of Chemistry.....	154
Table A.3 Selected bond lengths (Å) and angles (°) for Bnma, Bnzapp, Hmbo2p, Hmbt2p, and Habt6p. Table reproduced by permission of The Royal Society of Chemistry.....	155
Table A.4 Crystal and refinement data for Hcpp, and Hpbo2p.	156
Table A.5 Selected bond lengths (Å) and angles (°) for Hcpp and Hpbo2p.....	157
Table A.6 Crystal and refinement data for Zn(ppp) ₂ and Fe(ppp) ₃ . Table used with permission from Elsevier.....	158
Table A.7 Selected bond lengths (Å) and angles (°) for Zn(ppp) ₂ and Fe(ppp) ₃ . Table used with permission from Elsevier.	159
Table A.8 Crystal and refinement data for Cu(mbt2p) ₂ , Zn ₂ (mbt2p) ₄ , and Fe(mbt2p) ₃ . Table reproduced by permission of The Royal Society of Chemistry.....	160
Table A.9 Selected bond lengths (Å) and angles (°) for Cu(mbt2p) ₂ , Zn ₂ (mbt2p) ₄ , and Fe(mbt2p) ₃ . Table reproduced by permission of The Royal Society of Chemistry.....	161
Table A.10 Crystal and refinement data for Hppp and Cppp. Table reproduced by permission of The Royal Society of Chemistry.....	162
Table A.11 Selected bond lengths (Å) and angles (°) for Hppp and Cppp. Table reproduced by permission of The Royal Society of Chemistry.....	163
Table A.12 Crystal and refinement data for Hhpp, Bnhpp, and Chpp.....	164
Table A.13 Selected bond lengths (Å) and angles (°) for Hhpp, Bnhpp, and Chpp.	165

List of Figures

Figure 1.1 Cancer drug cisplatin and imaging agent ^{99m}Tc Bicasate (Neurolite®).	2
Figure 1.2 Cu(II) binding site in the copper domain of APP as elucidated from its solid state structure, adapted from ref. ²⁰ The geometry and the amino acids involved around the metal centre are depicted for illustrative purposes. Figure reproduced by permission of The Royal Society of Chemistry.....	8
Figure 1.3 Cu(II) coordination to A β , adapted from refs. ^{27,29} Left: component 1a/b, right: two likely structures for component 2. The geometry and the amino acids involved around the metal centre are depicted for illustrative purposes. Figure reproduced by permission of The Royal Society of Chemistry.....	12
Figure 1.4 The strongest binding site in α -syn, adapted from ref. ³⁸ The geometry and the amino acids involved around the metal centre are depicted for illustrative purposes. Figure reproduced by permission of The Royal Society of Chemistry.....	13
Figure 1.5 Two Cu(II) coordination modes for the octarepeat region of the prion protein, adapted from ref. ³⁹ Left: binding of one Cu(II) to PrP, right: binding of four Cu(II) to PrP. The geometry and the amino acids involved around the metal centre are depicted for illustrative purposes. Figure reproduced by permission of The Royal Society of Chemistry.	14
Figure 1.6 Ligands L ₁ -L ₇ containing aromatic nitrogen(s). Figure reproduced by permission of The Royal Society of Chemistry.....	19
Figure 1.7 Ligands L ₈ -L ₁₂ containing oxygen atoms and other scaffolds. Figure reproduced by permission of The Royal Society of Chemistry.....	24
Figure 1.8 The postulated reaction mechanism of amine insertion into maltol. ⁸³	30
Figure 1.9 HPO drug design overview.	32

Figure 2.1 Positron emission tomography tracers PIB and BF-227 used for <i>in vivo</i> plaque imaging. ⁹⁰ Modified figure reproduced by permission of The Royal Society of Chemistry.....	35
Figure 2.2 Novel pro-ligands Hmbo2p, Hmbt2p, Habt6p, Hpbo2p, and Hpbt2p.....	35
Figure 2.3 Solid state structures of A) Bnma and B) Bnzapp (synthetic intermediates for Habt6p), and pro-ligands: C) Hmbo2p, D) Hmbt2p, and E) Habt6p, represented as ellipsoid plots (50% probability). Solvent molecules and non O-H hydrogen atoms are omitted for clarity. Figure reproduced by permission of The Royal Society of Chemistry.	46
Figure 2.4 Solid state structures of A) Hccp and B) Hpbo2p, represented as ellipsoid plots (50% probability). Solvent molecules and hydrogen atoms are omitted for clarity.....	48
Figure 2.5 Absorbance (left) and fluorescence (right) properties of pro-ligands in a buffered aqueous solution at pH 7.4 at room temperature.	50
Figure 3.1 ¹ H NMR spectra comparing Hppp to Zn(ppp) ₂ (300 MHz, MeOD-d ₄ , 24.7 °C). Figure used with permission from Elsevier.	67
Figure 3.2 ¹ H NMR spectra comparing Hmbo2p (300 MHz), Ga(mbo2p) ₃ at 25 (600 MHz) and 65 °C (400 MHz) in DMSO-d ₆ . Figure reproduced by permission of The Royal Society of Chemistry.....	69
Figure 3.3 A) Solid state structure of [Zn(ppp) ₂] ₂ , represented as an ellipsoid plot (50% probability) of the asymmetric unit. Hydrogen atoms, solvent molecules, and the perchlorate ion are omitted for clarity; B) Solid state structure of one Fe center (Fe1) of complex Fe(ppp) ₃ , represented as an ellipsoid plot (50% probability). Hydrogen atoms and solvent molecules are omitted for clarity. Figure used with permission from Elsevier.	71
Figure 3.4 A) Hydrogen bonded water network within the Fe(ppp) ₃ unit cell. Hydrogen atoms are omitted for clarity. B) Partially solved solid state structure of Fe(zapp) ₃ , represented as an	

ellipsoid plot (50% probability). Hydrogen atoms and solvent molecules are omitted for clarity. Figure used with permission from Elsevier. 73

Figure 3.5 Solid state structures of metal complexes: A) $\text{Cu}(\text{mbt2p})_2$ (asymmetric unit as well as half of the complex around Cu2 centre related by inversion), B) $\text{Zn}_2(\text{mbt2p})_4$ (asymmetric unit), and C) $\text{Fe}(\text{mbt2p})_3$ (one isomer in the asymmetric unit), represented as ellipsoid plots (50% probability). Solvent molecules and hydrogen atoms are omitted for clarity. Figure reproduced by permission of The Royal Society of Chemistry. 75

Figure 3.6 Illustration of dissociation equilibria of Hmbo2p. 76

Figure 3.7 Speciation plots for Hmbo2p (A), $\text{Cu}(\text{mbo2p})_2$ (B), $\text{Zn}(\text{mbo2p})_3$ (C), and $\text{Fe}(\text{mbo2p})_3$ (D) using HYSS2009.¹¹³ The plots were constructed with ratios of 1:2 for Cu to Hmbo2p, and 1:3 for Zn and Fe, with concentration of Hmbo2p set to 25 μM (experimental titration conditions). Metal hydroxide formations that contribute to loss of complex formations at high pH are omitted. Figure reproduced by permission of The Royal Society of Chemistry. 77

Figure 3.8 Ascorbic acid (AA) (60 μM final) addition to $\text{Cu}(\text{mbo2p})_2$ (20 μM final) in HEPES buffer at pH 7.4, monitored after 2 hours and 1 day. Figure reproduced by permission of The Royal Society of Chemistry. 80

Figure 3.9 Formation of fluorescent product of coumarin-3-carboxylic acid and the hydroxyl radical in the presence of AA and Cu(II), either alone, or chelated to Hmbo2p or EDTA in HEPES buffer at pH 7.4 (ex. 395, em. 452). Figure reproduced by permission of The Royal Society of Chemistry. 81

Figure 3.10 $\text{Cu}(\text{zapp})_2$ in the presence of histidine after 1 minute, 3 hours, and 3 days in 10 mM HEPES at pH 7.4, as monitored by UV-vis spectroscopy. A spectrum of unchelated Hzapp is included for comparison. 83

Figure 4.1 Trolox-equivalent antioxidant capacity values of pro-ligands Hmbo2p, Hmbt2p, Habt6p and Vitamin E⁵⁸ represented as TEAC values at 1, 3, and 6 minutes. The values are an average of three trials with their associated relative standard deviations. Figure reproduced by permission of The Royal Society of Chemistry..... 95

Figure 4.2 Turbidity study of pro-ligands Hmbo2p, Hmbt2p, Habt6p, and EDTA represented as resolubilisation efficiency at pH 6.6 for Cu(II) and 7.4 for Zn(II). The values are an average of three trials with their associated relative standard deviations. Figure reproduced by permission of The Royal Society of Chemistry. 97

Figure 4.3 Representative TEM images of A β ₁₋₄₀ aggregation studies, in which A β was incubated with Cu(II) and Zn(II) in the presence and absence of Hmbo2p, with the scale bar at 500 nm. Figure reproduced by permission of The Royal Society of Chemistry. 98

Figure 4.4 Binding profiles of Hmbo2p and Hdpp to A β fibrils, as determined by displacement of ThT. The data represents an average of three trials, with associated relative standard deviation. The binding curve for Hmbo2p was determined with GraphPad. The horizontal line for Hdpp is for illustrative purposes and represents the mean value of all measurements; a binding curve does not fit these data. Figure reproduced by permission of The Royal Society of Chemistry..... 100

Figure 4.5 BEnd.3 cell line viability in the presence of compounds cisplatin, Hzapp, Cu(zapp)₂, Zn(zapp)₂, and Fe(zapp)₃. Values are an average of three trials with standard relative deviation. Individual data for each compound are graphed in Figure A.30. Modified figure used with permission from Elsevier. 102

Figure 4.6 Composite images with bEnd.3 cell line – A. blank; B. incubated with DAPI; C. incubated with Hpbt2p. Excitation 405 nm; emission 435-485 nm. Scale bar at 50 μ m. 106

Figure 5.1 Neurotransmitter acetylcholine (ACh), and therapeutics tacrine and rivastigmine.	109
Figure 5.2 Solid state structures of A. Hppp and B. Cppp, represented as ellipsoid plots (50% probability). Solvent molecules and hydrogen atoms are omitted for clarity.....	123
Figure 5.3 Inhibition of <i>eel</i> AChE by Hppp, Cppp, and tacrine at various concentrations. Modified figure reproduced by permission of The Royal Society of Chemistry.	124
Figure 5.4 Inhibition kinetics of Cppp (16 μ M) and tacrine (0.1455 μ M) with <i>eel</i> AChE: enzymatic activity vs. time. Modified figure reproduced by permission of The Royal Society of Chemistry.....	125
Figure 5.5 Inhibition kinetics of Cppp and tacrine with <i>eel</i> AChE: Lineweaver-Burk plots in the absence of inhibitor (control) or at different concentrations of Cppp and tacrine. Modified figure reproduced by permission of The Royal Society of Chemistry.....	127
Figure 5.6 UV-vis spectroscopy study following the reactions between Cppp and Hppp and metal ions Cu(II), Zn(II), and Fe(III).....	128
Figure 5.7 The first generation compound (Cppp), as well as two second generation designs.	130
Figure 5.8 Solid state structures of Hhpp, Bnhpp, and Chpp, represented as ellipsoid plots (50% probability). Hydrogen atoms are omitted for clarity.	132
Figure 5.9 Inhibition kinetics of Chpp and Cbppp with <i>eel</i> AChE: enzymatic activity vs. time.	135
Figure 6.1 Age-based hypothesis for AD (adapted from ref. 160).	138
Figure A.1 ^1H NMR spectrum of reaction intermediate of Hmbo2p (300 MHz, 25 $^\circ\text{C}$, DMSO- d_6).....	166
Figure A.2 ^1H NMR spectrum of Hmbo2p (300 MHz, 25 $^\circ\text{C}$, DMSO- d_6). Figure reproduced by permission of The Royal Society of Chemistry.....	167

Figure A.3 ^{13}C NMR spectrum of Hmbo2p (75 MHz, 25 °C, DMSO- d_6). Figure reproduced by permission of The Royal Society of Chemistry.....	167
Figure A.4 ^1H NMR spectrum of Hmbt2p (300 MHz, 25 °C, DMSO- d_6). Figure reproduced by permission of The Royal Society of Chemistry.....	168
Figure A.5 ^{13}C NMR spectrum of Hmbt2p (151 MHz, 25 °C, DMSO- d_6). Figure reproduced by permission of The Royal Society of Chemistry.....	168
Figure A.6 ^1H NMR spectrum of Habt6p (600 MHz, 25 °C, DMSO- d_6). Figure reproduced by permission of The Royal Society of Chemistry.....	169
Figure A.7 ^{13}C NMR spectrum of Habt6p (151 MHz, 25 °C, DMSO- d_6). Figure reproduced by permission of The Royal Society of Chemistry.....	169
Figure A.8 ^1H NMR spectrum of Hpbo2p (600 MHz, 25 °C, DCM- d_2).....	170
Figure A.9 ^{13}C NMR spectrum of Hpbo2p (151 MHz, 25 °C, DCM- d_2).....	170
Figure A.10 ^1H NMR spectrum of Hpbt2p (600 MHz, 25 °C, DMSO- d_6).	171
Figure A.11 ^{13}C NMR spectrum of Hpbt2p (151 MHz, 25 °C, DMSO- d_6).	171
Figure A.12 ^1H - ^{13}C HSCQ spectrum of Hpbo2p (600 MHz, 25 °C, DCM- d_2).....	172
Figure A.13 ^1H - ^{13}C HMBC spectrum of Hpbo2p (600 MHz, 25 °C, DCM- d_2).....	172
Figure A.14 ^1H NMR spectrum of Zn(mbo2p) $_2$ (300 MHz, 25 °C, DMSO- d_6). Figure reproduced by permission of The Royal Society of Chemistry.....	173
Figure A.15 ^{13}C NMR spectrum of Zn(mbo2p) $_2$ (151 MHz, 25 °C, DMSO- d_6). Figure reproduced by permission of The Royal Society of Chemistry.....	173
Figure A.16 ^1H NMR spectrum of Ga(mbo2p) $_3$ (400 MHz, 65 °C, DMSO- d_6). Figure reproduced by permission of The Royal Society of Chemistry.....	174

Figure A.17 ^{13}C NMR spectrum of $\text{Ga}(\text{mbo2p})_3$ (151 MHz, 25 °C, DMSO-d_6). Figure reproduced by permission of The Royal Society of Chemistry.....	174
Figure A.18 ^1H NMR spectrum of $\text{Zn}(\text{mbt2p})_2$ (300 MHz, 25 °C, DMSO-d_6). Figure reproduced by permission of The Royal Society of Chemistry.....	175
Figure A.19 ^{13}C NMR spectrum of $\text{Zn}(\text{mbt2p})_2$ (151 MHz, 25 °C, DMSO-d_6). Figure reproduced by permission of The Royal Society of Chemistry.....	175
Figure A.20 ^1H NMR spectrum of Chpp (300 MHz, 25 °C, MeOD-d_4).	176
Figure A.21 ^{13}C NMR spectrum of Chpp (75 MHz, 25 °C, MeOD-d_4).	176
Figure A.22 ^1H NMR spectrum of Cchpp (300 MHz, 25 °C, MeOD-d_4).	177
Figure A.23 ^{13}C NMR spectrum of Cchpp (75 MHz, 25 °C, MeOD-d_4).	177
Figure A.24 ^1H NMR spectrum of Cbpp (300 MHz, 25 °C, DCM-d_2).	178
Figure A.25 ^{13}C NMR spectrum of Cbpp (75 MHz, 25 °C, DCM-d_2).	178
Figure A.26 HPLC chromatograph for the Cbppp after preparative TLC. HPLC gradient used was 50 to 100% of MeOH in H_2O for 10 minutes, followed by 10 minutes of 100% MeOH with 0.8 ml/min flow.....	179
Figure A.27 Controls for the fibril binding experiment: fluorescence of fibrils, ThT, and Hmbo2p alone. Fluorescence is additive when fibrils are added to Hmbo2p, and when ThT is added to Hmbo2p. Enhancement of fluorescence is observed when ThT and fibrils are incubated together, and upon addition of ligand Hmbo2p, this fluorescence is partly quenched. Figure reproduced by permission of The Royal Society of Chemistry.....	180
Figure A.28 Linearity of ThT under the study conditions. Figure reproduced by permission of The Royal Society of Chemistry.....	181

Figure A.29 Binding constant, K_d , for ThT (corrected for its intrinsic fluorescence) to $A\beta_{1-40}$ (~600 nM) under the study conditions. Data are an average of three trials, with relative standard deviation. Figure reproduced by permission of The Royal Society of Chemistry..... 181

Figure A.30 BEnd.3 cell line viability in the presence of compounds Hzapp, $Cu(zapp)_2$, $Zn(zapp)_2$, and $Fe(zapp)_3$, with respect to the concentration of ligand Hzapp. Figure used with permission from Elsevier. 182

Figure A.31 Composite image with bEnd.3 cell line incubated with Hpbo2p; 20x magnification. Excitation 405 nm; emission 435-485 nm. 182

List of Schemes

Scheme 1.1 Catalytic production of reactive oxygen species by an amyloid-beta-metal complex; adapted from ref. ¹⁵	4
Scheme 1.2 The HPO scaffold.....	28
Scheme 2.1 Previously studied HPOs for the potential use in AD in the Orvig group.	34
Scheme 2.2 Pro-ligand Hmbo2p, Hmbt2p, and Habt6p synthesis. Scheme reproduced by permission of The Royal Society of Chemistry.....	45
Scheme 2.3 Pro-ligand Hpbo2p and Hpbt2p synthesis.....	47
Scheme 5.1 Synthetic routes for Chpp.....	131
Scheme 5.2 Synthetic route for Cbppp.	133

List of Abbreviations

8-HQ	8-hydroxyquinoline
^{99m} Tc Bicisate (Neurolite®)	^{99m} Tc- <i>N,N'</i> -(1,2-ethylenediyl)bis-L-cysteine diethyl ester
AA	ascorbic acid, vitamin C, (5R)-5-(1,2-dihydroxyethyl)-3,4-dihydroxy-2(5H)-furanone
AAS	atomic absorption spectroscopy
Aβ	amyloid-beta
ABTS	2,2'-azino-bis(3-ethylbenzothiazoline-6-sulfonic acid) diammonium salt
ACh	acetylcholine, 2-acetoxy-N,N,N-trimethylethanaminium
AChE	acetylcholinesterase
AD	Alzheimer's disease
Ala	alanine
anal	analytical
APP	amyloid precursor protein
Asn	asparagine
Asp	aspartic acid
α-syn	α-synuclein
ATCI	acetylthiocholine iodide
ATCUN	amino terminus copper and nickel binding
BACE	β-secretase enzyme
BBB	blood-brain barrier
bEnd.3	brain endothelial immortalised mouse neuronal cell line

BF-227	2-(2-[2-dimethylaminothiazol-5-yl]ethenyl)-6-(2-[fluoro]ethoxy)benzoxazole
B _{max}	maximal binding
Bnabt6p	1-(2-aminobenzo[d]thiazol-6-yl)-3-(benzyloxy)-2-methylpyridin-4(1H)-one
BnChpp	4-(3-(benzyloxy)-2-methyl-4-oxopyridin-1(4H)-yl)phenyl dimethylcarbamate
Bnhpp	3-benzyloxy-1-(4-hydroxyphenyl)-2-methyl-4(1H)-pyridinone
Bnma	3-benzyloxy-2-methyl-4(1H)-pyrone
Bnzapp	1-(4-aminophenyl)-3-(benzyloxy)-2-methylpyridin-4(1H)-one
BrCp-cresol	4-(bromomethyl)phenyl dimethylcarbamate
Cbppp	4-(((2-methyl-4-oxo-1-phenyl-1,4-dihydropyridin-3-yl)oxy)methyl)phenyl dimethylcarbamate
CCA	coumarin-3-carboxylic acid
Cchpp	4-(3-((dimethylcarbamoyl)oxy)-2-methyl-4-oxopyridin-1(4H)-yl)phenyl dimethylcarbamate
CHN	carbon, hydrogen, nitrogen
Chpp	4-(3-hydroxy-2-methyl-4-oxopyridin-1(4H)-yl)phenyl dimethylcarbamate
cisplatin	cis-diamminedichloroplatinum(II)
clogP	calculated water-octanol partition coefficient

Cp-cresol	p-tolyl dimethylcarbamate
Cppp	2-methyl-4-oxo-1-phenyl-1,4-dihydropyridin-3-yl dimethylcarbamate
CuBD	copper binding domain
CQ	clioquinol (5-chloro-7-iodo-quinolin-8-ol)
cyclam	1,4,8,11-tetraazacyclotetradecane
d	doublet (in case of NMR data) or day
DAPI	4',6-diamidino-2-phenylindole
DCM	methylene dichloride
Deferiprone	3-hydroxy-1,2-dimethylpyridin-4(1H)-one
DFT	density functional theory
DMEM	Dulbecco's Modified Eagle Medium
DMSO	dimethyl sulfoxide
DNA	deoxyribonucleic acid
DTNB	5,5'-dithiobis-2-nitrobenzoic acid
donepezil	(RS)-2-[(1-benzyl-4-piperidyl)methyl]-5,6-dimethoxy-2,3-dihydroinden-1-one
EA	elemental analysis
EC ₅₀	the concentration required for half of the maximal effect
EDTA	ethylenediaminetetraacetic acid
EGTA	ethylene glycol-bis(2-aminoethylether)-N,N,N',N'-tetraacetic acid
ENDIP	N ¹ ,N ² -bis(pyridine-2-yl-methyl)ethane-1,2-diamine

EPR	electron paramagnetic resonance
ESCI	electrospray/chemical ionisation
EtOAc	ethyl acetate
<i>fac</i>	facial isomer
FBS	fetal bovine serum
G-361	human epithelial melanoma cell line
Glu	glutamic acid
GLUT-1	glucose transporter type 1
Gly	glycine
h	hour
Habt6p	1-(2-aminobenzo[d]thiazol-6-yl)-3-hydroxy-2-methylpyridin-4(1H)-one
Hbt2p	1-(2-benzothiazolyl)-3-hydroxy-2-methyl-4(1H)-pyridinone
Hbt6p	1-(6-benzothiazolyl)-3-hydroxy-2-methyl-4(1H)-pyridinone
Hcmp	2-(3-hydroxy-2-methyl-4-oxopyridin-1(4H)-yl)acetic acid
Hcpp	1-(4-carboxyphenyl)-3-hydroxy-2-methyl-4-oxopyridine
Hdapp	2-methyl-3-hydroxy-1-(4-dimethylaminophenyl)-4(1H)-pyridinone
Hdpp	see Deferiprone
HEPES	4-(2-hydroxyethyl) piperazine-1-ethanesulfonic acid
HepG2	human epithelial hepatocellular carcinoma cell line

Hhpp	3-hydroxy-1-(4-hydroxyphenyl)-2-methyl-4(1H)-pyridinone
His	histidine
Hmbo2p	1-(benzo[d]oxazol-2-ylmethyl)-3-hydroxy-2-methylpyridin-4(1H)-one
Hmbt2p	1-(benzo[d]thiazol-2-ylmethyl)-3-hydroxy-2-methylpyridin-4(1H)-one
Hnpp	1-benzyl-3-hydroxy-2-methyl-4(1H)-pyridinone
HOMO	highest occupied molecular orbital
HOS	human epithelial and fibroblast osteosarcoma cell line
Hpbo2p	1-(4-(benzo[d]oxazol-2-yl)phenyl)-3-hydroxy-2-methylpyridin-4(1H)-one
Hpbt2p	1-(4-(benzo[d]thiazol-2-yl)phenyl)-3-hydroxy-2-methylpyridin-4(1H)-one
HPLC	high pressure liquid chromatography
Hppp	3-hydroxy-2-methyl-1-phenyl-4(1H)-pyridinone
HPO	hydroxypyridinone
HR-ESIMS	high-resolution electrospray ionisation mass spectrometry
HSAB	hard and soft acids and base
Hsapp	2-methyl-3-hydroxy-1-(4-methylaminophenyl)-4(1H)-pyridinone
Hz	Hertz
Hzapp	1-(4-aminophenyl)-3-hydroxy-2-methyl-4(1H)-pyridinone

IC ₅₀	the concentration required for half of the maximal inhibitory effect
ITC	isothermal titration calorimetry
IR	infrared
K-562	human lymphoblast leukemia cell line
K _d	dissociation constant
Kemp acid	<i>cis,cis</i> -1,3,5-trimethylcyclohexane-1,3,5-tricarboxylic acid
K _i	constant of inhibition
L	ligand
LC	liquid chromatography
log β/log K	stability constant
log BB	brain tissue to plasma distribution ratio
LUMO	lowest unoccupied molecular orbital
m	multiplet
M	metal or molar
MCF-7	human epithelial breast cancer cell line
Me	methyl
MeOH	methanol
<i>mer</i>	meridional isomer
MES	2-(<i>N</i> -morpholino) ethanesulfonic acid hydrate
Met	methionine
MilliQ	water with 18.2 MΩ•cm resistivity
MiLogP	see clogP

ML	metal-ligand complex
MP	metal-protein complex
MTT	(3-(4,5-dimethyl-2-thiazolyl)-2,5-diphenyl-2H-tetrazolium bromide
myricetin	3,5,7-trihydroxy-2-(3,4,5-trihydroxyphenyl)-4-chromenone
m/z	mass-to-charge ratio
NBS	<i>N</i> -bromosuccinimide
ND	neurodegenerative disease
NMR	nuclear magnetic resonance
P	protein
PBT2	(5,7-dichloro-2-((dimethylamino)methyl)-8- hydroxyquinoline
PBS	phosphate buffered saline
PCM	polarizable continuum model
PD	Parkinson's disease
PET	positron emission tomography
PIB	Pittsburgh Compound B, [<i>N</i> -methyl]2-(4'- methylaminophenyl)-6-hydroxybenzothiazole
p <i>K</i> _a	acid dissociation constant
pM	concentration of unchelated metal ions
PPA	polyphosphoric acid
PrD	prion diseases
PrP	prion protein

PrP ^{Sc}	protease-resistant prion protein
R _f	retardation factor
RGB	red, green, blue
rivastigmine	(S)-3-[1-(dimethylamino)ethyl]phenyl <i>N</i> -ethyl- <i>N</i> -methylcarbamate
ROS	reactive oxygen species
tacrine	1,2,3,4-tetrahydroacridin-9-amine
s	singlet
TEA	triethylamine
TEAC	Trolox-equivalent antioxidant capacity
TCI	Tokyo Chemical Industry, Co., Ltd.
TD	time dependent
TEM	transmission electron microscopy
ThT	Thioflavin-T, 4-(3,6-dimethyl-1,3-benzothiazol-3-ium-2-yl)- <i>N,N</i> -dimethylaniline chloride
TLC	thin layer chromatography
TPEN	<i>N,N,N',N'</i> -tetrakis(2-pyridylmethyl)ethylenediamine
TPSA	topological polar surface area
Trolox	6-hydroxy-2,5,7,8-tetramethylchromane-2-carboxylic acid
Tris	tris(hydroxymethyl)aminomethane
Tyr	tyrosine
UB3LYP	unrestricted, Becke, 3-parameter, Lee-Yang-Parr functional
UV	ultraviolet

UV-vis

ultraviolet-visible

V_i

initial velocity

WHO

World Health Organisation

Acknowledgements

This thesis was a result of a team effort. I want to thank all of the members of the department who helped me along the way, especially Jacquie for friendship and support, Kyle for conversations, Andrew for his shining attitude, Tulin for great humour, Danielle for being my NFL buddy; the chemists Lyndsey, HHH, Amanda, and Isaac for all the great tiki times; Robin for being a wonderful TA mentor; and members of the Kennepohl and Fryzuk groups.

I appreciate the help of the Orvig group members, especially Paloma, who was my rock during classes and exams, Yasmin, who helped me with all the beginnings of chemical synthesis set up and welcomed me to the group and the department, Cristina for all the positive energy and help, JC for the tremendous amount of work on the project, Caterina for being a pleasure to work and conference with, undergrads Gwen for the amazing work, and Mike and Stan for being good sports, Eric, and members of the department - Jessie and Elena for helping me with cell studies, NMR and MS/EA service staff, especially Marshall for his good nature, Dr. Brian Patrick for all his amazing tricks on my smallest crystals, and Helen for safety conscientiousness. For help with my project from those outside of the department – thank you to Dr. Kelly McNagny for providing the bEnd.3 cell line.

Special thanks to my boss, Dr. Chris Orvig, for being a great mentor, open to my comments, working hard on my behalf, and giving me the freedom to pursue my dreams.

Acknowledgements to the Alzheimer Society of Canada and Natural Sciences and Engineering Research Council of Canada for giving me financial support; and to boss for sending me to many conferences. Without these extremely generous actions, I would not have finished my work.

I would also like to thank my comprehensive exam committee members - Dr. Fryzuk for advice, encouragement, and reference letters, and Dr. Pierre Kennepohl for reference letters and giving me feedback on my thesis.

As well, thanks to my friends for the visits that kept me on track– Norah, Janey, Rob, and Rebecca; and to my friends in San Francisco, especially Naomi, Colin, and Fred who always make me feel welcomed.

The knowledge I possess is cumulative, and so I would like to acknowledge all of my past school and college teachers. For the greatest lessons and sources of inspiration – deepest gratitude to my mom, my grandmothers Vera and Tonya, and the rest of my family in Irkutsk, who always support me and exemplify that in any situation, it is possible to rise up and help other people, as well as the flora and the fauna. And, of course, my grandmother, Dr. Vera B. Pukhnarevich, is credited for my chemical destiny.

This thesis is dedicated to my biggest advocate, my mom.

Chapter 1: Introduction

This chapter will introduce the role of metals in biology and review the current literature on the role of metals in neurodegenerative diseases. The focus will shift to a specific family of chelating ligands, elaborating on its special features, as well as to how the remainder of the thesis unfolds in supporting the main hypothesis.

1.1 Contributions of inorganic chemistry to medicine

Metal ions are essential in biological systems. In the human body, there are metal ions such as the weakly bound, mobile Na^+ and K^+ that are present in high concentrations,¹ while others are present in lower amounts, but are also crucial to proper function.² For instance, iron in hemoglobin binds oxygen for its transport, zinc has a structural role in DNA-binding proteins,³ and copper has a catalytic role in enzymes such as superoxide dismutase.⁴ Not only do metals have structural and catalytic roles, but they are also found to be neurotransmitters.⁵ Tight regulation of metal ions is essential for normal function; in certain diseases misregulation leads to labile pools of metal ions that are toxic to the organism.⁶ Bioinorganic chemists have contributed to the understanding of the roles of metal ions in biological systems by identifying the function of metals in proteins, by creating ligand systems to mimic biological ones, and by pushing physical methods to probe these systems *in vivo*.

The other way in which inorganic chemists have contributed is through development of metal-containing agents for the purposes of treating or imaging diseases. The most famous modern example is cisplatin (Figure 1.1), which was approved by the U.S. Food and Drug

Administration in 1978 and is still used for cancer therapy.⁷ Other examples include NeuroLite® (^{99m}Tc Bicisate), a technetium containing radioimaging agent for cerebral blood flow.⁸

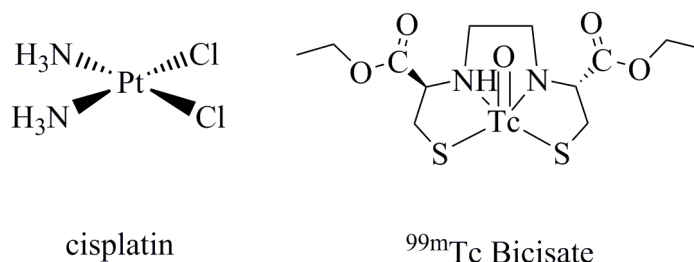


Figure 1.1 Cancer drug cisplatin and imaging agent ^{99m}Tc Bicasate (NeuroLite®).

1.2 Introduction to the role of inorganic chemistry in neurodegenerative diseases

In recent years, there has been increasing media coverage of neurodegenerative diseases (NDs) due to the realisation that, while deaths due to major diseases like cancer and stroke are on the decline,⁹ NDs still have no prevention or cure, and diagnosis is only definitive *post mortem*. Our population is ageing due to improved healthcare; therefore, NDs such as Alzheimer's disease (AD), Parkinson's disease (PD), and prion diseases (PrDs) are becoming more prevalent and the burden on our healthcare and economic systems is bound to become overwhelming unless there are major breakthroughs in drug development. According to the 2012 World Health Organization (WHO) report on dementia, over 35 million people are currently living with dementia, of which Alzheimer's disease is the biggest cause, and it is costing our world over \$US 600 billion a year.¹⁰

The difficulty of treating neurodegenerative diseases comes in part from a paucity of biomarkers to identify the onset and to monitor the progress of these diseases. By the time the symptoms

such as memory loss for AD and tremors for PD warrant a clinical diagnosis, the disease has progressed for years. The loss of neurons is significant at this point and many parts of the brain are already compromised beyond repair. Currently, the drugs that are offered only treat the symptoms – improving memory for AD patients, which works for 1-2 years in about a third of the patients,¹¹ and reducing movement inability in PD.¹² Disease progression is neither slowed down nor reversed. For prion diseases, there is currently no prescribed medication available.

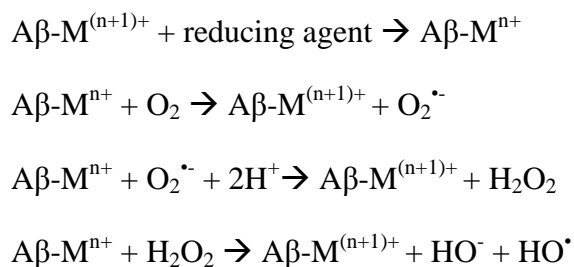
The incomplete understanding of disease pathology is a significant factor contributing to the difficulty in therapeutic agent discovery and development. What we do know is that the neurodegenerative diseases AD, PD, and PrDs have in common a key respective aberrant protein whose inherent propensity to misfold is increased in the presence of metal ions.¹³ In this way, coordination chemistry can offer us a way to understand disease progression as well as a guide to reversing it. First, Chapter 1.4 will examine the coordination of disease-associated metal ions (e.g. copper, zinc, iron, etc) to proteins associated with NDs (amyloid β ($A\beta$) for AD, α -synuclein (α -syn) for PD, and the prion protein (PrP) for the prion diseases), followed by relevant examples of chelating ligands designed to intervene in disease pathology in Chapter 1.5. Another way to interfere with metal ion binding to metalloproteins is to block the coordination sites on these proteins, but this strategy will not be discussed.

Neither association of metals with proteins nor metal binding therapy is limited to the field of neurodegeneration. About one third to a half of our enzymes contains metals that are key to their function. Chelating ligands that are used to successfully treat diseases abound – for example, iron and copper overload disorders can be clinically treated with such agents.¹⁴

1.3 Overview of metal ion roles in neurodegenerative diseases

1.3.1 Alzheimer's disease (AD)

Plaques and neurofibrillary tangles are the hallmarks, and are used as a *post mortem* markers, of AD.¹³ Cu(II) and Zn(II) are known to co-localise with plaques.⁶ The main component of plaques is A β , a protein with unknown function that is cleaved from its parent amyloid precursor protein (APP), resulting in 39 to 42 amino acid-long chains (the latter of which has a sequence DAEFRHDSGYEVHHQKLVFFAEDVGSNKGAIIGLMVGGVVIA). The most bio-relevant forms of A β are the soluble 40 and the insoluble 42 amino acid fragments, the latter being the most prevalent form found in plaques.⁶ In addition to crosslinking and increasing toxicity of A β , metal ions have another deleterious role in AD pathology.⁶ Cu(II) and Fe(III) are also known to generate reactive oxygen species (ROS) while bound to A β , and this catalytic process contributes to neuronal damage.⁶ It was shown that A β itself is able to reduce metal ions, but a greater amount of ROS is produced through the catalytic process that is represented in Scheme 1.1, below.¹⁵ Chapters 1.4.1 and 1.4.2 will review the latest understanding of binding sites and stabilities of metal ions copper, zinc, and iron with APP and A β .



Scheme 1.1 Catalytic production of reactive oxygen species by an amyloid-beta-metal complex; adapted from ref.¹⁵

1.3.2 Parkinson's disease (PD)

The first patient symptom leading to the diagnosis of PD is motor dysfunction arising from neuronal damage in the *substantia nigra pars compacta*.¹² In Parkinson's disease, the pathological features include Lewy bodies, comprised of α -synuclein and other components,¹² as well as elevation of Fe(III) with a concomitant decrease of the iron-storage protein ferritin in the brain.¹⁶ This unchelated iron can cycle through its oxidation states and produce ROS that are ultimately damaging to the surrounding neurons (as per Scheme 1.1). Chapter 1.4.3 will detail current information on α -syn binding.

1.3.3 Prion diseases (PrD)

Prion diseases are a collection of neurodegenerative diseases that affect many species.¹⁷ Mad cow disease (bovine spongiform encephalopathy) is the most widely known example; human versions of the diseases include the Creutzfeldt–Jakob disease, Gerstmann–Sträussler–Sheinker disease, and fatal familial insomnia.¹⁷ The prion protein (PrP) undergoes conversion to β sheet rich form PrP^{Sc}, which has been identified as the infectious agent of this disease.¹⁷ The PrP^{Sc} protein is then able to convert other PrP into malicious forms, which are prone to aggregate and precipitate, thus causing toxicity to the neuronal cells.¹⁷ Chapter 1.4.4 will present the current understanding of PrP binding to metal ions.

1.4 Metal ions binding to proteins implicated in neurodegenerative diseases (NDs)

This section reviews metal chelation to the amyloid precursor protein, as well as amyloid β , α -synuclein, and prion proteins that are implicated in AD, PD, and PrDs, respectively.

Since it was found that metal binding has an important role in disease pathology, researchers have tried to elucidate the ligands that bind metals *in vivo*. The coordination environment around the metal ions is guided by the same principles first established by Alfred Werner – we expect the metal ions to be coordinated by neutral or negatively charged ligands, whose number and arrangement around the centre depends on the oxidation state of the metal. Thus, for Cu(II) one expects to find four to six chelating groups in distorted geometries such as square planar, tetrahedral, square pyramidal, and octahedral. To uncover the identity of those four ligands, the hard and soft acids and bases (HSAB) theory may be used. For instance, since Cu(II) is a Lewis acid of intermediate strength, one expects to find nitrogen and oxygen atoms in its coordination sphere. Since the sequences of these proteins are known, there is a limited number of potential ligands available, and knowing the preferences of each metal ion of interest makes their revelation an easier endeavor. For instance, the binding of Cu(II) is expected to occur with the nitrogen-containing amino acid histidine, pendent amines and the free terminal NH₂ group, as well as backbone amide nitrogen atoms. Oxygen donor atoms may come from amino acids such as tyrosine, aspartate, backbone carbonyl groups, and water molecules.

As studying metal-protein interactions *in vivo* is not yet feasible, *in vitro* and computational studies are utilised. For *in vitro* studies, fragments of proteins are typically used, as they are easier to handle than full-length proteins. There is a variety of physical and analytical methods used to elucidate ligands: electron paramagnetic resonance (EPR), nuclear magnetic resonance (NMR) that relies on shifts in protein signals to determine groups that are in the vicinity of metal ions, and X-ray crystallography for those metal-protein complexes isolated as single crystals. While the latter technique provides a clearer picture of the coordination environment, depiction

of a protein in its solid state may not correspond to its behavior in solution, especially since some metal ions have exchanging ligands around them.

Accordingly, amino acids within monomeric forms of peptides APP, A β , α -syn, and PrP that participate in metal binding and binding constants will be discussed herein. Binding will be presented as the dissociation constant, K_d , which is calculated using eqn (1.1), where M represents the metal ion, P represents the protein or its fragment, and MP represents the metal-protein complex.

$$K_d = \frac{[M][P]}{[MP]} \quad (1.1)$$

Note that the K_d values presented herein are conditional in that they are only valid under the exact experimental conditions described; the advantages and disadvantages of using this estimation of metal binding are described elsewhere.¹⁸ Binding constants presented can be determined using the heat released upon coordination via isothermal titration calorimetry (ITC), a change in fluorescence, or circular dichroism, typically in a buffered solution. Most buffers consist of compounds Tris (tris(hydroxymethyl)aminomethane), HEPES (4-(2-hydroxyethyl)piperazine-1-ethanesulfonic acid), MES (2-(N-morpholino) ethanesulfonic acid hydrate) with 100-150 mM NaCl, or PBS (phosphate buffered saline) at pH 7.4 to create near-physiological conditions.

1.4.1 Amyloid precursor protein (APP)

Amyloid precursor protein (APP) is a ubiquitous 695 amino-acid trans-membrane protein¹⁹ that has been shown to bind Cu(I), Cu(II), Zn(II), and Fe(III). The most clear metal binding site on

APP is located in the Copper Binding Domain (CuBD), which has been shown to bind both Cu(I) and Cu(II) resulting in similar coordination spheres, as determined for the APP₁₃₃₋₁₈₉ fragment by X-ray crystallography.²⁰ Cu(I) is coordinated by amino acids His147, His151, and Tyr168, as well as a water molecule, resulting in a distorted square planar coordination; Cu(II) is in a distorted square pyramidal geometry with a second water molecule as the fifth ligand (Figure 1.2).²⁰ The sulphur of Met170 that has been implicated in metal binding instead of water by NMR studies of APP₁₂₄₋₁₈₉,²¹ is 7 Å away from the metal in the solid state, and is thus unlikely to participate in metal binding.²⁰ Additional EPR studies on the APP₁₂₄₋₁₈₉ fragments revealed distorted square pyramidal geometry around the Cu(II) centre.²¹ This discrepancy between the solution and solid states is not unexpected; in the study of the solid state structure, Cu(II) ions were added to pre-formed crystals of the apo-protein, and it is possible that the protein under these conditions could not rearrange to assume its optimal binding conformation.

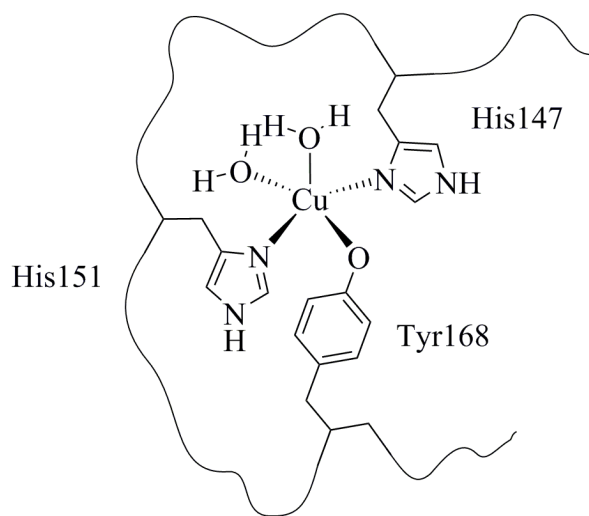


Figure 1.2 Cu(II) binding site in the copper domain of APP as elucidated from its solid state structure, adapted from ref.²⁰ The geometry and the amino acids involved around the metal centre are depicted for illustrative purposes. Figure reproduced by permission of The Royal Society of Chemistry.

An additional binding site for Cu(II) and Zn(II) has been identified in the E2 domain in the APP₂₉₅₋₅₀₀ fragment using X-ray crystallography.²² For Zn(II), three histidines (382, 432, and 436) as well as a water molecule are involved in binding to create a near tetrahedral geometry around the metal centre, while an additional histidine (313), is implicated in Cu(II) chelation.²² Binding constants K_d , as determined from ITC, are 13 ± 5 nM for Cu(II) and 3.9 ± 1.5 μ M for Zn(II) (Table 1.1).²² Another binding site for Zn(II) was identified in the 181-188 amino acid region, with two cysteines (188, 189) participating in binding.²³ As well, APP has been shown to interact with Fe(II), presumably through two glutamic acids 412 and 415 of the ferroxidase REXXE sequence.²⁴

1.4.2 Amyloid β (A β)

The A β fragments originate from the 600 amino acid region of the parent APP sequence; this does not include any of the binding sites of APP described above. As with other proteins that are prone to aggregate, the 40 and 42 amino acid-long A β fragments are difficult to study in order to elucidate the amino acids that participate in metal binding. Since it has been found that it is the first 16 residues that contain the strong metal binding site for Cu(II) and Zn(II), A β ₁₋₁₆ is the fragment that is most commonly studied.²⁵

Table 1.1 Coordination of biorelevant metal ions to metalloproteins implicated in neurodegenerative diseases. Table reproduced by permission of The Royal Society of Chemistry.

Protein	Metal	Ligands implicated in coordination	K_d and conditions
APP	Cu(I)	His147, His151, Tyr168, water ²⁰	e.g., APP-E2 for all the following: ²² 13±5 nM (ITC, pH 7.3 50 mM Tris, 150 mM NaCl, 20 °C) 3.9±1.5 µM (ITC, pH 7.3 20 mM HEPES, 150 mM NaCl, 20 °C)
	Cu(II)	His147, His151, Tyr168, 2 waters ²⁰ or His147, His151, Tyr168, Met170 ²¹ His313, His382, His432, His436, water ²²	
	Zn(II)	His382, His432, His436, water ²²	
Aβ	Fe(II)	Cys188, Cys189, others ²³ Glu412, Glu415, others ²⁴	e.g., Aβ ₁₋₂₈ for all the following: ³⁰ fluorescence: 2.5 µM (pH 7.2 10 mM HEPES); 28 µM (pH 7.4 100 mM Tris, 100 mM NaCl) ITC: 0.1 µM (pH 7.4 50 mM HEPES, 100 mM NaCl) fluorescence: 1.1±0.08 µM (pH 7.2 10 mM sodium phosphate buffer, 20 °C); 6.6±0.2 µM (pH 7.2 10 mM HEPES, 20 °C) ITC: 10±8 µM (pH 7.4 20 mM Tris, 100 mM NaCl, 25 °C)
	Cu(I)	His13, His14 ²⁶	
	Cu(II)	His6, Asp1-Ala2 carbonyl, Asp1 NH ₂ ; His13/14 (component 1a/b) ²⁷ His6, His13, His14, Ala2 carbonyl ²⁸ or His, Asp1 NH ₂ , Asp-Ala2 amine, Ala2-Glu3 carbonyl ²⁹ (component 2)	
	Zn(II)	His6, His13, His14, likely Asp1, Glu11 ³¹	
	Fe(II)	His6, His13/14, Asp1 NH ₂ group, carboxylic acid (Asp1 or Glu3) and carbonyl group (Asp1 or His6) ³²	
α-syn	Fe(III)	not detected ³³	120±160 nM α-syn for all the following: ³⁵ 36±36 µM Circular dichroism, pH 6.5 20 mM MES, 100 mM NaCl, 15 °C 470±80 µM
	Cu(II)	Met1 NH ₂ , deprotonated backbone nitrogen, Asp2, water ³⁴ His50, deprotonated backbone nitrogens from His50 and Val49, water ³⁶ Asp121, likely Asp119, Asn122, Glu123 ^{37,38}	
	Prion	His61, His69, His77, His85 (1 Cu) His, 2 backbone nitrogen, oxygen atoms (e.g. His61, Gly62, Gly63) (4 Cu) ³⁹	
			e.g., 4 octarepeat PrP region: 6.7 µM (fluorescence, pH 7.4 PBS, 20 °C) ⁴⁰

There are two Cu(II) binding modes that A β ₁₋₁₆ exhibits, one that predominates at pH 6.5 (component 1) and another at pH \geq 8 (component 2), as revealed by EPR.²⁹ Due to the presence of both components at physiological pH, the two binding modes are studied separately at their corresponding pH values. Within component 1, there are two structures in equilibrium (a and b), three binding positions of both involve His6, an Asp1-Ala2 carbonyl backbone oxygen, and a terminal NH₂ Asp1 group; the remaining coordination site is occupied by His13 and His14 for components 1a and 1b, respectively (Figure 1.3, left).²⁷ The second component has a less established coordination: it has been shown to bind to three histidines as well as the Ala2 carbonyl oxygen,²⁸ or a histidine, terminal NH₂, backbone nitrogen Asp1-Ala2, and backbone carbonyl Ala2-Glu3 (Figure 1.3, right).²⁹

The same region of A β is involved in binding other metal ions, such as Cu(I), Zn(II), and Fe(II/III). For instance, Cu(I) has linear coordination geometry via binding His13 and His14.²⁶ The coordination environment around Zn(II) has not been fully elucidated, as even the coordination number of 4 or 6 is not firmly established; by NMR the site is found to include all three histidine residues as well as possibly Asp1 and Glu11.³¹ Fe(II) was found to bind two histidines (6 and 13/14), a terminal NH₂ group, a carboxylic acid (Asp1 or Glu3) and a carbonyl group (Asp1 or His6) by NMR studies.³² Fe(III), on the other hand, was found to have no appreciable binding to A β by NMR and mass spectrometry.³³

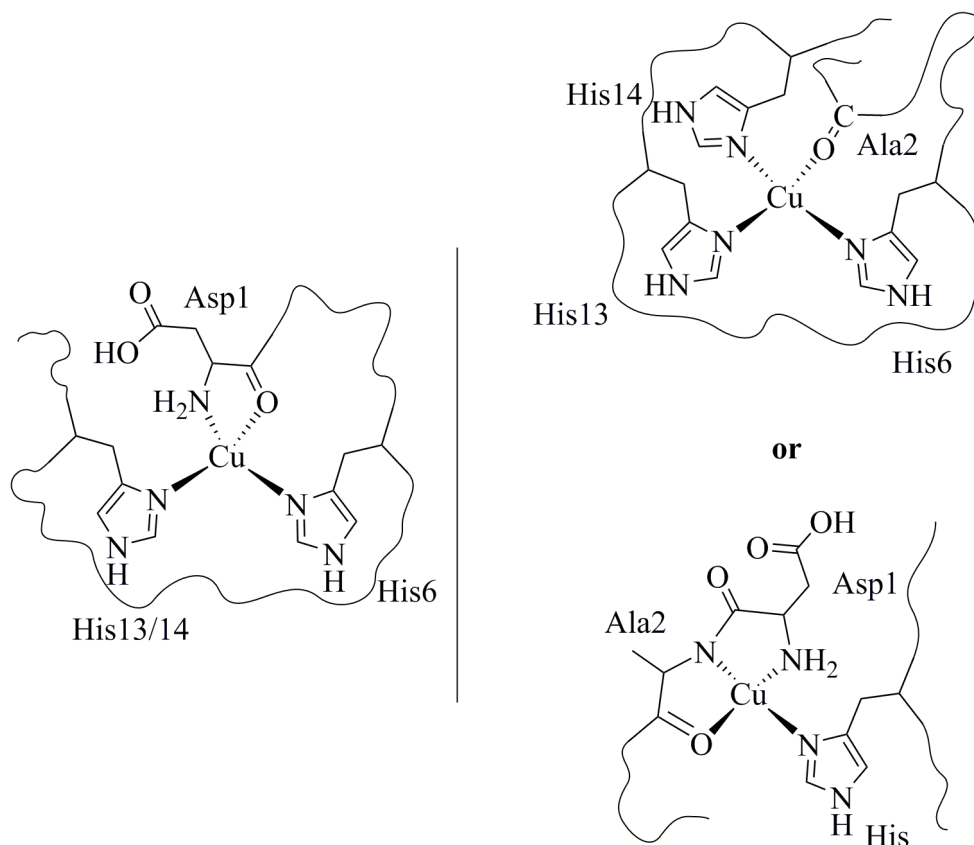


Figure 1.3 Cu(II) coordination to A β , adapted from refs.^{27,29} **Left: component 1a/b, right: two likely structures for component 2.** The geometry and the amino acids involved around the metal centre are depicted for illustrative purposes. Figure reproduced by permission of The Royal Society of Chemistry.

Affinities of A β of variable lengths (e.g. 16, 28, 40, 42) to Cu(II) have been established using a variety of methods and have been recently reviewed.³⁰ Estimations of K_d vary from 0.01 to 30 μM (see examples in Table 1.1) depending on the experiment, as different techniques require different concentrations and thus the speciation of protein may be different.³⁰ The authors note that it is challenging to establish not only the association of metals to A β *in vitro* in the monomeric form, but then to translate that into *in vivo* monomeric and aggregated forms of A β .³⁰ For Zn(II), K_d values also vary depending on length of A β and technique used, for example, K_d

= $10 \pm 8 \mu\text{M}$ as determined by ITC for low concentrations of $\text{A}\beta_{1-28}$, by fluorescence it has been established to be 1.1 and $6.6 \mu\text{M}$ depending on the buffer used (Table 1.1).³⁰

1.4.3 α -Synuclein (α -syn)

The C-terminus of α -synuclein is a 140 amino acid protein of unknown function found to bind divalent Fe, Ni, Co, and Mn ions, albeit very weakly.⁴¹ Asp121 is the main residue involved; this binding does not induce a major structural peptide change.⁴¹ Cu(II), conversely, was found to bind to α -syn with $K_d \sim 0.1 \mu\text{M}$ and increase the rate of its aggregation.⁴¹

α -Synuclein can accommodate up to three Cu(II) ions in two high affinity N-terminus sites and one low affinity site at the C-terminus.³⁸ At the N-terminus, the first binding site has contributions from the first four amino acids: the free NH_2 of Met1, a deprotonated backbone nitrogen, and Asp2, with an additional water molecule (Figure 1.4).³⁴ The second site is Asp121,³⁷ and Asp119, Asn122, and Glu123 as well.³⁸ The K_d values in order of decreasing strengths are: 120 nM, $36 \mu\text{M}$, $470 \mu\text{M}$ (Table 1.1), all estimated by monitoring metal titrations with circular dichroism.³⁵ Similar values have been reported in other reports, although there is much variation in experimental procedures and thus a variability of reported values.³⁸

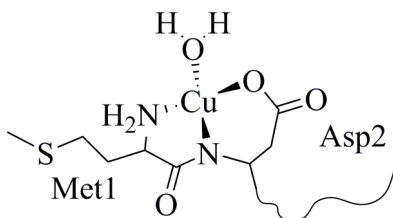


Figure 1.4 The strongest binding site in α -syn, adapted from ref.³⁸ The geometry and the amino acids involved around the metal centre are depicted for illustrative purposes. Figure reproduced by permission of The Royal Society of Chemistry.

1.4.4 Prion protein (PrP)

PrP has been shown to bind many metal ions, including Zn(II), Ni(II), and Mn(II), at two metal-binding regions of this 254 amino-acid long protein.⁴² PrP affinity for these metal ions is low, and thus, the focus will be on the strongest interacting metal Cu(II).⁴² The first section of the protein that participates in metal binding can bind up to 4 ions and consists of four “octarepeat” regions with amino acid sequence PHGGGWGQ.³⁹ The four histidine amino acids (61, 69, 77, and 85), one from each octarepeat, are involved in metal binding, coordination of which changes with addition of each copper (Figure 1.5) as determined by EPR.³⁹ For instance, the first Cu(II) is bound by 4 histidines (or 3 histidines and a water molecule) (component 3, Figure 1.5, left), while upon the binding of the fourth ion, each histidine is bound to a single copper with the two amide and one oxygen backbone donors as the other coordination sites (e.g. His61, Gly62, Gly63) (component 1, Figure 1.5, right).³⁹

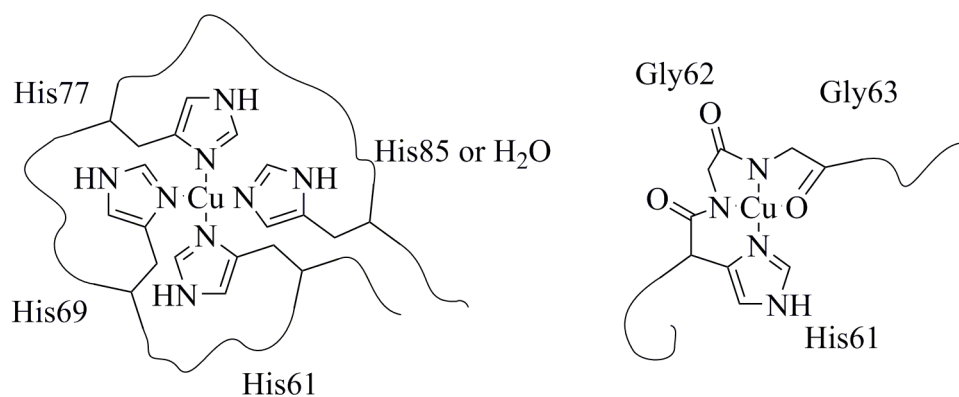


Figure 1.5 Two Cu(II) coordination modes for the octarepeat region of the prion protein, adapted from ref.³⁹ **Left: binding of one Cu(II) to PrP, right: binding of four Cu(II) to PrP.** The geometry and the amino acids involved around the metal centre are depicted for illustrative purposes. Figure reproduced by permission of The Royal Society of Chemistry.

The second metal binding site on PrP can bind two Cu(II) ions independently; each coordination site includes one of the histidine residues, 96 or 111, as well as two neighboring amide backbone nitrogens and an oxygen donor from water or another amino acid.⁴³ Due to the difficulties working with the full protein, studies for binding affinities are carried out with segments of the protein. There exists a great variety of estimations under a variety of conditions;¹⁸ the octarepeat K_d is estimated to be 6.7 μM by fluorescence (Table 1.1).⁴⁰

1.4.5 Metalloprotein summary and outlook

Consulting Table 1.1, some conclusions can be inferred about preference of metal ions for certain coordination environments in the APP, A β , α -syn, and PrP proteins. Focusing on Cu(II) coordination, it becomes apparent that the strong binding sites involve at least one, and up to four, aromatic nitrogen atoms from histidine amino acids. Less often there are also aliphatic tertiary deprotonated backbone nitrogens, and the free NH₂ terminus can also participate in binding. There is a variety of oxygen donors, such as from water, and tyrosine, glutamate, and aspartate amino acids, as well as backbone carbonyl groups. The affinities for Cu(II) can be generally estimated as 0.01-30 μM for A β , 0.120 nM for α -syn, and 6.7 μM for prion protein. It should be noted that these constants were determined in different conditions with different methods by different authors, in many cases with truncated proteins and in the presence of competitor ligands. Thus, these values cannot be compared to one another and it is pretty much impossible to standardise as traditional Werner-type stability constants (β or K). It would be beneficial in the future to have similar conditions to be able to compare binding constants among proteins, as well as definitively determine why using different methods with the same protein results in up to thousand-fold differences in K_d values, and to then establish which method is best

suited for this analysis. It should be added that although multiple K_d values can be determined experimentally for these proteins, figures approaching mM are unlikely to be relevant in a biological setting. Nonetheless, this information may be used for chelator design and to predict which synthetic ligands are likely to compete for metal ions with disease-relevant proteins.

1.5 Metal binding therapy

Given the negative effect that coordination of metal ions has on proteins that are associated with NDs, it is no surprise that medicinal chemists have started looking at chelation via multidentate ligands as a way to modify and possibly even reverse disease pathology.

1.5.1 Alzheimer's disease

With few exceptions, medicinal chemists who have an inorganic focus on drug development for AD are concerned with chelating copper ions, giving slightly less emphasis to zinc. Iron chelation, while important in terms of pacifying reactive oxygen species, remains outside of the vast majority of published work.

Since it was shown that common metal chelating ligands like bathocuproine, ethylene glycol tetraacetic acid (EGTA), and N,N,N',N'-tetrakis(2-pyridylmethyl)ethylenediamine (TPEN) are able to reverse amyloid aggregation *post mortem*,⁴⁴ chelators with more nuanced binding preferences have been studied to avoid the indiscriminate strong binding that is associated with EGTA-like compounds.⁴⁴ Additionally, it is important to obviate binding other divalent metals like Ca(II) and Mg(II), whose depletion has an adverse effect on plaque dissociation.⁴⁴

Following the ligand-metal preference of the HSAB paradigm, copper(II) and zinc(II) chelating ligands are chosen or designed to incorporate N and O atoms, while copper(I) chelators include S and N donors; Fe(III) binders have predominantly O atoms, as in the binding of the disease-relevant proteins (see above). Another consideration of ligand design includes metal binding affinity, which must be comparable to that of A β to compete for it, but not so exceedingly high as to compete with other essential metalloproteins for the metal ions.

In this section, the ligands will be arranged by their chelating groups, with one example chosen for each scaffold. The molecules include bidentate, tridentate, tetradentate, and macrocyclic examples, with a tabulation of the metal chelation studies of these potential therapeutic agents and considerations for ligand design. As a measure of metal binding, association with metal ions as determined by stability constants ($\log K$ or $\log \beta$, eqn (1.2), where M represents the metal ion and L represents the ligand) and concentrations of unchelated metal ions (pM, eqn (1.3), where M represents the metal ion under specific conditions) will be considered, as will dissociation constants K_d (eqn (1.1)).

$$\log \beta = \log\left(\frac{[ML]}{[M][L]}\right) \quad (1.2)$$

$$\text{pM} = -\log[M_{\text{free}}] \quad (1.3)$$

As a selection of chelating agents described herein participates in binding that has multiple compounds to one metal ion, multiple $\log \beta$ values will be included. $\log K$ values are calculated using the same eqn (1.2) as is used for $\log \beta$ values, with a difference being that it is calculated at

specific conditions and is encountered in the literature as $\log K_{eff}$ (effective) or $\log K_{cond}$ (conditional). Large positive pM values indicate low concentration of free uncomplexed metal ion, demonstrating effective metal complexation by the ligand. It should be noted that pM, $\log K$, and K_d values are conditional, and cannot be directly compared to $\log \beta$ values. As another indication of metal binding, metal-induced A β aggregate resolubilisation, and inhibition thereof, will be briefly mentioned.

1.5.1.1 Ligands based on aromatic nitrogens

As histidines play a big role in copper binding to the A β protein, most scaffolds have at least one aromatic nitrogen that participates in binding, (Figure 1.6).

The first examples, ligands L_1 ⁴⁵ and L_2 (ENDIP)⁴⁶ incorporate two aromatic nitrogens as electron donor groups (Figure 1.6). For L_1 , the 1:1 stoichiometry for Cu(II) and Zn(II) was demonstrated by Job's plots, and the solid-state structures confirmed the Cu(L_1)Cl₂ speciation for Cu(II) (where the metal is pentacoordinate and binds to the three ligand nitrogen atoms), while Zn(L_1)Cl₂ is bound to the two aromatic nitrogen atoms.⁴⁵ L_2 is a tetradentate derivative of TPEN that forms a 1:1 complex with Cu(II) and Zn(II) in solution.⁴⁶ EPR studies with L_2 reveal that its copper complex has distorted square planar geometry, while both EPR and NMR studies show co-existence of two Zn(II) complex isomers, potentially with an extra water ligand.⁴⁶ Assuming the N₃ bis(2-pyridylmethyl)amine binding motif retains the same binding affinity, L_1 has $\log \beta = 9.3$ for Cu(II) and 7.6 for Zn(II),⁴⁷ while L_2 has a much greater binding constants, 16.62 and 11.35 for Cu(II) and Zn(II), respectively (Table 1.2). L_1 is also able to dissociate and inhibit the formation of A β ₁₋₄₀ aggregates *in vitro* by stabilizing its oligomeric form.⁴⁵

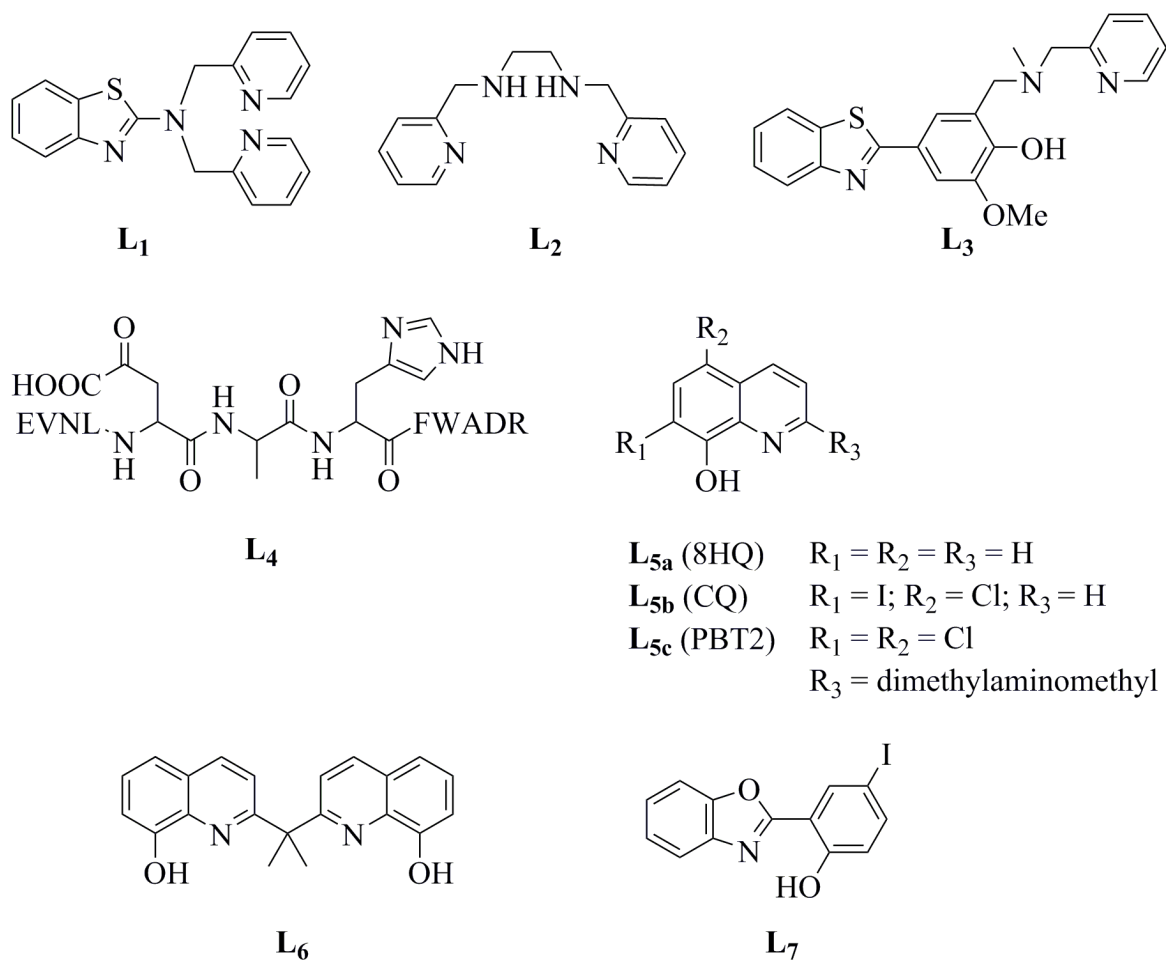


Figure 1.6 Ligands L₁-L₇ containing aromatic nitrogen(s). Figure reproduced by permission of The Royal Society of Chemistry.

The tridentate **L₃**⁴⁸ and tetradentate **L₄**⁴⁹ are examples of ligands that include one aromatic nitrogen plus aliphatic nitrogen atoms and oxygen atoms as coordinating groups (Figure 1.6). **L₄** is an activated pro-ligand that is released by BACE (β -secretase enzyme that cleaves amyloid precursor protein into A β fragments) from its protected form.⁴⁹ **L₄** is a peptide based on a variant of the APP sequence and in the activated form binds Cu(II), presumably as a tetradentate ligand, as it possesses an ATCUN (amino terminus Cu and Ni) binding motif.⁴⁹ **L₃** binds to Cu(II) in a 1:1 stoichiometry, while Zn(II) shows a mix of 1:1 and 2:1 coordination in a Job's plot.⁴⁸ The

solid-state structures, on the other hand, show a 2:1 Cu(II) binding with a pseudo-octahedral metal centre, whereas the Zn(II) complex is isolated as a 1:1 trinuclear complex, which shows again that the solution and solid states can correspond poorly.⁴⁸ **L**₃ has a similar affinity for Cu(II) to that of **L**₄, $\log \beta = 16.49$ compared to $\log K = 12.6$ (Table 1.2); however, the $\log \beta$ and $\log K$ values cannot be compared directly. As for their activity, **L**₃ is able to prevent and re-solubilise Cu(II)- and Zn(II)-mediated A β ₁₋₄₂ fibrils, forming oligomers,⁴⁸ while **L**₄ is able to prevent and re-solubilise A β ₁₋₄₀ aggregates, albeit incompletely.⁴⁹

Chelating ligands that have one aromatic nitrogen and a hydroxyl group, all based on the common core 8-hydroxyquinoline (8-HQ, **L**_{5a}), include **L**_{5b} (clioquinol, CQ),⁵⁰ **L**₆,⁵¹ and **L**₇⁵² (Figure 1.6). In the solid state, **L**_{5b} has been shown to form a 2:1 square planar complex with Cu(II), and a 2:1 Zn(II) complex with a trigonal bipyramidal geometry containing one water ligand.⁵³ Likewise, it shows the same speciation in solution studies.⁵⁴ **L**₆ is an example of linking two 8-HQ motifs together with a C(CH₃)₂ linker, in order to increase the denticity of the ligand.⁵¹ Solid state structure analyses of its metal complexes reveal 1:1 penta-coordinate centres for both Cu(II) and Zn(II) with extra oxygen or chlorine ligands.⁵¹ **L**₇ shows 2:1 complexation with Cu(II) and Zn(II) in solution studies, and EPR suggests that the Cu(II) centre of the complex has square planar geometry with a slight distortion.⁵²

According to their stability constants (Table 1.2), **L**₆ has the lowest metal affinity, $\log K = 15.9$ and 13.0 for Cu(II) and Zn(II), respectively, despite its tetradentate coordination.⁵¹ **L**_{5b} and **L**₇ share similar affinity for Cu(II), $\log \beta = 23$; while for Zn, **L**₇ has higher affinity, $\log \beta = 22$, than **L**_{5b}, $\log \beta = 16$.^{52,54} This may be due to conditions used because, in another study, Zn(II)

chelation ability is equally high for the two compounds.⁵² For their activity, **L**₆ reverses Cu(II)-mediated A β ₁₋₄₂ aggregation *in vitro*,⁵¹ and **L**₇ is able to reverse both Cu(II) and Zn(II)-mediated aggregation of A β ₁₋₄₀ *in vitro*.⁵²

It should be added that **L**_{5b} and its close derivative **L**_{5c} (Figure 1.6), belong to the well-studied and most well-developed (in clinical trials) family of compounds. **L**_{5b} was studied up to a pilot Phase 2 study,⁵⁰ but due to production difficulties no further studies have been done.⁵⁵

Meanwhile, **L**_{5c} (PBT2) is currently being evaluated in various clinical studies, including Phase 2 Alzheimer's disease and Huntington disease trials.⁵⁶ The therapeutic effects of **L**_{5c} are attributed not only to dissociating toxic A β aggregates, but also re-establishing equilibrium in metal ion species: it has been suggested that **L**_{5c} is a metal chaperone that transports Cu(II) and Zn(II) ions from areas of high concentrations (outside the cell near A β) to areas of insufficient metal ion concentration (inside the cell).⁵⁷

1.5.1.2 Oxygen-based ligands

Ligands that have oxygen atoms as the electron donors for metal coordination include **L**_{8a} (deferiprone),⁵⁸ **L**₉,⁵⁹ and **L**₁₀⁶⁰ (Figure 1.7). There are many derivatives of the hydroxypyridinone scaffold due to the successful use in the clinic of **L**_{8a} as an orally active iron chelator to treat thalassemia,⁶¹ but **L**_{8a} has been the most studied in terms of its coordination to Cu(II), Zn(II), and Fe(III). Notably, its chelating ability is greatest for Fe(III), due to the hardness of oxygen atoms, and the pK_a and stability constants remain the same for different ring N-substituents.⁶² In solution, for Fe(III), only the 3:1 species is present at pH 7.4.⁶³ In the

Table 1.2 Stability constants for chelating ligands in this section. Table reproduced by permission of The Royal Society of Chemistry.

Ligand	Cu(II)	Zn(II)	Conditions
N_3 motif of L_1 ⁴⁷	$\log \beta = 9.3$	$\log \beta = 7.6$	0.1 M KNO_3 , 25 °C
L_2 ⁴⁶	$\log \beta = 16.62$ $K_d = 3.98$ pm	$\log \beta = 11.35$ $K_d = 0.6$ μ M	0.2 M KCl , 25 °C
L_3 ⁴⁸	$\log \beta = 16.49(1)$ pCu = 7.0 (pH 6), 7.9 (pH 7.4)	$\log \beta = 15.19(1)$ pZn = 7.3 (pH 7.4)	$\log \beta$: 0.1 M $NaCl$, 25 °C pM: $[M]_{tot} = [L_3] = 50$ μ M
L_4 ⁴⁹	$\log K = 12.6$	n/a	pH 7.4 50 mM HEPES, competition study
L_{5b} ⁵⁴	$\log \beta_1 = 12.5(5)$ $\log \beta_2 = 23.4(7)$ pCu ~ 15.5 (pH 7.4)	$\log \beta_1 = 8.5(2)$ $\log \beta_2 = 16.1(6)$ pZn ~ 8.5 (pH 7.4)	methanol/0.1 M $(C_2H_5)_4N(ClO_4)$ (80/20 w/w), 25 °C
L_6 ⁵¹	$\log K = 15.9$	$\log K = 13.0$	methanol/pH 7.4 20 mM Tris, 150 mM $NaCl$, competition study
L_7 ⁵²	$\log \beta_1 = 14.444(9)$ $\log \beta_2 = 23.06(7)$ pCu = 11.06 (pH 6.6)	$\log \beta_1 = 13.55(8)$ $\log \beta_2 = 22.25(9)$ pZn = 10.98 (pH 7.4)	$\log \beta$: 0.10 M $NaCl$, 37 °C pM: $[M]_{tot} = 25$ μ M, $[L_7]_{tot} = 50$ μ M
L_{8a} Cu(II) and Fe(III) ⁶³ Zn(II) ⁶⁴	$\log \beta_1 = 10.42(1)$ $\log \beta_2 = 19.09(1)$	$\log \beta_1 = 7.24(2)$ $\log \beta_2 = 13.55(2)$ $\log \beta_3 = 15.2(2)$	Fe(III): $\log \beta_1 = 15.01(1)$ $\log \beta_2 = 27.3(1)$ $\log \beta_3 = 37.43(1)$ pFe = 20.67 $\log \beta$: Cu, Fe: 0.1 M KCl , 25 °C; Zn: 0.2 M KCl , 25 °C
L_{9a} ⁵⁹	$\log \beta_1 = 10.97(1)$ $\log \beta_2 = 25.35(2)$ pCu = 8.0 (pH 6.6) = 8.9 (pH 7.4)	$\log \beta_1 = 8.457(2)$ $\log \beta_2 = 14.165(6)$ pZn = 6.5 (pH 7.4)	pM: $[M]_{tot} = 10^{-6}$ M, $[L_8]_{tot} = 10^{-5}$ M 0.10 M $NaCl$, RT pCu: $[M]_{tot} = 25$ μ M, $[L_9]_{tot} = 50$ μ M pZn: $[M]_{tot} = 50$ μ M, $[L_9]_{tot} = 100$ μ M
L_{10} ⁶⁰	$\log \beta = 24.18(2)$ pCu = 6.6 (pH 6.6) = 7.5 (pH 7.4)	$\log \beta = 16.83(5)$ pZn = 3.9 (pH 7.4)	$\log \beta$: 0.16 M $NaCl$, 25 °C pM: $[M]_{tot} = [L_{10}]_{tot} = 0.001$ M
L_{11} Cu(II) ⁶⁵ Zn(II) ⁶⁶	$\log \beta = 28.09(3)$	$\log \beta = 15.5 (2)$	Cu(II): 0.1 M KCl , 25 °C Zn(II): 0.2 M $Na(ClO_4)$, 25 °C
L_{12} ⁶⁷		$\log \beta = 10.3 (2)$	Cu(I) $\log K = 19.2(1)$ $\log K_2 = 20.7(3)$ acetonitrile/pH 7.4 20 mM phosphate, 25 °C, competition study

presence of one tenth equivalent of Fe(III), the chelation of Cu(II) is almost exclusively 2:1 at pH 7.4, while at pH 6.6, there is about a 50/50 mix of the 2:1 and 1:1 species. This shows that even in the presence of Fe(III), Cu(II) will still bind despite having a lower stability constant.⁶³ Zn(II):**L**_{8a} coordination stoichiometry is 2:1 at pH 7.4, with a minority 1:1 component, and there is appearance of a 3:1 monoanion and [Zn(**L**_{8a})₂H₁] complexes at pH \geq 9.⁶⁴ The 4-aminophenyl derivative of **L**_{8a}, **L**_{8b} (Figure 1.7) has been isolated as a 2:1 Cu(II) complex with a distorted square planar centre, as characterised by X-ray crystallography.⁵⁸ Both hydroxypyridinone derivatives disaggregate A β ₁₋₄₀ metal-induced aggregates.⁵⁸

L_{9a} is a simplified version of the antioxidant myricetin (**L**_{9b}), with only one potential metal binding site.⁵⁹ At physiological pH, the ligand forms a mixture of 1:1 and 2:1 complexes with Cu(II) and Zn(II), but this binding, unexpectedly, does not have any effect on A β ₁₋₄₀ association *in vitro*.⁵⁹ Curiously, the parent compound **L**_{9b} (Table 1.2), is able to inhibit and reverse A β ₁₋₄₀ aggregation.⁶⁸ **L**₁₀, a tetrahydrosalen derivative, demonstrates almost exclusive 1:1 binding to Cu(II) at pH 6.6, and 1:1 Zn(II) complex formation near pH 7.4, with a minor component of unchelated Zn(II) and [ZnHL₁₀]⁺.⁶⁰ The 1:1 copper complex was also shown by X-ray crystallography to have a distorted square planar geometry. **L**₁₀ was shown to inhibit A β ₁₋₄₀ aggregation as well.⁶⁰ **L**_{8a}, **L**_{9a}, and **L**₁₀ have similar binding constants, $\log \beta = 20-25$ for Cu(II), and 13-17 for Zn(II) (Table 1.2).^{59,60,63,64}

re-solubilises aggregation of A β ₁₋₄₀ *in vitro*.⁶⁹ Because of its soft sulphur donors, **L₁₂** preferentially binds Cu(I) over Zn(II) with 10⁹ fold selectivity and forms 1:1 complexes, as well as Cu₆(L₁₂)₃ clusters.⁶⁷ Stability constants for these two ligands can be found in Table 1.2.

1.5.2 Parkinson's and prion diseases

One scaffold from AD that has been used in both PD and PrP models is **L_{5b}** (Figure 1.6). **L_{5b}** has been shown to bind iron and reverse its toxicity in a PD mouse model.⁷⁰ The effect of **L_{5b}**, however, is due to iron chelation that is independent of α -synuclein.⁷⁰ **L_{5b}** has high binding affinity to Fe(III), $\log \beta_3 = 36.9$, in 0.1 M Na(ClO₄) at 25 °C.⁷¹ As it cannot be further developed because of preparative problems (see above), other derivatives have been prepared using the same scaffold.¹³

As prion protein malformation is also influenced by Cu(II), **L_{5b}** has been assessed for prion disaggregation *in vitro*. In one study, **L_{5b}** was able to reverse conversion of PrP₂₃₋₂₃₀ into its infectious form.⁷² In another study, in which the fragment Pr₁₀₆₋₁₂₆ was used where there is only one Cu(II) binding site – at His111, incubation with Cu(II) and Zn(II) was actually seen to decrease formation of β sheets and **L_{5b}** obliterated that effect.⁷³ These studies show that there is significant work required to elucidate the effect of metal ions on protein toxicity as well as the effect of metal chelating ligands.

1.5.3 Chelating ligands summary and outlook

The survey of metal binders presented here includes a variety of electron donor groups, as are present in metalloproteins that are implicated in neurodegenerative diseases, such as aromatic

nitrogens, aliphatic nitrogens, and oxygen atoms. Most metal binders, despite their differences in donor groups and denticity, have similar binding affinities for both Cu(II) and Zn(II) and are able to compete with A β for these metal ions, as indicated by their metal complex formation constants as well as A β disaggregation studies. For instance, if we compare pM values of ligands with K_d values of proteins, it is evident that the synthesised chelating ligands are able to compete thermodynamically with disease-related proteins for Cu(II) and Zn(II).

Interestingly, it is seen that rigid bidentate ligands with two aromatic nitrogens have 1:1 chelation with Cu(II) and Zn(II) ions and need two or three additional ligands to complete the coordination sphere (ligands omitted from this section but discussed elsewhere).¹³ Conversely, bidentate ligands presented here that only have one aromatic nitrogen are able to bind in a 2:1 fashion (e.g. **L_{5b}** and **L₇**).

Successful application of a metal binder as a drug for neurodegenerative disease has yet to reach market; however, initial indications that this may be possible are starting to arise (as described above regarding **L_{5b}** and **L_{5c}**). With few *in vivo* studies of metal chelating ligands, it is as yet impossible to know what effect the denticity and binding constants have on disease progression. It remains to be seen whether aromatic nitrogens or 2:1 chelation is beneficial. As well, further studies are needed to ascertain whether administering unmasked chelating ligands has side effects, as metal ions can bind before the brain and diffuse through membranes, as was seen with the toxicity of the Zn(II) complex of **L_{5b}**.⁷⁴ Several labs are working on masked-chelation strategies by incorporating a boronic ester or a carbamate group into the **L_{5a}** scaffold.¹³

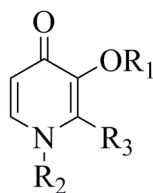
1.5.4 Conclusions

This section demonstrates how on the one hand, the bioinorganic community is investigating metal binding to disease-relevant proteins by employing the concepts of coordination number as well as the coordinating groups according to the HSAB model. Understanding the binding preferences of metal ions and knowing the sequences of relevant proteins should allow prediction of potential binding sites in large, complex structures. On the other hand, medicinal inorganic chemists, using the tools of coordination chemistry, create and study the effect of synthetic ligands to compete for metal ions with proteins. Neurodegenerative diseases present an enormous challenge for our society to create medicine for an extraordinarily complicated organ that we do not even begin to understand, even when it is functioning correctly. While coordination chemists are excited about their potential contribution to this field, they remain a minority in a vast pool of scientists enthusiastically promoting their potential ND solutions that are independent of metal ions. Yet, after over a thousand clinical trials that have yet to yield disease-modifying drugs, anyone's well-supported ideas and contribution should be appreciated.

Nonetheless, studying neurodegenerative diseases from the inorganic perspective has enabled further understanding of disease pathology features and the creation of novel potential therapeutics. Metal ions bind to and influence aggregation of proteins involved in Alzheimer's, Parkinson's, and prion diseases. It may be that metal ion imbalance, together with metal-protein interaction, are the biomarkers that help track disease progression. Our understanding of metal binding to these proteins facilitated development of novel classes of potential therapeutics, and one can only hope these will actually derail these diseases in the future.

1.6 Focus on HPOs

Compounds **L_{8a}** and **L_{8b}** (Figure 1.7) from Chapter 1.5.1.2 are of particular interest as they belong to the family of hydroxypyridinones (HPOs) that have been studied in the Orvig group over the last decades and they are at the centre of this thesis. As mentioned in the section, above, they are being considered as chelating agents by our, and other groups, with derivatives possible through the various positions on the molecules (Scheme 1.2).



Scheme 1.2 The HPO scaffold.

The “simplest” 3-hydroxy-4-pyridinone is known as Deferiprone (3-hydroxy-1,2-dimethylpyridin-4(1H)-one) with R₁ = H; R₂, R₃ = Me, an oral treatment for iron overload disorders.⁶¹ This bidentate ligand (and its R₂ derivatives) have the two oxygen atoms that are available for metal binding, and thus hard metals are preferred for binding, ions such as Fe(III), Al(III), In(III), and Ga(III).⁷⁵ With the first two ions, the application is in removing excess of the essential iron or the non-essential aluminum ions whose accumulation causes toxicity.⁷⁵ With the latter two ions, coordination to these metals is done for the purpose of creating imaging agents.⁷⁵ In these cases, the HPO ligands make a neutral tris complex with the metal. To potentially improve metal binding, individual bidentate HPOs have been linked together to result in hexacoordinate ligands on nitrilotriacetic, nitrilotripropionic, and Kemp acids.⁷⁶ On the other hand, if metal binding affinity and stoichiometry is kept the same, the *N*-substituent can be

varied to change properties of the compounds, for example by changing lipophilicity and thus cell uptake into certain organs of interest.⁷⁷ For example, when the R₂ substituent was 3-(4-phenyl-piperazin-1-yl)-propyl, the brain uptake of its radioactive Ga complex was seen to have improved due to increased lipophilicity.⁷⁸

Other permutations include replacing the methyl group at the R₃ position with an ethyl group, in which case Fe(III) chelation strength is not impacted.⁷⁹ As well, the hydroxyl group may be derivatised to achieve various goals. For example, a glucose moiety may be installed at the R₁ position for potential boost in brain uptake (see below),⁸⁰ or an adamantyl group for potential improved therapeutic activity.⁸¹

Yet another advantage in working with HPOs is that the starting materials are generally non-toxic and widely available. As is evident in the following chapters, the starting point of all reactions is amine insertion (Figure 1.8) of an amino acid (e.g. glycine (an amino acid found in our diet)) into maltol, a food additive that, when ordered from Sigma, comes with Halal and Kosher certificates.⁸²

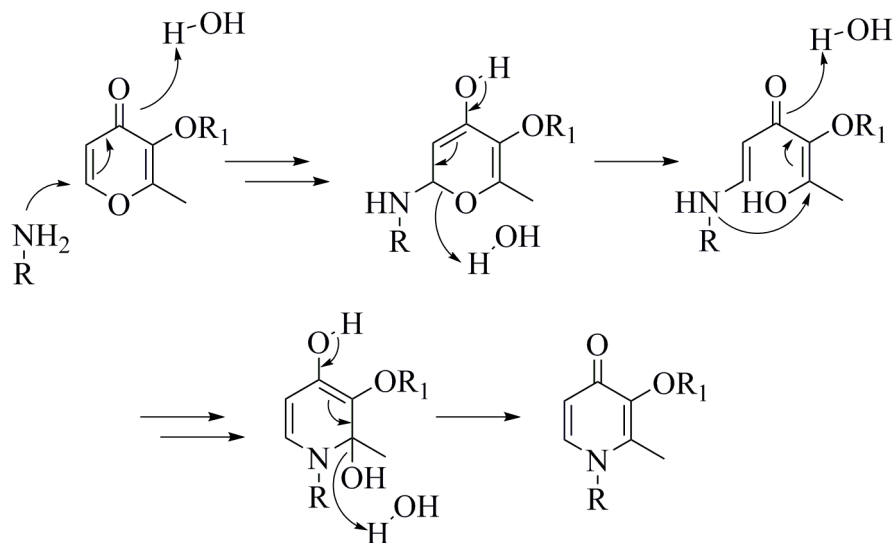


Figure 1.8 The postulated reaction mechanism of amine insertion into maltol.⁸³

1.7 Drug design considerations – multifunctional scaffold

Therefore, taking prior work into consideration, multifunctional design of HPOs into potential AD drugs is as follows (Figure 1.9):

- a) Metal binding. The metal binding activity is conserved with the two oxygen atoms. With various R_2 substituents, the Cu(II), Zn(II), and Fe(III) chelation is expected to remain the same as for previously studied HPOs.⁵⁸
- b) Amyloid-targeting. By installing groups at the R_2 that are known to bind to $A\beta$, it is hypothesised that the molecules will target the amyloid protein.^{58,84}
- c) Antioxidant activity. The hydroxyl group of the HPO is expected to retain its radical quenching ability via hydrogen donation when the R_2 group is a hydrogen atom.⁸⁰

- d) Enzymatic inhibition. By varying the R₁ group from a hydrogen to a carbamoyl, the metal chelation site may be masked and novel functionality may be gained. The carbamate group is present on the AD drug rivastigmine, which gives the drug its enzymatic inhibitory activity.⁸⁵

In addition to these activities, the following two features are also of importance:

- e) Toxicity. Concerns with cytotoxicity need to be addressed, realising that increased lipophilicity of compounds may lead to increased toxicity.
- f) Brain permeability. The brain, which is the intended location of compounds, is notoriously selective in letting molecules pass. Of the three interfaces between the brain and the rest of the body, the blood-brain barrier (BBB) is the largest and is considered to be the target in drug permeability.⁸⁶ The barrier is created by endothelial cells that are connected to one another by tight junctions and that have specific channels and transporters.⁸⁶ This setup ensures that only certain ions, neurotransmitters, and molecules enter the brain.⁸⁶ This selectivity is considered in drug design and initial testing for potential BBB permeability. First, there are predictions for passive permeability across the BBB; and second, the aid of transporters may be used. Ultimately, *in vivo* testing is necessary to determine whether there is adequate brain uptake; however, known pitfalls of compounds that do not pass through BBB can be avoided during the drug design stage, and *in vitro* tests can be performed to measure the success of this venture.

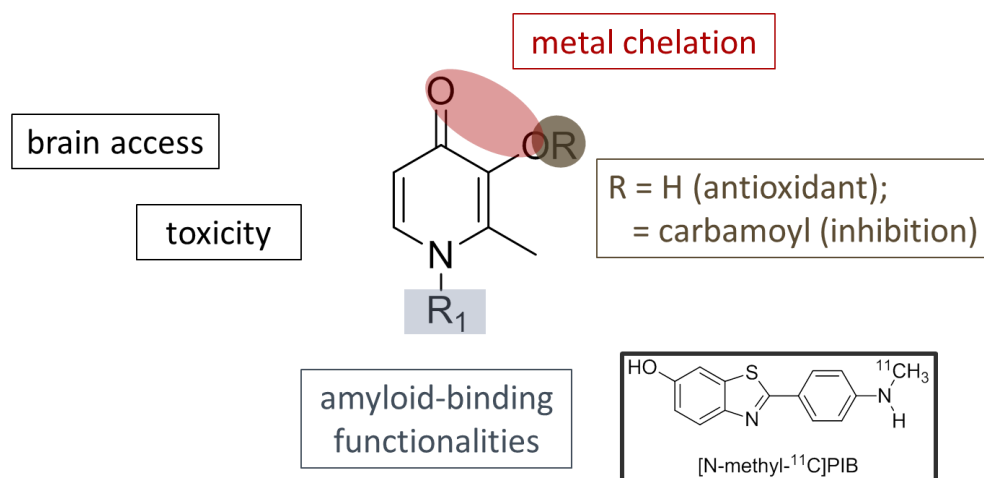


Figure 1.9 HPO drug design overview.

1.8 Thesis goal and overview

The goal of this work is to design, synthesise, characterise, and test novel compounds in *in vitro* assays related to Alzheimer's disease pathology. Due to the versatility of the hydroxypyridinone scaffold, it was chosen for the creation of the novel library of chelating ligands, and functional groups that comprise imaging agents for AD were incorporated into it, all of which is discussed in Chapter 2. The hypothesis that metal- and amyloid-binding functionalities were compatible within the scaffold was tested in metal- and amyloid-containing assays, the former of which is discussed in Chapter 3 and the latter in Chapter 4. Chapter 4 also addresses other activities of compounds, such as antioxidant ability, cytotoxicity, and cell permeability. The focus of Chapter 5 is on functionalising the hydroxyl group of the scaffold with an addition of the carbamoyl functionality, with the hypothesis that this will imbue the compounds with acetylcholinesterase inhibitory functionality, that which is exhibited by a class of drugs on the market for AD. The concluding Chapter 6 will define the remaining questions from this research project and outline further work that may address them.

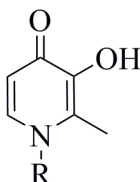
Chapter 2: Synthesis and characterisation of next generation pro-ligands

2.1 Introduction

Among the first compounds to be studied for the potential use as AD therapeutics in the Orvig group were repurposed HPOs **Hdpp** and **Hppp** (Scheme 2.1),⁸⁰ whose metal binding affinities were previously established (e.g. **Hppp**'s binding to In(III), Al(III), and Ga(III) reported in 1991⁸⁷). Other HPOs in the initial studies contained functional groups hydroxyphenyl (**Hhpp** (Scheme 2.1)⁸⁰), hexyl, and 4-(isobutyl)phenyl.⁸⁸ After the proof of concept experiments, to improve the potential activity, a methyl linker to the aryl group was introduced to provide more flexibility, thus transforming **Hppp** into **Hnbp** (Scheme 2.1).⁸⁹ The next improvement was to insert amyloid-beta binding functionalities, creating **Hdapp**, **Hsapp**, **Hzapp**, **Hbt6p**, and **Hbt2p** (Scheme 2.1).⁵⁸ For the latter seven compounds, copper chelation was verified in the solid state, although the binding to amyloid-beta was not confirmed experimentally. It should be noted that concurrently with this work, different benzothiazole derivatives were reported to regulate self- and zinc-mediated A β ₁₋₄₂ aggregation.⁸⁴

For this body of work, the design of pro-ligands (compounds that bind metal ions) follows a strategy that is a combination of the two - fragments of the known amyloid-binding agents, such as Pittsburgh Compound B (PIB) and BF-227⁹⁰ (Figure 2.1), are incorporated into the HPO scaffold replacing the methyl group of **Hdpp** (Scheme 2.1). As well, two different linkers are incorporated – methyl and phenyl. Thus, the five novel pro-ligands that were designed are **Hmbo2p**, **Hmbt2p**, **Habt6p**, **Hpbo2p**, and **Hpbt2p** (Figure 2.2). **Hmbt2p** is a derivative of **Hbt2p**, with a methyl linker, while **Habt6p** is an amine derivative of **Hbt6p** (Scheme 2.1), both of which have benzothiazole functionalities like PIB (Figure 2.1). **Hpbo2p** and **Hpbt2p** have

phenyl linkers and are envisioned to provide increased affinity toward amyloid-beta, as they mimic PIB more closely. **Hmbo2p** and **Hpbo2p** have benzoxazole functionalities, modeled after BF-227 (Figure 2.1).



	R=
Hdpp	methyl
Hppp	phenyl
Hhpp	4-hydroxyphenyl
Hnpp	benzyl
Hdapp	4-(<i>N,N</i> -dimethylamino)-phenyl
Hsapp	4-(<i>N</i> -methylamino)phenyl
Hzapp	4-aminophenyl
Hbt6p	6-benzothiazolyl
Hbt2p	2-benzothiazolyl

Scheme 2.1 Previously studied HPOs for the potential use in AD in the Orvig group.

The naming convention for compounds follows that used by the Orvig group in the last decades. For example, the letters of **Hmbo2p** represent the pro-ligand version (**H**) methyl-linked benzoxazol-2-yl substituted pyridinone. When bound to a metal ions such as copper(II), it is represented as **Cu(mbo2p)₂** to reflect the loss of the hydrogen atom and the stoichiometry of the complex. Other functionalities, such as a carbamoyl group, can replace the hydrogen, resulting in **Cmbo2p**.

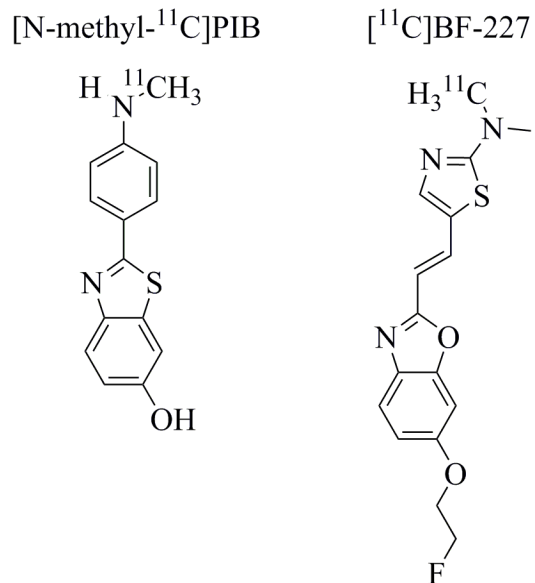


Figure 2.1 Positron emission tomography tracers PIB and BF-227 used for *in vivo* plaque imaging.⁹⁰

Modified figure reproduced by permission of The Royal Society of Chemistry.

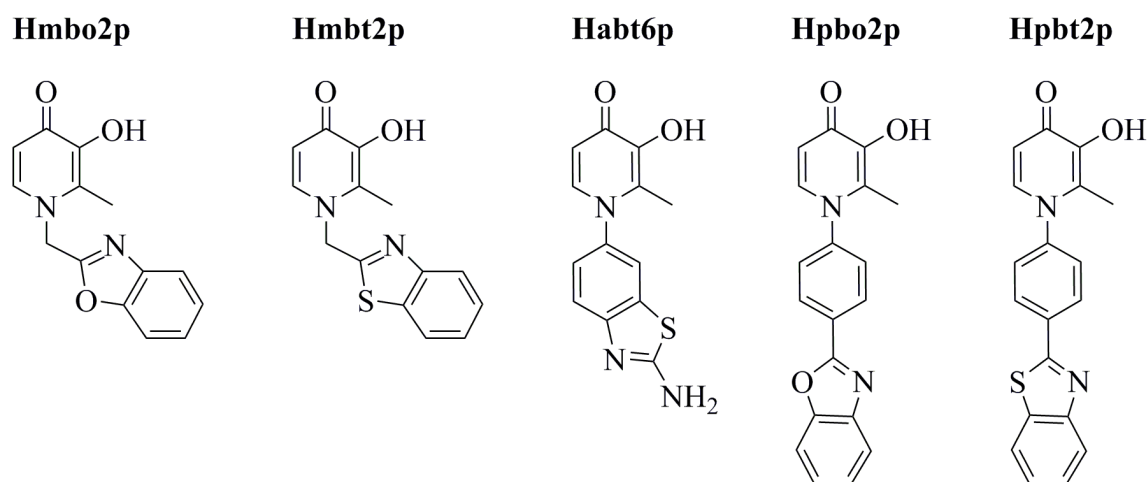


Figure 2.2 Novel pro-ligands Hmbo2p, Hmbt2p, Habt6p, Hpbo2p, and Hpbt2p.

In designing compounds, we take into account potential interactions within biological systems.

For compounds to be bioavailable, a balance of water and lipid solubility is required; this can be predicted using Lipinski's rules and other assessments.⁹¹ Lipinski's rules are a set of guidelines

that are based on the data available for all the drugs on the market. For a majority of them, their molecular weight is <500, clogP <5, and number of hydrogen donor and acceptor atoms are <5 and <10, respectively. While many drug properties fall outside these limits, they are good filters to apply to yet to be synthesised compounds. As the chemical space consists of a myriad of potential molecules of interest, it is advantageous to filter out compounds that may have low bioavailability before synthesizing them. Another concern is whether the molecule would pass through the BBB to reach the organ of interest. A predictor for passive BBB penetration is the log BB value; molecules with values >0.3 are likely to pass through the BBB, while those with values <-1.0 are not likely to penetrate the barrier.⁹² Log BB is computed using Clark's eqn (2.1).⁹² In this equation, TPSA is the topological polar surface area, which is an estimate of the sum of the areas of the polar molecules, and clogP is the calculated water-octanol partition coefficient, which is a measure of hydrophobicity.

$$\log BB = -0.0148 \text{ TPSA} + 0.152 \text{ clogP} + 0.139 \quad (2.1)$$

Another point to keep in mind is that introduction of the benzoxazole and benzothiazole fragments may introduce unwanted interaction with biological targets other than amyloid-beta. For instance, certain benzoxazole and benzothiazole containing compounds have been shown to have anti-cancer activity through interaction with various receptors.^{93,94}

2.2 Experimental

2.2.1 Materials and methods

All chemicals (including standards) and solvents were purchased from commercial suppliers (Aldrich, Alfa Aesar, Tokyo Chemical Industry Co., Ltd. (TCI) America) and used without

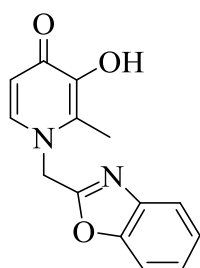
further purification. Water was purified to 18.2 MΩ•cm with a Elga Ultra Pure Lab System. Starting materials 2-(3-hydroxy-2-methyl-4-oxopyridin-1(4H)-yl)acetic acid (**Hcmp**),⁹⁵ 3-benzyloxy-2-methyl-4(1H)-pyrone (**Bnma**),⁹⁶ and **Hcpp**⁹⁷ were synthesised and purified according to previously reported procedures.

2.2.2 Instrumentation

¹H NMR and ¹³C NMR spectra were recorded with a Bruker AV-300 spectrometer at 300.13 MHz and 75.48 MHz, respectively, at 24.7 °C and calibrated using residual solvent peaks. 1D ¹H NMR and ¹³C NMR spectra, as well as 2D NMR spectra (heteronuclear single-quantum correlation (HSQC) and heteronuclear multiple-bond coherence (HMBC)) were recorded with a Bruker AV-600 spectrometer at 600.15 MHz and 150.92 MHz, respectively, at 25.0 °C by Dr. Maria Ezhova, Zorana Danilovic, or Helen Huang-Hobbs and calibrated using residual solvent peaks. Low-resolution mass analyses for ligands were performed with Waters LC-MS with an ESCI ion source. High-resolution mass spectra were obtained with a Waters/Micromass LCT, and elemental analyses (CHN) were done using a Carlo Erba Elemental Analyzer EA 1108, both of which were operated by David Wong, Derek Smith, or Marshall Lapawa. Infrared spectra were collected neat with a Thermo Scientific Nicolet 6700 FTIR spectrometer. For solid state structure analysis that was done by Dr. Brian Patrick, Bruker APEX DUO or Bruker X8 APEX II diffractometers with graphite monochromated Mo-K α radiation were used. Absorbance and fluorescence profiles of ligands were obtained with Hewlett-Packard 8543 and Agilent Cary Eclipse spectrophotometers, respectively.

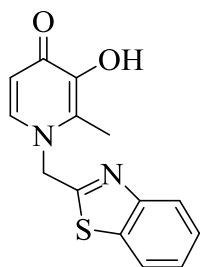
2.2.3 Synthesis and characterisation

1-(Benzo[d]oxazol-2-ylmethyl)-3-hydroxy-2-methylpyridin-4(1H)-one (**Hmbo2p**)



Hcmp (0.104 g, 0.570 mmol), 2-aminophenol (0.105 g, 0.965 mmol), and polyphosphoric acid (PPA) (1.8 g, 84% as phosphorous pentoxide) were combined in a 25 mL round bottom flask. The temperature of the mixture was gradually increased to 120 °C over 1 h, after which time the mixture was heated further to 220 °C and stirred for 5 h.⁹⁸ After it was cooled to room temperature, the solidified mixture was dissolved in 6 M NaOH and the pH was adjusted to 7 with 6 M HCl in an ice bath. The precipitated pink solid was collected by filtration and recrystallised from a hot MeOH/H₂O solution. The red precipitate was collected by filtration and dried *in vacuo* to yield **Hmbo2p** (0.060 g, 40%). Slow evaporation of **Hmbo2p** in DMSO at room temperature resulted in X-ray quality crystals. ¹H NMR (300 MHz, DMSO-d₆, 24.7 °C): δ = 7.75 (d, *J* = 7.3 Hz, 3 H), 7.34 - 7.46 (m, 2 H), 6.20 (d, *J* = 7.3 Hz, 1 H), 5.64 (s, 2 H), 2.25 (s, 3 H). ¹³C NMR (75 MHz, DMSO-d₆, 24.7 °C): δ = 169.69, 161.66, 150.36, 145.34, 140.25, 138.80, 129.18, 125.65, 124.85, 119.92, 111.26, 111.03, 49.74, 11.52. Anal. calcd (found) for C₁₄H₁₂N₂O₃: C, 65.62 (65.65); H, 4.71 (4.69); N, 10.93 (10.81%). HR-ESIMS *m/z* for C₁₄H₁₃N₂O₃ (M+H⁺) calcd (found): 257.0926 (257.0921). IR (cm⁻¹, total reflectance): 3165 (br), 1626, 1575, 1526, 1504, 1226.

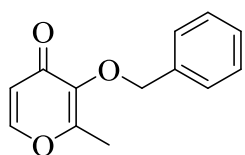
1-(Benzo[d]thiazol-2-ylmethyl)-3-hydroxy-2-methylpyridin-4(1H)-one (**Hmbt2p**)



Hcmp (0.102 g, 0.557 mmol), 2-aminobenzenethiol (0.060 mL, 0.561 mmol), and PPA (2.4 g, 84% as phosphorous pentoxide) were combined in a 25 mL

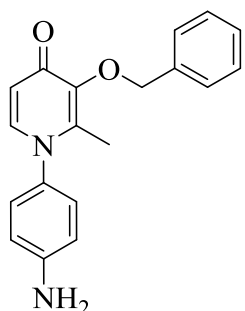
round bottom flask. The temperature of the mixture was gradually increased to 160 °C, and the mixture was heated for 72 h.⁹⁸ After the solution was cooled to room temperature, the resulting solidified mixture was dissolved in 6 M NaOH in an ice bath and the pH was adjusted to 7 with 6 M HCl. After an extraction with 3x70 mL of chloroform, the organic solution was washed with H₂O, dried over MgSO₄, and evaporated to dryness. The solid was recrystallised from hot MeOH, and X-ray quality crystals were obtained from the same solution. The green precipitate was collected by filtration and dried *in vacuo* to yield **Hmbt2p** (0.030 g, 20%). ¹H NMR (300 MHz, DMSO-d₆, 24.7 °C): δ = 8.10 (d, *J* = 7.99 Hz, 1 H), 8.00 (d, *J* = 7.54 Hz, 1 H), 7.81 (d, *J* = 6.62, 1 H), 7.41 – 7.75 (m, 2 H), 6.24 (d, *J* = 6.17 Hz, 1 H), 5.74 (br. s, 2 H), 2.23 (br. s, 3 H). ¹³C NMR (151 MHz, DMSO-d₆, 24.7 °C): δ = 169.62, 167.33, 152.41, 145.51, 138.58, 134.40, 128.97, 126.49, 125.49, 122.70, 122.46, 111.25, 54.17, 11.61. Anal. calcd (found) for C₁₄H₁₂N₂O₂S: C, 61.75 (61.23); H, 4.44 (4.53); N, 10.29 (10.11%). HR-ESIMS *m/z* for C₁₄H₁₃N₂O₂S (M+H⁺) calcd (found): 273.0698 (273.0699). IR (cm⁻¹, total reflectance): 3051 (br), 1625, 1568, 1528, 1504, 1206.

3-Benzyloxy-2-methyl-4(1H)-pyrone (Bnma)



Bnma⁹⁶ was dissolved in a minimum amount of hot ethanol, and X-ray quality crystals formed at 4 °C.

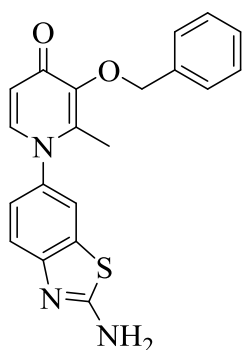
1-(4-Aminophenyl)-3-(benzyloxy)-2-methylpyridin-4(1H)-one (Bnzapp)



Bnma (3.493 g, 16.17 mmol) and p-phenylenediamine (2.253 g, 20.86 mmol) were combined in a 1:1 MeOH:H₂O solution in a 100 mL round

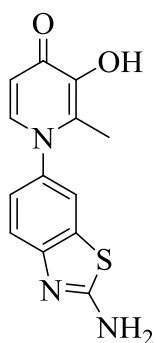
bottom flask. The pH was decreased to 5 by adding 12 M HCl. After 72 h reflux, the methanolic solution was decanted and the remaining oil was concentrated by evaporating to dryness *in vacuo* and separated by column chromatography (silica, 15:85 MeOH:EtOAc). Beige solid **Bnzapp** was collected and dried *in vacuo* (1.151 g, 23%). X-ray quality crystals were prepared by slow evaporation of a methanol solution. $^1\text{H NMR}$ (300 MHz, DMSO- d_6 , 24.7 °C): $\delta = 7.48$ (d, $J = 7.3$ Hz, 1 H), 7.27 - 7.45 (m, 5 H), 6.86 - 7.03 (m, $J = 8.5$ Hz, 2 H), 6.51 - 6.72 (m, $J = 8.5$ Hz, 2 H), 6.19 (d, $J = 7.5$ Hz, 1 H), 5.50 (s, 2 H), 5.06 (s, 2 H), 1.85 (s, 3 H). ESI-MS(+) m/z for $\text{C}_{19}\text{H}_{19}\text{N}_2\text{O}_2$ ($\text{M}+\text{H}^+$) calcd (found): 307.14 (307.3).

1-(2-Aminobenzo[d]thiazol-6-yl)-3-(benzyloxy)-2-methylpyridin-4(1H)-one (**Bnabt6p**)



Bnzapp (0.246 g, 0.804 mmol) and potassium thiocyanate (0.291 g, 3.00 mmol) were dissolved in 50 mL glacial acetic acid in a 100 mL round bottom flask. A solution of Br_2 (0.049 mL, 0.920 mmol) in 20 mL acetic acid was added dropwise to the flask.⁹⁹ After 72 h at room temperature, the mixture was neutralised with conc. ammonium hydroxide. After the solution was cooled, the orange polymer (by-product) was filtered off, and the remaining mixture was evaporated to dryness and separated by column chromatography (silica, 1:9 MeOH:DCM). Yellow oil **Bnabt6p** was dried *in vacuo* (0.095 g, 32% yield). $^1\text{H NMR}$ (300 MHz, DMSO- d_6 , 24.7 °C): $\delta = 7.75$ (d, $J = 2.3$ Hz, 1 H), 7.71 (s, 1 H), 7.61 (d, $J = 7.5$ Hz, 1 H), 7.30 - 7.45 (m, 5 H), 7.18 (dd, $J = 2.3, 8.5$ Hz, 1 H), 6.19 - 6.23 (m, 1 H), 5.07 (s, 2 H), 3.16 (d, $J = 5.0$ Hz, 2 H), 1.88 (s, 3 H). ESI-MS(+) for $\text{C}_{20}\text{H}_{18}\text{N}_3\text{O}_2$ ($\text{M}+\text{H}^+$) calcd (found): 364.11 (364.3).

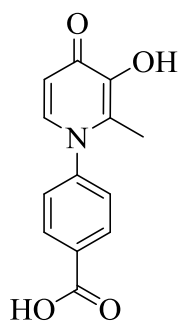
1-(2-Aminobenzo[d]thiazol-6-yl)-3-hydroxy-2-methylpyridin-4(1H)-one (Habt6p)



Bnabt6p (0.095 g, 0.262 mmol) was deprotected by reflux in 5 mL 33% HBr acetic acid for 1 h. At RT, ethyl acetate was added and off-white solid was collected by filtration. The solid was dissolved in dilute HCl (pH 2) and the acidic solution neutralised with 1 M NaOH. The peach-coloured precipitate was collected and dried *in vacuo* to yield **Habt6p** (0.038 g, 53%). Slow evaporation of

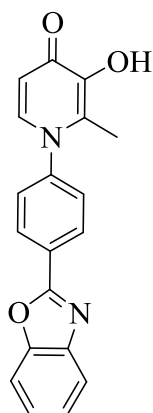
Habt6p in DMSO at room temperature resulted in X-ray quality crystals. ^1H NMR (600 MHz, DMSO- d_6 , 25.0 °C): δ = 8.01 (d, J = 6.66 Hz, 1H), 7.90 (br. s, 2 H), 7.88 (d, 1 H), 7.46 (d, J = 8.70 Hz, 1 H), 7.33 (dd, J = 8.45, 2.30 Hz, 1 H), 6.95 (d, J = 7.17 Hz, 1 H), 2.12 (s, 3H). ^{13}C NMR (151 MHz, DMSO- d_6 , 25.0 °C): δ = 168.51, 163.52, 153.44, 143.54, 139.93, 137.47, 134.29, 131.61, 124.00, 119.33, 117.63, 110.55, 14.19. HR-ESIMS m/z for $\text{C}_{13}\text{H}_{12}\text{N}_3\text{O}_2\text{S}$ ($\text{M}+\text{H}^+$) calcd (found): 274.0650 (274.0647). IR (cm^{-1} , total reflectance): 3089 (br), 1622, 1558, 1531, 1488, 1230.

1-(4-Carboxyphenyl)-3-hydroxy-2-methyl-4-oxopyridine (Hcpp)



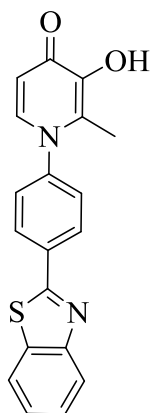
X-ray quality crystals of **Hcpp**⁹⁷ were grown from a saturated solution in DMSO/MeOH.

1-(4-(Benzo[d]oxazol-2-yl)phenyl)-3-hydroxy-2-methylpyridin-4(1H)-one (Hpbo2p)



Hcpp (0.2225 g, 0.908 mmol), 2-aminophenol (0.1003, 0.920 mmol), and polyphosphoric acid (PPA) (4.8 g, 84% as phosphorous pentoxide) were combined in a 50 mL round bottom flask. The temperature of the mixture was gradually increased to 120 °C over 1 h, after which time it was heated further to 160 °C and stirred for 24 h.⁹⁸ After cooling to room temperature, the solidified mixture was dissolved in 6 M NaOH until neutral pH was reached. The product was extracted with 3x70 mL chloroform, after which the organic layer was washed with H₂O twice, dried over MgSO₄, and evaporated to dryness. The resultant pink solid was washed with MeOH, and the remaining fluffy pale pink **Hpbo2p** (0.0261 g, % yield) was dried *in vacuo*. Slow evaporation of **Hpbo2p** in DMSO at room temperature resulted in X-ray quality crystals. ¹H NMR (600 MHz, DCM-d₂, 25.0 °C): δ = 8.40 - 8.43 (m, 2 H), 7.78 - 7.81 (m, 1 H), 7.64 - 7.67 (m, 1 H), 7.45 - 7.49 (m, 2 H), 7.42 (ddd, *J* = 7.55, 5.76, 1.51 Hz, 2 H), 7.38 (d, *J* = 7.14 Hz, 1 H), 6.42 (d, *J* = 7.14 Hz, 1 H), 2.15 (s, 3 H). ¹³C NMR (150 MHz, DMSO-d₆, 25.0 °C): δ = 170.64, 162.02, 151.56, 146.14, 144.49, 142.63, 138.02, 129.51, 128.92, 128.38, 128.15, 126.29, 125.43, 120.80, 111.32, 111.16, 14.01. Anal. calcd (found) for C₁₉H₁₄N₂O₃•1.25 H₂O: C, 66.95 (67.12); H, 4.88 (4.66); N, 8.22 (8.13%). HR-ESIMS *m/z* for C₁₉H₁₅N₂O₃(M+H⁺) calcd (found): 319.1083 (319.1079). IR (cm⁻¹, total reflectance): 3228 (br), 1626, 1562, 1492, 1242.

1-(4-(Benzo[d]thiazol-2-yl)phenyl)-3-hydroxy-2-methylpyridin-4(1H)-one (**Hpbtp**)



Hcpp (0.2015 g, 0.822 mmol), 2-aminophenol (0.88 μ L, 0.965 mmol), and polyphosphoric acid (PPA) (6 g, 84% as phosphorous pentoxide) were combined in a 50 mL round bottom flask. The mixture was heated at 140 $^{\circ}$ C for 24 h.⁹⁸

After cooling to room temperature, the solidified mixture was dissolved in 6 M NaOH and the pH was adjusted to 7 with 6 M HCl. The product was extracted with chloroform, which was washed with water and dried over MgSO_4 . After

evaporating to dryness, a few mL MeOH were added and the remaining solid was collected by a fine frit. To further purify the product, the solid was dissolved in dilute HCl, neutralised with 6 M NaOH and cooled in the fridge. The pink solid was collected on a fine frit and dried *in vacuo* to obtain **Hbtp** (0.0234 g, 8% yield). ^1H NMR (600 MHz, DMSO-d_6 , 24.7 $^{\circ}$ C): δ = 8.27 (d, J = 7.68 Hz, 2 H), 8.21 (d, J = 7.68 Hz, 1 H), 8.12 (d, J = 7.94 Hz, 1 H), 7.63 - 7.71 (m, 3 H), 7.59 (t, J = 7.04 Hz, 1 H), 7.48 - 7.54 (m, 1 H), 6.19 - 6.31 (m, 1 H), 2.04 (br. s., 3 H). ^{13}C NMR (151 MHz, DMSO-d_6 , 24.7 $^{\circ}$ C): δ = 169.85, 165.92, 153.55, 145.19, 143.69, 137.78, 134.76, 133.23, 128.37, 128.19, 126.90, 125.91, 123.15, 122.56, 113.57, 111.22, 13.47. Anal. calcd (found) for $\text{C}_{19}\text{H}_{14}\text{N}_2\text{O}_2\text{S}\cdot\text{H}_2\text{O}$: C, 66.45 (66.17); H, 4.40 (4.52); N, 8.16 (8.21%). HR-ESIMS m/z for $\text{C}_{19}\text{H}_{15}\text{N}_2\text{O}_2^{32}\text{S}$ ($\text{M}+\text{H}^+$) calcd (found): 335.0854 (335.0851). IR (cm^{-1} , total reflectance): 3080 (br), 1625, 1573, 1522, 1518, 1232.

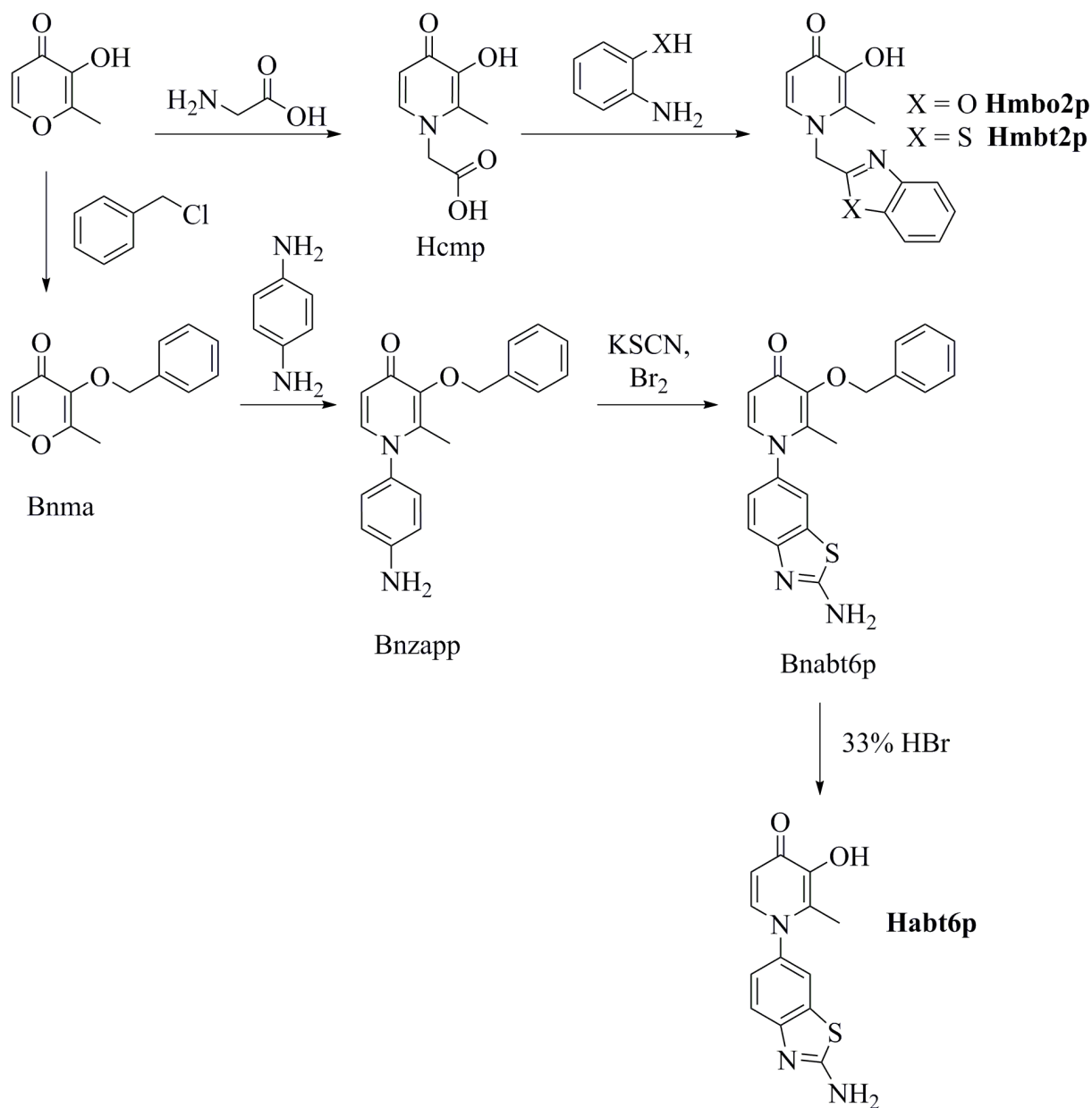
2.3 Results and discussion

For this study, the pro-ligands **Hmbo2p** and **Hmbt2p** (Figure 2.2) include a benzoxazole and a benzothiazole group, respectively, with the methylene linker providing a possible range of

motion for the amyloid-binding part.⁸⁹ **Habt6p** (Figure 2.2) contains an amine-bearing benzothiazole directly connected to the scaffold.

These three compounds were obtained in two-part syntheses that involve amine insertion⁹⁵ followed by cyclisation^{98,99} (Scheme 2.2). It was found that the yield was highest when **Hmbo2p** was prepared at high temperatures (over 200 °C) with short reaction times (under 8 hours), while **Hmbt2p** needed lower temperatures (160 °C) and longer reaction times (3 days). **Hmbo2p** could be isolated from the solution by filtration, while **Hmbt2p** was extracted. Interestingly, when the reaction of **Hmbo2p** was stopped prematurely or when the PPA contained an excess of water, two products were observed – **Hmbo2p** and a second, related, HPO. Using the masses of the two (257.4 and 275.4 m/z, respectively), and in consultation with the known mechanism of ring formation,¹⁰⁰ the second compound is likely an intermediate in the reaction. This intermediate was purified and its identity was postulated to be the amide intermediate (Figure A.1) using ¹H NMR spectroscopy, which reveals shifts in peaks, as well as two new peaks: the one at 9.57 ppm is likely the OH hydrogen, while the one at 3.16 ppm may be the NH hydrogen, although it may also be a solvent peak (Figure A.1).

First attempts at making **Habt6p** started with cyclisation on **Hzapp** (debenzylated Bnzapp), but it was found that the product formation was not reproducible and the product could not be easily isolated. Instead, when Bnzapp was used, the reaction proceeded well and the product could be isolated by column chromatography. There is an insoluble polymeric byproduct that is formed in the cyclisation reaction, and thus dilute conditions were used. Although the polymer was still formed to a small extent, it was easily filtered off after the reaction was complete.



Scheme 2.2 Pro-ligand Hmbo2p, Hmbt2p, and Habt6p synthesis. Scheme reproduced by permission of The Royal Society of Chemistry.

Pro-ligands **Hmbo2p**, **Hmbt2p**, and **Habt6p** were characterised by high resolution mass spectrometry (HR-MS), ^1H and ^{13}C NMR spectroscopy (Figures A.2-A.7), infrared (IR) spectroscopy, and elemental analysis (EA). Additionally, X-ray crystallography confirms the

structures of the three pro-ligands and the two synthetic intermediates of **Habt6p** (Figure 2.3), and shows that the main HPO ring retains its geometry with different substitutions off the ring. The summary of solid state structure data for the three pro-ligands, as well as for two synthetic intermediates Bnma and Bnzapp can be found in Tables A.1-A.3.

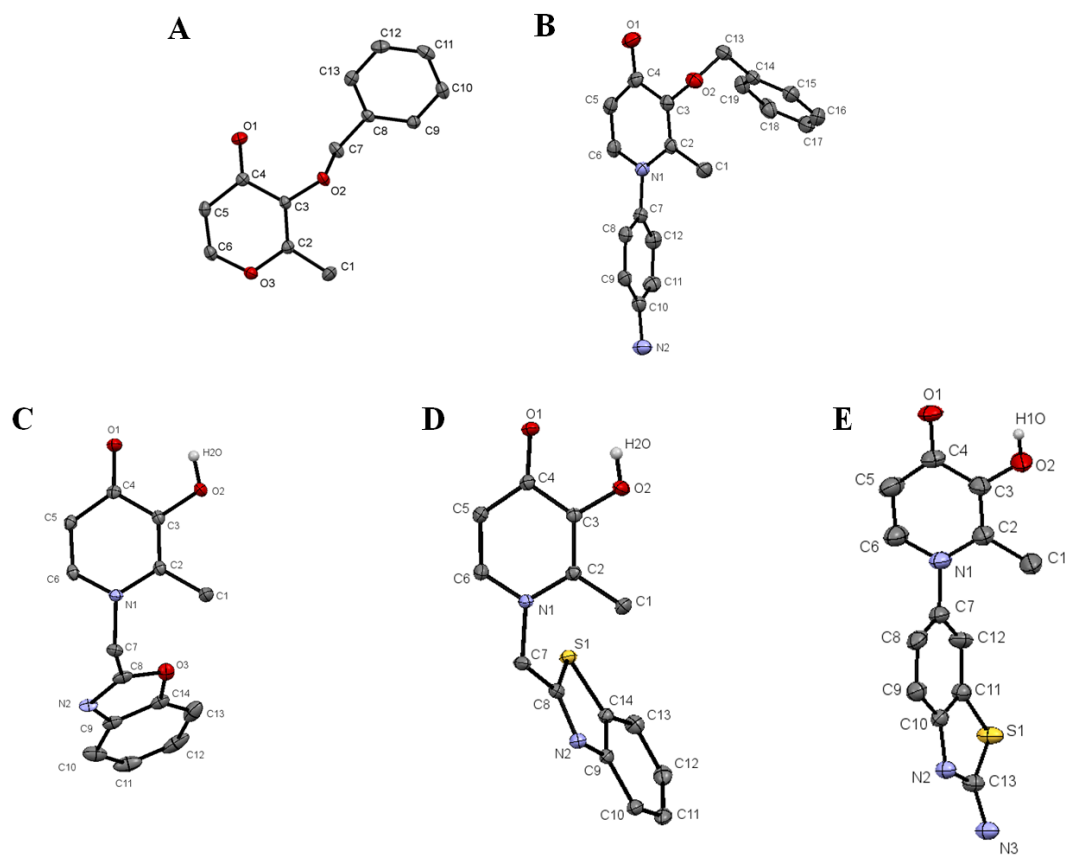
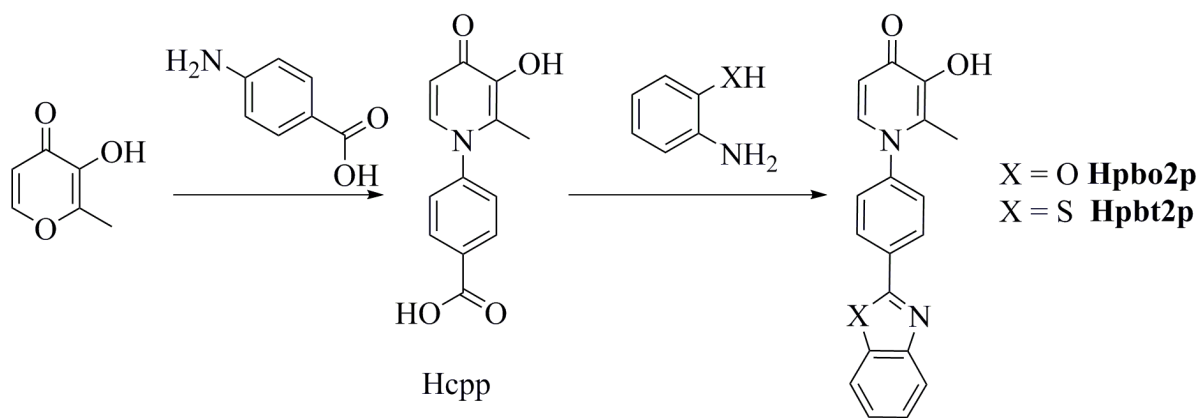


Figure 2.3 Solid state structures of **A) Bnma** and **B) Bnzapp** (synthetic intermediates for **Habt6p**), and **pro-ligands: C) Hmbo2p, D) Hmbt2p, and E) Habt6p**, represented as ellipsoid plots (50% probability). Solvent molecules and non O-H hydrogen atoms are omitted for clarity. Figure reproduced by permission of The Royal Society of Chemistry.

Hpbo2p and **Hpbt2p** were synthesised using synthetic route presented in Scheme 2.3, in a two-step procedure that ends in cyclisation^{98,99} leading to the phenyl-linked benzoxazole and benzothiazole. Yields were best with 24 hour reaction times, although they were still below 10% for the last step. Notably, the final products have low solubility across a range of solvents. These two pro-ligands were characterised by ¹H, ¹³C NMR spectroscopy (Figures A.8-A.11), HRMS, IR spectroscopy, and EA. Due to low solubility of **Hpbo2p**, the intensities of ¹³C NMR peaks were low, and some peaks, such as those arising from carbon atoms not bonded to hydrogen atoms, were difficult to distinguish from the noise of the baseline. To definitively assign peaks, 2D NMR spectroscopy was employed; thus with the aid of HSQC and HMBC (Figures A.12 and A.13), the peaks were identified and assigned.



Scheme 2.3 Pro-ligand Hpbo2p and Hpbt2p synthesis.

As well, single crystals of intermediate Hcpp and **Hpbo2p** were analysed by X-ray crystallography (Figure 2.4). Crystal and refinement data for Hcpp and **Hpbo2p**, as well as selected bond lengths and angles can be found in Tables A.4 and A.5. Likely due to packing effects, there is a noticeable bend in the benzoxazole, evinced by torsion angles between C13-

O3-C19-C18 at 3.5 ° and C13-N2-C14-C15 at 5.5 °; while in **Hmbo2p**, the torsion is minimal, at less than 1.2 °.

The pro-ligands **Hmbo2p**, **Hmbt2p**, **Habt6p**, **Hpbt2p**, and **Hpbo2p** comply with Lipinski's rules (Table 2.1), the values for which were calculated using software found at <http://www.molinspiration.com>. (It should be noted that logP value can be measured; when working with a library of compounds, it may be more convenient to estimate the logP value by calculations. In this case, the logP value is approximated with MiLogP by the aforementioned software). The title compounds have log BB values between -0.2 and -0.9 (Table 2.1), thus they may exhibit modest passive penetration through the BBB. These calculations suggest that the five pro-ligands are appropriate to investigate further as potential therapeutic agents for AD.

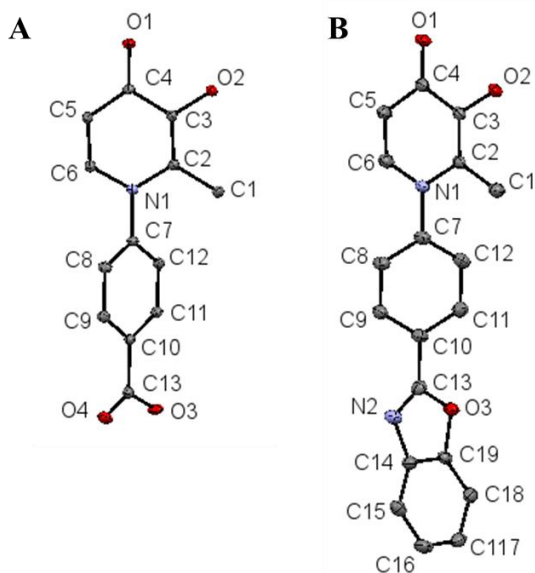


Figure 2.4 Solid state structures of A) Hccp and B) Hpbo2p, represented as ellipsoid plots (50% probability). Solvent molecules and hydrogen atoms are omitted for clarity.

Table 2.1 Lipinski's rules parameters and log BB calculated values for Hmbo2p, Hmbt2p, Habt6p, Hpbo2p, and Hpbt2p. Modified table reproduced by permission of The Royal Society of Chemistry.

	Hmbo2p	Hmbt2p	Habt6p	Hpbo2p	Hpbt2p
MW	256.26	272.32	273.31	318.33	334.4
MiLogP	1.02	1.16	1.22	2.71	3.35
TPSA	68.27	55.13	81.15	68.27	55.13
HBA	5	4	5	5	4
HBD	1	1	3	1	1
Lipinski's rules	pass	pass	pass	pass	pass
log BB	-0.72	-0.50	-0.88	-0.46	-0.17

Absorbance and fluorescence properties of pro-ligands are important for future studies.

Accordingly, UV-vis spectra in a buffered solution at pH 7.4 at room temperature were collected, and the results are illustrated in Figure 2.5. All ligands have a strong, broad absorbance peak in the 280-315 nm region. To identify the transitions responsible for the main spectral peaks of **Hmbo2p**, Dr. Jacqueline Cawthray performed TD-DFT calculations on the DFT optimised structure of the electronic ground state utilising UB3LYP/6-31+g(d,p) basis set and PCM model to account for water molecules. It was found that for **Hmbo2p**, the three main transitions were from HOMO to LUMO+1, HOMO-2 to LUMO, and from HOMO-1 to LUMO.¹⁰¹ The UV-vis spectral features of all compounds indicate that UV-vis absorbance spectroscopy can be used in various assays, as described in the later chapters. On the other hand, only **Hpbo2p** and **Hpbt2p** require excitation energies low enough for fluorescence studies with biological systems that will be described in the following chapters. Therefore, their fluorescence properties were studied by excitation at the highest absorbance (307 nm for **Hpbo2p** and 311 nm for **Hpbt2p**), with results depicted in Figure 2.5 (excitation maxima were 388 nm and 412 nm for **Hpbo2p** and **Hpbt2p**, respectively).

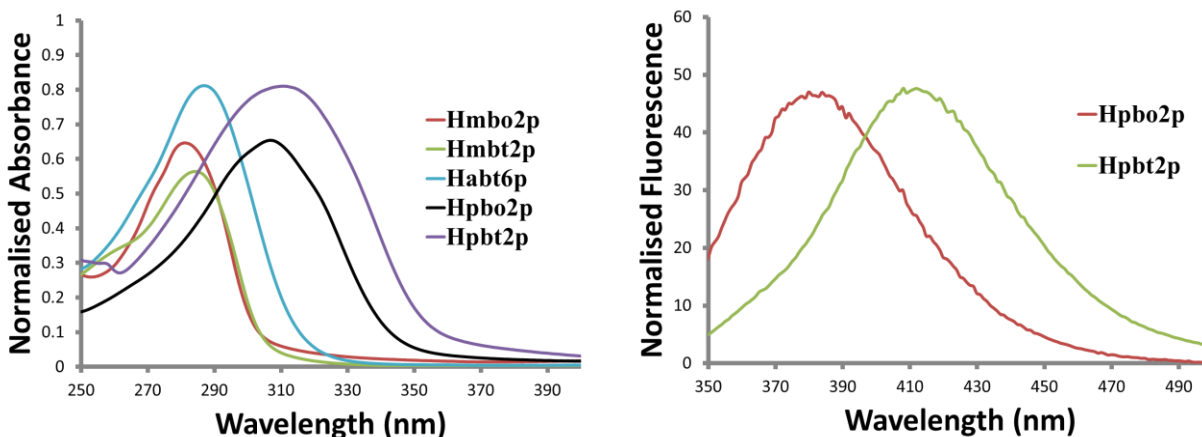


Figure 2.5 Absorbance (left) and fluorescence (right) properties of pro-ligands in a buffered aqueous solution at pH 7.4 at room temperature.

2.4 Conclusions

A small library of novel pro-ligands was successfully synthesised using mainly amine insertion and cyclisation reactions. Their design was based on the combination of the HPO metal-binding scaffold and the amyloid-binding functional groups of known PET imaging agents. The pro-ligands **Hmbo2p**, **Hmbt2p**, **Habt6p**, **Hpbo2p**, and **Hpbt2p** were characterised by standard methods (^1H NMR, ^{13}C NMR, IR spectroscopies, HRMS, and EA), and their identity and purity were established. Notably, solid state analysis confirms the structures of **Hmbo2p**, **Hmbt2p**, **Habt6p**, and **Hpbo2p**, and reveals a break in symmetry of the *N*-substituent when the oxygen in the benzoxazole group is replaced with sulfur (for **Hmbo2p** and **Hmbt2p**). The pro-ligands conform to Lipinski's rules in terms of their MW, logP, and HBD and HBA number of atoms, and have log BB values that are greater than -1.

After these compounds were purified and it was established that they are drug-like, they had to be tested in order to determine whether they possess properties that may make them potential AD

therapeutics. Subsequent chapters will present the investigation of the compatibility of the metal and amyloid-binding functionalities, as well as other activities of these chelating ligands.

Chapter 3: Metal binding studies with biorelevant metal ions in solution and solid states

3.1 Introduction

The role of metal ions in Alzheimer's disease is significant, as described in detail in Chapter 1. Accordingly, the study of the metal complexes of pro-ligands of interest was undertaken. The bulk of this chapter relates the synthesis and characterisation of metal complexes in the solid state. Six compounds are considered for these studies – the previously reported **Hppp**, **Hzapp**, and **Hbt2p**, and the three novel ones presented in this thesis – **Hmbo2p**, **Hmbt2p**, and **Habt6p**.

Previously, binding of **Hppp**, **Hzapp**, and **Hbt2p** to Cu was studied, and the complexes were characterised by IR, EA, and solid state structure analysis with X-ray crystallography.^{58,89} In this work, the complex formation is extended to Zn(II) and Fe(III) with these ligands in order to complete characterisation with biorelevant metal ions, as well as to study the effect of metal binding upon cytotoxicity, which is discussed in Chapter 4.

Hmbo2p, **Hmbt2p**, and **Habt6p** are novel ligands, and thus their metal-binding abilities were studied in more detail. First, they were chelated to a range of first-row transition metal ions (Cu(II), Zn(II), Ni(II), Fe(III), and Ga(III)) and the complexes were studied in the solid state by spectroscopies such as IR and NMR (where applicable), as well as elemental analysis and X-ray crystallography. As well, solution state studies were performed in order to determine the metal binding constants with Cu(II), Zn(II), and Fe(III). Finally, the matter of stability of the

complexes was considered in the presence of a reducing agent, and a biologically relevant chelating ligand.

The significance of these studies lies in proving that the amyloid-beta targeting functionality of novel compounds **Hmbo2p**, **Hmbt2p**, and **Habt6p** is compatible with metal binding. It has been previously observed that a range of substituents off the nitrogen in the HPO ring is tolerated without influencing metal chelation.⁶² Our goal was to confirm that metal binding is retained within our compounds, as well as to study the potential interactions that the complexes may encounter in biological systems to gain insight into their stability.

3.2 Experimental

3.2.1 Materials and methods

All chemicals and solvents were purchased from commercial suppliers (Aldrich, Alfa Aesar, Tokyo Chemical Industry Co., Ltd. (TCI) America, Eastman Organic Chemicals, Mallinckrodt) and used without further purification. Water was purified to 18.2 MΩ•cm by Elga Ultra Pure Lab System. Pro-ligands 3-hydroxy-2-methyl-1-phenyl-4(1H)-pyridinone (**Hppp**),⁸⁷ 1-(4-aminophenyl)-3-hydroxy-2-methyl-4(1H)-pyridinone (**Hzap**),⁵⁸ and 1-(2-benzothiazolyl)-3-hydroxy-2-methyl-4(1H)-pyridinone (**Hbt2p**)⁵⁸ were synthesised according to literature procedures by Dr. Lauren Scott.⁸⁹

3.2.2 Instrumentation

¹H NMR and ¹³C NMR spectra were recorded with a Bruker AV-300 spectrometer at 300.13 MHz and 75.48 MHz, respectively, at 24.7 °C and calibrated using residual solvent peaks. ¹H

NMR spectrum at 65.4 °C was recorded with a Bruker AV-400 at 400.19 MHz by Dr. Maria Ezhova. In addition, ^1H NMR and ^{13}C NMR spectra were recorded with a Bruker AV-600 spectrometer at 600.15 MHz and 150.92 MHz, respectively, at 25.0 °C by Dr. Maria Ezhova and Zorana Danilovic and calibrated using residual solvent peaks. Low-resolution mass spectra for metal complexes were obtained with a Bruker Esquire LC (samples analyzed by ESI-MS) or a Bruker Biflex IV (samples analyzed by MALDI-TOF). High-resolution mass spectra were obtained with a Waters/Micromass LCT, and elemental analyses (CHN) were done using a Carlo Erba Elemental Analyzer EA 1108. Bruker Esquire LC, Bruker Biflex IV, Waters/Micromass LCT, and Carlo Erba Elemental Analyzer EA 1108 were operated by David Wong, Derek Smith, Marco Yeung, and Marshall Lapawa. Infrared spectra were collected neat with a Perkin Elmer FTIR spectrometer. Spectrophotometric experiments were done with a Hewlett Packard 8453 UV-vis spectrophotometer and analyzed with HypSpec 1.1.3314 software.

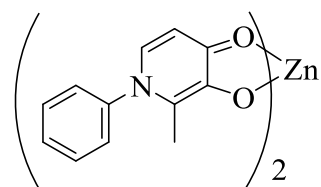
For solid state structure analysis, single crystals were mounted on a glass fiber and the measurements were done with a Bruker APEX DUO diffractometer with cross-coupled multilayer optics Cu-K α radiation or with graphite monochromated Mo-K α radiation. Data sets were collected and integrated using the Bruker SAINT¹⁰² software package. Data were corrected for absorption effects using the multi-scan technique (SADABS).¹⁰³ The structures were solved by direct methods¹⁰⁴ and all non-hydrogen atoms were refined anisotropically. All O-H hydrogen atoms were located in difference maps and refined isotropically, while all other hydrogen atoms were placed in calculated positions. All of solid state structure experiments and analyses were done by Dr. Brian O. Patrick.

3.2.3 Synthesis and characterisation

General procedure

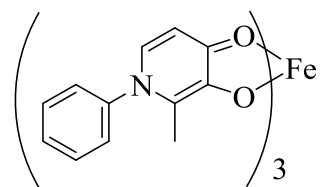
Unless otherwise specified, metal complexes were prepared by dropwise addition of 2 or 3 equivalents of ligand, in a minimum amount of MeOH with Et₃N, to 1 equivalent of a divalent or trivalent metal ion salt in a minimum amount of MeOH. The reactions were typically done in a 25 mL round bottom flask and stirred overnight, after which time the precipitate was collected on a fine frit, washed with MeOH and diethyl ether, and dried *in vacuo*. The complexes obtained were characterised as described below.

Bis(3-oxy-2-methyl-1-phenyl-4(1H)-pyridinonato)zinc(II), Zn(ppp)₂



Hppp (0.0338 g, 0.168 mmol) and zinc perchlorate hexahydrate (0.0317 g, 0.085 mmol) were used as described above, in a 10 mL round bottom flask. The reaction mixture was stirred overnight; solvent was removed *in vacuo* and H₂O (~ 5 mL) was added to precipitate the complex. The resultant white solid **Zn(ppp)₂** (0.015 g, 39% (first crop)) was collected by a fine frit and washed with H₂O and diethyl ether, and dried *in vacuo*. X-ray quality crystals were obtained from a saturated solution in MeOH by slow evaporation at room temperature. ¹H NMR (300 MHz, MeOD-d₄, 24.7 °C): δ = 7.55 - 7.64 (m, 3 H), 7.48 (d, *J* = 7.08 Hz, 1 H), 7.35 - 7.42 (m, 2 H), 6.64 (d, *J* = 6.85 Hz, 1 H), 2.19 (s, 3 H). ¹³C NMR (75 MHz, MeOD-d₄, 24.7 °C): δ = 172.77, 155.04, 144.17, 135.24, 133.73, 131.11, 130.86, 127.78, 109.82, 14.81. HR-ESIMS *m/z* for C₂₄H₂₀N₂O₄⁶⁴Zn (M⁺) calcd (found): 464.0715 (464.0719). IR (cm⁻¹, total reflectance): 3204, 3537, 1608, 1590, 1538, 1506, 1468, 1290, 760.

Tris(3-oxy-2-methyl-1-phenyl-4(1H)-pyridinonato)iron(III), Fe(ppp)₃

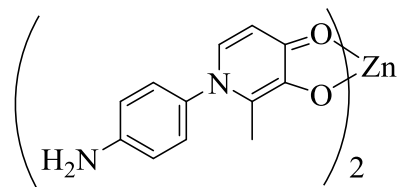


Hppp (0.0374 g, 0.186 mmol) and iron perchlorate hexahydrate (0.0287 g, 0.062 mmol) were used as described above, in a 10 mL round bottom flask. Solvent was removed *in vacuo* and H₂O (~ 5 mL)

was added to precipitate the complex after an overnight reaction. The resultant red solid

Fe(ppp)₃ (0.0171 g, 41% (first crop)), collected on a fine frit, washed with H₂O and diethyl ether, and dried *in vacuo*. X-ray quality crystals were obtained from a saturated solution in an acetonitrile/water mixture. HR-ESIMS *m/z* for C₃₆H₃₁⁵⁶FeN₃O₆ (M+H⁺) calcd (found): 657.1562 (657.1554). IR (cm⁻¹, total reflectance): 1588, 1538, 1504, 1468, 768.

Bis(1-(4-aminophenyl)-3-oxy-2-methyl-4(1H)-pyridinonato)zinc(II), Zn(zapp)₂

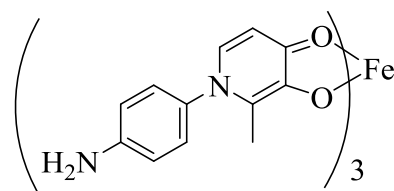


Hzapp (0.0516 g, 0.239 mmol) in min. amount of 50/50 MeOH:H₂O solution (~ 15 mL) was added dropwise to a 50 mL round bottom flask containing zinc perchlorate hexahydrate

(0.0484 g, 0.130 mmol) dissolved in min. amount of same solvent (~ 5 mL). The pH of the mixture was raised to 7 with NaOH and it was left stirring overnight. The resultant beige solid **Zn(zapp)₂** (0.0342 g, 54% (first crop)) was collected on a fine frit and washed with acetone, and dried *in vacuo*. ¹H NMR (300 MHz, DMSO-d₆, 24.7 °C): δ = 7.27 (d, *J* = 6.85 Hz, 1 H), 6.99 (d, *J* = 8.68, Hz, 2 H), 6.63 (d, *J* = 8.45 Hz, 2 H), 6.29 (d, *J* = 6.85 Hz, 1 H), 5.46 (s, 2 H), 2.03 (s, 3 H). ¹³C NMR (75 MHz, DMSO-d₆, 24.7 °C): δ = 171.32, 155.39, 149.19, 132.57, 131.29, 128.98, 126.80, 113.59, 106.78, 13.89. Anal. calcd (found) for C₂₄H₂₂N₄O₄Zn • 2 H₂O: C, 54.20 (54.57); H, 4.93 (4.82); N, 10.53 (10.30%). HR-ESIMS *m/z* for C₂₄H₂₃N₄O₄⁶⁴Zn (M+H⁺)

calcd (found): 495.1011 (495.1007). IR (cm⁻¹, total reflectance): 3360, 3328, 1608, 1588, 1540, 1512, 1464, 1292, 764.

Tris(1-(4-aminophenyl)-3-oxy-2-methyl-4(1H)-pyridinonato)iron(III), Fe(zapp)₃



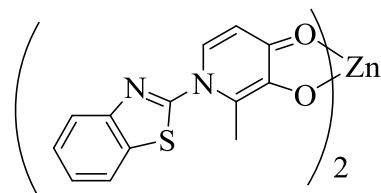
Hzap (0.117 g, 0.542 mmol) in min. amount of 50/50

MeOH/H₂O (~ 25 mL) was added dropwise to a 50 mL round

bottom flask containing iron perchlorate hexahydrate (0.0134 g,

0.029 mmol) dissolved in the same solvent (~ 5 mL). The pH was increased to 7 with aq. NaOH and the reaction was stirred overnight. The red precipitate **Fe(zapp)₃** (0.0858 g, 65% yield) was collected on a fine frit. The solid was recrystallised from an acetonitrile/water solution to yield single crystals that resulted in partially solved solid-state structure as analyzed by X-ray crystallography; they were used in the following analyses after being dried *in vacuo*. Anal. calcd (found) C₃₆H₃₃FeN₆O₆•1.5 H₂O: C, 59.35 (59.09); H, 4.98 (4.82); N, 11.54 (10.94%). HR-ESIMS m/z for C₃₆H₃₄⁵⁶FeN₆O₆ (M+H⁺) calcd (found): 702.1889 (702.1912). IR (cm⁻¹, total reflectance): 3356, 3236, 1608, 1594, 1538, 1510, 1468, 1292, 766.

Bis(1-(2-benzothiazolyl)-2-methyl-3-oxy-4-pyridinonato)zinc(II), Zn(bt2p)₂



Hbt2p (0.0327 g, 0.127 mmol) and EtN₃ (17.7 μL, 127 mmol)

dissolved in a min. amount of 9:1 MeOH:DCM (~ 10 mL) were

added dropwise to a 25 mL round bottom flask containing zinc

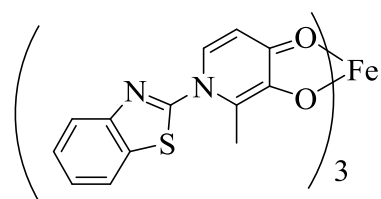
perchlorate hexahydrate (0.0237 g, 0.064 mmol) dissolved in min. amount of the same solvent

(~ 3 mL). The solution was stirred overnight, and the volume of the solvent was reduced to one

third *in vacuo*. The flask was cooled in the freezer and the resultant beige solid **Zn(bt2p)₂**

(0.0208 g, 55% (first crop)) was collected by a fine frit and dried *in vacuo*. ^1H NMR (300 MHz, DMSO- d_6 , 24.7 °C): δ = 8.25 (d, J = 7.77, 1 H), 8.12 (d, J = 7.99, 1 H), 7.88 (d, J = 6.85, 1 H), 7.57 – 7.70 (m, 2 H), 6.51 (d, J = 7.08 Hz, 1 H), 2.33 (s, 3 H). ^{13}C NMR (75 MHz, DMSO- d_6 , 24.7 °C): δ = 173.90, 160.69, 155.05, 149.18, 134.98, 133.11, 127.31, 126.94, 126.63, 123.58, 122.82, 108.21, 13.60. Anal. calcd (found) for $\text{C}_{26}\text{H}_{18}\text{N}_4\text{O}_4\text{S}_2\text{Zn} \cdot \text{H}_2\text{O}$: C, 52.22 (52.47); H, 3.37 (3.28); N, 9.37 (8.93%). HR-ESIMS m/z for $\text{C}_{26}\text{H}_{19}\text{N}_4\text{O}_4\text{S}_2^{64}\text{Zn} (\text{M} + \text{H}^+)$ calcd (found): 579.0145 (579.0139). IR (cm^{-1} , total reflectance): 1604, 1552, 1512, 1468, 1268, 694.

Tris(1-(2-benzothiazolyl)-2-methyl-3-oxy-4- pyridinonato)iron(III), **Fe(bt2p)**₃



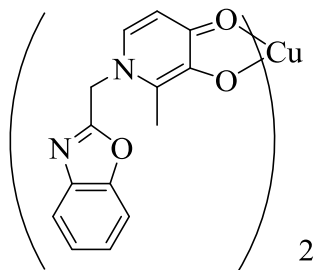
Hbt2p (0.0268 g, 0.104 mmol) and EtN_3 (15 μL , 108 μmol) in min. amount of 9:1 MeOH:DCM (~ 10 mL) were added dropwise to a 25 mL round bottom flask containing iron perchlorate

hexahydrate (0.0159 g, 0.034 mmol) dissolved in min. amount of the same solvent (~3 mL).

After the reaction stirred overnight, solvent was reduced to a third of the volume *in vacuo*. After the solution was cooled in the freezer, the resultant red solid **Fe(bt2p)**₃ (0.0099 g, 32% (first crop)) was collected on a fine frit and dried *in vacuo*. Anal. calcd (found) for $\text{C}_{39}\text{H}_{27}\text{FeN}_6\text{O}_6\text{S}_3 \cdot 3 \text{H}_2\text{O}$: C, 53.12 (53.17); H, 3.77 (3.52); N, 9.53 (9.50%). HR-ESIMS m/z for $\text{C}_{39}\text{H}_{28}^{56}\text{FeN}_6\text{O}_6\text{S}_3 (\text{M} + \text{H}^+)$ calcd (found): 828.0582 (828.0583). IR (cm^{-1} , total reflectance): 1590, 1544, 1504, 1464, 1276, 662.

Bis(1-(benzo[d]oxazol-2-ylmethyl)-3-oxy-2-methylpyridinon-4(1H)-ato)copper(II),

Cu(mbo2p)₂

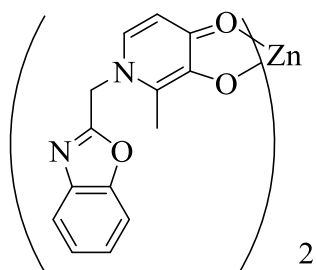


Copper perchlorate hexahydrate (0.011 g, 0.030 mmol) and **Hmbo2p** (0.015 g, 0.059 mmol) were used as described above, resulting in a green solid **Cu(mbo2p)₂** (0.008 g, 47%). Anal. calcd (found) for C₂₈H₂₂CuN₄O₆•0.5 H₂O: C, 57.68 (57.42); H, 3.98 (3.86); N, 9.61 (9.43%). HR-ESIMS *m/z* for C₂₈H₂₃⁶³CuN₄O₆ (M+H⁺) calcd (found):

574.0914 (574.0919). IR (cm⁻¹, total reflectance): 1596, 1540, 1507, 1477, 1242, 743.

Bis(1-(benzo[d]oxazol-2-ylmethyl)-3-oxy-2-methylpyridinon-4(1H)-ato)zinc(II),

Zn(mbo2p)₂

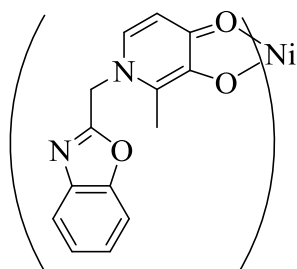


Zinc perchlorate hexahydrate (0.015 g, 0.040 mmol) and **Hmbo2p** (0.020 g, 0.078 mmol) were used as described above, with a modification. After an overnight reaction, H₂O was added to precipitate the complex, resulting in a beige solid **Zn(mbo2p)₂** (0.014 g, 60%), which was handled as described above. ¹H NMR (300 MHz,

DMSO-d₆, 24.7 °C): δ = 7.74 (dd, *J* = 6.62, 2.06 Hz, 2 H), 7.61 (d, *J* = 6.85, 1 H), 7.33 – 7.50 (m, 2 H), 6.33 (d, *J* = 6.85 Hz, 1 H), 5.71 (s, 2 H), 2.32 (s, 3 H). ¹³C NMR (151 MHz, DMSO-d₆, 25.0 °C): δ = 171.79, 161.66, 155.81, 150.33, 140.31, 133.26, 128.79, 125.66, 124.87, 119.95, 111.04, 107.44, 51.05, 12.00. Anal. calcd (found) for C₂₈H₂₂N₄O₆Zn•1.5 H₂O: C, 55.78 (55.77); H, 4.18 (3.89); N, 9.29 (9.06%). Maldi-TOF MS(+) *m/z* calcd (found): 575.09 (575.0 ([HZn(mbo2p)₂]⁺, M+H⁺)). IR (cm⁻¹, total reflectance): 1598, 1543, 1506, 1482, 1241, 744.

Bis(1-(benzo[d]oxazol-2-ylmethyl)-3-oxy-2-methylpyridinon-4(1H)-ato)nickel(II),

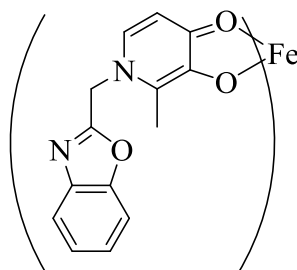
Ni(mbo2p)₂



Nickel chloride hexahydrate (0.008 g, 0.034 mmol) and **Hmbo2p** (0.018 g, 0.070 mmol) were used as described above, resulting in the off-white solid **Ni(mbo2p)₂** (0.018 g, 81%). Anal. calcd (found) for $C_{28}H_{22}N_3NiO_6 \cdot 3.5 H_2O$: C, 53.19 (52.94); H, 4.62 (4.48); N, 8.86 (8.67%). HR-ESIMS m/z for $C_{28}H_{23}N_4^{58}NiO_6$ ($M+H^+$) calcd (found): 569.0971 (569.0995). IR (cm^{-1} , total reflectance): 1606, 1548, 1505, 1486, 1241, 747.

Tris(1-(benzo[d]oxazol-2-ylmethyl)-3-oxy-2-methylpyridinon-4(1H)-ato)iron(III),

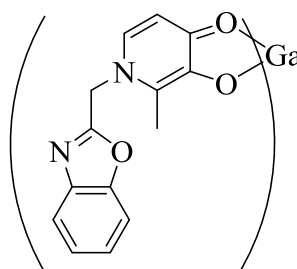
Fe(mbo2p)₃



Iron perchlorate hexahydrate (0.023 g, 0.050 mmol) and **Hmbo2p** (0.039 g, 0.152 mmol) were used as described above, resulting in a red solid **Fe(mbo2p)₃** (0.023 g, 52%). Anal. calcd (found) for $C_{42}H_{33}FeN_6O_9 \cdot 3 H_2O$: C, 57.61 (57.67); H, 4.49 (4.30); N, 9.60 (9.53%). HR-ESIMS m/z for $C_{42}H_{34}^{56}FeN_6O_9$ ($[HFe(mbo2p)_3]^+$, $M+H^+$) calcd (found): 822.1737 (822.1750). IR (cm^{-1} , total reflectance): 1599, 1542, 1506, 1485, 1241, 747.

Tris(1-(benzo[d]oxazol-2-ylmethyl)-3-oxy-2-methylpyridinon-4(1H)-ato)gallium(III),

Ga(mbo2p)₃

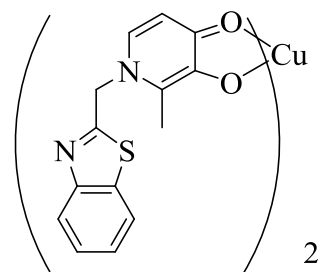


Gallium nitrate hydrate (0.007 g, 0.019 mmol) and **Hmbo2p** (0.018 g, 0.070 mmol) were used as described above, with a variation. After an

overnight reaction, the methanol was removed *in vacuo* and H₂O was added to precipitate the complex. The resultant beige solid was collected by a fine frit and washed with MeOH and diethyl ether. It was then recrystallised from MeOH, collected on a fine frit, and dried *in vacuo*, resulting in **Ga(mbo2p)₃** (0.010 g, 47%). ¹H NMR (400 MHz, DMSO-d₆, 65 °C): δ = 7.71-7.79 (m, 3 H), 7.36-7.43 (m, 2 H), 6.42 (d, *J* = 6.83, 1 H), 5.73 (s, 2 H), 2.32 (s, 3 H). ¹³C NMR (151 MHz, DMSO-d₆, 25.0 °C): δ = 168.75, 161.35, 153.30, 150.38, 140.25, 134.53, 129.46, 125.65, 124.85, 120.05, 111.07, 106.78, 51.16, 12.27. Anal. calcd (found) for C₄₂H₃₃GaN₆O₉•2.5 H₂O: C, 57.29 (57.55); H, 4.35 (4.26); N, 9.54 (9.17%). HR-ESIMS *m/z* for C₄₂H₃₃⁶⁹GaN₆NaO₉ (M+Na⁺) calcd (found): 857.1463 (857.1470). IR (cm⁻¹, total reflectance): 1602, 1544, 1514, 1486, 1240, 746.

Bis(1-(benzo[d]thiazol-2-ylmethyl)-3-oxy-2-methylpyridinon-4(1H)-ato)copper(II),

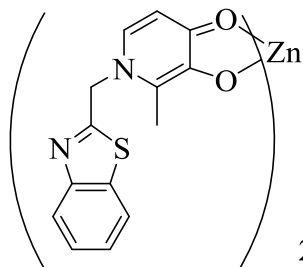
Cu(mbt2p)₂



Copper perchlorate hexahydrate (0.018 g, 0.047 mmol) and **Hmbt2p** (0.026 g, 0.094 mmol) were used as described above, resulting in a green solid **Cu(mbt2p)₂** (0.021 g, 70% yield). X-ray quality crystals were obtained from a saturated solution of DMSO. HR-ESIMS *m/z* for C₂₈H₂₃⁶³CuN₄O₄S₂ (M+H⁺) calcd (found): 606.0457 (606.0455). Anal. calcd (found) for C₂₈H₂₂CuN₄O₄S₂•1.5 H₂O: C, 53.11 (52.98); H, 3.98 (3.95); N, 8.85 (8.82%). IR (cm⁻¹, total reflectance): 1594, 1538, 1506, 1476, 1287, 762.

Bis(1-(benzo[d]thiazol-2-ylmethyl)-3-oxy-2-methylpyridinon-4(1H)-ato)zinc(II),

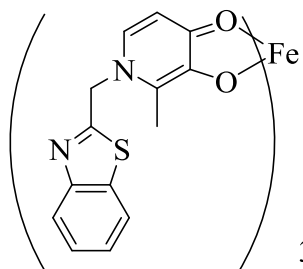
Zn(mbt2p)₂



Zinc perchlorate hexahydrate (0.016 g, 0.043 mmol) and **Hmbt2p** (0.023 g, 0.086 mmol) were used as described above, resulting in a pale green solid **Zn(mbt2p)₂** (0.019 g, 74%). X-ray quality crystals were obtained from a saturated solution of acetonitrile/H₂O. ¹H NMR (300 MHz, DMSO-d₆, 24.7 °C): δ = 8.08 (dd, *J* = 7.99, 0.91 Hz, 1 H), 7.99-8.01 (m, 1H), 7.67 (d, *J* = 6.85, 1 H), 7.41 – 7.55 (m, 2 H), 6.36 (d, *J* = 6.85 Hz, 1 H), 5.80 (s, 2 H), 2.30 (s, 3 H). ¹³C NMR (151 MHz, DMSO-d₆, 25.0 °C): δ = 171.85, 167.68, 156.07, 152.53, 134.47, 132.98, 128.39, 126.52, 125.50, 122.80, 122.53, 107.46, 55.57, 12.16. Anal. calcd (found) for C₂₈H₂₂N₄O₄S₂Zn: C, 55.31 (55.39); H, 3.65 (3.99); N, 9.21 (8.85%). HR-ESIMS *m/z* for C₂₈H₂₃N₄O₄S₂⁶⁴Zn (M+H⁺) calcd (found): 607.0452 (607.0439). IR (cm⁻¹, total reflectance): 1594, 1544, 1504, 1486, 1254, 758.

Tris(1-(benzo[d]thiazol-2-ylmethyl)-3-oxy-2-methylpyridinon-4(1H)-ato)iron(III),

Fe(mbt2p)₃

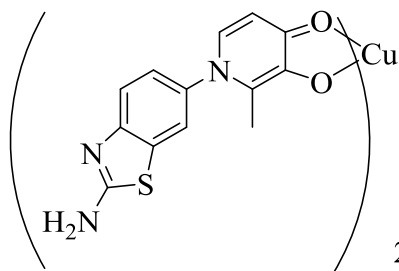


Iron perchlorate hexahydrate (0.014 g, 0.031 mmol) and **Hmbt2p** (0.025 g, 0.094 mmol) were used as described above. After an overnight reaction, the volume of the clear red solution was reduced to a third *in vacuo*. The red solid **Fe(mbt2p)₃** was isolated as described above (0.009 g, 32%). X-ray quality crystals were obtained from a saturated solution of acetonitrile and H₂O. Anal. calcd (found) for C₄₂H₃₃FeO₆S₃: C, 58.00 (58.09); H, 3.82 (4.15);

N, 9.48 (9.53%). HR-ESIMS m/z for $C_{42}H_{34}^{56}FeN_6O_6S_3$ ($M+H^+$) calcd (found): 870.1051 (870.1049). IR (cm^{-1} , total reflectance): 1626, 1576, 1542, 1504, 1210, 750.

Bis(1-(2-aminobenzothiazol-6-yl)-3-oxy-2-methylpyridinon-4(1H)-ato)copper(II),

Cu(abt2p)₂



Copper perchlorate hexahydrate (0.012 g, 0.032 mmol) and **Habt6p** (0.018 g, 0.063 mmol) were used as described above, resulting in a green solid **Cu(abt6p)₂** (0.012 g, 57%). Anal. calcd (found) for $C_{26}H_{20}CuN_6O_4S_2 \cdot 1.5 H_2O$: C, 49.16 (49.15); H, 3.65 (3.39); N, 13.23 (12.81). HR-ESIMS m/z for $C_{26}H_{21}^{63}CuN_6O_4S_2$ ($M+H^+$) calcd (found): 608.0362 (608.0356). IR (cm^{-1} , total reflectance): 3460, 1626, 1590, 1538, 1508, 1278, 724.

3.2.4 Binding affinities

The pK_a values for **Hmbo2p**, **Hmbt2p**, and **Habt2p** were determined by spectrophotometric titration.⁶⁰ Concentrated methanol stock solutions of each were diluted to $\sim 25 \mu M$ in 0.1 M KCl H_2O , with MeOH making up at most 1% of the solution. During titrations, the pH was increased from 2.5 to 11.5 by addition of base, and at each point UV-vis data was collected after equilibration of the species 25 °C. The data were fitted with HypSpec 1.1.33.¹⁰⁵ Log β values for **Hmbo2p** were determined using spectrophotometric titrations under the same conditions, in the presence of 1, 0.5, and 0.33 equivalents of metals Cu(II), Zn(II), and Fe(III). The data were fitted using HypSpec 1.1.33.¹⁰⁵ Stability constants for all ligand-metal species could be fitted, with the exception of the 3:1 **Hmbo2p**:Cu(II) species.

3.2.5 Stability

To study complex stability in a buffered solution in the presence of a reducing agent, a 1:2 Cu(II) complex of **Hmbo2p** was made *in situ* in 10 mM HEPES buffer at pH 7.4, to a concentration of ~ 20 μM (final), with methanol making up 1% of the 2 mL volume. UV-vis spectra were collected before and after addition of Cu(II) to ensure complete reaction and equilibration. Then, 60 μM (final) of ascorbic acid dissolved in H_2O was added, and UV-vis spectra were collected at 2 hours and 1 day thereafter. Between measurements, the solution was stored in the dark at room temperature. As controls, the copper complex complex was incubated in the buffered solution without ascorbic acid.

To investigate Cu(II) stability against reduction, **Hmbo2p** (20 μM) and EDTA (10 μM) were pre-incubated with Cu(II) (10 μM) in 10 mM HEPES buffer at pH 7.4, after which point coumarin-3-carboxylic acid (300 μM) and ascorbic acid (300 μM) were added. The fluorescence signal of the product of the radical reaction was followed continuously for 10 min (ex. 395 nm, em. 452 nm).¹⁰⁶ As control, no chelator was used in the pre-incubation period of the study.

To study the stability of the complex in the presence of another chelator, 0.02 mM **Cu(zapp)₂** solution in 10 mM HEPES buffer at pH 7.4 was incubated with 0.20 mM histidine. The solution was monitored for 3 days by UV-vis spectroscopy, and as a control, the complex alone was monitored over this time period in HEPES buffer.

3.3 Results and discussion

3.3.1 Metal complex preparation and characterisation

The synthesis of complexes was achieved by combining metal ions with ligands in appropriate ratios under various conditions adapted from the literature. For pro-ligands **Hppp**, **Hmbo2p**, **Hmbt2p**, and **Habt2p**, it was performed in methanol, for **Hbt2p** in dichloromethane/methanol solution, with triethylamine as a base,⁵⁸ while for **Hzapp**, a water-methanol solution with sodium hydroxide as a base was used.⁸⁷

In each case, combining 2:1 or 3:1 ratios of ligand to metal to divalent or trivalent metals, respectively, resulted in the desired species, which was confirmed by various methods, as described below. It was noted that in general, Cu(II) complexes precipitated out of solution, while using the same procedure required reduction of volume or using more polar solvents to precipitate the desired Zn(II) and Fe(III) complexes. When these measures were not taken, isolated yields tended to be moderate.

First, binding of previously studied ligands **Hppp**, **Hzapp**, and **Hbt2p** to Zn(II) and Fe(III) will be discussed. When prepared and isolated in the absence of water, the complexes of **Hppp** were found to be deliquescent, and were challenging to purify. Their tendency to hydrate is evident in solid state analysis, as **Hppp** crystallised with water bound to **Zn(ppp)₂**, while each Fe(III) center has six waters in the solid state (see below). The presence of solvent species and/or perchlorate ions was evident in the elemental analyses for these two complexes, and the elemental composition could not be confirmed for the bulk **Zn(ppp)₂** and **Fe(ppp)₃**. On the

other hand, elemental analyses for complexes of **Hzap** and **Hbt2p** confirmed purity of the bulk material, revealing none to several waters present per metal center.

To confirm complete complexation, Zn(II) complexes were studied by NMR spectroscopy (as they are diamagnetic) by taking spectra of the reaction mixture and comparing them to those of the starting materials. While it is expected that all reactions herein go to completion, the isolated yields are lower, presumably due to high solubility of the complexes. It should be noted that the zinc coordination sphere is not saturated when the 2:1 ligand to metal stoichiometry is used, thus bridging ligands and water molecules are observed in X-ray crystallography studies, as described below. As well, metal binding studies (described below) reveal a binding constant for the 3:1 ligand to metal species, and it is present at high pH. When this ratio was used during reactions, a 3:1 complex was not present in high yield and could not be isolated, although its presence is confirmed with mass spectrometry (data not shown).

The comparison of NMR spectra reveals shifts in hydrogen and carbon peaks upon binding of **Hppp**, **Hzap**, and **Hbt2p** to Zn(II). The most drastic shifts were observed for atoms around the pyridinone ring. For instance, as can be seen in Figure 3.1, the biggest shift upon Zn coordination with **Hppp** is downfield with H5 (marked by symbol +) and upfield with H6 (symbol #), consistent with other NMR studies of coordination of HPOs to diamagnetic metals.¹⁰⁷

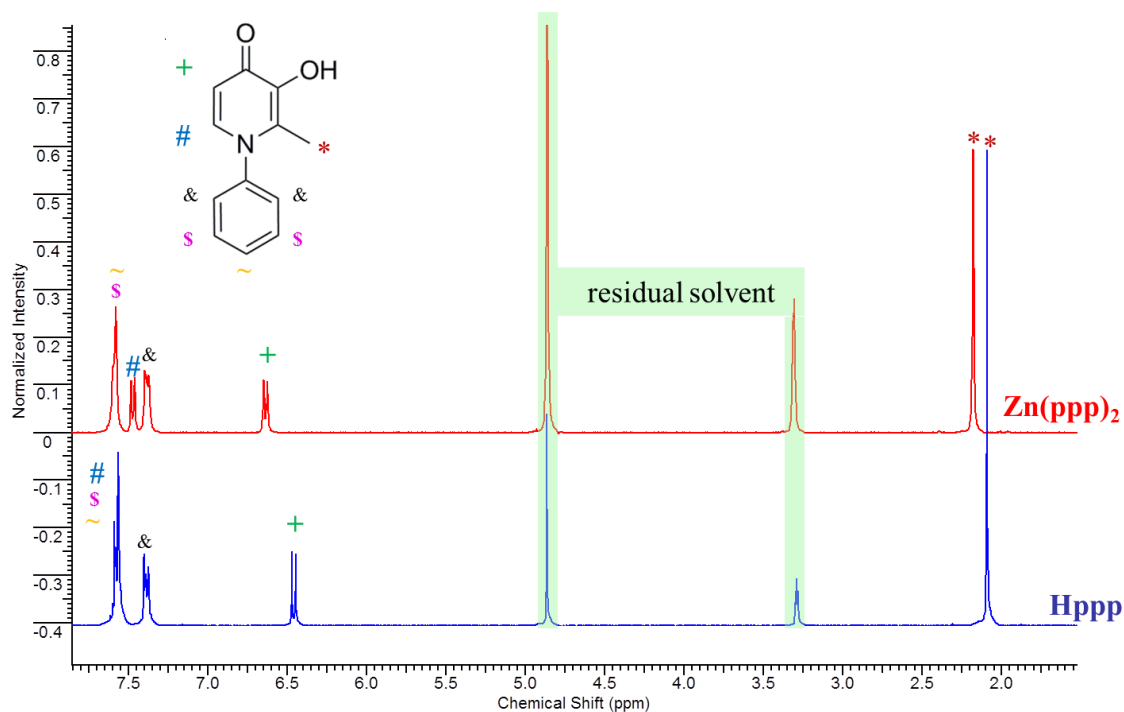


Figure 3.1 ^1H NMR spectra comparing Hppp to $\text{Zn}(\text{ppp})_2$ (300 MHz, MeOD-d_4 , 24.7 °C). Figure used with permission from Elsevier.

Metal complexation is also confirmed by IR spectroscopy for all complexes. For example, comparing IR spectra of ligands **Hppp**, **Hzap**, and **Hbt2p** to their corresponding Zn(II) and Fe(III) complexes, several observations were made (Table 3.1). In metal complexes, save **Zn(ppp)₂**, it was found that the peak due to the OH stretch is absent, as is expected due to deprotonation upon binding. Peaks in the fingerprint region that are assigned to the C=O and ring stretching, and CH bending modes had a bathochromic shift upon complexation, consistent with previous observations.⁵⁸ As well, new peaks were observed in the 600-800 cm^{-1} region that are assigned to new metal-oxygen vibrations. The two peaks in the OH region for **Zn(ppp)₂** might be due to water or residual uncoordinated compound, as suggested to exist in the solid state (see below).

Table 3.1 Selected IR bands and their assignments.¹⁰⁸ Symbols denote the following: * obscured by an adjacent peak, ν stretching, δ_{as} asymmetric in plane bend. Table used with permission from Elsevier.

	Signature IR peaks (cm ⁻¹)				
	ν NH	ν OH	ν C=O, ring, δ_{as} CH	ν CO	ν MO
Hppp		3200	1626, 1599, 1579, 1537, 1485	1296	
Zn(ppp)₂		3204, 3537	1608, 1590, 1538, 1506, 1468	1290	760
Fe(ppp)₃			* , 1588, 1538, 1504, 1468	*	768
Hzapp	* , 3313	3204	1622, * , 1555, 1512, 1487	1292	
Zn(zapp)₂	3360, 3328		1608, 1588, 1540, 1512, 1464	1292	764
Fe(zapp)₃	3356, 3236		1608, 1594, 1538, 1510, 1468	1292	766
Hbt2p		3091	1624, 1576, 1538, 1508, 1483	1302	
Zn(bt2p)₂			1604, 1552, * , 1512, 1468	1268	694
Fe(bt2p)₃			1590, 1544, * , 1504, 1464	1276	662

Finally, mass spectrometry confirms 2:1 and 3:1 ligand to metal ratios for Zn(II) and Fe(III) complexes, respectively. These species are confirmed by the isotopic pattern in the low resolution spectra and with the accurate mass measurements by high resolution spectrometry. Interestingly, low resolution spectra for complexes with divalent species indicated that there are $[M_2L_3]^+$ (where **M** is the metal and **L** is the ligand) species present as well, likely an effect induced by the ionisation techniques. For instance, these species were observed for **Zn(ppp)₂**, **Zn(zapp)₂**, and **Zn(bt2p)₂** with m/z masses of 728, 775, and 901 for the tallest peaks in ESI-MS(+).

Having established complexation conditions for the previously studied ligands, **Hmbo2p** was used as a representative ligand to establish metal chelation profiles for the novel proligands **Hmbp2p**, **Hmbt2p**, and **Habt6p**. Hmbo2p was combined in 2:1 proportions with the divalent metals Cu(II), Zn(II), and Ni(II), and in 3:1 with the trivalent Fe(III) and Ga(III). Metal binding

was confirmed by NMR and IR spectroscopies, similar to the observations described above. The identity and the purity of these complexes were also established using HR-MS and EA.

To further study the Zn(II) and Ga(III) complexes, NMR spectroscopy was employed to reveal ^1H and ^{13}C shifts upon complexation (Figures A.14-A.19). Notably, in the case of Ga(III), the room temperature spectrum reveals the presence of multiple isomers (seen as peak splitting of the ^1H spectra), which is not observed at higher temperatures (Figure 3.2). Metal binding of **Hmbt2p** to the biorelevant metals Cu(II), Zn(II), and Fe(III) and of **Habt6p** with Cu(II) was also confirmed with all the methods outlined above.

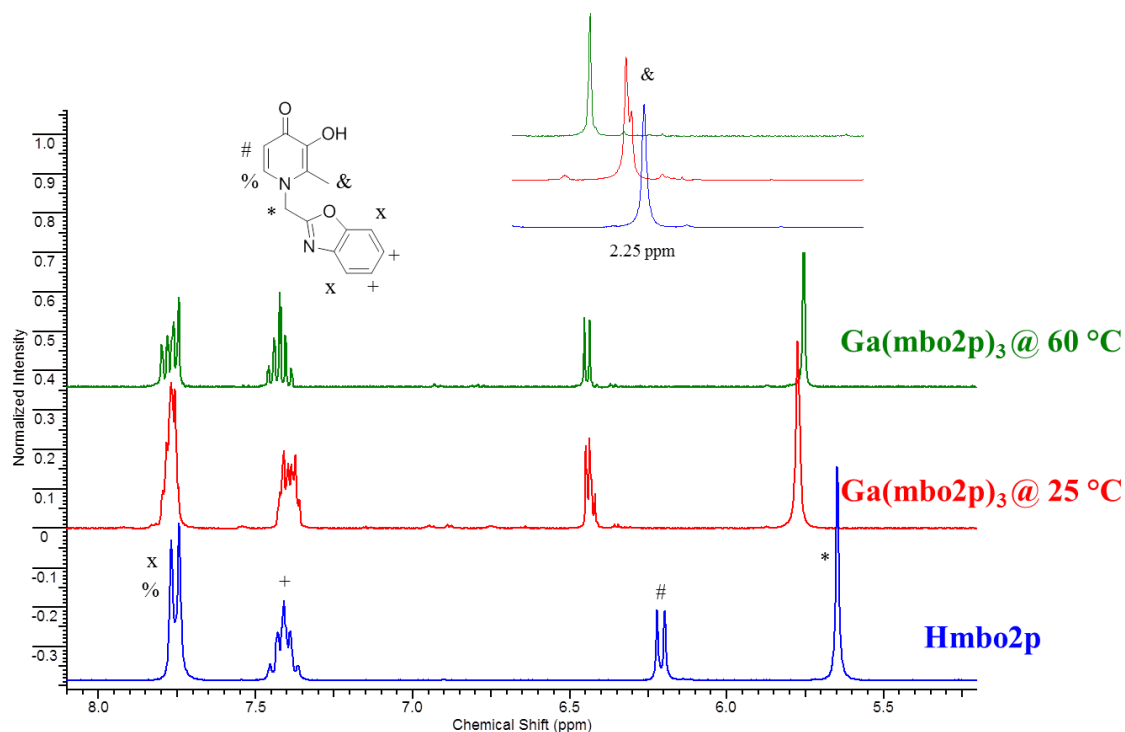


Figure 3.2 ^1H NMR spectra comparing Hmbo2p (300 MHz), $\text{Ga}(\text{mbo2p})_3$ at 25 (600 MHz) and 65 °C (400 MHz) in DMSO-d_6 . Figure reproduced by permission of The Royal Society of Chemistry.

Single crystals suitable for X-ray crystallography for complexes **Zn(ppp)₂**, **Fe(ppp)₃**, **Cu(mbt2p)₂**, **Zn(mbt2p)₂**, and **Fe(mbt2p)₃** were obtained by slow evaporation of saturated solutions, as detailed in the experimental section, above; crystal and refinement data are summarised in Tables A.6 and A.7 (for complexes with **Hppp**) Tables A.8 and A.9 (for complexes with **Hmbt2p**).

The complex between Zn(II) and **Hppp** crystallised as a tetramer – with four Zn(II) molecules per eight ligands (Figure 3.3), consistent with the 1:2 stoichiometry seen in HRMS. With each tetramer there are also two coordinating water molecules, two non-coordinating methanol solvent molecules, and a disordered perchlorate ion. As the ligand on each end retains its neutral form, the water molecule replaces the oxygen in coordination to Zn, and the perchlorate ion balances out the charge. Each tetramer contains two dimers that are related to each other by inversion symmetry. Interestingly, each dimer contains two Zn centers with different geometries. The Zn1 center has distorted square pyramidal geometry with 4 oxygen atoms from ligands and one from a water molecule, while the Zn2 center has distorted octahedral geometry with six oxygen atoms from the ligands. As can be seen in Figure 3.3, the ligand bridges between the two Zn centers, with Zn-Zn distance 3.0326(4) Å (Table A.7). Zn-O distances range from 2.00 to 2.11 Å, with an exception of an oxygen atom that belongs to a ligand that is bridging between the two centers, with distance equal to 2.37 Å (e.g. Zn2-O4, Figure 3.3, Table A.7).

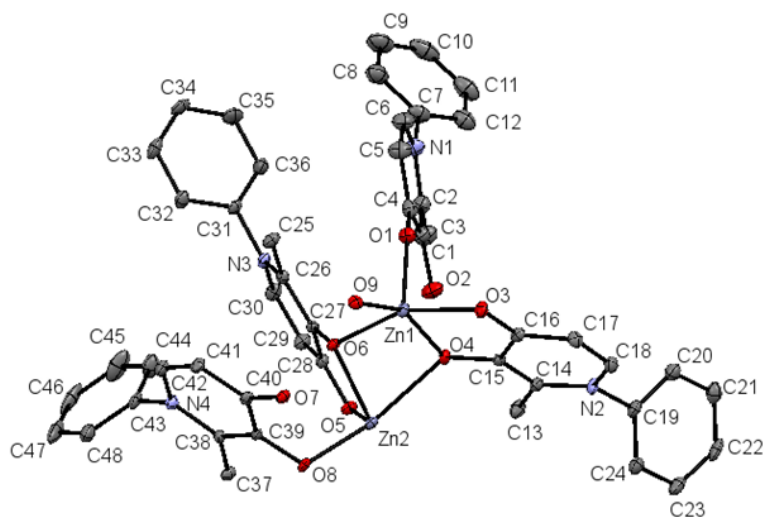
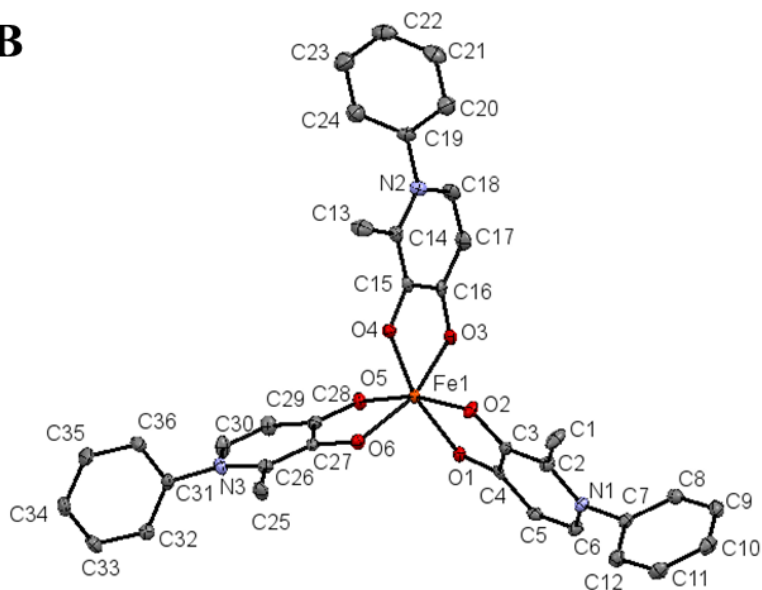
A**B**

Figure 3.3 A) Solid state structure of $[\text{Zn}(\text{ppp})_2]_2$, represented as an ellipsoid plot (50% probability) of the asymmetric unit. Hydrogen atoms, solvent molecules, and the perchlorate ion are omitted for clarity; B) Solid state structure of one Fe center (Fe1) of complex $\text{Fe}(\text{ppp})_3$, represented as an ellipsoid plot (50% probability). Hydrogen atoms and solvent molecules are omitted for clarity. Figure used with permission from Elsevier.

This provides a third example of a Zn-pyridinone complex characterised by X-ray crystallography. **Hdpp** was found in a **Zn(dpp)₂** complex with distorted square pyramidal geometry¹⁰⁹ and incorporated into a mixed hydrotris(3,5-phenylmethylpyrazolyl)borate ligand system, showing distorted trigonal bipyramidal geometry.¹¹⁰ This latter coordination environment and geometry models catalytic sites in matrix metalloproteases.¹¹⁰ Interestingly, the 3-hydroxy-2-methyl-pyran-4-one analogue of the Zn(II) complex crystallises with two metal centers – one in octahedral and one in square-pyramidal geometry, but with no bridging ligands, with the rest of the sites occupied by water molecules.¹⁰⁹

The complex between ligand **Hppp** and Fe(III) revealed two hexadentate iron centers and twelve non-coordinating solvent molecules in the asymmetric unit. Both Fe(III) centers have three ligands coordinating via the oxygen atoms (e.g. Figure 3.3), each with slightly distorted octahedral geometry (Table A.7). Other HPO ligands are seen to crystallise as fac Fe(III) isomers, such as 1-ethyl-3-hydroxy-2-methylpyridin-4-one¹¹¹ and 1-(2'-methoxyethyl)2-methyl-3-hydroxy-4-pyridinone.⁶² In the present case, the Fe1 center is a fac isomer, while the Fe2 center is a mer isomer, with the Fe-O distances that range from 1.97 to 2.07 Å (Table A.7). The water molecules within the unit cell make a hydrogen bonded network (Figure 3.4), similar to fac **Fe(dpp)₃** crystallised with 12 waters.¹¹²

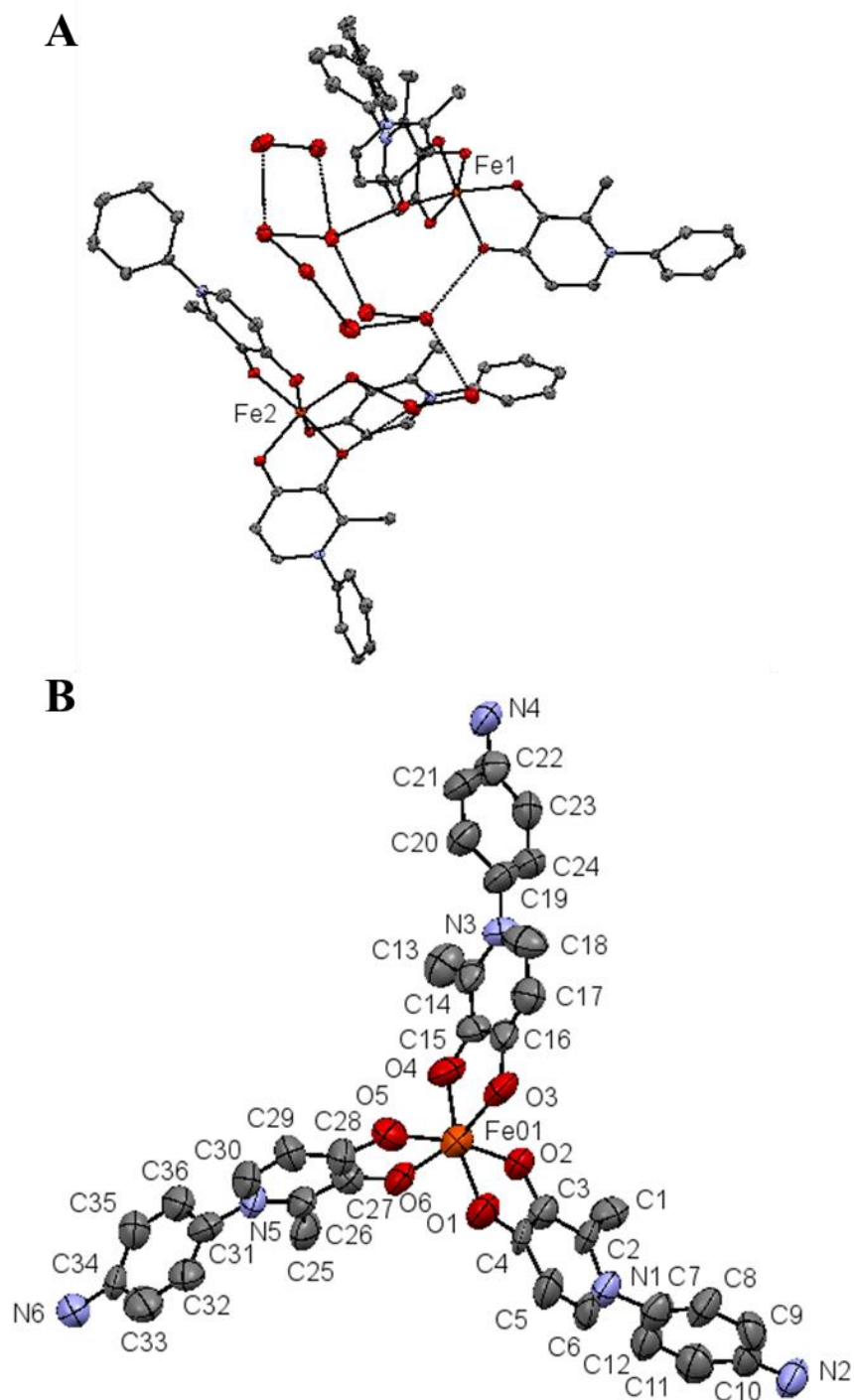


Figure 3.4 A) Hydrogen bonded water network within the $\text{Fe}(\text{ppp})_3$ unit cell. Hydrogen atoms are omitted for clarity. B) Partially solved solid state structure of $\text{Fe}(\text{zapp})_3$, represented as an ellipsoid plot (50% probability). Hydrogen atoms and solvent molecules are omitted for clarity. Figure used with permission from Elsevier.

As well, a partial solid state structure was obtained for **Fe(zapp)₃**, and it revealed a *fac* isomer with 10 water molecules per metal center. The geometry is distorted octahedral (Figure 3.4), with Fe-O distances ranging from 1.98 to 2.06 Å. Similar to **Fe(ppp)₃**, there is a hydrogen bonded water network within the crystal, which in this case is more extensive, involving water molecules from multiple unit cells.

Crystals of Cu(II), Zn(II), and Fe(III) with **Hmbt2p** were also grown and subsequently studied by X-ray crystallography (Figure 3.5). The **Cu(mbt2p)₂** complex reveals the expected 2:1 ligand-to-metal stoichiometry with a nearly square planar geometry and an inversion centre with respect to the HPO core ring at the metal site. Interestingly, there are two Cu(II) centres in each unit cell, with different benzothiazole ring orientations (Figure 3.5). Around the Cu1 centre, the flexible rings are oriented in the same direction, while around the Cu2 centre, the benzothiazole functionalities are oriented in opposite directions. Each **Zn₂(mbt2p)₄** complex contains 4 ligands that are bridging between the two Zn(II) centres resulting in distorted trigonal bipyramidal geometry. This is similar to the observed solid state analysis of **Zn(ppp)₂**, above, which revealed multiple zinc sites, and provides a fourth example of a zinc hydroxypyridinone complex. The **Fe(mbt2p)₃** complex crystallises with the ligands oriented in a disordered fashion around the octahedral iron centre, such that one ligand changes orientation, resulting in both the *mer* and the *fac* isomers being present in the unit cell. Crystallographic details for these three structures can be found in Tables A.8 and A.9.

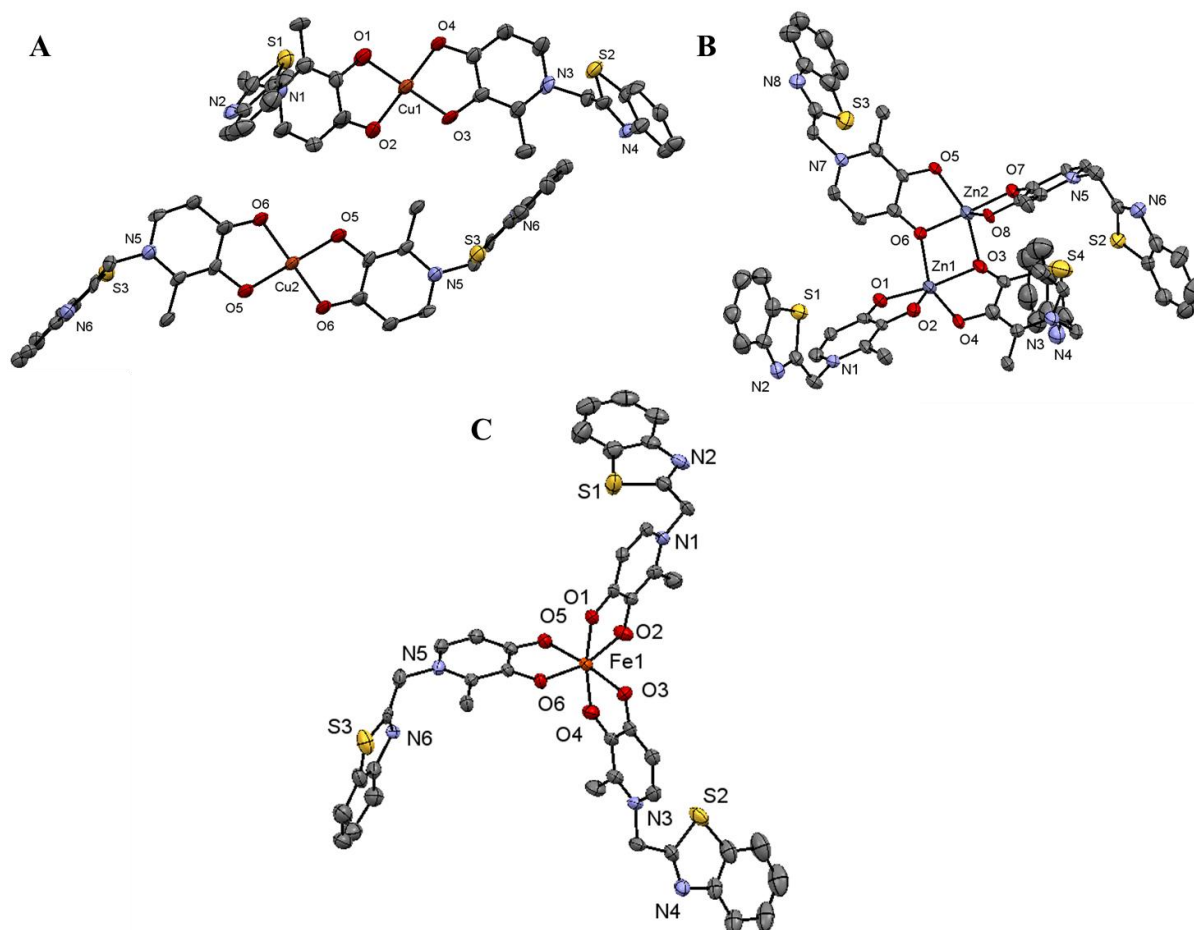


Figure 3.5 Solid state structures of metal complexes: A) $\text{Cu}(\text{mbt}2\text{p})_2$ (asymmetric unit as well as half of the complex around $\text{Cu}2$ centre related by inversion), B) $\text{Zn}_2(\text{mbt}2\text{p})_4$ (asymmetric unit), and C) $\text{Fe}(\text{mbt}2\text{p})_3$ (one isomer in the asymmetric unit), represented as ellipsoid plots (50% probability). Solvent molecules and hydrogen atoms are omitted for clarity. Figure reproduced by permission of The Royal Society of Chemistry.

3.3.2 Binding affinities

First, the $\text{p}K_{\text{a}}$ values of **Hmbo2p**, **Hmbt2p**, and **Habt6p** were determined via spectrophotometric titrations. It was found that **Hmbo2p** and **Hmbt2p** have a pair of nearly identical $\text{p}K_{\text{a}}$ values, at 2.814 (2) and 2.905 (3), and 9.563 (1) and 9.555 (1) (ascribed to the acidic and the basic $\text{p}K_{\text{a}}$ values, respectively) while **Habt6p** has an extra value assigned to the NH_2 group, 2.579 (4),

3.496 (1), and 9.653 (1) (ascribed to the first acidic, the second acidic, and the basic pK_a values).

Figure 3.6 represents events involved in acid dissociation of **Hmbo2p** during a titration.

According to a calculated speciation plot for **Hmbo2p** (Figure 3.7), at low pH, the ligand is protonated at the carbonyl oxygen group, rendering it a positive [**H₂mbo2p**]⁺ species, while at high pH, the ligand is fully deprotonated, making it an [**mbo2p**]⁻ species. Finally, at neutral pH, the pro-ligand exists in its neutral, **Hmbo2p**, form.

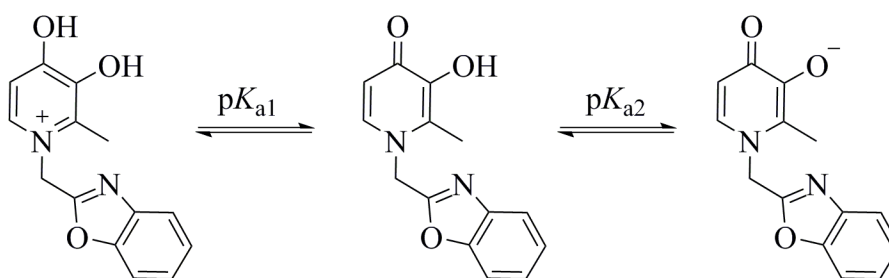


Figure 3.6 Illustration of dissociation equilibria of Hmbo2p.

As the stability constants of the ligands with bio-relevant metal ions are critical in inferring the potential ability of these compounds to compete with amyloid species for metal ions, they were determined. Because of the similarity of the pK_a values of the three pro-ligands, **Hmbo2p** was chosen as a representative model for determination of $\log \beta$ values (eqn 3.1) with Cu(II), Zn(II), and Fe(III), and results can be found in Table 3.2.

$$\log \beta_n = \log \left(\frac{[ML_n]}{[M][L]^n} \right) \quad (3.1)$$

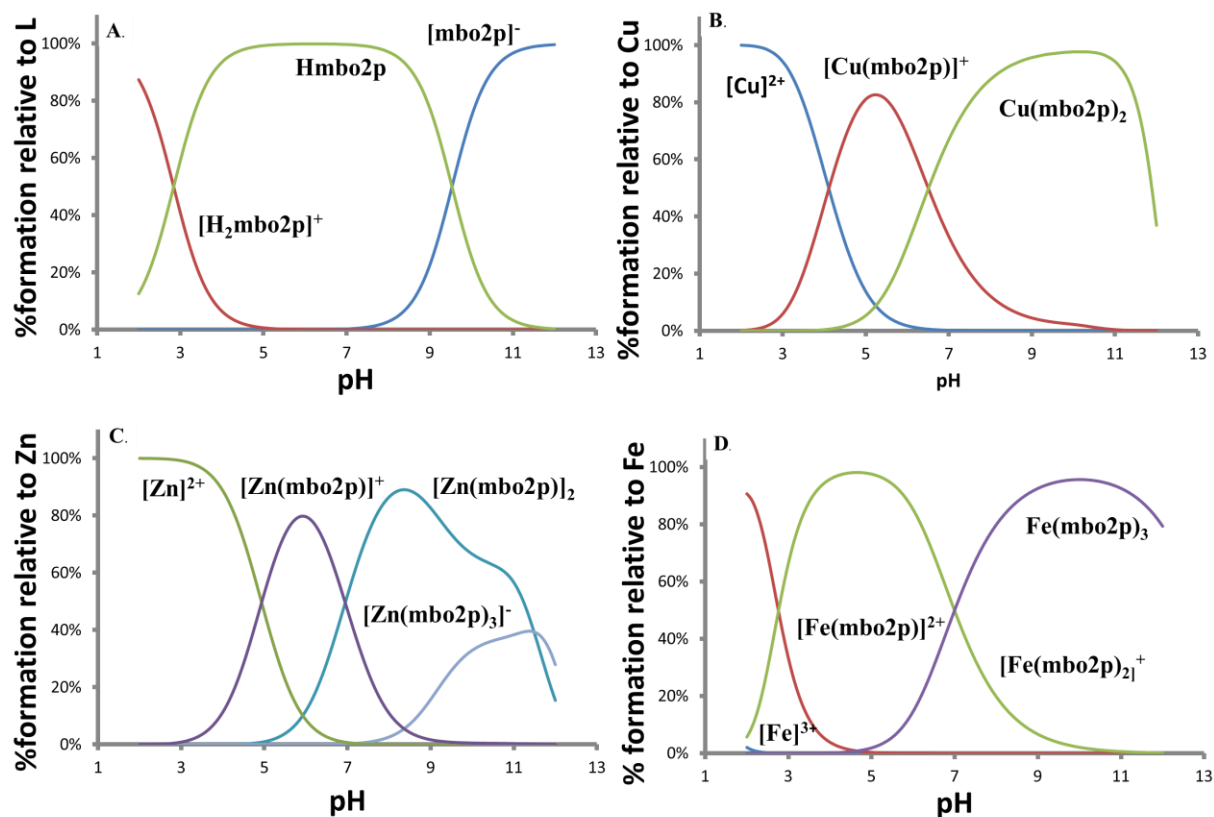


Figure 3.7 Speciation plots for Hmbo2p (A), Cu(mbo2p)₂ (B), Zn(mbo2p)₃ (C), and Fe(mbo2p)₃ (D) using HYSS2009.¹¹³ The plots were constructed with ratios of 1:2 for Cu to Hmbo2p, and 1:3 for Zn and Fe, with concentration of Hmbo2p set to 25 μM (experimental titration conditions). Metal hydroxide formations that contribute to loss of complex formations at high pH are omitted. Figure reproduced by permission of The Royal Society of Chemistry.

Table 3.2 Stability constants for Hmbo2p with Cu(II), Zn(II), and Fe(III) in 0.1 M KCl H₂O at 25 °C, with standard deviation given in parentheses. Table reproduced by permission of The Royal Society of Chemistry.

M:L _n ; n =	Cu(II)	Zn(II)	Fe(III)
1	10.172 (2)	9.380 (3)	14.855 (16)
2	18.403 (10)	16.779 (14)	26.874 (26)
3	n/a	21.484 (86)	34.793 (55)

Consulting the speciation plots in Figure 3.7, the primary species are **Cu(mbo2p)₂**, **Zn(mbo2p)₂**, and **Fe(mbo2p)₃** at physiological pH under the experimental conditions. At higher pH, the Zn speciation is [**Zn(mbo2p)₃**]⁻, leaving one equivalent of the ligand uncomplexed. Another indication of metal binding ability is the pM value (eqn 3.2), which is indicative of the free metal ion concentration in solution - the greater the value, the less free metal ion there is. The pM values, like speciation plots, take into account not only the metal complex stability constants, but also the ligand pK_a values and metal ion hydrolysis. Under titration conditions (i.e. 25 μM ligand, 12.5 μM Cu(II) or Zn(II), or 8.3 μM Fe(III)), pM values calculated with the aid of HYSS2009¹¹³ are 7.2 and 8.0 for Cu at pH 6.6 and 7.4, respectively, 7.8 for Zn, and 17.1 for Fe, both at pH 7.4. Based on these values, these pro-ligands are expected to compete with amyloid species for metal ions as they are comparable to the dissociation constant, K_d, of Aβ, which are estimated to be in the micromolar range (see Chapter 1).

$$\text{pM} = -\log[\text{M}_{\text{free}}] \quad (3.2)$$

3.3.3 Stability

Having confirmed metal chelation in solid and solution states, the stability of complexes was considered. This is an important concern for our bidentate ligands, as in a biological system neither of the experimental set ups above are relevant. That is, neither the procedure used for synthesis of metal complexes (using organic solvents and strong bases), nor the set up used for titrations (in the presence of 0.15 M KCl) reflect what is likely to happen in a biological system, such as a cell or an organ.

First, the stability of a metal complex in the presence of a reducing agent was considered, as A β -Cu(II) complex has been shown to produce ROS in the presence of biological reducing agents, such as ascorbic acid (AA, Vitamin C).¹¹⁴ As well, it has been shown that A β itself can reduce Cu(II) and Fe(III) in the process of generating ROS.¹¹⁵ Therefore, if a ligand could stabilise the metal ions obviating redox chemistry, it may alleviate oxidative stress. Accordingly, a Cu(II) complex of **Hmbo2p** made *in situ* was challenged with ascorbic acid, and the stability of the complex was monitored over a one day period in a buffered solution at pH 7.4.¹¹⁶ As can be seen in Figure 3.8, the spectrophotometric features of the complex remain largely unchanged after the AA challenge. This may mean that once chelated by HPOs, Cu(II) will be inaccessible to A β for production of ROS. However, it is possible that a certain amount of Cu(II) is still accessible for ROS production, and since this a catalytic process, a small amount can be sufficient for potential oxidative damage.

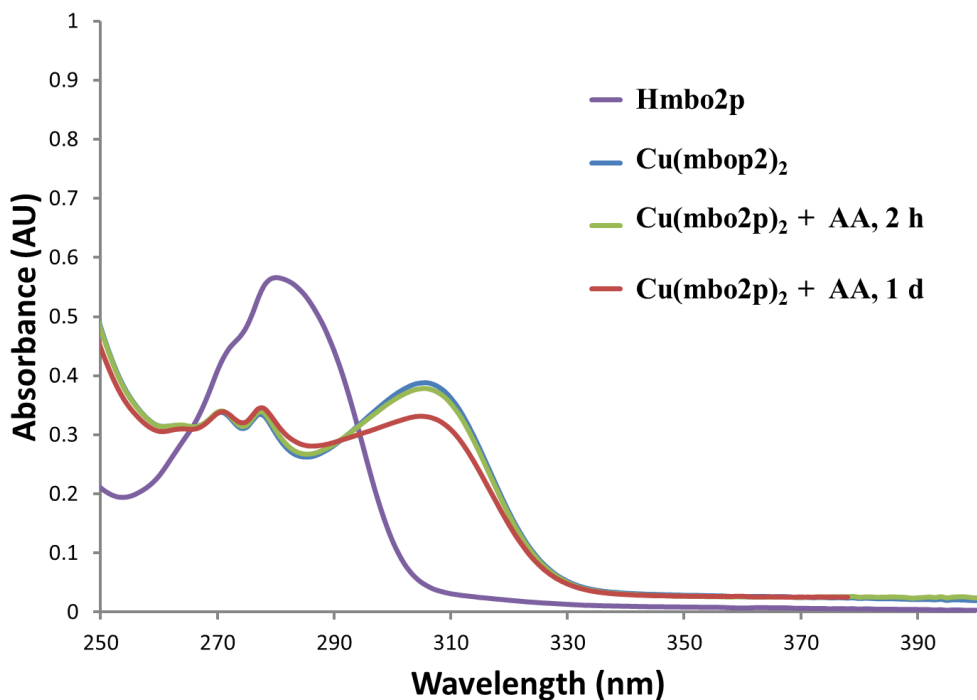


Figure 3.8 Ascorbic acid (AA) (60 μM final) addition to $\text{Cu}(\text{mbo2p})_2$ (20 μM final) in HEPES buffer at pH 7.4, monitored after 2 hours and 1 day. Figure reproduced by permission of The Royal Society of Chemistry.

To investigate this point, we incubated the $\text{Cu}(\text{mbo2p})_2$ complex with coumarin-3-carboxylic (3-CCA) and ascorbic acids.¹⁵ Under the experimental conditions, that is, in a reducing environment, Cu(II) is reduced to Cu(I) and hydroxyl radicals (OH^\bullet) are produced. These react with 3-CCA to produce a fluorescent product, 7-hydroxy-coumarin-3-carboxylic acid¹⁵ (this is represented as the blue (no ligand) graph in Figure 3.9). When a strong ligand, such as EDTA, is preincubated with Cu(II), no compound is observed, and thus we conclude that the radical production is prevented (green trace in Figure 3.9). The radical generation is greatly diminished in the presence of the ligand **Hmbo2p** that was chosen as the representative ligand for this study (red trace in Figure 3.9), as compared to when copper is not bound, but the action of the ligand is not as significant as that of EDTA.

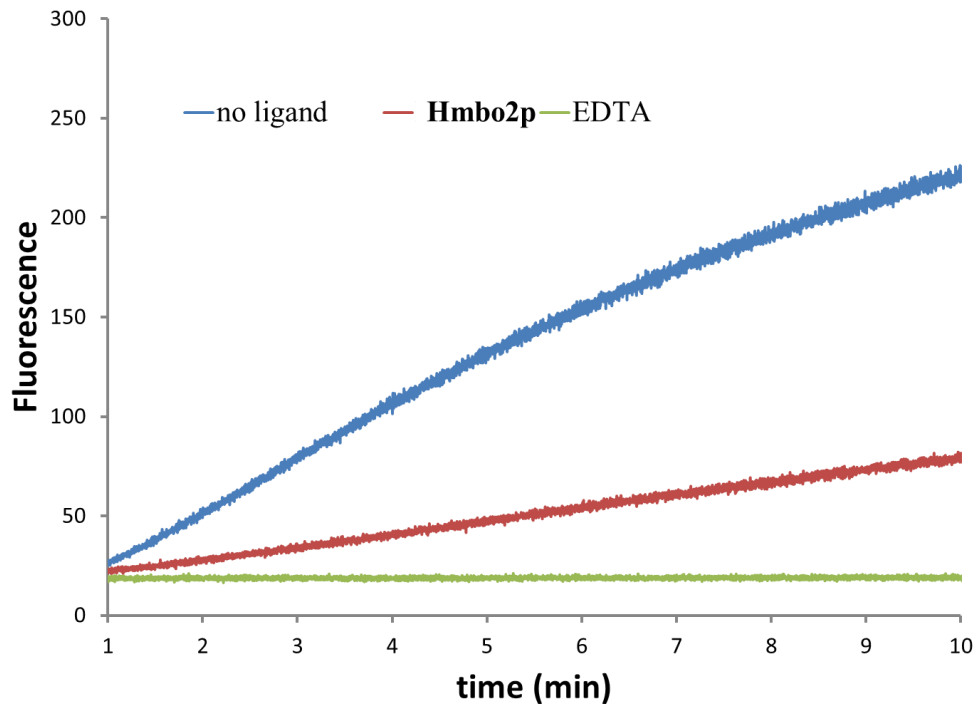


Figure 3.9 Formation of fluorescent product of coumarin-3-carboxylic acid and the hydroxyl radical in the presence of AA and Cu(II), either alone, or chelated to Hmbo2p or EDTA in HEPES buffer at pH 7.4 (ex. 395, em. 452). Figure reproduced by permission of The Royal Society of Chemistry.

Next, the effect of other ligands on the copper complex was studied. The relevance of this study comes from the fact that during the cytotoxicity studies, the cells are incubated in a DMEM cell medium, which contains 15 amino acids, including histidine and cystine, both at 0.20 mM concentration, and is supplemented with fetal bovine serum albumin, all of which can bind metal ions. It also contains high concentration of sodium (NaCl, 110 mM; NaHCO₃, 44 mM), potassium (KCl, 5 mM), calcium (CaCl₂, 1.8 mM), and magnesium (MgSO₄, 0.8 mM) and glucose (25 mM).¹¹⁷

HPO ligands independent of the substituent off the nitrogen on the ring have similar $\log \beta$ values; for **Hmbo2p**, $\log \beta$ and $\log \beta_2$ for Cu(II) were 10.17, and 18.40 under our conditions; these values are essentially the same for histidine, with Smith and Martell reporting them to be 10.16 and 18.07.¹¹⁸ Therefore, since histidine is present at higher concentrations than our ligand (ratios ranging from 20,000:1 to 3:1), if we add copper to a solution containing histidine and our ligand, the Cu(II) will be expected to bind primarily histidine at pH 7.4. This is confirmed with speciation plots using Hyss2009; e.g. at 10:1 histidine:copper complex ratio, over 90% of copper is chelated to histidine. This setup is different from experimental conditions. In contrast to the theoretical speciation plots with Hyss2009 software, under experimental conditions the pre-made complex is added to solution, and so we do not have unchelated copper at the onset. Therefore, if the copper complex is kinetically stable, it may not transchelate. Thus, *in vitro* experiments were necessary to investigate potential transchelation.

Unfortunately, the cell medium contains species that have high absorbance in the UV-vis region, and thus it is not suitable for monitoring stability of our complexes that absorb in the same region. Consequently, we chose a system that would represent the medium with a metal binder by administering 0.20 mM histidine to 0.02 mM **Cu(zapp)₂** solution in 10 mM HEPES buffer at pH 7.4. As can be seen in Figure 3.10, we found that most of the complex became unchelated, and we presume that it is due to copper binding to histidine, which is present at much higher concentration than our ligand. We do see that a portion of the complex remain intact.

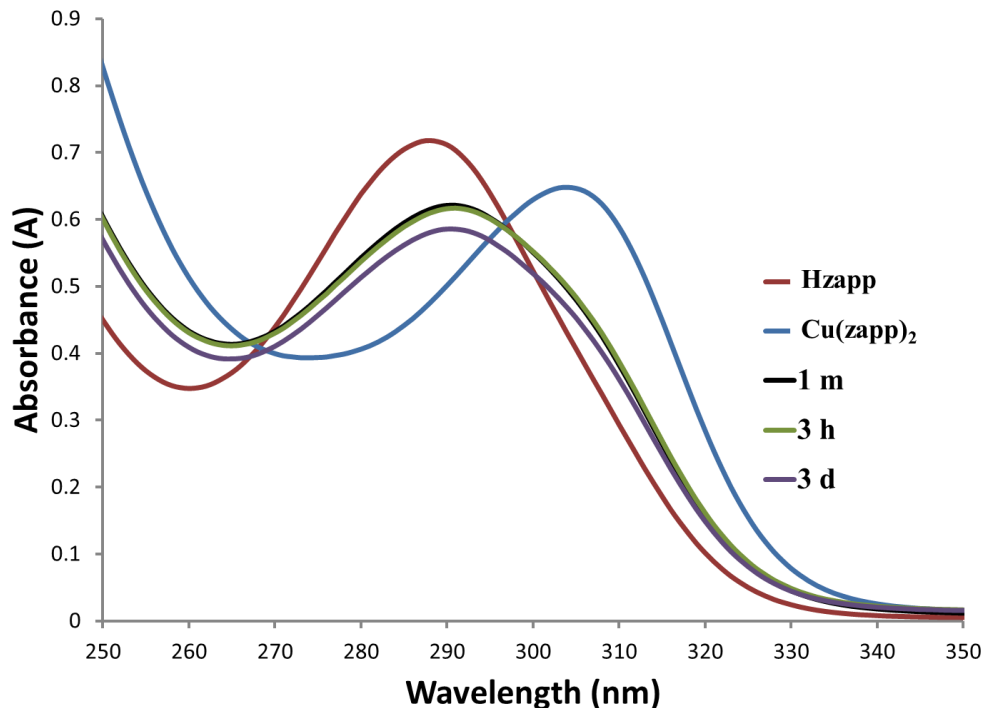


Figure 3.10 Cu(zapp)₂ in the presence of histidine after 1 minute, 3 hours, and 3 days in 10 mM HEPES at pH 7.4, as monitored by UV-vis spectroscopy. A spectrum of unchelated Hzapp is included for comparison.

The cell medium is a much more complex solution than that which we use for our trial, containing other metals and ligands (such as other amino acids and albumin). We do not know for certain how our complexes fare in the medium, but we predict that there is significant transchelation. For complexes to be stable in this environment, they have to be kinetically inert and have high metal binding constants; thus we expect our Fe(III) complexes to fare better than the Cu(II) and the Zn(II) complexes. Most literature reports do not comment on stability of the complexes in media (as will be discussed in more detail in Chapter 4). Present at higher concentrations, ligands in the medium are likely to compete for metals within complexes, and thus complex concentration may not be accurately estimated. In our case, especially the Cu(II) and Zn(II) complexes are likely to be significantly perturbed by the species in the cell medium.

This may explain why some results, including ours, show that cytotoxicity is on the same order of magnitude upon chelation to certain metal ions (see below). This should be taken into consideration when interpreting biological results of complexes, especially of those complexes that have low denticity and moderate binding constants.

It should be noted that like the cell medium, blood plasma and cerebrospinal fluid (CSF) are multi-component systems containing a myriad of endogenous chelating agents with various affinities for metal ions. Interestingly, concentrations of amino acids and proteins is significantly lower in the CSF than in the plasma.⁸⁶ For example, while the total amino acid concentration is typically 3 mM in the plasma, it is about one third of that in the CSF.⁸⁶ The concentration of albumin is even more significantly reduced, with its concentration in CSF at 0.4 mg/mL, down from 70 mg/mL in the plasma.⁸⁶

3.4 Conclusions

The initial studies focused on synthesising and characterising metal complexes in the solid state. Zn(II) and Fe(III) complexes with **Hppp**, **Hzap**, and **Hbt2p** were prepared by combining metals with ligands in the presence of base, and analysed by MS, IR and NMR spectroscopies, and EA (where applicable). For novel ligands **Hmbo2p**, **Hmbt2p**, and **Habt6p**, Cu(II) complexes were likewise prepared and analysed by the aforementioned techniques. As well, single crystals of **Zn(ppp)₂**, **Fe(ppp)₃**, **Cu(mbt2p)₂**, **Zn(mbt2p)₂**, and **Fe(mbt2p)₃** were isolated and studied by X-ray crystallography. The Cu(II) and Fe(III) complexes revealed the expected stoichiometries, with 2:1 and 3:1 ligand to metal ratios, with the expected distorted square planar and octahedral geometries. On the other hand, the two Zn(II) complexes revealed more complex

binding, with bridging ligands and coordinating water molecules. Meanwhile, in mass spectra, the 2:1 species was predominant, and NMR spectra appeared uncomplicated, as compared to the spectra of the Ga(III) complex. This is another reminder that single crystals may not be reflective of the bulk solid, and that solid and solution state speciations may differ.

Titration studies were carried out to determine the pK_a values for the novel pro-ligands **Hmbo2p**, **Hmbt2p**, and **Habt6p**, and they were similar to those reported in the literature for other HPOs. Metal binding studies with **Hmbo2p** were carried out to determine the binding constants for Cu(II), Zn(II), and Fe(III). It was found that under the experimental conditions, as expected, the ligand to metal ratios are 2:1 for copper and zinc, and 3:1 for iron. With these studies, it was confirmed that the metal binding ability of our HPOs is retained when the amyloid-beta binding group is introduced. Metal binding is possible via the two oxygen atoms on the HPO ring, and the expected chelation ratio for the bidentate ligands is observed.

The stability of metal chelators was also established with selected Cu(II) complexes. In one study, **Cu(mbo2p)₂** complex was challenged with a reducing agent. While the copper complex remained largely intact, the production of ROS species was not completely quenched. Moreover, when the complex **Cu(zapp)₂** was challenged with another chelator, which is present in higher concentrations in the medium used for cellular work, transchelation was seen. It is crucial to remember that solution and solid state studies are performed in different environments and that one must be aware of the speciation of the complexes in biologically relevant solutions.

Chapter 4: *In vitro* characterisation of pro-ligands: antioxidant activity, amyloid binding, and cell studies

4.1 Introduction

As is introduced in Chapter 1, the versatility of the HPO scaffold comes from its ability to combine many functionalities within it. The studies of metal binding activity with Cu(II), Zn(II), and Fe(III) are presented in Chapter 3, while this chapter considers other functionalities envisioned in the drug design: amyloid-binding, radical quenching activity in the absence of metal ions, cytotoxicity studies, and cell permeability studies.

It should be mentioned that although the benzothiazole functionality has been previously introduced into the HPO scaffold,⁵⁸ whether or not the functional group that mimics PET imaging agents (Figure 2.1) enables the ligand to interact with amyloid-beta (A β) was not established. Therefore, an important goal of this work was to determine the compatibility of the metal- and amyloid-binding functionalities.

Of the five novel pro-ligands, three of them – **Hmbo2p**, **Hmbt2p**, and **Habt6p**, (Figure 2.2) were chosen for the initial studies. In certain experiments, a model compound was chosen as a representative for the series of pro-ligands. Whenever possible, the representative compound was **Hmbo2p** – compared to the rest, it is easily obtained, has the lowest environmental impact due to shorter reaction time and avoidance of extraction solvents, and is soluble across a wide range of solvents. **Hpbo2p** and **Hpbt2p** (Figure 2.2) were not studied in the majority of these

studies due to solubility limitations; however, their favourable spectral features enabled us to study them in cell permeability studies, which are done by fluorescence microscopy.

Accordingly, for the radical quenching ability of pro-ligands, Trolox-equivalent antioxidant capacity assay was used.¹¹⁹ This assay has been previously used to compare well-known antioxidant Vitamin E to HPOs such as **Hppp**, **Hpnp**,⁸⁹ **Hdpp**, **Hdapp**, **Hsapp**, **Hzapp**, **Hbt6p**, and **Hbt2p**.⁵⁸ The interaction of pro-ligands was studied with A β in monomeric and aggregated forms. For the monomeric form of A β ₁₋₄₀, turbidity studies were used in the presence and absence of Cu(II) and Zn(II);⁵⁸ this study was previously used to characterise **Hppp**, **Hphp**,⁸⁹ **Hdpp**, **Hzapp**, and **Hbt6p**.⁵⁸ While for the aggregated forms of A β , TEM studies were undertaken¹²⁰ and binding affinity was established.¹²¹ The cytotoxicity and cell permeability studies were done with the bEnd.3 cell line, which is a brain endothelial mouse cell line that was immortalised by an introduction of a polyoma virus middle-T antigen.¹²² It is particularly useful because it has been shown that the bEnd.3 cell line creates a monolayer that acts as an *in vitro* BBB model.^{123,124} The cell line expresses elements of the tight junctions and transporter proteins for glucose (GLUT-1) and amino acids (System L) that are found in the BBB.¹²⁴ The attractiveness of using this cell line is that it is easier to manage than primary neuronal cell lines that are slow-growing and lose their integrity at higher passaging numbers.¹²³ Previously, to establish whether the HPOs are likely to go through the BBB, the glycosylated radioiodinated compound was studied in rats by direct injection into the common carotid artery that in part supplies blood to the brain.⁵⁸ As well, this cell line was used in cytotoxicity studies; before, HepG2 cell line was used,^{58,89} which is a human cancerous liver cell line.

4.2 Experimental

4.2.1 Materials and methods

All chemicals (including standards) and solvents were purchased from commercial suppliers (Aldrich, Alfa Aesar, Tokyo Chemical Industry Co., Ltd. (TCI) America, Fisher, Acros Organics) and used without further purification. Metal AAS standards were purchased from Alfa Aesar. Pro-ligand **Hdpp** was purchased from Sigma-Aldrich and used without further purification. Amyloid- β_{1-40} was purchased from EZBiolab. Supplies for biological studies were purchased from Invitrogen Life Technologies. Water was purified to 18.2 M Ω •cm with an Elga Ultra Pure Lab System. The syntheses and characterisation of the pro-ligands **Hmbo2p**, **Hmbt2p**, and **Habt6p** are described in Chapter 2. The synthesis of **Hppp**, **Hzapp**, **Hbt2p**, and the syntheses and characterisation of Zn(II) and Fe(III) metal complexes of **Hzapp** are described in Chapter 3. **Cu(zapp)₂** was synthesised by Dr. Lauren Scott.⁸⁹

4.2.2 Instrumentation

Spectrophotometric experiments (TEAC assay) were done with a Hewlett Packard 8453 UV-vis spectrophotometer. For protein aggregation studies, a Hitachi H7600 Transmission Electron Microscope (TEM) was used by Dr. Jacqueline Cawthray. Fluorescence studies were performed with an Agilent Cary Eclipse spectrophotometer. Cytotoxicity and turbidity studies were done using a DTX880 plate (UV-vis) reader. For cell permeability studies, an Olympus Fluoview FV1000 Laser Scanning Confocal Microscope was used with diode laser excitation at 405 nm and DAPI filter detection (435-485 nm), with 20x and 60x (the latter of which was oil-immersed) objectives; the images were collected by Dr. Jacqueline Cawthray. The images were then analysed with ImageJ software.¹²⁵

4.2.3 Trolox-equivalent antioxidant capacity (TEAC) assay

The ability of our compounds to scavenge radicals was established using a TEAC assay following a literature procedure.¹¹⁹ Reagent 2,2'-azino-bis(3-ethylbenzothiazoline-6-sulfonic acid) diammonium salt (ABTS) (39.3 mg, 0.071 mmol) was dissolved in minimum volume of H₂O and added to an aqueous solution containing potassium persulfate (K₂S₂O₈) (6.9 mg, 0.026 mmol). After mixing, the combined solution was diluted to 10 mL in a volumetric flask and stored at room temperature in a dark place for 16 h to form the ABTS^{•+} radical. The ABTS^{•+} solution was used the following day and diluted to achieve an initial absorbance of 0.7, typically a 50-100-fold dilution. Stock solutions (2.5 mM in MeOH) of the 6-hydroxy-2,5,7,8-tetramethylchromane-2-carboxylic acid (Trolox) standard, **Hmbo2p**, **Hmbt2p**, and **Habt6p** were prepared. These stock solutions were diluted in such a way as to achieve a decrease in absorbance from 20 to 80% of 2 mL of the 2,2'-azino-bis(3-ethylbenzothiazoline-6-sulfonic acid) diammonium salt radical solution upon addition of the compounds. The final concentration ranges were 2-13 μM for **Hmbo2p**, 2-10 μM for **Hmbt2p**, and 7-22 μM for **Habt6p**. Triplicate measurements at four concentrations were performed, resulting in a linear correlation between concentration and % quenching for each time point. The slope of the quenching of the radical by the compounds was compared to that of Trolox at 1, 3, and 6 minutes by means of division, resulting in the Trolox index. The Trolox index for each compound at each time point is graphed on a common scale and can be compared to literature values.^{58,59,89}

4.2.4 Amyloid-β aggregation studies

The turbidity assay and the TEM experiment were performed according to previously established methods.^{89,120} The protein solution was prepared by dissolving 1 mg of synthetic Aβ₁₋₄₀ in 1 mL

of H₂O and sonicating it twice for 30 seconds to achieve full dissolution. The solution was filtered with a 0.2 µm syringe filter and its absorbance was recorded at 280 nm to determine the concentration of the stock solution ($\epsilon = 1450/\text{M cm}$). For the metal and ligand solutions, a buffer containing 20 mM HEPES and 150 mM NaCl solution was pre-treated with Chelex resin overnight before filtering it with a 0.22 µm Millipore filter. For half of the buffer, the pH was adjusted to 7.4, while for the other half, it was adjusted to pH 6.6. Solutions of Cu(II) AAS standard, Zn(II) AAS standard, and the pro-ligands were prepared such that the 200 µM Cu(II) solutions were at pH 6.6, and the 200 µM Zn(II) solutions at 7.4 pH. Solutions of pro-ligands at 200 µM and EDTA at 100 µM were prepared at both pHs.

For the experiment, solutions containing A β_{1-40} (25 µM), metal ion (25 µM), and the ligand (150 µM for title compounds and 75 µM for EDTA) were prepared in quadruplicate. Turbidity samples were placed in a 96-well plate that was agitated for 45 minutes at 37 °C and the absorbance measurements were taken at 405 nm using a plate reader. The TEM samples were placed in 0.5 mL Eppendorf tubes, which were agitated for 17 hours at 220 rpm at 37 °C. Glow-discharged grids were treated with A β samples (3 µL) for 5 minutes at room temperature. After the excess sample was removed with filter paper, 2% aqueous uranyl acetate stain (10 µL) was applied for 5 minutes. The liquid was removed using filter paper and the grids were air dried. Images were taken with TEM at 80 kV. TEM images were taken by Dr. Jacqueline Cawthray.

4.2.5 Binding to A β_{1-40} fibrils

The following studies were carried out according to literature procedures.¹²¹ Fibrils were prepared by incubating 0.5 mg of A β_{1-40} in 0.5 mL of H₂O in an Innova-44 shaker set at 200

RPM for 72 h at 37 °C. For each trial, 1.995 mL of 10 mM phosphate buffer with 1 mM EDTA at pH 7.4 was mixed with fibrils and compound(s) in a cuvette and fluorescence was measured with a fluorimeter after a 2 h incubation at 485 nm.

The presence of fibrils was confirmed with a Thioflavin-T (ThT) fluorescence study (Figure A.27). As blanks and controls, fluorescence was determined for each component individually, as well as in different combinations with each other (e.g. **Hmbo2p** and ThT) to exclude signal increase due to interactions other than that between ThT and fibrils (Figure A.27).

To determine the K_d (concentration of half-maximum binding) of ThT, 5 μ L of the fibril solution was incubated with ThT at concentrations ranging from 0.5 to 10.0 μ M. After subtracting fluorescence from ThT alone (Figure A.28), the data were analyzed with GraphPad Prism (version 4.00 for Windows, GraphPad Software, San Diego California USA, www.graphpad.com) using one site binding (hyperbola) fit with no constraints using the eqn 4.1, below, where B_{max} is the maximal binding (Figure A.29).

$$Y = \frac{B_{max} \times X}{K_d + X} \quad (4.1)$$

To determine the IC_{50} (concentration of half-maximum inhibition), 0 to 30.0 μ L concentration of compounds **Hdpp** and **Hmbo2p** were added to 2.5 μ M solution of ThT with fibrils. After the incubation period, fluorescence was measured. Fluorescence of the solution with no inhibitor was taken as the point of maximal (100%) binding of ThT, and the rest of the measurements were calculated accordingly. The % ThT binding vs concentration of pro-ligands was graphed and analyzed with GraphPad Prism (version 4.00 for Windows, GraphPad Software, San Diego

California USA, www.graphpad.com) with eqn 4.2, sigmoidal dose-response with variable slope, with no constraints taken into account, after transforming the concentration into log[C].

$$Y = \text{bottom} + \frac{(\text{top}-\text{bottom})}{1 + 10^{(\log EC_{50}-x) * \text{HillSlope}}} \quad (4.2)$$

Consequently, the values obtained for ThT K_d at 2.5 μM and pro-ligand IC_{50} were used in eqn 4.3 to determine the inhibition constant, K_i .

$$K_i = \frac{IC_{50}}{1 + [\text{ThT}]/K_d} \quad (4.3)$$

Calculation for K_i for **Hmbo2p** was as follows:

$$K_i = \frac{9.57 \mu\text{M}}{1 + 2.57 \mu\text{M}/3.17 \mu\text{M}}$$

4.2.6 Cytotoxicity

The bEnd.3 cell line was grown in Dulbecco's Modified Eagle Medium (DMEM) supplemented with 10% fetal bovine serum, 100 units/mL penicillin, and 100 $\mu\text{g}/\text{mL}$ streptomycin (all final concentrations), under 5% CO_2 atmosphere at 37 $^\circ\text{C}$. Stock solutions of compounds were prepared in DMSO, and then diluted to the necessary concentrations in the cell media for addition to the cells. The final concentration of DMSO in each well was less than 0.5%. The concentration ranges used for compounds were as follows: **Hmbo2p**: 0.21 μM to 177 μM , **Hmbt2p**: 0.20 μM to 165 μM , **Habt6p**: 0.13 μM to 551 μM , and cisplatin 0.15 μM to 665 μM for the first part of the study; and **Hppp**: 0.30 μM to 1299 μM , **Hzapp**: 0.20 μM to 867 μM , **Hbt2p**: 0.06 μM to 246 μM , cisplatin 0.18 μM to 764 μM , **Cu(zapp)₂**: 0.02 μM to 66 μM ,

Zn(zapp)₂: 0.03 μM to 109 μM , **Fe(zapp)₃**: 0.11 μM to 76 μM for the second part of the study. The cytotoxicity of pro-ligands was determined with the MTT (3-(4,5-dimethyl-2-thiazolyl)-2,5-diphenyl-2H-tetrazolium bromide) assay.¹²⁶ Each well in the 96-well plate was plated with 10,000 cells in 100 μL aliquots, and after 24 hours, varying concentrations of compounds were added in 100 μL aliquots. The effects of six concentrations for compounds were measured in triplicate. After a three day incubation period, 50 μL of 6 mM MTT solution was added, and after 3 h, the liquid in each well was removed and 100 μL DMSO was added. The absorbance was determined at 595 nm using a plate reader. Data were analyzed with GraphPad Prism (version 4.00 for Windows, GraphPad Software, San Diego California USA, www.graphpad.com) by first transforming the concentration into $\log[\text{C}]$, and running a sigmoidal dose-response with variable Hill Slope fit (with no restrictions on the top or the bottom values) according to eqn 4.2. Solubility limits of **Cu(zapp)₂** and **Fe(zapp)₃** resulted in incomplete data sets for fitting.

4.2.7 Cell permeability

The bEnd.3 cell line was grown in Dulbecco's Modified Eagle Medium (DMEM) supplemented with 10% fetal bovine serum, 100 units/mL penicillin, and 100 $\mu\text{g}/\text{mL}$ streptomycin (all final concentrations), under 5% CO_2 atmosphere at 37 $^\circ\text{C}$. Stock solutions of **Hpbo2p** and **Hpbt2p** were prepared in DMSO fresh (3.8 mM and 3.3 mM, respectively), and stock DAPI (18 mM) was prepared in H_2O and stored at -20 $^\circ\text{C}$. The stock solutions were diluted to yield a 36 nM solution of DAPI in PBS (pH 7.4), 38 μM of **Hpbo2p** in DMEM medium, and 33 μM of **Hpbt2p** in DMEM medium.

Each well in the 96-well imaging plate was plated with 10,000 cells in 100 μ L aliquots, and after 24 hours, 100 or 200 μ L of **Hpbo2p**, **Hpbt2p**, and DAPI were added to each well. After a 15 minute incubation, the medium was removed, and the cells were washed with PBS (pH 7.4) three times and 100 μ L of PBS was added to each well. The images were taken within two hours of preparation of the samples. During sample imaging, the scanning confocal microscope was set up to take fluorescence and light images with varying objectives (20x and 60 x) that were later combined using ImageJ software.¹²⁵ As a blank control, cells alone were used; as positive control, DAPI¹²⁷ was used. Using the software, the two channels were split into 16-bit images and were combined into one image (using gray and blue channels), after which the composite was reset to RGB colour. The “sharpen” tool was used to enhance features of the blank; “window” and “level” adjustments were made on the light images cells with **Hpbt2p**, **Hpbo2p**, and DAPI to correct for overexposure.

4.3 Results and discussion

4.3.1 Trolox-equivalent antioxidant capacity (TEAC) assay

Phenol-containing compounds, including HPOs, have been previously shown to possess radical quenching ability.¹²⁸ Having this part of antioxidant activity is an important feature of our compounds, as oxidative stress plays a negative role in neurodegeneration.^{129,130} An *in vitro* Trolox-equivalent antioxidant capacity (TEAC) assay¹¹⁹ was performed to establish the radical scavenging ability of **Hmbo2p**, **Hmbt2p**, and **Habt6p** (Figure 2.2). The ability of compounds to quench a pre-formed radical is spectrophotometrically determined at 1, 3, and 6 minutes; the results are summarised in Figure 4.1. The antioxidant activity of the pro-ligand **Hmbt2p** is on par with Vitamin E, a known antioxidant; the values for **Hmbt2p** and **Habt6p**, on the other

hand, are lower. Overall, the values for these compounds show that they possess hydrogen-donating antioxidant activity.

As the TEAC test is a preliminary measure of potential antioxidant activity that has certain limitations,¹³¹ and it has been recently shown that in some experiments HPOs are not effective in halting radical chain reactions,¹³² in full evaluation we take into consideration the studies with the metal complex in pro-oxidant conditions (described in Chapter 3.3.3).

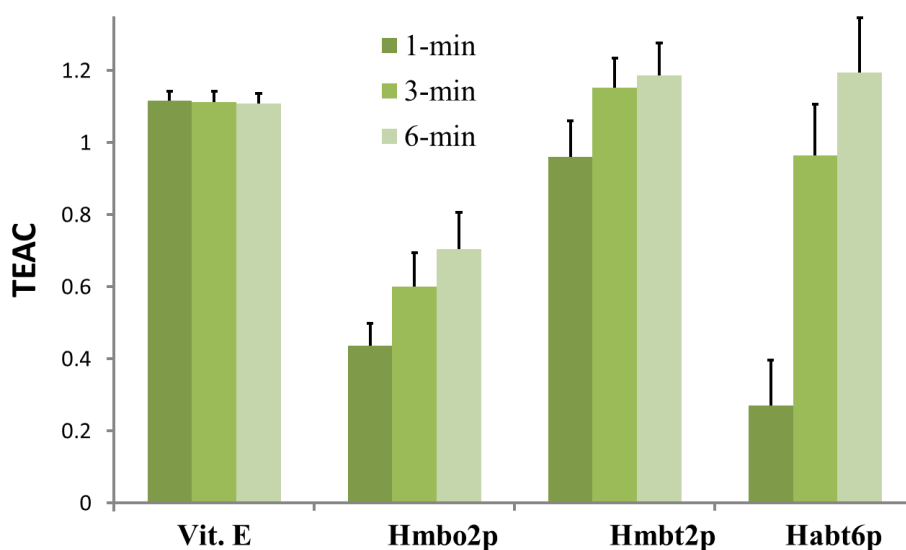


Figure 4.1 Trolox-equivalent antioxidant capacity values of pro-ligands Hmbo2p, Hmbt2p, Habt6p and Vitamin E⁵⁸ represented as TEAC values at 1, 3, and 6 minutes. The values are an average of three trials with their associated relative standard deviations. Figure reproduced by permission of The Royal Society of Chemistry.

4.3.2 Amyloid- β aggregation studies

The ability of compounds **Hmbo2p**, **Hmbt2p**, and **Habt6p** (Figure 2.2) to prevent aggregation of $A\beta_{1-40}$ was assessed by a turbidity assay,^{58,89} in which $A\beta_{1-40}$ is incubated in the presence of either or both a metal ion (Zn(II) or Cu(II)) or/and a ligand (including EDTA as a standard). When $A\beta$ is incubated alone, it shows little aggregation, while metal ions and agitation promote aggregation, which can be seen as an increase in absorbance due to the “turbidity” of the solution. Figure 4.2 is constructed by taking the absorbance of the $A\beta_{1-40}$ alone and setting it as 100% and with metal as 0% resolubilised. For the cases with extra components, the average absorbance from the assay was subtracted from that of the metal with $A\beta$ and divided by latter, thus resulting from % resolubilisation. The error bars are the standard deviation divided by the average from each assay. When incubated with $A\beta$ and a metal ion, ligands were able to partially dissociate amyloid aggregates (Figure 4.2). As can be seen from the graph, EDTA, which has $\log \beta$ values of 18.8 for Cu(II) and 16.5 for Zn(II),¹³³ is able to dissociate the aggregates well (80-100%). **Hdpp** (Scheme 2.1) has also been shown to dissociate amyloid aggregates to 80%.⁵⁸ As the $\log \beta$ values for the title compounds equal or exceed those of EDTA and **Hdpp**, the N-substituents may be playing a role in disaggregation ability that is not related to chelation of metal ions. In fact, when the ligands were incubated with $A\beta_{1-40}$ monomers in the absence of metal ions, they were able to induce a similar effect to metals – aggregation was observed to an extent of 30-40% (Figure 4.2). This may mean that the amyloid-binding groups are interacting with $A\beta_{1-40}$ in such a way as to induce aggregation, which may be why **Hmbo2p**, **Hmbt2p**, and **Habt6p** are not able to completely dissociate amyloid aggregates.

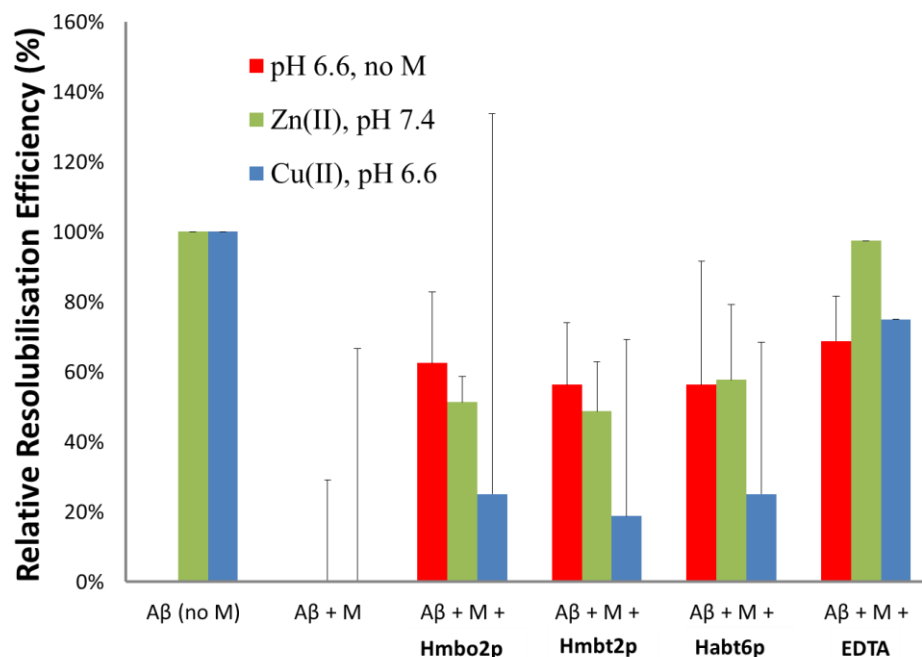


Figure 4.2 Turbidity study of pro-ligands Hmbo2p, Hmbt2p, Habt6p, and EDTA represented as resolubilisation efficiency at pH 6.6 for Cu(II) and 7.4 for Zn(II). The values are an average of three trials with their associated relative standard deviations. Figure reproduced by permission of The Royal Society of Chemistry.

To further study the interaction between the compounds and A β , TEM was used to study the morphology of the aggregation samples. As can be seen from Figure 4.3, the protein incubated alone forms long fibrillar structures, while Cu(II) and Zn(II) ions induce morphological changes. When incubated with the protein in the absence of metal ions, **Hmbo2p** that was chosen as a representative compound induces formation of shorter fibrils. **Hmbo2p** also changes the morphology of A β ₁₋₄₀ in the presence of metal ions, resulting in smaller sized, largely amorphous aggregates of the protein. Further studies are necessary to determine whether this is beneficial, but Figure 4.3 suggests that **Hmbo2p** interacts with the protein and influences its morphology.

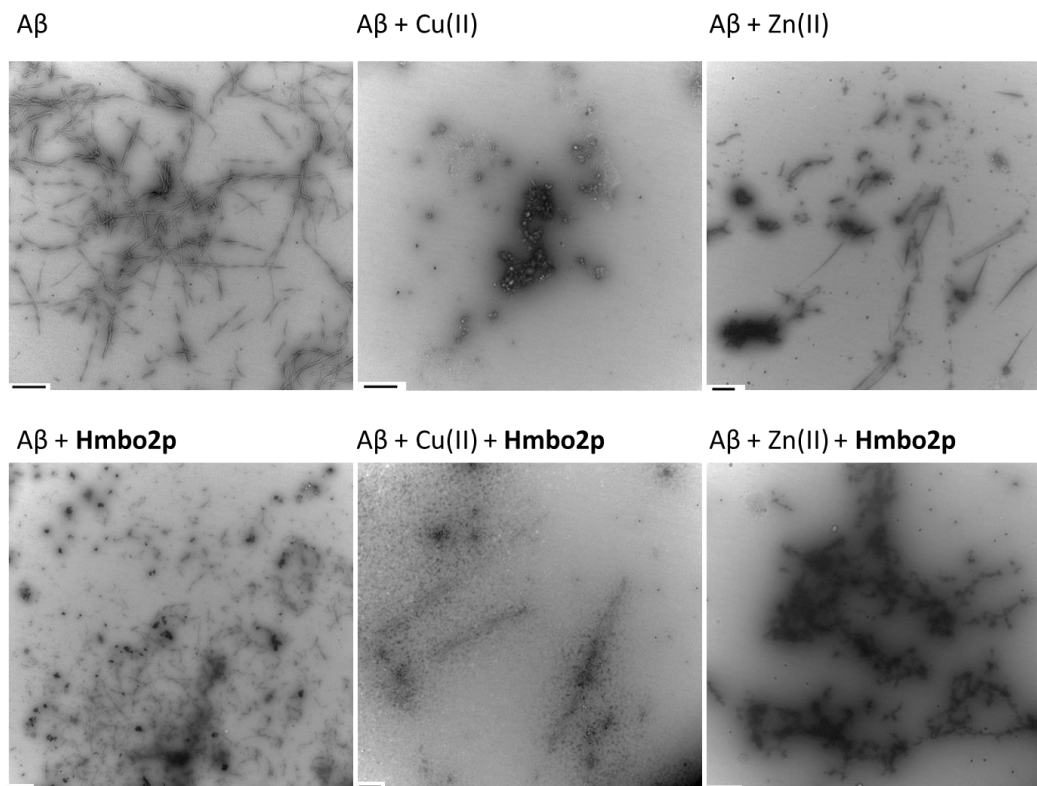


Figure 4.3 Representative TEM images of $A\beta_{1-40}$ aggregation studies, in which $A\beta$ was incubated with $Cu(II)$ and $Zn(II)$ in the presence and absence of $Hmbo2p$, with the scale bar at 500 nm. Figure reproduced by permission of The Royal Society of Chemistry.

4.3.3 Binding to $A\beta_{1-40}$ fibrils

The benzothiazole and benzoxazole functionalities were envisioned to provide HPOs amyloid-binding ability. To test this hypothesis, the binding of **Hmbo2p** and **Hdpp** to $A\beta_{1-40}$ fibrils was established using a fluorescence binding assay. Again, **Hmbo2p** was chosen as a representative compound for this series of pro-ligands, while **Hdpp** represents an HPO with a substituent not designed for binding (Figure 2.1). Since these compounds do not exhibit favourable excitation profiles because they require high energy excitation, that which excites amino acids within the amyloid protein, inhibition studies with Thioflavin-T (ThT) were performed. ThT is a known

binder of amyloid aggregates and its fluorescence is greatly enhanced in the presence of fibrillar formations,¹³⁴ and it is the precursor to imaging agents PIB and BF-227.⁹⁰

When ThT is incubated with pre-formed fibrils of A β , a binding profile is obtained based on the fluorescent enhancement. Upon addition of compound **Hdpp** to a solution of ThT and pre-formed fibrils, no change in fluorescence was observed (Figure 4.4), indicating that **Hdpp** does not likely interact with fibrils. Conversely, when **Hmbo2p** was incubated, a concentration-dependent decrease in ThT fluorescence was observed (Figure 4.4). This decrease in fluorescence is associated with decreased ThT binding, and thus we believe that our compound outcompetes ThT and interacts with the amyloid fibril. The inhibition constant, K_i , is determined to be $5.42 \pm 3.68 \mu\text{M}$, which is within 1 order of magnitude of some compounds that are solely amyloid binders (e.g. a derivative of PIB (Figure 2.1) without the hydroxyl group was determined to have K_i of $0.2 \mu\text{M}$).¹²¹

Thus, in terms of amyloid targeting, it is concluded that **Hmbo2p** is able to interact with both monomeric forms of A β , as well as with aggregated forms, and it is due to the benzoxazole functionality.

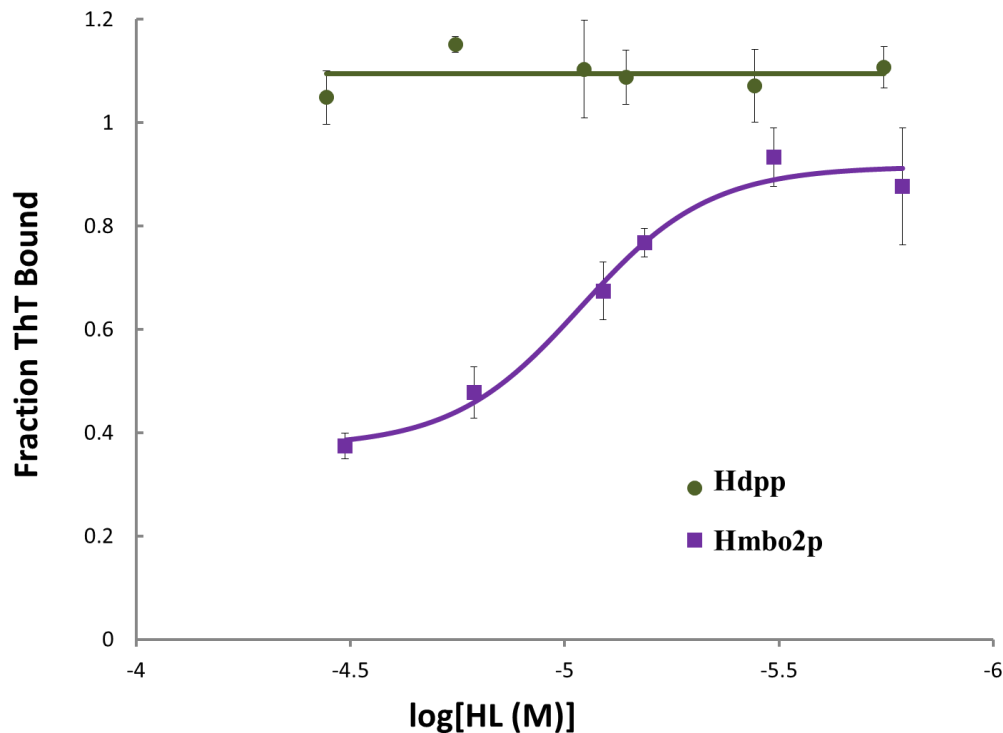


Figure 4.4 Binding profiles of Hmbo2p and Hdpp to A β fibrils, as determined by displacement of ThT. The data represents an average of three trials, with associated relative standard deviation. The binding curve for Hmbo2p was determined with GraphPad. The horizontal line for Hdpp is for illustrative purposes and represents the mean value of all measurements; a binding curve does not fit these data. Figure reproduced by permission of The Royal Society of Chemistry.

4.3.4 Cytotoxicity

For an initial measure of cytotoxicity of novel pro-ligands **Hmbo2p**, **Hmbt2p**, **Habt6p**, as well as previously studied HPOs **Hppp**, **Hzap**, and **Hbt2p** the mouse neuronal cell line, bEnd.3,¹²⁴ was used. The values from an MTT assay that determines EC₅₀, the concentration at which half of the cells are alive, appear in Table 4.1. As a reference, compound cisplatin (Figure 1.1), a cancer drug,¹³⁵ was used, for which two EC₅₀ values were obtained as the cytotoxicity of the two sets of compounds were determined on at two different times. It was found that HPOs have

increased toxicity in this immortalised cell line with respect to cisplatin. The EC₅₀ values for pro-ligands **Hppp** and **Hzapp** were previously established to be 17⁸⁹ and 92⁵⁸ μM, respectively, in a human liver cancer cell line (HepG2), compared to an average value of 12 μM for cisplatin. While in this cell line, the pro-ligands show a slight increase in toxicity compared to cisplatin, the trend of increased lipophilicity leading to increased toxicity holds true.^{58,89} It should be noted that this cell line is an immortalised one, and as mentioned in section 2.1, benzoxazole and benzothiazole derivatives possess anti-cancer properties.^{93,94} We found that more hydrophilic HPO derivatives as well as other benzoxazole- and benzothiazole-containing potential therapeutics for AD display low toxicity (up to 200 μM concentrations) in this cell line.¹³⁶ Thus, it is important to investigate toxicity further; for example, in a primary cell line, and to determine the proportion of live vs dead cell populations. As well as keep the hydrophobicity of HPO substituents in mind during drug design.

Table 4.1 EC₅₀ values with their respective 95% confidence intervals, as calculated by GraphPad Prism for cisplatin, Hmbo2p, Hmbt2p, Habt6p, Hppp, Hzapp, and Hbt2p. Notes: a. first part of study, b. second part of study.

	EC ₅₀ (μM)	95% Confidence Intervals (μM)
cisplatin	37.3 ^a	29.6 to 47.1
	53.5 ^b	42.1 to 68.0
Hmbo2p	4.4	2.7 to 7.1
Hmbt2p	2.5	2.1 to 3.1
Habt6p	6.5	3.9 to 11
Hppp	3.9	2.7 to 5.7
Hzapp	27.5	21.6 to 35.0
Hbt2p	12.8	10.2 to 16.0

In the second part of the study, the effect of metal chelation on toxicity was determined in the same cell line. Compound **Hzap** and its Cu(II), Zn(II), and Fe(III) complexes were considered. As solubility limits of the Cu(II) and Fe(III) complexes resulted in our inability to calculate the EC₅₀ values, the data are presented as cell viability in relation to increasing concentrations of compounds (Figure 4.5).

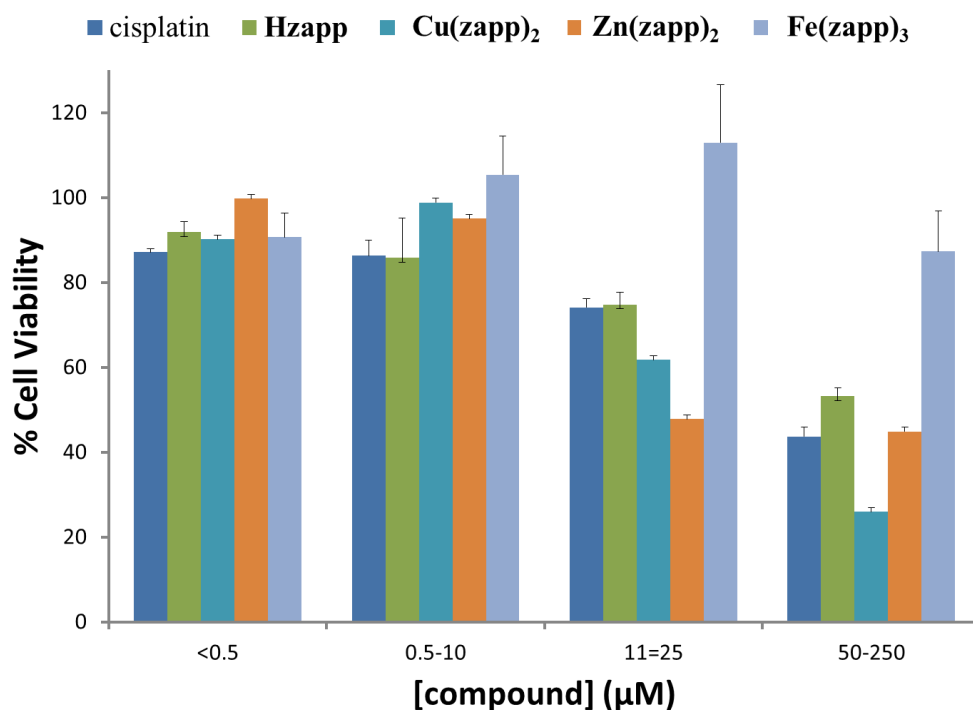


Figure 4.5 BEnd.3 cell line viability in the presence of compounds cisplatin, Hzap, Cu(zapp)₂, Zn(zapp)₂, and Fe(zapp)₃. Values are an average of three trials with standard relative deviation. Individual data for each compound are graphed in Figure A.30. Modified figure used with permission from Elsevier.

It should be noted that the concentrations in Figure 4.5 are listed according to the complex, and each Cu(II) and Zn(II) complex contains two ligands, while each Fe(III) complex contains three. When the cell viability data are graphed according to the concentration of **Hzap** (Figure A.30),

it is apparent that the 50% cell viability for **Hzapp**, **Cu(zapp)₂**, and **Zn(zapp)₂**, is reached within a very narrow concentration range. On the other hand, the iron complex is less toxic to the cells.

In the literature, metal complexes have been shown to either increase, decrease, or not have a significant effect on cytotoxicity when compared to the unchelated ligand. For example, in cell lines K-562 (leukemia), MCF-7 (breast cancer), G-361 (melanoma), and HOS (osteogenic sarcoma) Cu(II) and Fe(III) complexes of bidentate N⁶-benzylaminopurine derivatives were found to be more toxic than the pro-ligands,¹³⁷ while Zn(II) and Fe(III) monodentate 6-benzylamino-9-isopropylpurine derivatives had EC₅₀ values on the same order of magnitude as the pro-ligands.^{138,139} In other cases, copper binding decreased EC₅₀ by about an order of magnitude with monodentate 4-nitropyridine N-oxides in several cell lines,¹⁴⁰ while quinone thiosemicarbazone derivatives displayed higher EC₅₀ for Cu(II) complexes over the pro-ligands¹⁴¹ and quercetin was found to have similar toxicity compared to its Zn complex, with the EC₅₀ for the complex lower in some cell lines.¹⁴² This survey illustrates that metal chelation may or may not have an effect on cytotoxicity, and it is important to study each case individually.

It is important to note that the speciation of the metal complexes may change upon introduction of the cell media, which contains amino acids and albumin. Most literature reports cited herein do not comment on stability of the complexes in media. It may be difficult to establish the true concentration of metal complexes in solution due to the presence of endogenous chelating ligands. For instance, the stability studies in Chapter 3.3.3 demonstrate that the **Cu(zapp)₂** complex is not stable when incubated with the excess of histidine that is present in the cell medium. Thus, there is likely significant transchelation in the Cu(II) and Zn(II) complexes in

our studies, and this may lead to similar results when the IC₅₀ values for compounds and complexes are compared. Therefore, for our and other ligands that have low denticity and moderate binding constants, stability of the complexes in a complex solution has to be taken into account when interpreting results.

4.3.5 Modelling BBB penetration

As an initial model of BBB permeability, the permeability into the bEnd.3 cell line was used. In the literature, this immortalised endothelial mouse brain cell line has been studied for its beneficial properties that make it a good *in vitro* model for the BBB. In our hands, the cell line bEnd.3 had the same morphology and doubling rate as has been illustrated in the literature.¹²⁴ With each passage of the cells (from 15 to 50), there was no difference in morphology detected with a microscope. Depending on the density of seeded cells, complete confluence (coverage of the flask) was achieved from 1 to 7 days. The way that permeability is assessed with this cell line is done by growing the monolayer on a TranswellsTM, which is a specialised well set up that allows for the top and the bottom of the cell layer to be exposed to different media. Then, a radioactive substrate is added to one medium and aliquots of the other medium are collected and measured with a scintillation counter.^{123,124}

As a first measure of permeability through the cell, we determined the cell uptake of compounds by fluorescence. This assay is developed in order to study the different permeabilities into the cell – for instance, since the bEnd.3 cell line expresses GLUT-1 receptors, we can use this in future *in vitro* assays before going to animal studies in order to determine which compounds have the best activity. For this study, the pro-ligands **Hmbo2p**, **Hmbt2p**, and **Habt6p** do not

have the appropriate spectral features (Figure 2.5), as they absorb in the UV region, excitation of which would excite components within the cell. Therefore, **Hpbt2p** and **Hpbo2p** were considered for these studies, as they have better profiles (Figure 2.5). The lowest excitation available for cell studies was a laser at 405 nm, and as can be observed in Figure 2.5, only a tail end of the absorbance remains at that wavelength. Nonetheless, we were able to observe fluorescence, which was stronger for **Hpbt2p** than for **Hpbo2p**, possibly due to the fact that 405 nm could excite only a small portion of the molecules.

As a blank, the bEnd.3 cell line was studied in the absence of compounds. It was observed that the cells do not have fluorescence by themselves when excited at 405 nm and observed in the blue region (435-485 nm) (Figure 4.6, A). The reagent DAPI was used as control, as it is known to bind DNA.¹²⁷ It was observed that the nuclei of cells became fluorescent when incubated with this reagent (Figure 4.5, B). When the cells were incubated with **Hpbt2p**, there was fluorescence as well, but it was observed in the periphery of the cells (Figure 4.6, C). The cells incubated with **Hpbo2p** gave very weak fluorescence (Figure A.31), possibly due to low absorbance at 405 nm. These are initial studies that determine that these two ligands are able to enter the cell. For a full permeability assay, determination whether they also exit the cells will need to be performed. As well, considerations with protein-free media and various growing conditions will need to be undertaken for better mimic of the BBB.^{123,124}

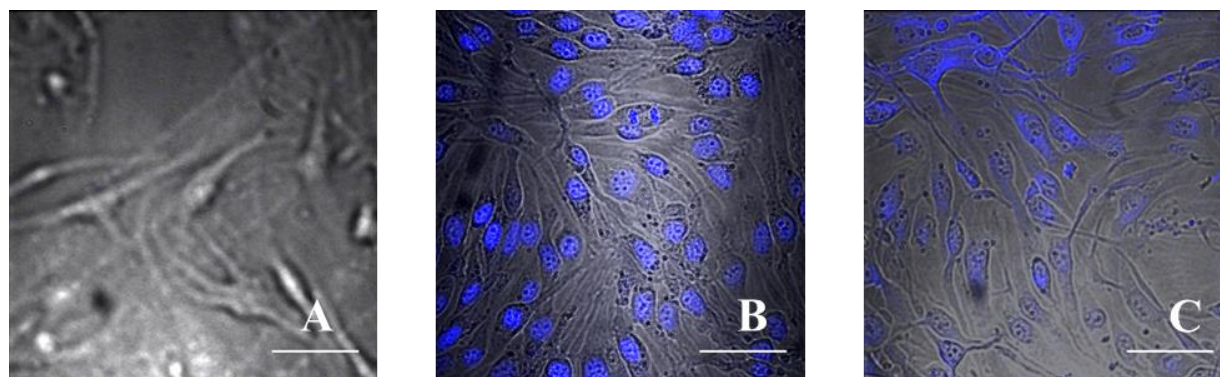


Figure 4.6 Composite images with bEnd.3 cell line – A. blank; B. incubated with DAPI; C. incubated with Hpbt2p. Excitation 405 nm; emission 435-485 nm. Scale bar at 50 μm .

4.4 Conclusions

With **Hmbo2p** it was shown that amyloid-binding functionality was successfully inserted into the HPO scaffold. First, with **Hmbo2p** it was shown that the inhibition constant is 5 μM with aggregated forms of $\text{A}\beta_{1-40}$, while there is no binding with **Hdpp**, which does not possess the benzoxazole functionality. With TEM studies, it was shown that **Hmbo2p** interacts with $\text{A}\beta_{1-40}$ and changes its morphology in the presence of metal ions Cu(II) and Zn(II). It is important to note that it has been reported in the literature that incubation with an amyloid targeting chelator increased toxicity of $\text{A}\beta_{1-40}$ by inducing oligomerization.⁴⁵ Therefore, it is important to study this point in future studies.

Pro-ligands **Hmbo2p**, **Hmbt2p**, and **Habt6p** were found to have moderate to high radical quenching abilities in the absence of metal ions in the TEAC assay, albeit this test is done in methanol over 6 minutes, which may not be biologically relevant. As well, cytotoxicities of these pro-ligands and **Hppp**, **Hzap**, and **Hbt2p** were found to be greater than that of the reference compound cisplatin in a neuronal cell line. **Cu(zapp)₂**, **Zn(zapp)₂**, and **Fe(zapp)₃**

were also studied to determine the effect of chelation to metal ions; however, the EC₅₀ values obtained are of limited usefulness due to significant transchelation in the biological medium. Finally, as an initial measure of BBB permeability, compounds **Hpbt2p** and **Hpbo2p** were found to permeate into bEnd.3 cells, as evaluated with a fluorescent microscope.

Chapter 5: Hydroxypyridinones as acetylcholinesterase inhibitors

5.1 Introduction

The versatility of the hydroxypyridinone scaffold comes in part from the possibility of functionalising the hydroxyl group. This strategy has been used with dual purpose – to imbue the molecules with an additional functionality, as well as to mask the metal chelation site until the compound is delivered across the BBB (thus transforming a *ligand* into a *prodrug*). For example, a glucose moiety was used to potentially increase the uptake of HPOs into the brain by taking advantage of specialised glucose transporters.⁸⁰ It was shown that an enzyme, β -glucosidase from *Agrobacterium faecalis*, is able to deglycosylate the pro-drugs *in vitro*, releasing the pro-ligand.⁸⁰ Thus, it is envisioned that the glycosylated compounds may access the brain, where they would be activated and re-gain their metal-binding activity.

In a similar fashion, the HPO scaffold may be functionalised with other groups. For the purposes of this work, a carbamate was chosen due to its importance in treatment of AD patients. The drugs on the market for AD only treat the symptoms – improving memory for AD patients, which works for 1-2 years in about a third of the patients.¹¹ These drugs are based on the *cholinergic hypothesis*, that the first symptoms of AD – such as memory loss – stem from the loss of cholinergic activity.¹⁴³ Acetylcholinesterase (AChE) is an enzyme that breaks down neurotransmitter acetylcholine (2-acetoxy-*N,N,N*-trimethylethanaminium, ACh) (Figure 5.1). As ACh is depleted in AD patients, inhibitors of AChE such as tacrine (1,2,3,4-tetrahydroacridin-9-amine), rivastigmine ((*S*)-3-[1-(dimethylamino)ethyl]phenyl *N*-ethyl-*N*-methylcarbamate), (Figure 5.1) and donepezil have been used in therapy with some success.¹¹

Rivastigmine is particularly interesting due to its irreversible inhibitory action on the enzyme. After its inhibitory effect, the carbamate moiety is covalently linked to the enzyme, while the phenol group of the molecule is exposed, as has been confirmed by X-ray crystallography.⁸⁵ Thus, it was envisioned that masking the hydroxyl group of the HPO would add AChE inhibition functionality, and that after exerting it, the molecule would have its metal binding functionality restored.

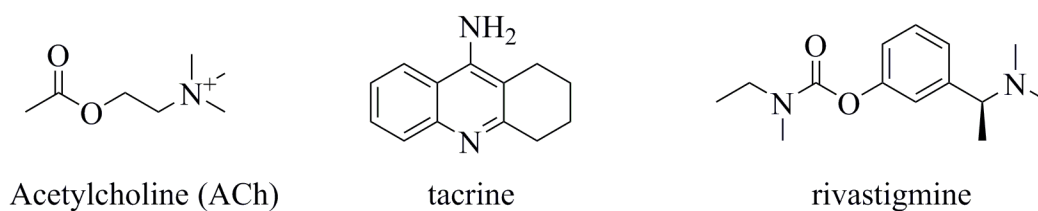


Figure 5.1 Neurotransmitter acetylcholine (ACh), and therapeutics tacrine and rivastigmine.

The strategy of combining metal binders with AChE inhibitors has been used by other researchers. For example, tacrine has been linked to the 8HQ scaffold¹⁴⁴ and *N*¹,*N*¹-dimethyl-*N*⁴-(pyridin-2-ylmethyl)benzene-1,4-diamine,¹⁴⁵ while the carbamate moiety has been used to functionalise the 8HQ scaffold.¹⁴⁶

Hppp was chosen as a model compound for initial studies due to it being synthetically accessible as well as thoroughly investigated as a member of a library of chelators for potential application in AD.^{80,89} After a synthetic route for the prodrug **Cppp** (C(arbamated)ppp) was found and its structure was confirmed, the ability of **Cppp** to bind metal ions, inhibit AChE, and be activated by it were investigated *in vitro*. To gain insight into its inhibitory action, kinetic studies with **Cppp** and AChE were performed. Based on these results, second generation compounds **Cbppp**

and **Chpp** were synthesised and characterised in order to improve the inhibitory activity of the HPOs.

5.2 Experimental

5.2.1 Materials and methods

All reagents and solvents were reagent grade and used without further purification unless otherwise specified. Pyridine and triethylamine were dried over potassium hydroxide.

Acetylthiocholine iodide (ATCI) and 5,5'-dithiobis-2-nitrobenzoic acid (DTNB) were purchased from TCI, whereas acetylcholinesterase from *Electrophorus electricus* (*eel*AChE) was purchased from Sigma.

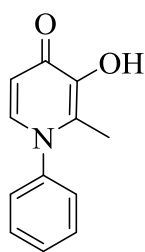
5.2.2 Instrumentation

^1H NMR and ^{13}C NMR spectra were recorded with a Bruker AV-300 spectrometer at 300.13 MHz and 75.48 MHz, respectively, at 24.7 °C and calibrated using residual solvent peaks. Low-resolution mass spectra for metal complexes were obtained with a Waters LC-MS with an ESCI ion source. High-resolution mass spectra were obtained with a Waters/Micromass LCT, and elemental analyses (CHN) were done using a Carlo Erba Elemental Analyzer EA 1108, which were operated by David Wong, Derek Smith, Marco Yeung, or Marshall Lapawa. An automated column chromatography system (Teledyne ISCO CombiFlash Rf) was used to separate compounds that were loaded using a solid load cartridge with celite onto RediSep Rf Gold 12 g silica column. SiliCycle glass backed thin layer chromatography extra hard layer (silica, 60 Å, 20 cm x 20 cm, 250 µm thickness) analytical plates were used for compound separations as well. The HPLC comprised of a Waters 600 controller, a 2487 dual absorbance detector, and a 600

Delta pump, with a Synergi 4 μm Hydro-RP (C18 with polar end capping, 80 \AA , 250 x 4.6 mm) column. UV-Visible data were collected using a Hewlett-Packard 8543 diode array spectrophotometer and a DTX880 plate reader (for inhibition studies) and Varian Cary 5000 (for enzyme kinetic studies). For solid state structure analysis, single crystals were mounted on a glass fiber and the measurements were done with a Bruker APEX DUO diffractometer with cross-coupled multilayer optics Cu-K α radiation or with graphite monochromated Mo-K α radiation. Data sets were collected and integrated using the Bruker SAINT¹⁰² software package. Data were corrected for absorption effects using the multi-scan technique (SADABS).¹⁰³ Direct methods were used to solve the structures of **Hppp**,¹⁰⁴ **Cppp**,¹⁰⁴ **Bnhpp**,¹⁰⁴ **Hhpp**,¹⁴⁷ and **Chpp**,¹⁴⁷ and all non-hydrogen atoms were refined anisotropically. All O-H hydrogen atoms were located in difference maps and refined isotropically, while all other hydrogen atoms were placed in calculated positions. All of solid state structure data sets were collected by Dr. Brian O. Patrick, who also solved and refined the structures of **Hppp**, **Cppp**, and **Bnhpp**.

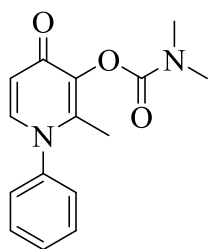
5.2.3 Synthesis and characterisation

3-Hydroxy-2-methyl-1-phenylpyridin-4(*1H*)-one (**Hppp**)



Hppp was prepared according to a previously reported method.⁸⁷ Single crystals of **Hppp** were obtained via slow evaporation of a saturated solution in CH₃OH at room temperature. ¹H NMR (300 MHz, CD₃OD, 24.7 °C): δ = 7.51 - 7.65 (m, 4 H), 7.35 - 7.45 (m, 2 H), 6.48 (d, J = 7.08 Hz, 1 H), 2.11 (s, 3 H). ¹³C NMR (75 MHz, CD₃OD, 24.7 °C): δ = 171.70, 146.99, 143.35, 139.45, 133.06, 131.21, 131.01, 128.11, 112.69, 13.91. Anal. calcd (found) for C₁₂H₁₁NO₂: C, 71.63 (71.90); H, 5.51 (5.66); N, 6.96 (7.33). HR-ESIMS m/z for C₁₂H₁₂NO₂ (M+H⁺) calcd (found): 202.0868 (202.0865).

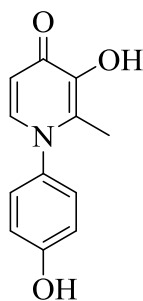
2-Methyl-4-oxo-1-phenyl-1,4-dihydropyridin-3-yl dimethylcarbamate (C_{ppp})



C_{ppp} was prepared following a previously described method with some variations.¹⁴⁸ **H_{ppp}** (0.2268 mg, 1.13 mmol) in 10 mL of dry CH₂Cl₂ was stirred for 5 minutes. To this solution, pyridine (0.3 mL, 3.72 mmol) and triethylamine (0.25 mL, 1.79 mmol) were added, and the solution was stirred for an additional 10 minutes. To the flask, *N,N*-dimethylchlorocarbamate (0.137 mL, 1.49 mmol) was added dropwise and the solution was left to react overnight. The mixture was quenched with water (10 mL), dichloromethane was used to extract the product, and the organic fraction was washed with 5 % aqueous sodium hydroxide (2 x 10 mL), and brine (2 x 10 mL). The combined organic extracts were dried over MgSO₄, filtered, and dried *in vacuo*. The light red crystal solid was recrystallised from CH₃OH/ethyl acetate solution (59.7 mg) at -20 °C, collected by filtration and dried *in vacuo*; single crystals suitable for X-ray analysis were obtained from the same solution. Yield: 19% (first crop). ¹H NMR (300 MHz, CD₃OD, 24.7 °C): δ = 7.78 (d, *J* = 7.54 Hz, 1 H), 7.57 - 7.68 (m, 3 H), 7.43 - 7.53 (m, 2 H), 6.56 (d, *J* = 7.54 Hz, 1 H), 3.17 (s, 3 H), 3.02 (s, 3 H), 2.06 (s, 3 H). ¹³C NMR (75 MHz, CD₃OD, 24.7 °C): δ = 174.15, 155.69, 145.26, 142.95, 142.78, 141.09, 131.40, 131.34, 128.19, 117.01, 37.27, 37.07, 14.85. Anal. calcd (found) for C₁₅H₁₆N₂O₃: C, 66.16 (65.92); H, 5.91 (5.84); N, 10.29 (10.32). HR-ESIMS *m/z* for C₁₅H₁₇N₂O₃ (M+H⁺) calcd (found): 273.1241 (273.1239).

Route 1 for the synthesis of Chpp

3-Hydroxy-1-(4-hydroxyphenyl)-2-methyl-4(1H)-pyridinone (Hhpp)

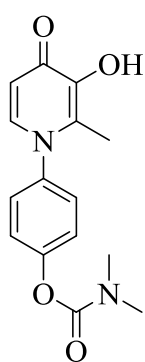


Hhpp was synthesised according to a general procedure for amine insertion.⁹⁵ This is a procedure simplified from that previously published by our group.¹⁰⁷ In a 100 round bottom flask, maltol (3 g, 23.8 mmol) and 4-aminophenol (3.9 g, 35.8 mmol) were combined with 45 mL H₂O, 4.5 mL 1 M HCl, and 15 mL MeOH. The reaction was refluxed for 24 hours, after which time the solid was filtered and washed with methanol several times. The off-white powder (0.8039 g, 16% yield) was dried *in vacuo*. X-ray quality crystals were obtained by evaporation of a saturated DMSO solution. ¹H NMR (300 MHz, DMSO-d₆, 24.7 °C) δ = 7.48 (d, *J* = 7.31 Hz, 1 H), 7.21 (d, *J* = 8.68 Hz, 2 H), 6.87 (d, *J* = 8.68 Hz, 2 H), 6.17 (d, *J* = 7.31 Hz, 1 H), 1.94 (s, 3 H). ESI-MS(+) *m/z* for C₁₂H₁₂NO₃ (M + H⁺) calcd (found): 218.08 (218.3).

Chpp and **Cchpp** were synthesised following to a previously reported method.¹⁴⁸ **Hhpp** (0.25 g, 1.15 mmol) was combined with 6 mL DCM, 0.25 mL TEA and 0.3 mL pyridine in a 25 mL round bottom flask. The solution was stirred for 10 minutes, after which time, *N,N*-dimethylcarbonyl chloride (92 μL, 1.29 mmol) was added. The reaction mixture was left stirring for two days, during which time the disappearance of starting material was monitored by mass spectrometry. The reaction mixture was quenched with 10 mL water and stirred for 15 minutes. DCM extractions were collected, washed with water, and dried over MgSO₄. After filtration, DCM was evaporated to dryness *in vacuo*, leaving behind a yellow-orange solid of mixed products (0.209 mg).

To separate the two products, flash column chromatography was used with a RediSep Rf Gold 12 g silica column with a gradient from 0 to 13.5 % MeOH in DCM for 25 minutes at 30 ml/min flow. Two peaks were observed, and the fractions for each were evaporated to dryness and the remaining solids were analysed, as detailed below.

4-(3-Hydroxy-2-methyl-4-oxopyridin-1(4H)-yl)phenyl dimethylcarbamate (Chpp)



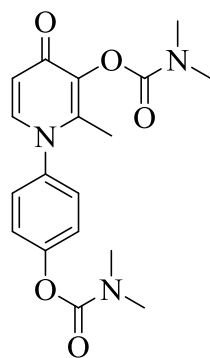
Chpp (68.3 mg, 33% of crude product) was recovered as a fluffy, white powder.

X-ray quality crystals were grown from MeOH. ^1H NMR (300 MHz, MeOD- d_4 , 24.7 °) δ = 7.60 (d, J = 7.31 Hz, 1 H), 7.44 (m, J = 8.68 Hz, 2 H), 7.33 (m, J = 8.68 Hz, 2 H), 6.47 (d, J = 7.08 Hz, 1 H), 3.15 (s, 3 H), 3.02 (s, 3 H), 2.14 (s, 3 H). ^{13}C NMR (75 MHz, MeOD- d_4 , 24.7 °) δ = 171.77, 156.25, 153.76, 146.99, 140.30, 139.58, 133.17, 129.23, 124.54, 112.73, 37.09, 36.90, 13.91. Anal. calcd (found)

for $\text{C}_{15}\text{H}_{16}\text{N}_2\text{O}_4$: C, 62.49 (62.60); H, 5.59 (5.61); N, 9.72 (9.53). HR-ESIMS m/z for

$\text{C}_{15}\text{H}_{17}\text{N}_2\text{O}_4$ ($\text{M}+\text{H}^+$) calcd (found): 289.1187 (289.1188).

4-(3-((Dimethylcarbamoyl)oxy)-2-methyl-4-oxopyridin-1(4H)-yl)phenyl dimethylcarbamate (Cchpp)



Cchpp (58.7 mg, 28% of crude product) was recovered as an off-white

powder. ^1H NMR (300 MHz, MeOD- d_4 , 24.7 °) δ = 7.79 (d, J = 7.54 Hz, 1 H), 7.49 (m, J = 8.91 Hz, 2 H), 7.35 (m, J = 8.91 Hz, 2 H), 6.55 (d, J = 7.54 Hz, 1 H), 3.16 (d, J = 3.43 Hz, 6 H), 3.02 (d, J = 3.65 Hz, 6 H), 2.07 (s, 3 H).

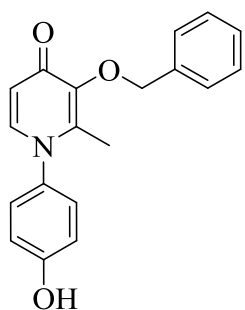
^{13}C NMR (75 MHz, MeOD- d_4 , 24.7 °) δ = 173.80, 155.80, 155.31, 153.66,

144.97, 142.55, 140.78, 139.50, 129.05, 124.42, 116.73, 36.98, 36.81, 36.78, 36.62, 14.59. Anal.

calcd (found) for $C_{18}H_{21}N_3O_5$: C, 60.16 (59.87); H, 5.89 (5.92); N, 11.69 (11.54). HR-ESIMS m/z for $C_{18}H_{18}N_3O_5$ ($M+H^+$) calcd (found): 360.1559 (360.1553).

Route 2 for the synthesis of Chpp

3-Benzyloxy-1-(4-hydroxyphenyl)-2-methyl-4(1H)-pyridinone (Bnhpp)

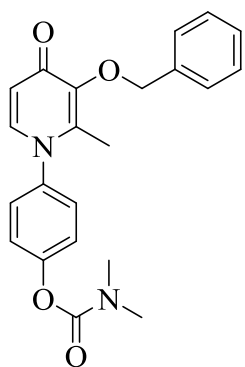


Bnhpp was synthesised according to a previously published procedure.¹⁰⁷

X-ray quality crystals were obtained from a saturated solution of MeOH at -20 °C. 1H NMR (300 MHz, DMSO- d_6 , 24.7 °) δ = 9.96 (s, 1 H), 7.52 (d, J = 7.31 Hz, 1 H), 7.27 - 7.45 (m, 5 H), 7.17 (m, 2 H), 6.85 (m, 2 H), 6.20 (d, J = 7.54 Hz, 1 H), 5.06 (s, 2 H), 1.84 (s, 3 H). HR-ESIMS m/z for

$C_{19}H_{18}NO_3$ ($M+H^+$) calcd (found): 308.1287 (308.1279).

4-(3-(Benzyloxy)-2-methyl-4-oxopyridin-1(4H)-yl)phenyl dimethylcarbamate (BnChpp)

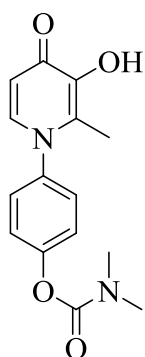


Bnhpp (0.2756 g, 0.898 mmol) was combined with 8 mL DCM, 0.25 TEA, and 0.3 mL pyridine in a 25 mL round bottom flask, following a modified literature procedure.¹⁴⁸ After 10 min of stirring, *N,N*-dimethylcarbamoyl chloride (100 μ L) was added to the solution. The solution was stirred overnight at room temperature. To quench the reaction, 10 mL of H_2O was added, and the solution was stirred for 5 min. Extractions with DCM and

ethyl acetate were collected and washed with base. After drying over $MgSO_4$, the organic fractions were combined and evaporated to dryness *in vacuo*, leaving red solid **BnChpp** (0.2779 g, 81 % yield). 1H NMR (300 MHz, MeOD- d_4 , 24.7 °) δ = 7.65 (m, J = 7.31 Hz, 1 H), 7.41 -

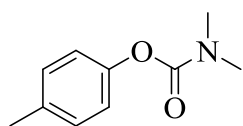
7.48 (m, 2 H), 7.14 - 7.41 (m, 7 H), 6.54 (m, $J = 7.31$ Hz, 1 H), 5.14 (s, 2 H), 3.13 (s, 3 H), 3.01 (s, 3 H), 1.89 (s, 3 H). ^{13}C NMR (75 MHz, MeOD- d_4 , 24.7 °) $\delta = 175.64, 156.07, 153.74, 146.81, 145.20, 141.60, 140.05, 138.63, 130.35, 129.54, 129.48, 129.11, 124.57, 117.23, 74.64, 37.08, 36.88, 14.97$. Anal. calcd (found) for $\text{C}_{22}\text{H}_{22}\text{N}_2\text{O}_4 \cdot 0.25 \text{H}_2\text{O}$: C, 69.00 (68.91); H, 5.92 (5.67); N, 7.32 (7.07). HR-ESIMS m/z for $\text{C}_{22}\text{H}_{23}\text{N}_2\text{O}_4$ ($\text{M}+\text{H}^+$) calcd (found): 379.1658 (379.1661).

4-(3-Hydroxy-2-methyl-4-oxopyridin-1(4H)-yl)phenyl dimethylcarbamate (Chpp)



BnChpp (0.1002 g) was combined with 3 mL 33% HBr in a 10 mL round bottom flask using a previously reported procedure for deprotection of the benzyl group.⁵⁸ The solution was refluxed for 2.5 hours, after which point ethyl acetate was added. After the extraction, the organic solvent was evaporated to dryness, resulting in 56 mg of crude product that was purified according to conditions above to yield **Chpp**.

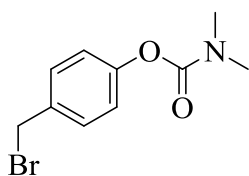
p-Tolyl dimethylcarbamate (Cp-cresol)



In a 25 mL round bottom flask, p-cresol (0.3146 g, 2.9 mmol) was combined with 8 mL DCM, 0.4 mL pyridine, and 0.3 mL TEA. After stirring for 10 minutes, *N,N*-dimethylcarbamoyl chloride (0.319 mL, 3.5 mmol) was added. The reaction mixture was stirred overnight at room temperature, after which point 10 mL water was added to quench the reaction. The solution was stirred 10 min, and 3x20 mL of DCM was used to extract the product. The organic layer was washed with water, dried over MgSO_4 , and evaporated to dryness, yielding a yellow oil. Water was added to the oil, and an additional extraction with ethyl acetate from water was performed, with the organic layer being washed

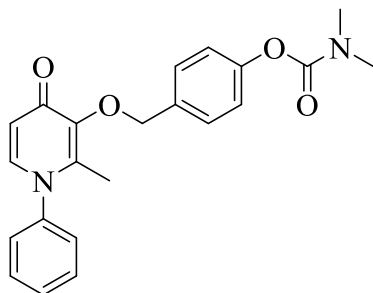
with water and evaporated to dryness, yielding a yellow oily solid (0.3057 g, 59%). ^1H NMR (300 MHz, CDCl_3 , 24.7 °) δ = 7.15 (d, J = 8.45 Hz, 2 H), 7.01 (d, 2 H), 3.06 (s, 3 H), 2.98 (s, 3 H), 2.33 (s, 3 H). ^{13}C NMR (75 MHz, CDCl_3 , 24.7 °) δ = 154.65, 148.91, 134.16, 129.25, 121.03, 36.12, 35.87, 20.33. ESI-MS(+) m/z for $\text{C}_{10}\text{H}_{14}\text{NO}_2$ ($\text{M} + \text{H}^+$) calcd (found): 180.10 (180.4).

4-(Bromomethyl)phenyl dimethylcarbamate (BrCp-cresol)



In a 50 mL round bottom flask, Cp-cresol (0.420 g, 2.3 mmol), benzoyl peroxide (0.0520 g, 0.2 mmol), and *N*-bromosuccinimide (NBS) (0.472 g, 2.7 mmol) were combined in 25 mL of chloroform dried over MgSO_4 . The solution was refluxed at 50 °C and the reaction was monitored by mass spectrometry. After 24 hours of reaction, one more eq. of NBS was added and reaction was continued for 24 hours. The reaction mixture was quenched with water, and the product of interest was extracted into 20 mL DCM three times, washed with water three times, and dried over MgSO_4 . The filtered solvent was evaporated to dryness, resulting in 0.5607 g of crude product. To purify the product, flash column chromatography was used with a RediSep Rf 12 g Gold silica column with an isocratic elution with DCM over 5 minutes at 30 mL/min flow, yielding 0.1907 g (32 % yield). ^1H NMR (300 MHz, DCM-d_2 , 24.7 °) δ = 7.39 (d, J = 8.45 Hz, 2 H), 7.09 (d, J = 8.45 Hz, 2 H), 4.52 (s, 2 H), 3.07 (br. s., 3 H), 2.98 (br. s., 3 H). ^{13}C NMR (75 MHz, DCM-d_2 , 24.7 °) δ = 155.03, 152.18, 135.32, 130.49, 122.68, 36.99, 36.80, 33.65. ESI-MS(+) m/z for $\text{C}_{10}\text{H}_{13}\text{BrNO}_2$ ($\text{M} + \text{H}^+$) calcd (found): 258.01/260.01 (258/260).

4-(((2-methyl-4-oxo-1-phenyl-1,4-dihydropyridin-3-yl)oxy)methyl)phenyl dimethylcarbamate (Cbppp)



In a 25 mL round bottom flask, **Hppp** (0.0584 g, 0.29 mmol) and **BrCp-cresol** (0.0687 g, 0.27 mmol) were combined in 10 mL of DMF. Subsequently, K_2CO_3 (0.1146 g, 8.3 mmol) was added and the reaction proceeded at 60 °C overnight. To quench the reaction, H_2O was added, and the solution was stirred for 10 minutes. Ethyl acetate was used to extract the product; the organic layer was washed with water, and dried over $MgSO_4$. Finally, the solvent was evaporated to dryness, leaving an orange oil. The product was purified by analytical TLC with 5% MeOH in DCM as the eluent, resulting in a pale yellow film-like oil (0.0303 g, 18 % yield). 1H NMR (300 MHz, DCM- d_2 , 24.7 °) δ = 7.48 - 7.51 (m, 3 H), 7.44 (d, J = 8.45 Hz, 2 H), 7.28 (d, J = 7.54 Hz, 1 H), 7.21 - 7.25 (m, 2 H), 7.06 - 7.09 (m, 2 H), 6.36 (d, J = 7.54 Hz, 1 H), 5.19 (s, 2 H), 3.08 (s, 3 H), 2.97 (s, 3 H), 1.87 (s, 3 H). ^{13}C NMR (75 MHz, DCM- d_2 , 24.7 °) δ = 173.95, 155.23, 152.06, 146.08, 142.45, 141.54, 139.27, 135.32, 130.36, 130.30, 129.86, 127.45, 122.20, 117.09, 72.66, 37.00, 36.82, 14.77. HR-ESIMS m/z for $C_{22}H_{23}N_2O_4$ ($M+H^+$) calcd (found): 379.1658 (379.1653). The HPLC gradient used for verification of purification by TLC was 50 to 100% of MeOH in H_2O for 10 minutes, followed by 10 minutes of 100% MeOH with 0.8 ml/min flow.

5.2.4 Enzymatic activity - inhibition

AChE inhibitory activity was evaluated by the colorimetric method of Ellman¹⁴⁹ at 25 °C using AChE from *eel*AChE and acetylthiocholine iodide (ATCI) as a substrate. The assay for each sample was performed in triplicate. 5 U/mL *eel*AChE solutions were prepared dissolving 500 U

of enzyme in 1 mL of MilliQ water with 1% gelatin and diluting it to 100 mL in a volumetric flask. The solution was used directly or frozen in Eppendorf tubes at -20 °C for later use. Stock inhibitor solutions were freshly prepared in DMSO and diluted in MilliQ water to afford a range of concentrations for sigmoidal inhibition curves maintaining the final DMSO concentrations in all assays at 2% maximum v/v, including controls. A typical assay for initial studies of **Hppp** and **Cppp** consisted of 50 μ L of *eel*AChE solution, at a final concentration of 0.083 U/mL; 2745 μ L of 0.1 M phosphate buffer pH 8; 100 μ L of DTNB (0.01 M prepared in 0.1 M phosphate buffer pH 8 with 0.017 M of sodium bicarbonate), and 100 μ L of inhibitor solution. The reactants were mixed in a 3 mL cuvette and the mixture was incubated at 25 °C for 5 min allowing the enzyme and the inhibitor to interact. Subsequently, the addition of 10 μ L 0.075 M ATCI (substrate) initiated the Ellman reaction. The absorbance at 412 nm was recorded after 2 min. A blank was prepared for each assay replacing the inhibitor and the enzyme with water, and as a control the inhibitor was replaced with water to determine 100% enzymatic activity. For **Cphp**, **Ccphp**, and **Cbppp** the experiment was performed in a 96-well plate. All components were added in the same amounts, while their concentrations were decreased tenfold by dilution in a buffer in order to account for a 10 time decrease in volume of the cell vs a cuvette. In a typical experiment, 50 μ L of 0.5 U/mL *eel*AChE solution was combined with 100 μ L of inhibitor, and 100 μ L of DTNB (0.001 M prepared in 0.1 M phosphate buffer pH 8 with 0.0017 M of sodium bicarbonate). The plate was agitated at 36 rpm for 5 minutes, after which point 10 μ L of ATCI (0.0075 M) was added to each well. The plate was inserted into a plate reader that was set up to shake it for 1 minute on a medium linear setting, take absorbance at 405 nm, wait for 1 minute, and take another reading. The IC_{50} value is defined as the concentration of compound that reduces the enzymatic activity by 50% with respect to that without inhibitor.

The sigmoidal dose response curves were analyzed and fitted by nonlinear regression using GraphPad Prism 5 (Graphpad Software, Inc., La Jolla, CA, USA). For all HPO compounds studied, due to solubility limits, 100% inhibition was never reached; therefore, the top limit was set at 100% for fitting of the data. Otherwise, no restrictions were used.

5.2.5 Acetylcholinesterase inhibition kinetics

Determination of reversibility of inhibition

The assay was performed at room temperature using the Ellman method¹⁴⁹ with AChE from *ee*lAChE and ATCI as a substrate in a fashion similar to that described above. In a 25 mL scintillation vial 16.440 mL pH 8 phosphate buffer, 600 μ L DTNB, and 300 μ L enzyme were mixed. Tacrine, **Cppp**, **Chpp**, or **Cbppp** as an inhibitor (600 μ L) was added and the rate of the enzymatic activity was assessed at time points 5, 10, 15, 30 and 60 min. At those time points, 2.990 mL was removed and placed in a cuvette, to which 10 μ L of 0.075 M ATCI was added. After 15 seconds of vigorous mixing, the rate of reaction was monitored by recording absorbance at 412 nm for 1 min. The slope between the readings at 0 and 1 min was used as the rate of the ATCI hydrolysis by the enzyme. The final concentrations in each vial were: 0.083 U/mL of the enzyme, 0.348 mM DTNB with 0.619 mM sodium bicarbonate, and 0.1455 μ M tacrine, and 16 μ M **Cppp**, 102 μ M **Chpp**, or 282 μ M **Cbppp**. The control solution had no inhibitor added. The results are represented as a linear relationship between time and reaction velocity, with reversible inhibitors displaying a line parallel to the x-axis, while irreversible inhibitors have a negative slope.

Determination of the competitiveness of inhibitors

The assay was performed at room temperature using the Ellman method¹⁴⁹ with AChE from *eel*AChE and ATCI as a substrate in a fashion similar to that described above. To determine the rate of AChE in the absence of inhibitors, in a cuvette, pH 8 phosphate buffer, 50 μ L enzyme, and 100 μ L DTNB were mixed. For the five trials, various amounts of ATCI substrate (1, 5, 10, 50, and 100 μ L) were added to the cuvette, giving a final volume of 3 mL, and after 15 seconds of rigorous mixing, the absorbance at 412 was recorded for 3.5 min. To determine the rate of AChE in the presence of inhibitors, tacrine (final concentration 0.029 μ M) or **Cppp** (final concentration 53.86 μ M) was added 2 min prior to the addition of ATCI. As the initial reaction velocity (V_i), the slope between 0 and 0.3 min was used. The results are represented as a linear relationship between $1/[S]$ and $1/V_i$.

5.2.6 Prodrug metal ion binding activity and activation *in vitro*

To investigate the metal ion binding ability of **Cppp**, it was incubated with Cu(II), Zn(II) and Fe(III) separately in 2:1 ligand to metal ion ratios for Cu(II) and Zn(II), and in 3:1 for Fe(III) in a buffered solution at pH 7.4. As well, all three metal ions were added at the same time to a buffered solution containing **Cppp**. For comparison, **Hppp** was studied under the same conditions. All solutions were monitored for several hours to allow equilibration.

Cppp, **Chpp**, and **Cbppp** were incubated with an excess of *eel*AChE for 1 h and 24 h in 0.1 M sodium phosphate buffer, pH 7.4 with 100 mM NaCl (**Cppp**) or 0.1 M phosphate buffer, pH 8.0 (**Chpp** and **Cbppp**). The respective metabolites were extracted from the mixture using ethyl acetate and analyzed by ESI-MS. As well, the enzymatic reactions of **Hppp**, **Hhpp**, **Chppp**, and

Cbppp were followed by TLC (5% MeOH in DCM) over one hour. At 0, 10, 20, 30, 45, and 60 minutes, the reaction mixtures were spotted onto a TLC plate and run. The R_f values for the four compounds were compared one to another, and a dilute solution of $\text{Fe}(\text{ClO}_4)_3 \cdot 6\text{H}_2\text{O}$ was applied to each spot to test for metal ion chelation.

5.3 Results and discussion

5.3.1 First generation study

5.3.1.1 Synthesis and characterisation

Hppp, the pro-ligand chosen as a model compound for carbamation, was carbamated in a one-step reaction. The product, **Cppp**, was characterised by MS, NMR spectroscopy, and EA. As well, single crystals of both **Hppp** and **Cppp** were obtained and analyzed by X-ray crystallography (Table A.10, Figure 5.2). Solid state analysis confirms the structure of the compounds, and reveals little change to the HPO scaffold (Table A.11), save for elongation of the C3-O2 bond by 0.05 Å due to the carbamate functional group. Having found an easy route to get the desired carbamated model compound, it was tested for AChE inhibitory activity.

This synthetic route was also used to synthesise carbamated derivatives **Czapp** and **Cmbo2p**, as well as that of maltol. The identity of these compounds was confirmed with LRMS and ^1H NMR spectroscopy; however, purification and complete characterisation were not attempted due to the performance of the model compound **Cppp** in the *in vitro* studies.

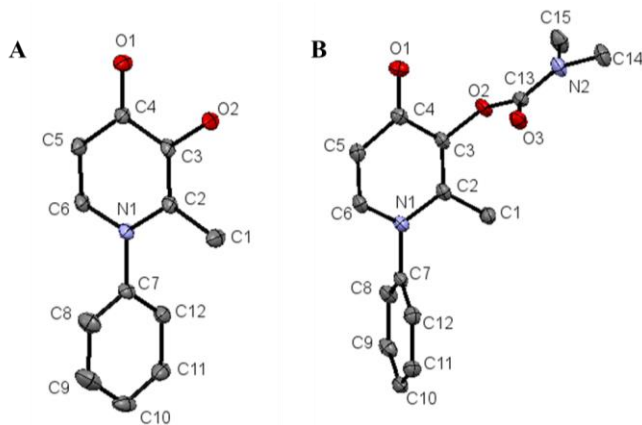


Figure 5.2 Solid state structures of **A. Hppp** and **B. Cppp**, represented as ellipsoid plots (50% probability). Solvent molecules and hydrogen atoms are omitted for clarity.

5.3.1.2 Acetylcholinesterase inhibition

First, the ability of the model compound **Cppp** to inhibit AChE activity was assessed by Ellman's colorimetric assay,¹⁴⁹ using AChE from the *Electrophorus electricus* (Electric *eel*; *eel*AChE), with tacrine ($IC_{50} = 0.0744 \mu\text{M}$) as the reference standard. The IC_{50} value, the concentration of compound at which 50% of inhibition is observed, for **Cppp** was compared to that of **Hppp**. As can be seen in Figure 5.3, **Cppp** ($IC_{50} = 49.8 \mu\text{M}$) is not significantly better than its parent molecule, **Hppp** ($IC_{50} = 201 \mu\text{M}$). As well, this activity is about an order of magnitude less than that of rivastigmine ($5.50 \mu\text{M}$).¹⁵⁰ The fact that carbamation of **Hppp** improved its activity by only four-fold suggested that **Cppp** does not inhibit AChE via decarbamation, as was originally envisioned. This was confirmed by kinetic and *in vitro* activation studies (see below), as well as computational docking studies that show that the carbamate is not well positioned in the active site of the enzyme; the computational studies were not performed by the author and therefore are not discussed here, but can be found elsewhere.¹³⁶

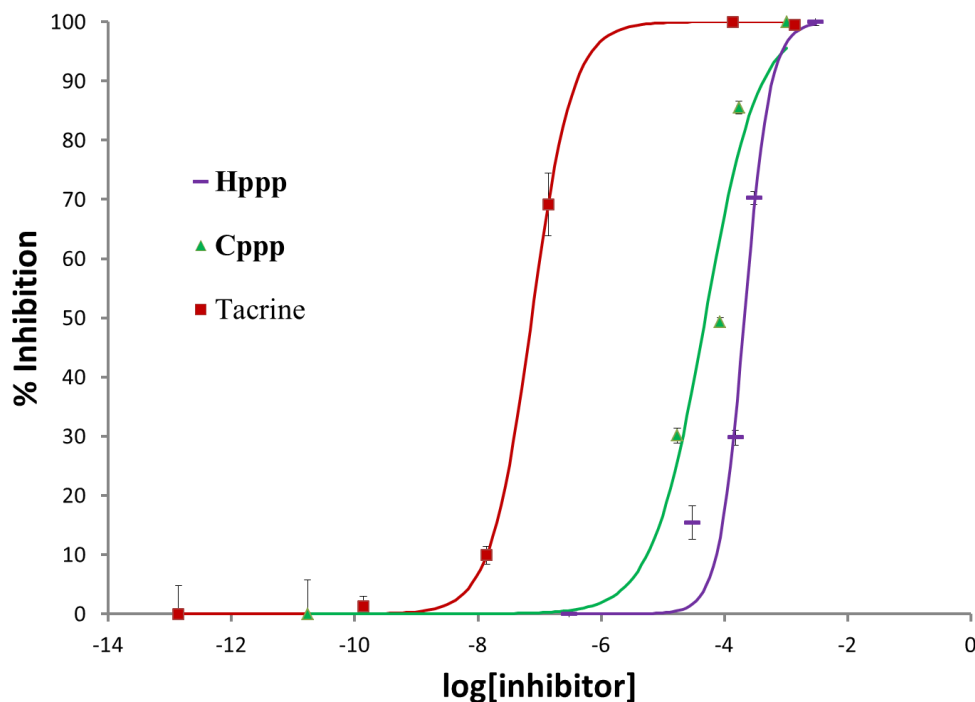


Figure 5.3 Inhibition of *eel*AChE by Hppp, Cppp, and tacrine at various concentrations. Modified figure reproduced by permission of The Royal Society of Chemistry.

5.3.1.3 Kinetic studies

Reversibility of inhibition

After it was confirmed that **Hppp** and **Cppp** are inhibitors of acetylcholine esterase, their action was further examined with kinetic studies. Inhibitors can be classified as either reversible (in cases where the enzyme is not modified) or irreversible (in cases where the inhibitor permanently modifies the enzyme during the inhibition process).¹⁵¹ It was envisioned that **Hppp** would be a reversible inhibitor, while **Cppp** would be irreversible, as it was designed based on an irreversible inhibitor rivastigmine; however, our inhibition studies (above) suggested that the modes of action may not be different.

For the study, **Cppp**, and a reference compound tacrine were incubated with *eel*AChE in the presence of reagent DTNB, and the velocity of enzymatic activity on acetylthiocholine iodide (ATCI) was monitored for one hour. In the absence of an inhibitor, the kinetic profile of the enzyme presents a horizontal line (Figure 5.4). When tacrine, a known reversible inhibitor¹⁵² is incubated with the enzyme, the time of incubation does not impact the rate of activity, although it is lower due to the inhibitor's presence. Likewise, **Cppp**, showed a similar kinetic pattern to that presented by tacrine (Figure 5.4), indicating that it too is a reversible inhibitor. These results confirmed the hypothesis that **Cppp** is a reversible inhibitor and that the carbamate may not come off during the inhibitory process (and this is confirmed with our further studies, see below).

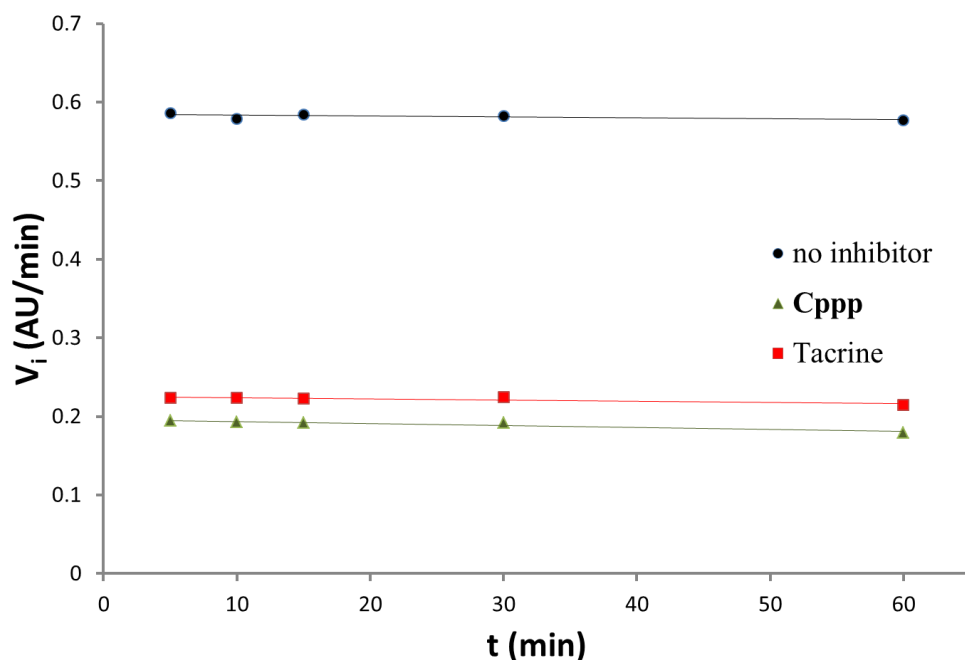


Figure 5.4 Inhibition kinetics of Cppp (16 μ M) and tacrine (0.1455 μ M) with *eel*AChE: enzymatic activity vs. time. Modified figure reproduced by permission of The Royal Society of Chemistry.

Competitiveness of inhibitors

After determining that **Cppp** acts as a reversible inhibitor, it was further examined in kinetic studies. A reversible inhibitor can be classified as either complete or partial, and within complete inhibition, there are competitive, non-competitive, or uncompetitive inhibitors, based on interaction with the enzyme and its substrate.¹⁵¹ Lineweaver-Burk plots (double reciprocal plots of substrate concentration vs. velocity of substrate turnover) are a convenient way to visualise and examine enzyme kinetics.¹⁵³ Competitive inhibitors bind to the enzyme and prohibit it from interacting with the substrate; these produce lines with different slopes that intersect the uninhibited enzyme at the y-axis on the Lineweaver-Burk plot.¹⁵¹ Non-competitive inhibition occurs when the substrate is able to interact with the inhibitor-enzyme complex, but this interaction does not result in product formation; these produce lines with different slopes that intersect to the left of the y-axis.¹⁵¹ In the case of uncompetitive inhibition, the inhibitor can only interact with the substrate-enzyme complex; these produce lines with the same slope as the uninhibited enzyme, and thus, there is no intercept.¹⁵¹ As well, inhibitors may exhibit mixed-type behaviour as well as partial inhibitory behaviour.¹⁵¹

To determine their modes of action, **Cppp** and a reference compound tacrine were incubated with *eel*AChE and its substrate ATCI in varying concentrations. Enzymatic turnover was monitored for 3.5 minutes to determine velocity of reaction. The data are represented as a Lineweaver–Burk plot, which plots the inverse of substrate concentration vs. the inverse of the initial velocity of reaction.¹⁵³ The reference line is produced by the enzyme without an inhibitor present. Figure 5.5 illustrates that the line produced by **Cppp** and tacrine intersect the reference

spectrum in the second quadrant. This means that they are not competitive or uncompetitive inhibitors, but are either non-competitive or mixed non-competitive/competitive inhibitors. This is consistent with previous reports that classify tacrine as a mixed non-competitive/competitive inhibitor.¹⁵⁴ According to our computational studies, it is expected that **Cppp** interacts with the active site of the enzyme.¹³⁶ Overall, it was determined that **Cppp** is a reversible, potentially mixed competitive/ non-competitive inhibitor that may work by interacting with the catalytic site, but without permanently altering it.

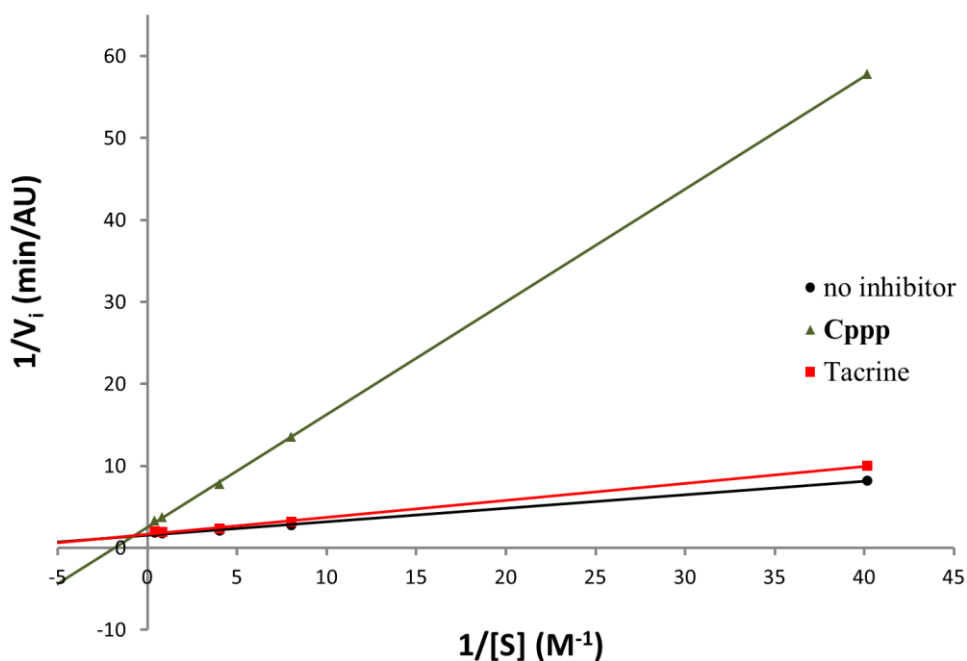


Figure 5.5 Inhibition kinetics of Cppp and tacrine with *ee*/AChE: Lineweaver-Burk plots in the absence of inhibitor (control) or at different concentrations of Cppp and tacrine. Modified figure reproduced by permission of The Royal Society of Chemistry.

5.3.1.4 Prodrug metal binding activity and activation *in vitro*

Another aspect to carbamation of the HPO scaffold involves masking of the metal chelation ability. To confirm this point, **Cppp** was incubated with Cu(II), Zn(II), and Fe(III) and the reaction was followed by UV-vis spectroscopy. No spectral changes associated with metal chelation were observed (Figure 5.6). This is in contrast to the behavior of **Hppp**, the spectral characteristics of which change dramatically upon addition of metal ions (Figure 5.6).

To confirm that the prodrug **Cppp** was not decarbamated by the enzyme, it was incubated with *eel*AChE, and the extracts were studied by mass spectrometry. As anticipated, no trace of **Hppp** was found, which is consistent with data showing that it is a reversible inhibitor that, according to computational studies, is not well positioned in the active site for irreversible inhibition.¹³⁶

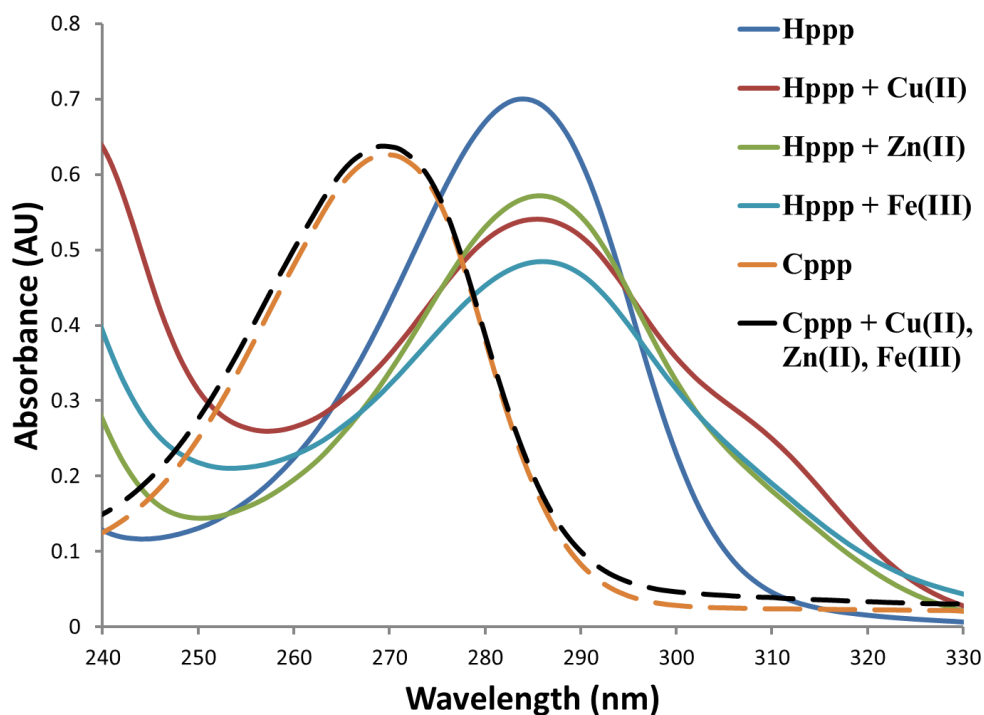


Figure 5.6 UV-vis spectroscopy study following the reactions between Cppp and Hppp and metal ions Cu(II), Zn(II), and Fe(III).

5.3.1.5 Conclusions

Carbamation of the model compound **Hppp** was successfully achieved with dimethylcarbamoyl chloride in DCM, with the use of TEA and pyridine. The product **Cppp** was analysed by NMR spectroscopy, MS, and EA, and its structure was confirmed by X-ray crystallography. **Cppp** was studied for its metal chelation ability, and its ability to inhibit AChE by determining its IC_{50} .

While a prodrug that has a masked chelation site and has acetylcholine esterase inhibitory activity was successfully synthesised, its activity does not come from irreversible inhibition. The obtained data suggest that the carbamate does not come off **Cppp**, and thus the molecule does not re-gain its metal-chelating ability. Computational studies¹³⁶ suggest that the carbamate is not well-positioned in the active site. It was hypothesised that there might be steric hindrance from the carbamate being positioned close to the main HPO ring. These observations were taken into account in creating second generation prodrugs, and this project is described below.

5.3.2 Second generation compounds

The new approach of converting the HPO scaffold into an irreversible inhibitor takes into account the inaccessibility of the carbamate. Two modifications to the scaffold were considered (Figure 5.7): in one, the carbamate is positioned on the *N*-substituent of the HPO, while in another approach, the carbamate is linked to the HPO ring by a spacer. In considering which spacer to select in the latter case, we had to ensure that the molecule returns to the HPO scaffold that is able to bind metal ions. To select the appropriate spacer, we were inspired by Cohen and coworkers, who showed that in a similar context, the benzyl ether linker is eliminated upon enzymatic removal of a protecting group¹⁵⁵ (as is illustrated in Figure 5.7).

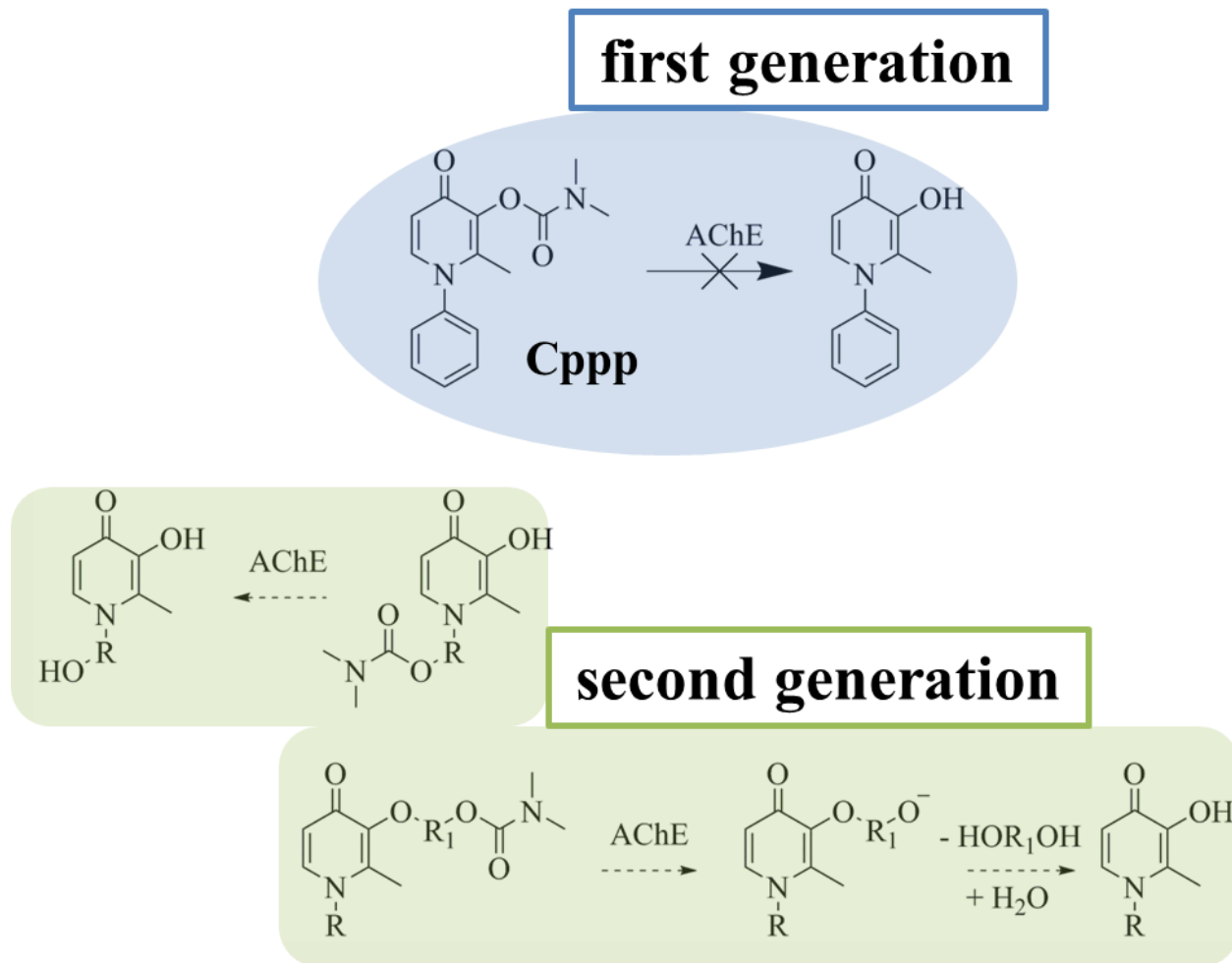
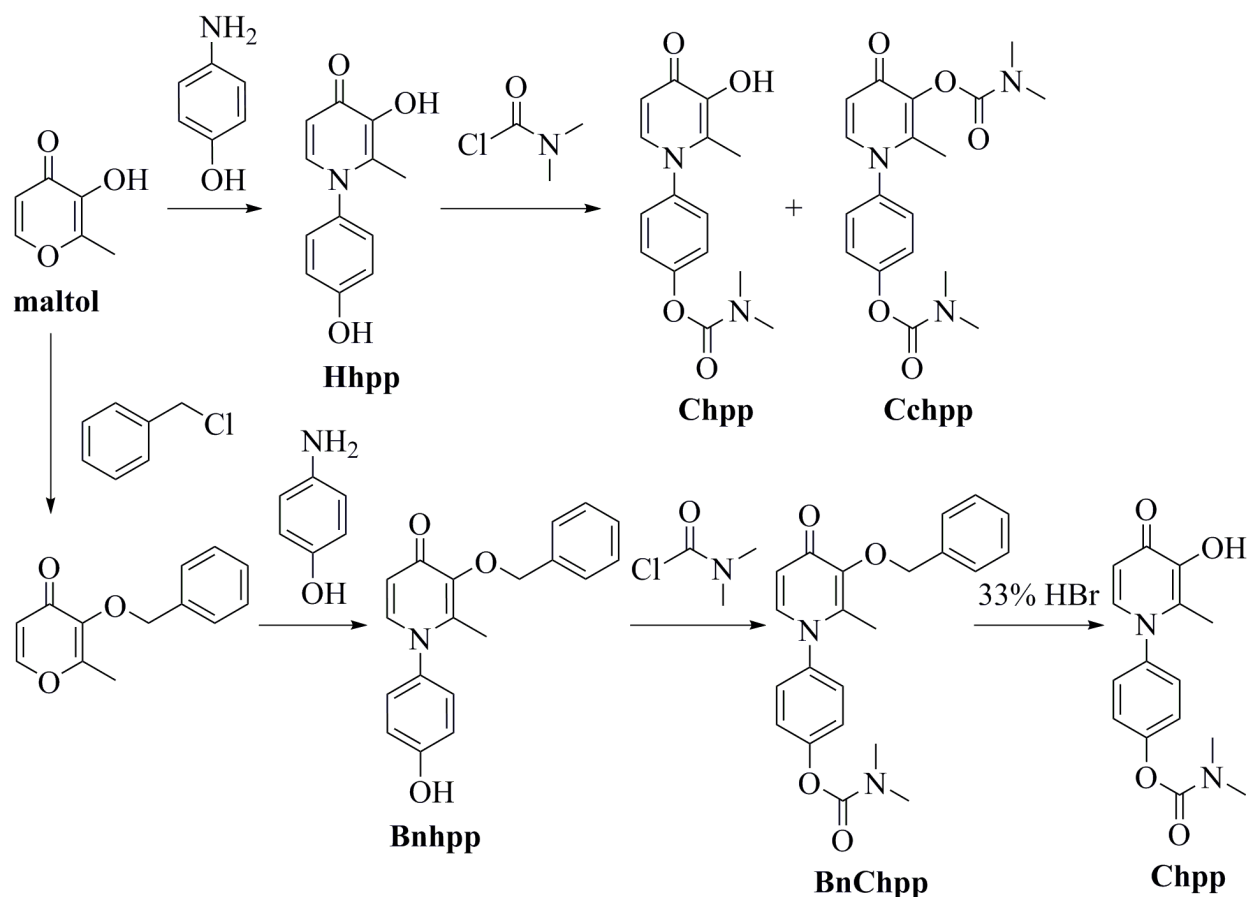


Figure 5.7 The first generation compound (Cppp), as well as two second generation designs.

5.3.2.1 Synthesis and characterisation

Synthesis of compound **Chpp** followed the synthetic routes in Scheme 5.1. The product could be obtained using two routes. In the first, **Hhpp** is reacted with *N,N*-dimethylcarbamoyl chloride,¹⁴⁸ resulting in both singly and doubly carbamated compounds, **Chpp** and **Cchpp** that were separated by column chromatography. The second route avoids the doubly carbamated by-product by starting with a benzyl protected starting material, **Bnhpp**. After carbamation, **BnChpp** must be debenzylated; and while both these routes result in **Chpp**, the second requires

two extra steps. Identity and purity of **Chpp** and **Cchpp** were established with ^1H , ^{13}C NMR spectroscopies (Figures A.20-A.23), HRMS, and EA.



Scheme 5.1 Synthetic routes for Chpp.

Starting materials **Hhpp** and **Bnhpp**, as well as **Chpp** were analysed by X-ray crystallography and their solid state structures appear in Figure 5.8. Crystal refinement data and selected bonds and angles can be found in Tables A.12 and A.13. As can be seen from Table A.13, the HPO ring retains its bond distances across the three compounds

Compound **Cbppp** was synthesised using the route in Scheme 5.2. First, p-cresol is carbamated¹³⁶ and brominated using NBS,¹⁵⁵ and then it is reacted¹⁵⁵ with **Hppp**. The product **Cbppp** is purified using analytical TLC, as it was found to interact with silica and not to elute from a column. It was characterised by ¹H and ¹³C NMR spectroscopies (Figures A.24 and A.25) and HRMS. Due to its consistency, it could not be analysed by EA, instead, HPLC was used to provide an assessment of its purity (Figure A.26). The small peaks due to impurities that elute prior to the peak corresponding to **Cbppp** were not observed after purification. The peak shape was noticeably broad, due to its late elution and low velocity of the mobile phase.

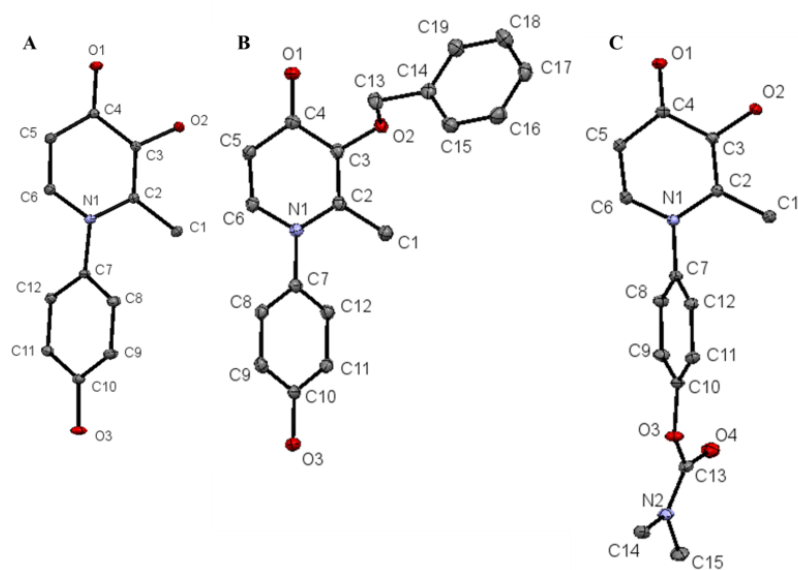
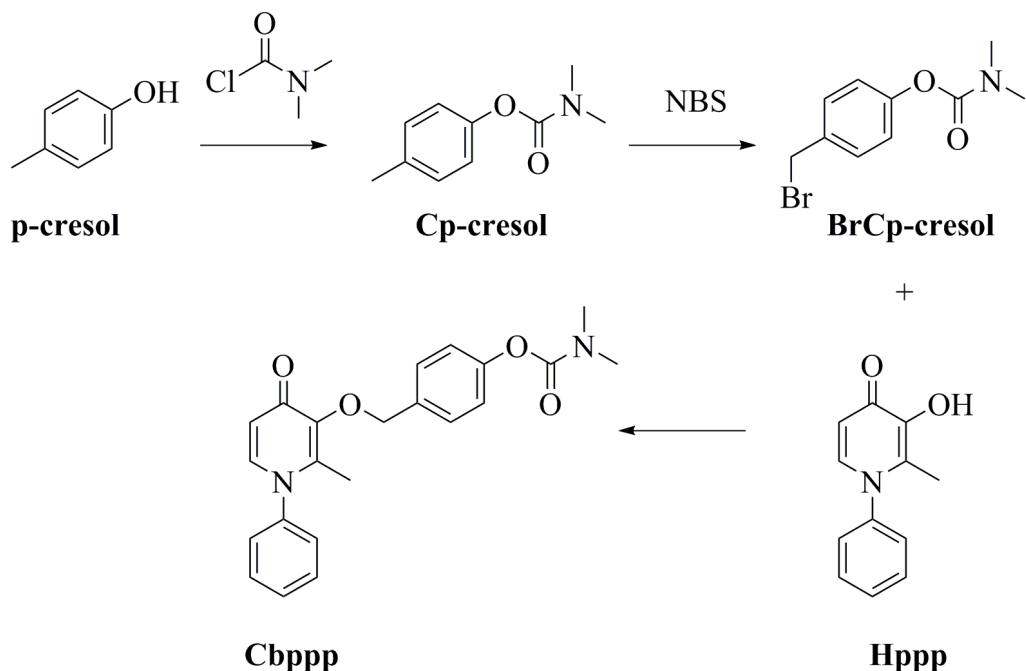


Figure 5.8 Solid state structures of Hhpp, Bnhpp, and Chpp, represented as ellipsoid plots (50% probability). Hydrogen atoms are omitted for clarity.



Scheme 5.2 Synthetic route for Cbppp.

5.3.2.2 Acetylcholinesterase inhibition

In vitro acetylcholinesterase activity was established for new compounds **Chpp**, **Cchpp**, **Cbppp**, as well as for the fragment Cp-cresol. As can be seen from Table 5.1, moving the carbamate to the substituent of the nitrogen of the HPO, or introducing a linker does not result in improved inhibitory activity. To investigate whether this was due to reversible mode of action, further experiments, as detailed below, were performed. It was also noted that the carbamated fragment C-p-cresol has inhibitory activity that is about an order of magnitude weaker.

Table 5.1 IC₅₀ values for *eel*AChE activity *in vitro* for Hppp, Chph, Ccphp, Cbppp, and C-p cresol.

	IC ₅₀ (μM)
Hppp	219.9
Cphp	347.6
Ccphp	252.3
Cbppp	216.5
C-p cresol	1282

5.3.2.3 Kinetic studies

Substrate turnover (of acetylthiocholine iodide) was monitored over 60 minutes. In this study, 20 mL of solution containing enzyme and inhibitor was incubated, and at time points 5, 10, 15, 30, and 60 minutes, 3 mL of the solution was taken out to be studied for the initial rate of reaction (V_i) after addition of ATCI. It was determined that compared to control (no inhibitor present), the compounds **Chpp** and **Cbppp** presented similar profiles – that is, the turnover rate remained nearly constant over time (Figure 5.9). If the compounds had irreversible inhibition during the one hour study, the turnover rate would decrease.

5.3.2.4 Prodrug activation

Another piece of evidence suggesting that the inhibition observed from **Chppp** and **Cbppp** is reversible comes from analysing drug activation extracts by mass spectrometry. Peaks corresponding to pro-ligands **Hhpp** and **Hppp** were not observed after 1 or 24 hours of incubation with AChE. As well, the reaction was studied by TLC for one hour; at 0, 10, 20, 30, 45, and 60 minutes, the reactions of **Hppp**, **Hhpp**, **Chpp**, and **Cbppp** with AChE were monitored by spotting them on a TLC plate that was placed in a chamber with 5% MeOH in DCM solution. The R_f values of each compound were compared. It was observed that **Hhpp** created a smear, while the rest of the compounds ran as distinct bands. After the one hour of

incubation, no evidence of decarbamation was observed. As well, inactivation of **Cbpp** was confirmed with a chelation test, in which a drop of dilute methanol solution of $\text{Fe}(\text{ClO}_4)_3$ hexahydrate came in contact with the TLC spot and remained uncoloured. Conversely, **Hppp** was brightly coloured under the same conditions. As both **Hhpp** and **Chppp** have a binding functionality, this test does not work to distinguish between these two compounds. After one hour, the reactions were stopped by adding ethylacetate in order to extract the compounds for mass spectrometry analysis. As well, ten drops of the dilute $\text{Fe}(\text{ClO}_4)_3$ were added to a separate set of MS samples. Consistent with previous results, no fragments were observed in **Chpp** and **Cbppp** samples. As well, only the 2:1 **Chpp**:iron complex was observed, and no **Cbppp** iron complex was observed.

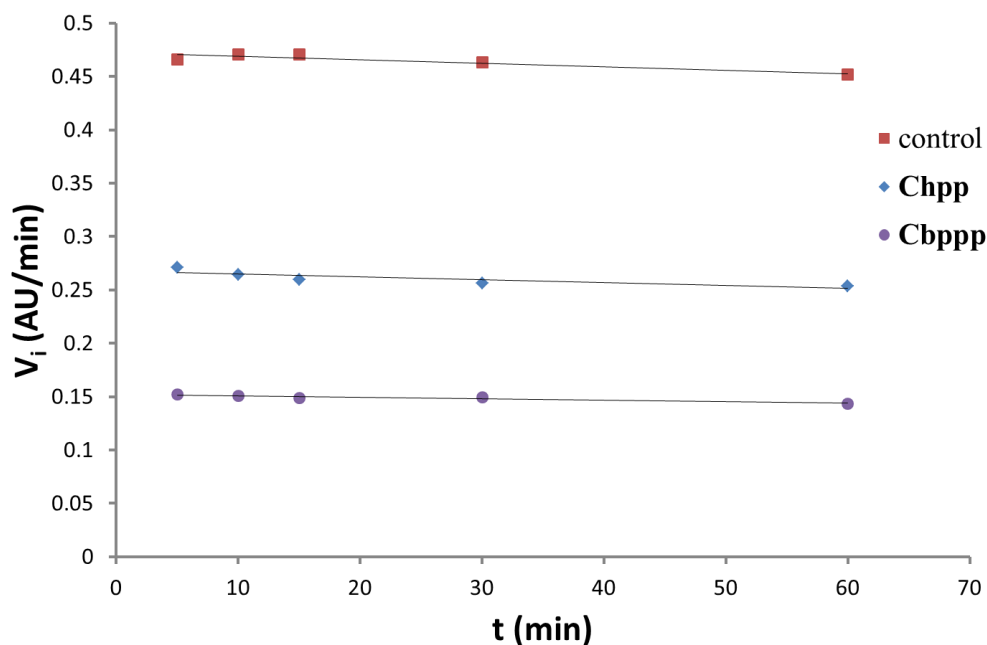


Figure 5.9 Inhibition kinetics of Chpp and Cbppp with *eelAChE*: enzymatic activity vs. time.

5.3.2.5 Conclusions

A second generation of compounds was designed and two model compounds – **Chpp** and **Cbppp** were synthesised. The identity and purity of **Chppp** was confirmed with ^1H and ^{13}C NMR spectroscopy, HRMS, and EA, as well as X-ray crystallography studies of the single crystals that were obtained. As well, one route leading to **Chppp** produced doubly carbamated **Cchpp**, which was characterised by NMR spectroscopy, HRMS, as well as EA. The compound **Cbppp** was analysed by ^1H , ^{13}C NMR spectroscopy, HRMS, and the purity was established by HPLC studies. It was determined that the second generation compounds **Chpp** and **Cbppp** act as reversible inhibitors of AChE during the time scale of the experiment. Their IC_{50} values, kinetic profiles, and drug activation with *eel*AChE were established in *in vitro* studies, and it was observed that the inhibitory activity does not improve on that of the first generation compound **Hppp**. However, it was noted that the activity of these compounds improves over the carbamated fragment C-pcresol.

5.4 Conclusions

In summary, a novel function, the acetylcholinesterase activity of HPO compounds, was established in *eel*AChE. It was observed that the novel carbamated compound **Cppp** had improved inhibitory activity over the parent compound **Hppp**, although the activity of the former was reversible and the metal binder was not released in the inhibitory process. The second attempt to improve activity of **Hppp** yielded two frameworks, from which model compounds **Chpp** and **Cbppp** were chosen for synthesis and characterisation. These compounds were also determined to be reversible inhibitors that were not activated by the enzyme. Overall, **Cppp** had the highest acetylcholinesterase activity of all HPOs studied.

Chapter 6: Conclusions and future work

6.1 General comments

The prevalence and economic impact of Alzheimer's and other neurodegenerative diseases continue to grow as our ever-increasing population ages. The pressure to discover a therapeutic agent intensifies with failing clinical trials and our continuing inability to definitively diagnose and prevent Alzheimer's disease (AD). While our incomplete understanding of neurodegenerative disease initiation and progression is a barrier to our ability to treat it, certain relevant avenues of research have gained traction in recent years, prompting extensive study of chelating ligands from various structural families.

Although the metal binding properties across the majority of these compounds are strikingly similar, only one family of metal binding agents, that of PBT2 (5,7-dichloro-2-((dimethylamino)methyl)-8-hydroxyquinoline) (Figure 1.6), is currently in clinical trials for treatment of Alzheimer's and Huntington's diseases (see Chapter 1). The so-far successful development of this member of the hydroxyquinoline family is in part explained by its ability to bind excess Cu(II) and Zn(II) ions in the brain, thus diminishing the amount of amyloid plaque formation and relocating these metal ions to depleted compartments.⁵⁷ The theory on which the mode of action of this metal chaperone relies is the amyloid hypothesis,¹⁵⁶ which postulates that the aggregation of amyloid- β ($A\beta$) into plaques is the cause of Alzheimer's disease.¹⁵⁶ While no drug based on this hypothesis has been successful in clinical trials,¹⁵⁷ it remains a major force behind academic and industrial efforts.¹⁵⁸ The challenges on the clinical front come in part from the fact that these trials are conducted for short periods of time on patients with advanced dementia, and it may be that these are not the optimal conditions for assessment of AD

therapeutics. Another reason may be the multifactorial nature of this disease. For example, Cu(II), Zn(II), and Fe(III), which are found in brain plaques in increased concentrations,¹⁵⁹ play a dual role in AD – they are believed not only to expedite the aggregation of amyloid protein, but also to contribute to toxicity of the amyloid plaques in part by increasing the production of ROS.⁶ The deleterious role of metal ions provides the rationale behind the clinical candidate PBT2.

The complex nature of this disease, in which a myriad of biochemical changes in the brain ultimately leads to neuronal loss, may arise from a yet unknown cause, of which amyloid cascade is a downstream part (Figure 6.1).¹⁶⁰ Thus, tackling several of the pathological features may be advantageous in solving this multifactorial disease.

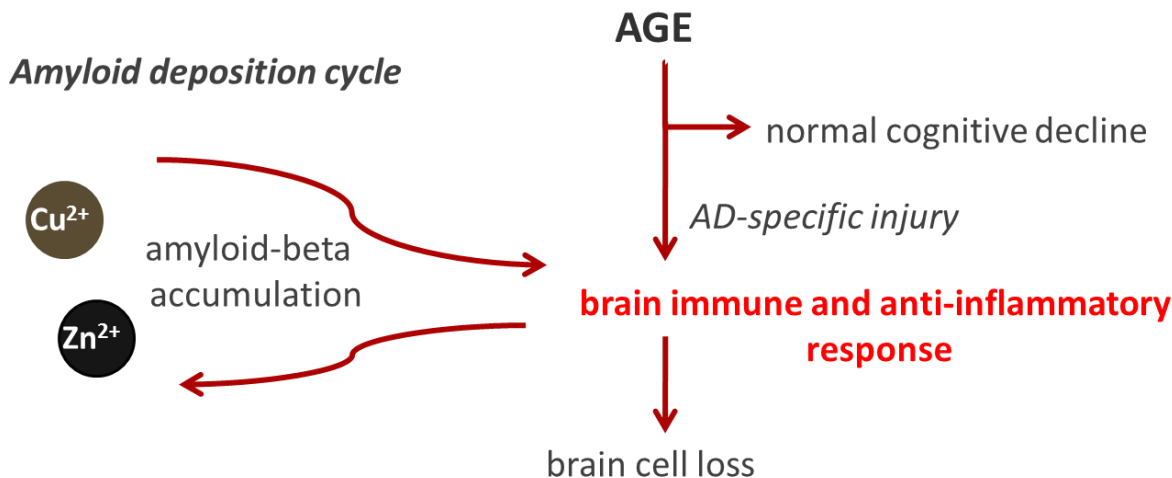


Figure 6.1 Age-based hypothesis for AD (adapted from ref. 160).

6.2 Conclusions from this body of work

Accordingly, this thesis presented a library of metal binders that were designed for addressing the multiple factors of Alzheimer's disease. Five novel 3-hydroxy-4-pyridinone compounds with benzoxazole and benzothiazole functionalities, fifteen metal complexes, and four carbamate derivatives were synthesised and structurally characterised by standard methods.

6.2.1 Multifunctional HPO scaffold

As was envisioned, the HPO scaffold combined within it multiple functionalities. It was established that amyloid- and metal-binding functionalities were compatible within the scaffold. As well, the compounds retained moderate to high radical quenching ability, and were found to permeate through a cell membrane as an initial measure of BBB permeability. A possible point for concern that future work can address is the toxicity of the ligands, as well as the toxicity of the amyloid species created through the binding interaction.

6.2.2 Enzyme activity

Through masking the hydroxyl group of the HPO scaffold, the carbamoyl group effectively prevented metal ion binding of the compounds. It was found that these compounds have reversible acetylcholinesterase inhibitory activity. As the compounds did not release metal binding functionality, future designs can address this point.

6.3 Future work

As the work presented here is comprised of thorough fundamental research studies of the library of HPO compounds, future work will entail further *in vitro* and *in vivo* studies to determine the efficacy of these compounds in biological systems that mimic AD states.

6.3.1 A β interaction

For future work, interaction with A β_{1-42} should be considered, as it is the more toxic form of the protein in AD.

First, binding studies with A β_{1-42} can be performed with compounds **Hpbt2p** and **Hpbo2p**, as they are excited at a longer wavelength than **Hmbo2p**; therefore, direct binding studies can be done. This way the impact of one atom between the two compounds (oxygen and sulfur) on the binding may be examined. Secondly, TEM studies with A β_{1-42} can be performed as well to investigate morphological changes upon binding of compounds to the protein. Also of interest is the cytotoxic effect ligand interaction may have on A β ; the studies to address this point are outlined in Chapter 6.3.3, below.

6.3.2 BBB permeability studies

Continuing the development of an *in vitro* model of BBB penetration with the bEnd.3 cell line is required in order to screen compounds before going to *in vivo* studies. The setup of this experiment involves the use of radioactive compounds. HPOs have been radiolabeled previously,⁵⁸ but the process was laborious and the installment of the iodine modified the compound. Development of an easier iodination route was attempted by the author of this thesis,

but the work was not successful. In further work, labelling studies may shift to other radioactive elements, such as isotopes of carbon that may be used to install a handle for measuring concentration of all HPOs without modifying them significantly. Alternatively, other assays to determine concentration during cell permeability may be considered.

6.3.3 Cytotoxicity

One consideration for future studies of cytotoxicity is working with different cell lines. As well, cytotoxicity in the presence of $A\beta_{1-42}$ and metal ions is important to establish. This has been done with alamarBlue® assay¹⁶¹ that was shown to be better than the MTT assay used herein for pro-ligands and metal complexes as $A\beta$ toxicity is different to that resulting from ligand-based interactions.¹⁶² This assay takes advantage of viable, non-damaged cells converting blue compound 7-hydroxy-3H-phenoxazin-3-one-10-oxide into a red-fluorescing compound 7-hydroxy-3H-phenoxazin-3-one.

Bibliography

- (1) Williams, R. J. P. *Q. Rev. Chem. Soc.* **1970**, *24*, 331–365.
- (2) Williams, D. R. *Chem. Rev.* **1972**, *72*, 203–213.
- (3) Orvig, C.; Abrams, M. J. *Chem. Rev.* **1999**, *99*, 2201–2204.
- (4) Holm, R. H.; Kennepohl, P.; Solomon, E. I. *Chem. Rev.* **1996**, *96*, 2239–2314.
- (5) Frederickson, C. J.; Koh, J.-Y.; Bush, A. I. *Nat. Rev. Neurosci.* **2005**, *6*, 449–462.
- (6) Bush, A. I.; Tanzi, R. E. *Neurotherapeutics* **2008**, *5*, 421–432.
- (7) Jamieson, E. R.; Lippard, S. J. *Chem. Rev.* **1999**, *99*, 2467–2498.
- (8) Liu, S. *Chem. Soc. Rev.* **2004**, *33*, 445–461.
- (9) Alzheimer's Association. *Alzheimer's and Dementia: The Journal of the Alzheimer's Association* **2012**, *8*, 131–168.
- (10) World Health Organization. *Dementia - a public health priority. United Kingdom* **2012**.
- (11) Giacobini, E. *Ann. N.Y. Acad. Sci.* **2006**, *920*, 321–327.
- (12) Samii, A.; Nutt, J. G.; Ransom, B. R. *Lancet* **2004**, *363*, 1783–1793.
- (13) Rodríguez-Rodríguez, C.; Telpoukhovskaia, M.; Orvig, C. *Coord. Chem. Rev.* **2012**, *256*, 2308–2332.
- (14) Scott, L. E.; Orvig, C. *Chem. Rev.* **2009**, *109*, 4885–4910.
- (15) Guilloreau, L.; Combalbert, S.; Sournia-Saquet, A.; Mazarguil, H.; Faller, P. *Chembiochem* **2007**, *8*, 1317–1325.
- (16) Connor, J. R.; Snyder, B. S.; Arosio, P.; Loeffler, D.; LeWitt, P. *J. Neurochem.* **1995**, *65*, 717–724.
- (17) Prusiner, S. B. *Proc. Natl. Acad. Sci. U. S. A.* **1998**, *95*, 13363–13383.
- (18) Arena, G.; La Mendola, D.; Pappalardo, G.; Sóvágó, I.; Rizzarelli, E. *Coord. Chem. Rev.* **2012**, *256*, 2202–2218.

- (19) Kang, J.; Lemaire, H. G.; Unterbeck, A.; Salbaum, J. M.; Masters, C. L.; Grzeschik, K. H.; Multhaup, G.; Beyreuther, K.; Müller-Hill, B. *Nature* **1987**, *325*, 733–736.
- (20) Kong, G. K.-W.; Adams, J. J.; Harris, H. H.; Boas, J. F.; Curtain, C. C.; Galatis, D.; Masters, C. L.; Barnham, K. J.; McKinstry, W. J.; Cappai, R.; Parker, M. W. *J. Mol. Biol.* **2007**, *367*, 148–161.
- (21) Barnham, K. J.; McKinstry, W. J.; Multhaup, G.; Galatis, D.; Morton, C. J.; Curtain, C. C.; Williamson, N.; White, A. R.; Hinds, M. G.; Norton, R. S.; Beyreuther, K.; Masters, C. L.; Parker, M. W.; Cappai, R. *J. Biol. Chem.* **2003**, *278*, 17401–17407.
- (22) Dahms, S. O.; Könnig, I.; Roeser, D.; Gührs, K.-H.; Mayer, M. C.; Kaden, D.; Multhaup, G.; Than, M. E. *J. Mol. Biol.* **2012**, *416*, 438–452.
- (23) Bush, A. I.; Multhaup, G.; Moir, R. D.; Williamson, T. G.; Small, D. H.; Rumble, B.; Pollwein, P.; Beyreuther, K.; Masters, C. L. *J. Biol. Chem.* **1993**, *268*, 16109–16112.
- (24) Duce, J.; Tsatsanis, A.; Cater, M.; James, S.; Robb, E.; Wikhe, K.; Leong, S. L.; Perez, K.; Johanssen, T.; Greenough, M.; Cho, H.-H.; Galatis, D.; Moir, R. D.; Masters, C. L.; McLean, C.; Tanzi, R. E.; Cappai, R.; Barnham, K. J.; Ciccotosto, G. D.; Rogers, J. T.; Bush, A. I. *Cell* **2010**, *142*, 857–867.
- (25) Minicozzi, V.; Stellato, F.; Comai, M.; Dalla Serra, M.; Potrich, C.; Meyer-Klaucke, W.; Morante, S. *J. Biol. Chem.* **2008**, *283*, 10784–10792.
- (26) Hureau, C.; Balland, V.; Coppel, Y.; Solari, P. L.; Fonda, E.; Faller, P. *J. Biol. Inorg. Chem.* **2009**, *14*, 995–1000.
- (27) Drew, S. C.; Noble, C. J.; Masters, C. L.; Hanson, G. R.; Barnham, K. J. *J. Am. Chem. Soc.* **2009**, *131*, 1195–1207.
- (28) Drew, S. C.; Masters, C. L.; Barnham, K. J. *J. Am. Chem. Soc.* **2009**, *131*, 8760–8761.
- (29) Dorlet, P.; Gambarelli, S.; Faller, P.; Hureau, C. *Angew. Chem., Int. Ed.* **2009**, *48*, 9273–9276.
- (30) Zawisza, I.; Rózga, M.; Bal, W. *Coord. Chem. Rev.* **2012**, *256*, 2297–2307.
- (31) Gaggelli, E.; Janicka-Klos, A.; Jankowska, E.; Kozłowski, H.; Migliorini, C.; Molteni, E.; Valensin, D.; Valensin, G.; Wiczerzak, E. *J. Phys. Chem. B* **2008**, *112*, 100–109.
- (32) Bousejra-ElGarah, F.; Bijani, C.; Coppel, Y.; Faller, P.; Hureau, C. *Inorg. Chem.* **2011**, *50*, 9024–9030.

- (33) Valensin, D.; Migliorini, C.; Valensin, G.; Gaggelli, E.; La Penna, G.; Kozłowski, H.; Gabbiani, C.; Messori, L. *Inorg. Chem.* **2011**, *50*, 6865–6867.
- (34) Jackson, M. S.; Lee, J. C. *Inorg. Chem.* **2009**, *48*, 9303–9307.
- (35) Rasia, R. M.; Bertoncini, C. W.; Marsh, D.; Hoyer, W.; Cherny, D.; Zweckstetter, M.; Griesinger, C.; Jovin, T. M.; Fernández, C. O. *Proc. Natl. Acad. Sci. U. S. A.* **2005**, *102*, 4294–4299.
- (36) Valensin, D.; Camponeschi, F.; Luczkowski, M.; Baratto, M. C.; Remelli, M.; Valensin, G.; Kozłowski, H. *Metallomics* **2011**, *3*, 292–302.
- (37) Binolfi, A.; Lamberto, G. R.; Duran, R.; Quintanar, L.; Bertoncini, C. W.; Souza, J. M.; Cerveñansky, C.; Zweckstetter, M.; Griesinger, C.; Fernández, C. O. *J. Am. Chem. Soc.* **2008**, *130*, 11801–11812.
- (38) Binolfi, A.; Quintanar, L.; Bertoncini, C. W.; Griesinger, C.; Fernández, C. O. *Coord. Chem. Rev.* **2012**, *256*, 2188–2201.
- (39) Chattopadhyay, M.; Walter, E. D.; Newell, D. J.; Jackson, P. J.; Aronoff-Spencer, E.; Peisach, J.; Gerfen, G. J.; Bennett, B.; Antholine, W. E.; Millhauser, G. L. *J. Am. Chem. Soc.* **2005**, *127*, 12647–12656.
- (40) Hornshaw, M. P.; McDermott, J. R.; Candy, J. M.; Lakey, J. H. *Biochem. Biophys. Res. Commun.* **1995**, *214*, 993–999.
- (41) Binolfi, A.; Rasia, R. M.; Bertoncini, C. W.; Ceolin, M.; Zweckstetter, M.; Griesinger, C.; Jovin, T. M.; Fernández, C. O. *J. Am. Chem. Soc.* **2006**, *128*, 9893–9901.
- (42) Jackson, G. S.; Murray, I.; Hosszu, L. L.; Gibbs, N.; Waltho, J. P.; Clarke, R.; Collinge, J. *Proc. Natl. Acad. Sci. U. S. A.* **2001**, *98*, 8531–8535.
- (43) Gralka, E.; Valensin, D.; Porciatti, E.; Gajda, C.; Gaggelli, E.; Valensin, G.; Kamysz, W.; Nadolny, R.; Guerrini, R.; Bacco, D.; Remelli, M.; Kozłowski, H. *Dalton Trans.* **2008**, 5207–5219.
- (44) Cherny, R. A.; Legg, J. T.; Mclean, C. A.; Fairlie, D. P.; Huang, X.; Atwood, C. S.; Beyreuther, K.; Tanzi, R. E.; Masters, C. L.; Bush, A. I. *Biochemistry* **1999**, *274*, 23223–23228.
- (45) Zhang, Y.; Chen, L.-Y.; Yin, W.-X.; Yin, J.; Zhang, S.-B.; Liu, C.-L. *Dalton Trans.* **2011**, *40*, 4830–4833.
- (46) Lakatos, A.; Zsigó, E.; Hollender, D.; Nagy, N. V.; Fülöp, L.; Simon, D.; Bozsó, Z.; Kiss, T. *Dalton Trans.* **2010**, *39*, 1302–1315.

- (47) Romary, J. K.; Barger, J. D.; Bunds, J. E. *Inorg. Chem.* **1968**, *7*, 1142–1145.
- (48) Sharma, A. K.; Pavlova, S. T.; Kim, J.; Finkelstein, D.; Hawco, N. J.; Rath, N. P.; Kim, J.; Mirica, L. M. *J. Am. Chem. Soc.* **2012**, *134*, 6625–6636.
- (49) Folk, D. S.; Franz, K. J. *J. Am. Chem. Soc.* **2010**, *132*, 4994–4995.
- (50) Ritchie, C. W.; Bush, A. I.; Mackinnon, A.; Macfarlane, S.; Mastwyk, M.; MacGregor, L.; Kiers, L.; Cherny, R.; Li, Q.-X.; Tammer, A.; Carrington, D.; Mavros, C.; Volitakis, I.; Xilinas, M.; Ames, D.; Davis, S.; Beyreuther, K.; Tanzi, R. E.; Masters, C. L. *Arch. Neurol.* **2003**, *60*, 1685–1691.
- (51) Deraeve, C.; Boldron, C.; Maraval, A.; Mazarguil, H.; Gornitzka, H.; Vendier, L.; Pitié, M.; Meunier, B. *Eur. J. Inorg. Chem.* **2008**, *14*, 6826–6896.
- (52) Rodríguez-Rodríguez, C.; Sánchez De Groot, N.; Rimola, A.; Alvarez-Larena, A.; Lloveras, V.; Vidal-Gancedo, J.; Ventura, S.; Vendrell, J.; Sodupe, M.; González-Duarte, P. *J. Am. Chem. Soc.* **2009**, *131*, 1436–1451.
- (53) Vaira, M. Di; Bazzicalupi, C.; Orioli, P. *Inorg. Chem.* **2004**, *43*, 3795–3797.
- (54) Budimir, A.; Humbert, N.; Elhabiri, M.; Osinska, I.; Biruš, M.; Albrecht-Gary, A.-M. *J. Inorg. Biochem.* **2011**, *105*, 490–496.
- (55) Adlard, P.; Cherny, R.; Finkelstein, D.; Gautier, E.; Robb, E.; Cortes, M.; Volitakis, I.; Liu, X.; Smith, J. P.; Perez, K.; Laughton, K.; Li, Q.-X.; Charman, S.; Nicolazzo, J.; Wilkins, S.; Deleva, K.; Lynch, T.; Kok, G.; Ritchie, C. W.; Tanzi, R. E.; Cappai, R.; Masters, C. L.; Barnham, K. J.; Bush, A. I. *Neuron* **2008**, *59*, 43–55.
- (56) Prana Biotechnology. Limited, *Prana Doses First Patient in the “IMAGINE” Phase II Alzheimer’s Disease Trial; FDA Approval to Commence Huntington’s Disease Clinical Trial Using Prana’s PBT2*, 2012, media releases, accessed 3 June 2012, [http://www.pranabio.com/downloads/Media Releases/Media Releases 2012/March 6 2012 First patient dosing IMAGINE trial.pdf](http://www.pranabio.com/downloads/Media%20Releases/Media%20Releases%202012/March%206%202012%20First%20patient%20dosing%20IMAGINE%20trial.pdf), [http://www.pranabio.com/downloads/Media Releases/Media Releases 2012/January 4 2012 PR IND final \(3\).pdf](http://www.pranabio.com/downloads/Media%20Releases/Media%20Releases%202012/January%204%202012%20PR%20IND%20final%20(3).pdf).
- (57) Crouch, P. J.; Savva, M. S.; Hung, L. W.; Donnelly, P. S.; Mot, A. I.; Parker, S. J.; Greenough, M.; Volitakis, I.; Adlard, P.; Cherny, R.; Masters, C. L.; Bush, A. I.; Barnham, K. J.; White, A. R. *J. Neurochem.* **2011**, *119*, 220–230.
- (58) Scott, L. E.; Telpoukhovskaia, M.; Rodríguez-Rodríguez, C.; Merkel, M.; Bowen, M. L.; Page, B. D. G.; Green, D. E.; Storr, T.; Thomas, F.; Allen, D. D.; Lockman, P. R.; Patrick, B. O.; Adam, M. J.; Orvig, C. *Chem. Sci.* **2011**, *2*, 642–648.

- (59) He, X.; Park, H. M.; Hyung, S.-J.; Detoma, A. S.; Kim, C.; Ruotolo, B. T.; Lim, M. H. *Dalton Trans.* **2012**, *41*, 6558–6566.
- (60) Storr, T.; Merkel, M.; Song-Zhao, G. X.; Scott, L. E.; Green, D. E.; Bowen, M. L.; Thompson, K. H.; Patrick, B. O.; Schugar, H. J.; Orvig, C. *J. Am. Chem. Soc.* **2007**, *129*, 7453–7463.
- (61) Galanello, R. *Ther. Clin. Risk Manag.* **2007**, *3*, 795–805.
- (62) Dobbin, P. S.; Hider, R. C.; Hall, A. D.; Taylor, P. D.; Sarpong, P.; Porter, J. B.; Xiao, G.; Van der Helm, D. *J. Med. Chem.* **1993**, *36*, 2448–2458.
- (63) Nurchi, V. M.; Crisponi, G.; Pivetta, T.; Donatoni, M.; Remelli, M. *J. Inorg. Biochem.* **2008**, *102*, 684–692.
- (64) Jakusch, T.; Gajda-Schranz, K.; Adachi, Y.; Sakurai, H.; Kiss, T.; Horváth, L. *J. Inorg. Biochem.* **2006**, *100*, 1521–1526.
- (65) Motekaitis, R. J.; Rogers, B. E.; Reichert, D. E.; Martell, A. E.; Welch, M. J. *Inorg. Chem.* **1996**, *35*, 3821–3827.
- (66) Kodama, M.; Kimura, E. *Dalton Trans.* **1977**, 2269–2276.
- (67) Pujol, A. M.; Gateau, C.; Lebrun, C.; Delangle, P. *J. Am. Chem. Soc.* **2009**, *131*, 6928–6929.
- (68) DeToma, A. S.; Choi, J.-S.; Braymer, J. J.; Lim, M. H. *ChemBioChem* **2011**, *12*, 1198–1201.
- (69) Chen, T.; Wang, X.; He, Y.; Zhang, C.; Wu, Z.; Liao, K.; Wang, J.; Guo, Z. *Inorg. Chem.* **2009**, *48*, 5801–5819.
- (70) Kaur, D.; Yantiri, F.; Rajagopalan, S.; Kumar, J.; Mo, J. Q.; Boonplueang, R.; Viswanath, V.; Jacobs, R.; Yang, L.; Beal, M. F. *Neuron* **2003**, *37*, 899–909.
- (71) Turnquist, T. D.; Sandell, E. B. *Anal. Chim. Acta* **1968**, *42*, 239–245.
- (72) Treiber, C.; Simons, A.; Multhaup, G. *Biochemistry* **2006**, *45*, 6674–6680.
- (73) Kawahara, M.; Koyama, H.; Nagata, T.; Sadakane, Y. *Metallomics* **2011**, *3*, 726–734.
- (74) Arbiser, J. L.; Kraeft, S. K.; Van Leeuwen, R.; Hurwitz, S. J.; Selig, M.; Dickersin, G. R.; Flint, A.; Byers, H. R.; Chen, L. B. *Mol. Med. (Manhasset, NY, U. S.)* **1998**, *4*, 665–670.
- (75) Santos, M. A. *Coord. Chem. Rev.* **2008**, *252*, 1213–1224.

- (76) Chaves, S.; Marques, S. M.; Matos, A. M. F.; Nunes, A.; Gano, L.; Tuccinardi, T.; Martinelli, A.; Santos, M. A. *Chem. Eur. J.* **2010**, *16*, 10535–10545.
- (77) Santos, M. A.; Marques, S. M.; Chaves, S. *Coord. Chem. Rev.* **2012**, *256*, 240–259.
- (78) Santos, M. A.; Gil, M.; Gano, L.; Chaves, S. *J. Biol. Inorg. Chem.* **2005**, *10*, 564–580.
- (79) Schlindwein, W.; Waltham, E.; Burgess, J.; Binsted, N.; Nunes, A.; Leite, A.; Rangel, M. *Dalton Trans.* **2006**, 1313–1321.
- (80) Schugar, H.; Green, D. E.; Bowen, M. L.; Scott, L. E.; Storr, T.; Böhmerle, K.; Thomas, F.; Allen, D. D.; Lockman, P. R.; Merkel, M.; Thompson, K. H.; Orvig, C. *Angew. Chem. Int. Ed.* **2007**, *119*, 1746–1748.
- (81) Petrović Peroković, V.; Prugovečki, B.; Car, Ž. *Croat. Chem. Acta* **2013**, *86*, 317–323.
- (82) Sigma. Maltol <http://www.sigmaaldrich.com/catalog/product/aldrich/w265608?lang=en®ion=CA> (accessed Jan 22, 2014).
- (83) Saghaie, L.; Sadeghi, M. M.; Nikazma, A. *Res. Pharm. Sci.* **2006**, *1*, 40–48.
- (84) Nunes, A.; Marques, S. M.; Quintanova, C.; Silva, D. F.; Cardoso, S. M.; Chaves, S.; Santos, M. A. *Dalton Trans.* **2013**, *42*, 6058–6073.
- (85) Bar-On, P.; Millard, C. B.; Harel, M.; Dvir, H.; Enz, A.; Sussman, J. L.; Silman, I. *Biochemistry* **2002**, *41*, 3555–3564.
- (86) Abbott, N. J.; Patabendige, A. A. K.; Dolman, D. E. M.; Yusof, S. R.; Begley, D. J. *Neurobiol. Dis.* **2010**, *37*, 13–25.
- (87) Zhang, Z.; Rettig, S. J.; Orvig, C. *Inorg. Chem.* **1991**, *30*, 509–515.
- (88) Green, D. E.; Bowen, M. L.; Scott, L. E.; Storr, T.; Merkel, M.; Böhmerle, K.; Thompson, K. H.; Patrick, B. O.; Schugar, H. J.; Orvig, C. *Dalton Trans.* **2010**, *39*, 1604–1615.
- (89) Scott, L. E.; Page, B. D. G.; Patrick, B. O.; Orvig, C. *Dalton Trans.* **2008**, 6364–6367.
- (90) Nordberg, A.; Rinne, J. O.; Kadir, A.; Långström, B. *Nat. Rev. Neurol.* **2010**, *6*, 78–87.
- (91) Leeson, P. *Nature* **2012**, *481*, 455–456.
- (92) Clark, D. E.; Pickett, S. D. *Drug Discovery Today* **2000**, *5*, 49–58.
- (93) Hutchinson, I.; Jennings, S.; Vishnuvajjala, B. R.; Westwell, A. D.; Stevens, M. F. G. *J. Med. Chem.* **2002**, *45*, 744–747.

- (94) Aiello, S.; Wells, G.; Stone, E. L.; Kadri, H.; Bazzi, R.; Bell, D. R.; Stevens, M. F. G.; Matthews, C. S.; Bradshaw, T. D.; Westwell, A. D. *J. Med. Chem.* **2008**, *51*, 5135–5139.
- (95) Zhang, Z.; Rettig, S. J.; Orvig, C. *Can. J. Chem.* **1992**, *70*, 763–770.
- (96) Barta, C.; Sachs-Barrable, K.; Jia, J.; Thompson, K. H.; Wasan, K. M.; Orvig, C. *Dalton Trans.* **2007**, 5019–5030.
- (97) Molenda, J. J.; Jones, M. M.; Johnston, D. S.; Walker, E. M.; Cannon, D. J. *J. Med. Chem.* **1994**, *37*, 4363–4370.
- (98) Hein, D. W.; Alheim, R. J.; Leavitt, J. J. *J. Am. Chem. Soc.* **1957**, *79*, 427–429.
- (99) Hasegawa, M.; Nishigaki, N.; Washio, Y.; Kano, K.; Harris, P.; Sato, H.; Mori, I.; West, R. I.; Shibahara, M.; Toyoda, H.; Wang, L.; Nolte, R. T.; Veal, J. M.; Cheung, M. *J. Med. Chem.* **2007**, *50*, 4453–4470.
- (100) So, Y.; Heeschen, J. P. *J. Org. Chem.* **1997**, *62*, 3552–3561.
- (101) Telpoukhovskaia, M. A.; Rodríguez-Rodríguez, C.; Cawthray, J. F.; Scott, L. E.; Page, B. D. G.; Alí-Torres, J.; Sodupe, M.; Bailey, G. A.; Patrick, B. O.; Orvig, C. *Metallomics* **2014**, *6*, 249–262.
- (102) SAINT. Version 7.68A. Bruker AXS Inc., Madison, Wisconsin, USA. (1997-2010).
- (103) Bruker AXS Inc., Madison, Wisconsin, U. *SADABS. Bruker Nonius area detector scaling and absorption correction - V2008/1*; 2008.
- (104) Altomare, A.; Burla, M. C.; Camalli, M.; Cascarano, G. L.; Giacovazzo, C.; Guagliardi, A.; Moliterni, A. G.; Polidori, G.; Spagna, R. *J. Appl. Crystallogr.* **1999**, *32*, 115–119.
- (105) HypSpec. Stability Constant Computation Programs.
<http://www.hyperquad.co.uk/HypSpec.htm>.
- (106) Talmard, C.; Bouzan, A.; Faller, P. *Biochemistry* **2007**, *11*, 13658–13666.
- (107) Green, D. E.; Ferreira, C. L.; Stick, R. V.; Patrick, B. O.; Adam, M. J.; Orvig, C. *Bioconjugate Chem.* **2005**, *16*, 1597–1609.
- (108) Nelson, W. O.; Karpishin, T. B.; Rettig, S. J.; Orvig, C. *Can. J. Chem.* **1988**, *66*, 123–131.
- (109) Ahmed, S. I.; Burgess, J.; Fawcett, J.; Parsons, S. A.; Russell, D. R.; Laurie, S. H. *Polyhedron* **2000**, *19*, 129–135.
- (110) Puerta, D. T.; Cohen, S. M. *Inorg. Chem.* **2003**, *42*, 3423–3430.

- (111) Xiao, G.; Van der Helm, D.; Hider, R. C.; Dobbin, P. S. *Dalton Trans.* **1992**, 3265–3271.
- (112) Clarke, E. T.; Martell, A. E.; Reibenspies, J. *Inorg. Chim. Acta* **1992**, *196*, 177–183.
- (113) Alderighi, L.; Gans, P.; Ienco, A.; Peters, D.; Sabatini, A.; Vacca, A. *Coord. Chem. Rev.* **1999**, *184*, 311–318.
- (114) Haeffner, F.; Smith, D. G.; Barnham, K. J.; Bush, A. I. *J. Inorg. Biochem.* **2005**, *99*, 2403–2422.
- (115) Huang, X.; Atwood, C. S.; Hartshorn, M. A.; Multhaup, G.; Goldstein, L. E.; Scarpa, R. C.; Cuajungco, M. P.; Gray, D. N.; Lim, J.; Moir, R. D.; Tanzi, R. E.; Bush, A. I. *Biochemistry* **1999**, *38*, 7609–7616.
- (116) Barnard, P. J.; Bayly, S. R.; Holland, J. P.; Dilworth, J. R.; Waghorn, P. A. *Q. J. Nucl. Med. Mol. Imaging* **2008**, *52*, 235–244.
- (117) Life Technologies. DMEM, high glucose, pyruvate <http://www.lifetechnologies.com/ca/en/home/technical-resources/media-formulation.9.html> (accessed Jan 29, 2014).
- (118) Smith, R. M.; Martell, A. E. *Critical Stability Constants, Vols. 1-6*; Springer US: Boston, MA, 1974.
- (119) Re, R.; Pellegrini, N.; Proteggente, A.; Pannala, A.; Yang, M.; Rice-Evans, C. *Free Radical Biol. Med.* **1999**, *26*, 1231–1237.
- (120) Jones, M. R.; Service, E. L.; Thompson, J. R.; Wang, M. C. P.; Kimsey, I. J.; DeToma, A. S.; Ramamoorthy, A.; Lim, M. H.; Storr, T. *Metallomics* **2012**, *4*, 910–920.
- (121) Lockhart, A.; Ye, L.; Judd, D. B.; Merritt, A. T.; Lowe, P. N.; Morgenstern, J. L.; Hong, G.; Gee, A. D.; Brown, J. J. *Biol. Chem.* **2005**, *280*, 7677–7684.
- (122) Montesano, R.; Pepper, M. S.; Möhle-Steinlein, U.; Risau, W.; Wagner, E. F.; Orci, L. *Cell* **1990**, *62*, 435–445.
- (123) Brown, R. C.; Morris, A. P.; O’Neil, R. G. *Brain Res.* **2007**, *1130*, 17–30.
- (124) Omid, Y.; Campbell, L.; Barar, J.; Connell, D.; Akhtar, S.; Gumbleton, M. *Brain Res.* **2003**, *990*, 95–112.
- (125) Rasband, W. S. *ImageJ*. National Institute of Health.
- (126) Mosmann, T. *J. Immunol. Methods* **1983**, *65*, 55–63.
- (127) Kapuscinski, J. *Biotech. Histochem.* **1995**, *70*, 220–233.

- (128) Van Acker, S. A. B. E.; Van Den Berg, D.; Tromp, M. N. J. L.; Griffioen, D. H.; Van Bennekom, W. P.; Van Der Vijgh, W. J. F.; Bast, A. *Free Radical Biol. Med.* **1996**, *20*, 331–342.
- (129) Marcus, D. L.; Thomas, C.; Rodriguez, C.; Simberkoff, K.; Tsai, J. S.; Strafaci, J.; Freedman, M. L. *Exp. Neurol.* **1998**, *150*, 40–44.
- (130) Miranda, S.; Opazo, C.; Larrondo, L. F.; Muñoz, F. J.; Ruiz, F.; Leighton, F.; Inestrosa, N. C. *Prog. Neurobiol.* **2000**, *62*, 633–648.
- (131) Tian, X.; Schaich, K. M. *J. Agric. Food. Chem.* **2013**, *61*, 5511–5519.
- (132) Ramsaywack, S.; Vogels, C. M.; Ricker, S. L.; Westcott, S. A.; Barclay, L. R. C. *Chem. Res. Toxicol.* **2013**, *26*, 399–409.
- (133) Smith, R. M.; Martell, A. E. *Sci. Total Environ.* **1987**, *64*, 125–147.
- (134) LeVine, H. *Protein Sci.* **1993**, *2*, 404–410.
- (135) National Cancer Institute. Cisplatin <http://www.cancer.gov/cancertopics/druginfo/cisplatin> (accessed Nov 1, 2013).
- (136) Telpoukhovskaia, M. A.; Patrick, B. O.; Rodríguez-Rodríguez, C.; Orvig, C. *Mol. Biosyst.* **2013**, *9*, 792–805.
- (137) Maloň, M.; Trávníček, Z.; Maryško, M.; Zbořil, R.; Mašláň, M.; Marek, J.; Doležal, K.; Rolčík, J.; Kryštof, V.; Strnad, M. *Inorg. Chim. Acta* **2001**, *323*, 119–129.
- (138) Trávníček, Z.; Krystof, V.; Sipl, M. *J. Inorg. Biochem.* **2006**, *100*, 214–225.
- (139) Trávníček, Z.; Popa, I.; Cajan, M.; Zboril, R.; Krystof, V.; Mikulík, J. *J. Inorg. Biochem.* **2010**, *104*, 405–417.
- (140) Puszko, A.; Brzuszkiewicz, A.; Jezierska, J.; Adach, A.; Wietrzyk, J.; Filip, B.; Pełczynska, M.; Cieslak-Golonka, M. *J. Inorg. Biochem.* **2011**, *105*, 1109–1114.
- (141) Afrasiabi, Z.; Stovall, P.; Finley, K.; Choudhury, A.; Barnes, C.; Ahmad, A.; Sarkar, F.; Vyas, A.; Padhye, S. *Spectrochim. Acta, Part A* **2013**, *114C*, 114–119.
- (142) Tan, J.; Wang, B.; Zhu, L. *Bioorg. Med. Chem. Lett.* **2009**, *17*, 614–620.
- (143) Terry, A. V.; Buccafusco, J. J. *J. Pharmacol. Exp. Ther.* **2003**, *306*, 821–827.

- (144) Fernández-Bachiller, M. I.; Pérez, C.; González-Muñoz, G. C.; Conde, S.; López, M. G.; Villarroya, M.; García, A. G.; Rodríguez-Franco, M. I. *J. Med. Chem.* **2010**, *53*, 4927–4937.
- (145) Kochi, A.; Eckroat, T. J.; Green, K. D.; Mayhoub, A. S.; Lim, M. H.; Garneau-Tsodikova, S. *Chem. Sci.* **2013**, *4*, 4137–4145.
- (146) Zheng, H.; Youdim, M. B. H.; Fridkin, M. *ACS Chem. Biol.* **2010**, *5*, 603–610.
- (147) Sheldrick, G. M. *Acta Crystallogr., Sect. A: Found. Crystallogr.* **2008**, *64*, 112–122.
- (148) Harrison, B. A.; Whitlock, N. A.; Voronkov, M. V.; Almstead, Z. Y.; Gu, K.; Mabon, R.; Gardyan, M.; Hamman, B. D.; Allen, J.; Gopinathan, S.; McKnight, B.; Crist, M.; Zhang, Y.; Liu, Y.; Courtney, L. F.; Key, B.; Zhou, J.; Patel, N.; Yates, P. W.; Liu, Q.; Wilson, A. G. E.; Kimball, S. D.; Crosson, C. E.; Rice, D. S.; Rawlins, D. B. *J. Med. Chem.* **2009**, *52*, 6515–6518.
- (149) Ellman, G. L.; Courtney, K. D.; Andres, V.; Featherstone, R. M. *Biochem. Pharmacol.* **1961**, *7*, 88–95.
- (150) Luo, W.; Li, Y.-P.; Tan, J.-H.; Gu, L.-Q.; Huang, Z.-S. *J. Enzyme Inhib. Med. Chem.* **2011**, *26*, 706–711.
- (151) Bisswanger, H. *Enzyme Kinetics*; 2nd ed.; Wiley-VCH Verlag GmbH & Co. KGaA: Weinheim, Germany, 2008.
- (152) Dawson, R. M. *Neurosci. Lett.* **1990**, *118*, 85–87.
- (153) Lineweaver, H.; Burk, D. *J. Am. Chem. Soc.* **1934**, *56*, 658–666.
- (154) Snape, M. F.; Misra, A.; Murray, T. K.; De Souza, R. J.; Williams, J. L.; Cross, A. J.; Green, A. R. *Neuropharmacol.* **1999**, *38*, 181–193.
- (155) Perez, C.; Daniel, K. B.; Cohen, S. M. *ChemMedChem* **2013**, *8*, 1662–1667.
- (156) Hardy, J.; Higgins, G. *Science* **1992**, *256*, 184–185.
- (157) Hardy, J. *J. Neurochem.* **2009**, *110*, 1129–1134.
- (158) Teich, A. F.; Arancio, O. *Biochem. J.* **2012**, *446*, 165–177.
- (159) Lovell, M.; Robertson, J. D.; Teesdale, W. J.; Campbell, J. L.; Markesbery, W. R. *J. Neurol. Sci.* **1998**, *158*, 47–52.
- (160) Herrup, K. *J. Neurosci.* **2010**, *30*, 16755–16762.

- (161) Sharma, A. K.; Pavlova, S. T.; Kim, J.; Kim, J.; Mirica, L. M. *Metallomics* **2013**, *5*, 1529–1536.
- (162) Wogulis, M.; Wright, S.; Cunningham, D.; Chilcote, T.; Powell, K.; Rydel, R. E. *J. Neurosci.* **2005**, *25*, 1071–1080.

Appendices

Appendix A – Crystallographic data

A.1 Novel pro-ligands and their precursors

Table A.1 Crystal and refinement data for Bnma and Bnzapp. Table reproduced by permission of The Royal Society of Chemistry.

crystal data	Bnma	Bnzapp
formula	C ₁₃ H ₁₂ O ₃	C ₁₉ H ₁₈ N ₂ O ₂
Fw	216.23	306.35
crystal system	orthorhombic	monoclinic
space group	<i>Pbca</i>	<i>P2₁/c</i>
a (Å)	12.1889(5)	8.8050(8)
b (Å)	8.9564(4)	18.358(2)
c (Å)	20.1062(9)	9.8145(8)
α (deg)	90	90
β (deg)	90	92.016(5)
γ (deg)	90	90
V [Å ³]	2195.0(2)	1585.5(2)
Temp (K)	100.0(2)	100.0(2)
Z	8	4
D _{calcd} [g/cm ³]	1.309	1.283
μ (Mo Kα) [cm ⁻¹]	0.93	0.84
F ₀₀₀	912.00	648.00
θ _{min} -θ _{max} (deg)	2.63-30.03	2.31-25.30
<i>hkl</i> range	-16/17,-12/12,-26/28	-10/10,-22/22,-11/11
reflections collected	21800	21917
Independent reflections (R _{int})	3208 (0.032)	2909 (0.066)
observed reflection [I>2s(I)]	2586	1812
agreement indexes [I>2s(I)]	R(F) = 0.038 R _w (F ²) = 0.094	R(F) = 0.043 R _w (F ²) = 0.090
agreement indexes (all data)	R(F) = 0.052 R _w (F ²) = 0.102	R(F) = 0.094 R _w (F ²) = 0.110
GOF (all data)	1.02	1.04

Table A.2 Crystal and refinement data for Hmbo2p, Hmbt2p, and Habt6p. Table reproduced by permission of The Royal Society of Chemistry.

crystal data	Hmbo2p	Hmbt2p • MeOH	Habt6p
formula	C ₁₄ H ₁₂ N ₂ O ₃	C ₁₅ H ₁₆ N ₂ O ₃ S	C ₁₃ H ₁₁ N ₃ O ₂ S
Fw	256.26	304.36	273.31
crystal system	triclinic	monoclinic	triclinic
space group	<i>P</i> -1	<i>P</i> 2 ₁ / <i>c</i>	<i>P</i> -1
a (Å)	7.1289(9)	12.0704(6)	7.5968(2)
b (Å)	7.144(1)	8.6513(4)	8.3252(2)
c (Å)	13.037(2)	14.2450(7)	11.0399(3)
α (deg)	82.538(4)	90	97.196(2)
β (deg)	83.524(4)	107.286(1)	108.876(2)
γ (deg)	61.968(4)	90	110.229(2)
V [Å ³]	580.1(2)	1420.3(1)	597.40(3)
Temp (K)	100.0(2)	100.0(2)	90.0(1)
Z	2	4	2
D _{calcd} [g/cm ³]	1.467	1.423	1.519
μ (Mo Kα) [cm ⁻¹]	1.05	2.40	2.72
F ₀₀₀	268.00	640.00	284.00
θ _{min} -θ _{max} (deg)	3.16-28.36	2.79-30.21	2.93-23.84
<i>hkl</i> range	-9/9,-9/9,-17/17	-17/17,-12/11, -20/19	-8/7,-9/9,0/12
reflections collected	10260	25294	13379
independent	2878 (0.035)	4187 (0.040)	3623 (0.041)
reflections (R _{int})			
observed reflection [I>2s(I)]	2095	3487	2939
agreement indexes [I>2s(I)]	R(F) = 0.044 R _w (F ²) = 0.095	R(F) = 0.034 R _w (F ²) = 0.087	R(F) = 0.053 R _w (F ²) = 0.135
agreement indexes (all data)	R(F) = 0.069 R _w (F ²) = 0.106	R(F) = 0.044 R _w (F ²) = 0.093	R(F) = 0.068 R _w (F ²) = 0.144
GOF (all data)	1.01	1.03	0.99

Table A.3 Selected bond lengths (Å) and angles (°) for **Bnma**, **Bnzapp**, **Hmbo2p**, **Hmbt2p**, and **Habt6p**. Table reproduced by permission of The Royal Society of Chemistry.

Atoms	Bnma (X=O3)	Bnzapp (X=N1)	Habt6p (X=N1)
	Distance (Å)		
C3-O2	1.3766(12)	1.385(3)	1.367(3)
C4-O1	1.2397(13)	1.264(3)	1.273(3)
C2-X	1.3667(12)	1.385(3)	1.401(3)
C2-C3	1.3566(14)	1.366(3)	1.371(3)
C3-C4	1.4603(14)	1.444(3)	1.442(4)
C4-C5	1.4559(15)	1.420(3)	1.441(4)
C5-C6	1.3401(15)	1.352(3)	1.351(3)
C6-X	1.3554(13)	1.366(3)	1.367(3)
Angle (°)			
C8-C7-N1-C6	n/a	-107.8(2)	-71(2)
C12-C7-N1-C6	n/a	72.0(3)	111.3(17)
C12-C7-N1-C2	n/a	-111.6(2)	-81(2)
C8-C7-N1-C2	n/a	68.6(3)	96.4(16)

Atoms	Hmbo2p (X=O3)	Hmbt2p (X=S1)
	Distance (Å)	
C3-O2	1.3626(10)	1.3540(14)
C4-O1	1.2711(10)	1.2719(14)
C2-N1	1.3796(11)	1.3768(15)
C2-C3	1.3736(12)	1.3746(16)
C3-C4	1.4388(12)	1.4401(16)
C4-C5	1.4171(12)	1.4183(16)
C5-C6	1.3565(12)	1.3613(16)
C6-N1	1.3584(11)	1.3587(15)
C7-N1	1.4773(11)	1.4715(15)
C8-C7	1.4877(13)	1.5046(16)
C8-N2	1.289(4)	1.2926(15)
C9-N2	1.453(4)	1.3944(15)
C9-C14	1.3813(13)	1.4074(16)
C14-X	1.364(5)	1.7331(12)
C8-X	1.365(3)	1.7461(12)
Angle (°)		
C8-C7-N1-C6	83.48(10)	104.90(12)
C8-C7-N1-C2	-92.78(10)	2.09(16)
C9-C14-X-C8	3.1(2)	-177.94(12)
C14-C9-N2-C8	0.4(4)	0.48(14)
C10-C9-C14-X	177.67(17)	-179.53(9)
C13-C14-C9-N2	-0.60(14)	177.92(11)

Table A.4 Crystal and refinement data for Hcpp, and Hpbo2p.

crystal data	Hcpp • H ₂ O	Hpbo2p
Formula	C ₁₃ H ₁₃ NO ₅	C ₁₉ H ₁₄ N ₂ O ₃
Fw	263.24	318.32
crystal system	triclinic	monoclinic
space group	<i>P</i> -1	<i>P</i> 2 ₁ / <i>c</i>
a (Å)	7.2778(9)	11.025(1)
b (Å)	7.5001(9)	8.3192(9)
c (Å)	10.7223(13)	16.520(2)
α (deg)	89.697(3)	90
β (deg)	83.948(3)	94.516(5)
γ (deg)	89.066(3)	90
V [Å ³]	581.93(12)	1510.5(3)
Temp (K)	90.0(1)	100.0(1)
Z	2	4
D _{calcd} [g/cm ³]	1.502	1.400
μ (Mo Kα) [cm ⁻¹]	1.17	0.96
F ₀₀₀	276.00	664.00
θ _{min} -θ _{max} (deg)	2.81-30.05	3.08-25.61
<i>hkl</i> range	-10/10,-10/10, -15/14	-13/13,-9/9,- 19/19
reflections collected	19632	10669
independent reflections (R _{int})	3425 (0.037)	2718 (0.056)
observed reflection [I>2s(I)]	2662	2018
agreement indexes [I>2s(I)]	R(F) = 0.039 R _w (F ²) = 0.095	R(F) = 0.060 R _w (F ²) = 0.164
agreement indexes (all data)	R(F) = 0.057 R _w (F ²) = 0.104	R(F) = 0.083 R _w (F ²) = 0.175
GOF (all data)	1.02	1.14

Table A.5 Selected bond lengths (Å) and angles (°) for Hcpp and Hpbo2p.

Atoms	Hcpp	Hpbo2p
	Distance (Å)	
C3-O2	1.3635(13)	1.361(4)
C4-O1	1.2748(13)	1.260(4)
C2-N1	1.3805(14)	1.397(4)
C2-C3	1.3743(15)	1.372(4)
C3-C4	1.4353(15)	1.441(4)
C4-C5	1.4223(16)	1.432(4)
C5-C6	1.3639(15)	1.359(4)
C6-N1	1.3602(14)	1.362(4)
	Angle (°)	
C8-C7-N1-C6	-63.31(14)	-54.6(4)
C12-C7-N1-C6	114.12(12)	123.2(3)
C12-C7-N1-C2	-65.27(14)	-53.5(4)
C8-C7-N1-C2	117.30(12)	128.7(3)

A.2 Metal complexes

Table A.6 Crystal and refinement data for $\text{Zn}(\text{ppp})_2$ and $\text{Fe}(\text{ppp})_3$. Table used with permission from Elsevier.

crystal data	$\text{Zn}_4(\text{ppp})_8(\text{H}_2\text{O})_2$ $(\text{ClO}_4)_2(\text{MeOH})_2$	$\text{Fe}(\text{ppp})_3(\text{H}_2\text{O})_6$
Formula	$\text{C}_{100}\text{H}_{102}\text{N}_8\text{O}_{30}\text{Zn}_4\text{Cl}_2$	$\text{C}_{36}\text{H}_{42}\text{FeN}_3\text{O}_6$
Fw	2228.27	764.58
crystal system	monoclinic	monoclinic
space group	$P 2_1/n$	$P 2_1/n$
a (Å)	9.4434(4)	12.4671(2)
b (Å)	32.509(2)	16.8835(3)
c (Å)	15.6077(7)	34.9820(5)
α (deg)	90	90
β (deg)	95.599(2)	98.786(1)
γ (deg)	90	90
V [Å ³]	4768.6(4)	7276.9(2)
Temp (K)	90.0(1)	90.0(1)
Z	2	8
D_{calcd} [g/cm ³]	1.550	1.396
μ (Mo K α) [cm ⁻¹]	11.38	4.81
F_{000}	2300	3208.00
$\theta_{\text{min}}-\theta_{\text{max}}$ (deg)	2.62-27.86	2.22-26.36
hkl range	-13/11,-45/43, -21/20	-15/15,-21/20,- 43/43
reflections collected	47359	67610
independent reflections (R_{int})	12687 (0.046)	14856 (0.039)
observed reflection [$I > 2s(I)$]	9123	11883
agreement indexes [$I > 2s(I)$]	$R(F) = 0.049$	$R(F) = 0.040$
agreement indexes (all data)	$R_w(F^2) = 0.099$	$R_w(F^2) = 0.085$
	$R(F) = 0.082$	$R(F) = 0.056$
	$R_w(F^2) = 0.110$	$R_w(F^2) = 0.092$
GOF (all data)	1.03	1.03

Table A.7 Selected bond lengths (Å) and angles (°) for Zn(ppp)₂ and Fe(ppp)₃. Table used with permission from Elsevier.

Distance (Å)			
Zn(1)-O(1)	2.0015(19)	Fe(1)-O(1)	2.0726(14)
Zn(1)-O(3)	2.0567(18)	Fe(1)-O(2)	1.9867(15)
Zn(1)-O(4)	2.0507(18)	Fe(1)-O(3)	2.0278(14)
Zn(1)-O(6)	2.0656(17)	Fe(1)-O(4)	2.0068(14)
Zn(1)-O(9)	2.0046(19)	Fe(1)-O(5)	2.0262(15)
Zn(2)-O(4)	2.3671(18)	Fe(1)-O(6)	2.0152(14)
Zn(2)-O(5)	2.0244(17)	Fe(2)-O(7)	2.0414(15)
Zn(2)-O(6)	2.0947(17)	Fe(2)-O(8)	1.9739(14)
Zn(2)-O(8)	2.0917(18)	Fe(2)-O(9)	2.0308(14)
Zn(1)-Zn(2)	3.0326(4)	Fe(2)-O(10)	2.0421(14)
		Fe(2)-O(11)	2.0487(14)
		Fe(2)-O(12)	1.9800(15)

Angle (°)			
O(1)-Zn(1)-O(9)	108.89(8)	O(2)-Fe(1)-O(4)	90.74(6)
O(1)-Zn(1)-O(4)	98.32(7)	O(2)-Fe(1)-O(5)	165.91(6)
O(9)-Zn(1)-O(4)	152.15(8)	O(4)-Fe(1)-O(5)	102.38(6)
O(4)-Zn(1)-O(6)	82.60(7)	O(6)-Fe(1)-O(5)	80.12(6)
O(8)-Zn(2)-O(4)	157.92(6)		
O(6)-Zn(2)-O(4)	74.74(7)		

Table A.8 Crystal and refinement data for Cu(mbt2p)₂, Zn₂(mbt2p)₄, and Fe(mbt2p)₃. Table reproduced by permission of The Royal Society of Chemistry.

crystal data	Cu(mbt2p) ₂	Zn ₂ (mbt2p) ₄ •MeOH	Fe(mbt2p) ₃ •H ₂ O•ACN
Formula	C ₄₂ H ₃₃ N ₆ O ₆ S ₃ Cu _{1.5}	C ₅₇ H ₄₈ N ₈ O ₉ S ₄ Zn ₂	C ₄₄ H ₃₈ N ₇ O ₇ S ₃ Fe
Fw	909.23	1248.01	928.84
crystal system	triclinic	orthorhombic	monoclinic
space group	<i>P</i> -1	<i>Pbca</i>	<i>C</i> 2/ <i>c</i>
a (Å)	12.370(4)	22.4860(7)	15.703(3)
b (Å)	12.679(4)	16.5586(5)	25.796(3)
c (Å)	13.471(4)	28.6689(11)	24.222(3)
α (deg)	62.131(7)	90	90
β (deg)	86.789(9)	90	99.532(3)
γ (deg)	84.702(8)	90	90
V [Å ³]	1860(1)	10674.5(6)	9676(2)
Temp (K)	90.0(2)	90.0(1)	90.0(1)
Z	2	8	8
D _{calcd} [g/cm ³]	1.624	1.553	1.275
μ [cm ⁻¹]	(Cu Kα) 32.02	(Cu Kα) 31.28	(Mo Kα) 4.94
F ₀₀₀	933.00	5136.00	3848.00
θ _{min} -θ _{max} (deg)	25.28-50.56	3.08-65.19	2.45-27.13
<i>hkl</i> range	-13/13,-13/13,-14/14	-23/24,-18/17,-33/33	-20/20,-33/33,-31/31
reflections collected	15353	60460	44564
independent reflections (R _{int})	4690(0.085)	8655(0.079)	10735(0.043)
observed reflection [I>2s(I)]	9555	5535	8060
agreement indexes [I>2s(I)]	R(F) = 0.090 R _w (F ²) = 0.246	R(F) = 0.085 R _w (F ²) = 0.224	R(F) = 0.068 R _w (F ²) = 0.178
agreement indexes (all data)	R(F) = 0.134 R _w (F ²) = 0.304	R(F) = 0.132 R _w (F ²) = 0.258	R(F) = 0.087 R _w (F ²) = 0.188
GOF (all data)	1.08	1.08	1.06

Table A.9 Selected bond lengths (Å) and angles (°) for Cu(mbt2p)₂, Zn₂(mbt2p)₄, and Fe(mbt2p)₃·H₂O·ACN. Table reproduced by permission of The Royal Society of Chemistry.

Atoms	Cu(mbt2p) ₂	Zn ₂ (mbt2p) ₄	Fe(mbt2p) ₃ •H ₂ O•ACN
	Distance (Å)		
C3-O2	1.33(2)	1.336(10)	1.326(4)
C4-O1	1.28(2)	1.279(10)	1.294(4)
C2-N1	1.33(3)	1.382(11)	1.370(4)
C2-C3	1.40(3)	1.392(13)	1.384(4)
C3-C4	1.43(3)	1.442(13)	1.420(5)
C4-C5	1.40(3)	1.410(12)	1.412(4)
C5-C6	1.39(3)	1.357(13)	1.365(4)
C6-N1	1.38(3)	1.345(11)	1.362(4)
C7-N1	1.49(2)	1.462(11)	1.480(4)
C8-C7	1.47(3)	1.509(13)	1.490(5)
C8-N2	1.31(2)	1.295(12)	1.309(4)
C9-N2	1.40(3)	1.399(12)	1.396(5)
C9-C14	1.40(3)	1.408(14)	1.390(5)
C14-S1	1.73(2)	1.724(10)	1.726(4)
C8-S1	1.73(3)	1.749(9)	1.735(4)
O1-M1	1.901(13)	2.029(6)	2.065(2)
O2-M1	1.884(13)	1.982(6)	1.986(2)
	Angle (°)		
O1-M1-O3	172.4(7)	167.2(3)	88.45(9)
O2-M1-O4	175.1(8)	111.2(3)	96.10(10)
O1-M1-O4	95.6(6)	99.2(2)	168.10(10)
O3-M1-O6	n/a	76.2(2)	94.23(13)
C8-C7-N1-C6	81(2)	-96.0(9)	-94.3(4)
C8-C7-N1-C2	-97(2)	78.7(10)	82.2(4)
C9-C14-S1-C8	0.5(13)	-0.5(7)	1.2(3)
C14-C9-N2-C8	-2(2)	0.5(11)	-0.6(4)
C10-C9-C14-S1	178.7(14)	-179.3(8)	177.5(3)
C13-C14-C9-N2	176.9(16)	-179.4(9)	179.8(4)
C3-O2-M1-O1	14.3(16)	6.2(5)	-4.5(2)
C3-O2-M1-O3	-171(1)	-177.7(5)	-91.4(2)
C3-O2-M1-O4	-69(5)	-91.7(5)	-173.0(2)
C3-O2-M1-O6	n/a	102.2(5)	51.2(5)

A.3 Acetylcholinesterase inhibitors and their precursors

Table A.10 Crystal and refinement data for Hppp and Cppp. Table reproduced by permission of The Royal Society of Chemistry.

crystal data	Hppp	Cppp
Formula	C ₁₂ H ₁₁ NO ₂ MeOH	C ₁₅ H ₁₆ N ₂ O ₃
Fw	233.26	272.30
crystal system	triclinic	triclinic
space group	P ₋₁	P ₋₁
a (Å)	7.597(1)	7.9251(4)
b (Å)	9.601(2)	8.3409(4)
c (Å)	9.999(2)	11.1686(6)
α (deg)	100.928(4)	97.746(3)
β (deg)	111.838(3)	110.719(3)
γ (deg)	107.261(3)	95.600(3)
V [Å ³]	608.4(2)	1114.6(2)
Temp (K)	90(1)	100(2)
Z	2	2
D _{calcd} [g/cm ³]	1.273	1.338
μ (Mo Kα) [cm ⁻¹]	0.91	0.94
F ₀₀₀	248	288
θ _{min} -θ _{max} (deg)	2.33-28.78	2.75-28.26
<i>hkl</i> range	-10/10, -12/13, - 13/13	-10/10, -11/10, - 14/14
reflections collected	13793	12110
independent reflections (R _{int})	3135 (0.039)	3322 (0.027)
observed reflection [I>2s(I)]	2250	2665
agreement indexes [I>2s(I)]	R(F) = 0.050 R _w (F ²) = 0.131	R(F) = 0.042 R _w (F ²) = 0.108
agreement indexes (all data)	R(F) = 0.075 R _w (F ²) = 0.147	R(F) = 0.055 R _w (F ²) = 0.118
GOF (all data)	1.04	1.02

Table A.11 Selected bond lengths (Å) and angles (°) for Hppp and Cppp. Table reproduced by permission of The Royal Society of Chemistry.

Hppp		Cppp	
Distance (Å)			
C3-O2	1.353(2)	C3-O2	1.404(1)
C4-O1	1.261(2)	C4-O1	1.252(2)
C2-N1	1.381(2)	C2-N1	1.389(2)
C2-C3	1.368(2)	C2-C3	1.363(2)
C3-C4	1.436(2)	C3-C4	1.447(2)
C4-C5	1.413(2)	C4-C5	1.447(2)
C5-C6	1.357(2)	C5-C6	1.354(2)
C6-N1	1.360(2)	C6-N1	1.373(2)
Angle (°)			
C8-C7-N1-C6	-70.15(19)	C8-C7-N1-C6	104.07(14)
C12-C7-N1-C6	107.45(16)	C12-C7-N1-C6	-75.52(15)
C12-C7-N1-C2	-71.92(19)	C12-C7-N1-C2	101.48(14)
C8-C7-N1-C2	110.48(16)	C8-C7-N1-C2	-78.93(15)

Table A.12 Crystal and refinement data for Hhpp, Bnhpp, and Chpp.

crystal data	Hhpp	Bnhpp	Chpp
Formula	C ₁₂ H ₁₁ NO ₃	C ₁₉ H ₁₇ NO ₃	C ₁₅ H ₁₆ N ₂ O ₄
Fw	217.23	307.34	288.31
crystal system	monoclinic	monoclinic	monoclinic
space group	P 2 ₁ /n	P 2 ₁ /c	P 2 ₁ /c
a (Å)	6.9995(4)	13.1866(10)	12.2747(7)
b (Å)	12.1494(7)	10.9733(8)	8.2453(4)
c (Å)	11.8141(6)	10.6958(8)	13.8197(8)
α (deg)	90	90	90
β (deg)	104.097(1)	104.089(4)	90.651(2)
γ (deg)	90	90	90
V [Å ³]	974.41(9)	1501.1(2)	1398.58(13)
Temp (K)	90.0(1)	90.0(1)	90.0(1)
Z	4	4	4
D _{calcd} [g/cm ³]	1.4806	1.360	1.3691
μ (Mo Kα) [cm ⁻¹]	1.08	7.47	1.01
F ₀₀₀	456.3	648.00	608.3
2θ _{min} -2θ _{max} (deg)	4.88-60.18	3.46-65.4	3.32-60.16
hkl range	-9/9,-17/17,-16/14	-15/13,-9/12, -10/12	-17/17,-11/11,-19/19
reflections collected	19606	8986	26644
independent	2860 (0.0324)	2539 (0.045)	4110 (0.0278)
reflections (R _{int})			
observed reflection [I>2s(I)]	2616	2312	2616
agreement indexes [I>2s(I)]	R(F) = 0.0382	R(F) = 0.036	R(F) = 0.0366
agreement indexes (all data)	R(F) = 0.0417 R _w (F ²) = 0.1085	R(F) = 0.040 R _w (F ²) = 0.098	R(F) = 0.0445 R _w (F ²) = 0.1102
GOF (all data)	1.08	1.05	1.02

Table A.13 Selected bond lengths (Å) and angles (°) for Hhpp, Bnhpp, and Chpp.

Atoms	Hhpp	Bnhpp	Chpp
	Distance (Å)		
C3-O2	1.3561(11)	1.385(3)	1.367(3)
C4-O1	1.2823(10)	1.264(3)	1.273(3)
C2-N1	1.3796(11)	1.385(3)	1.401(3)
C2-C3	1.3783(12)	1.366(3)	1.371(3)
C3-C4	1.4354(12)	1.444(3)	1.442(4)
C4-C5	1.4220(13)	1.420(3)	1.441(4)
C5-C6	1.3664(12)	1.352(3)	1.351(3)
C6-N1	1.3589(12)	1.366(3)	1.367(3)
	Angle (°)		
C8-C7-N1-C6	-116.1(1)	-60.4(1)	64.5(0)
C12-C7-N1-C6	65.8(1)	118.7(8)	-112.7(9)
C12-C7-N1-C2	-108.0(0)	-65.5(3)	65.8(5)
C8-C7-N1-C2	70.0(8)	115.2(6)	-116.8(9)

Appendix B – Compound characterisation

B.1 Novel pro-ligands and their precursors

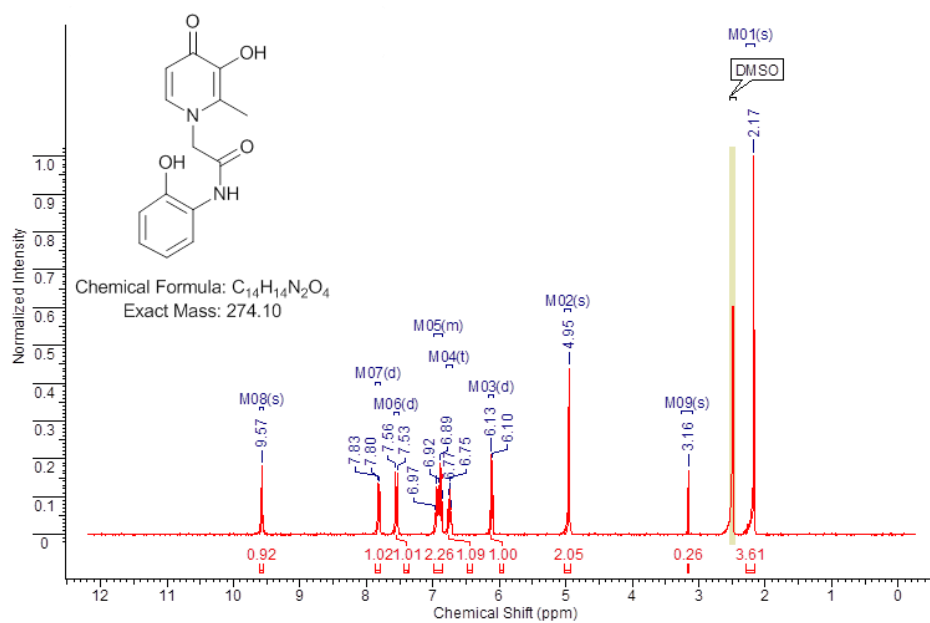


Figure A.1 1H NMR spectrum of reaction intermediate of Hmbo2p (300 MHz, 25 °C, DMSO- d_6).

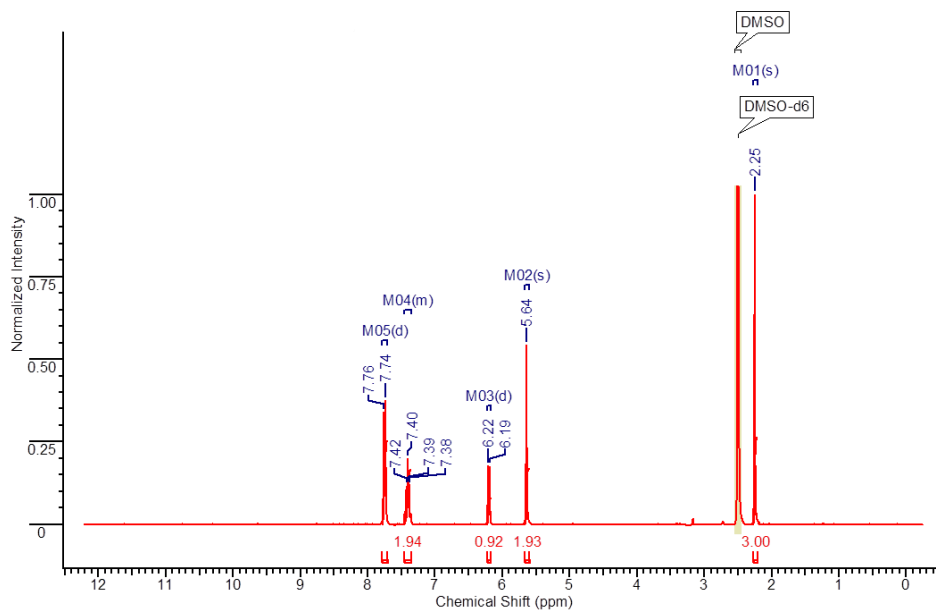


Figure A.2 ^1H NMR spectrum of Hmbo2p (300 MHz, 25 °C, DMSO-d_6). Figure reproduced by permission of The Royal Society of Chemistry.

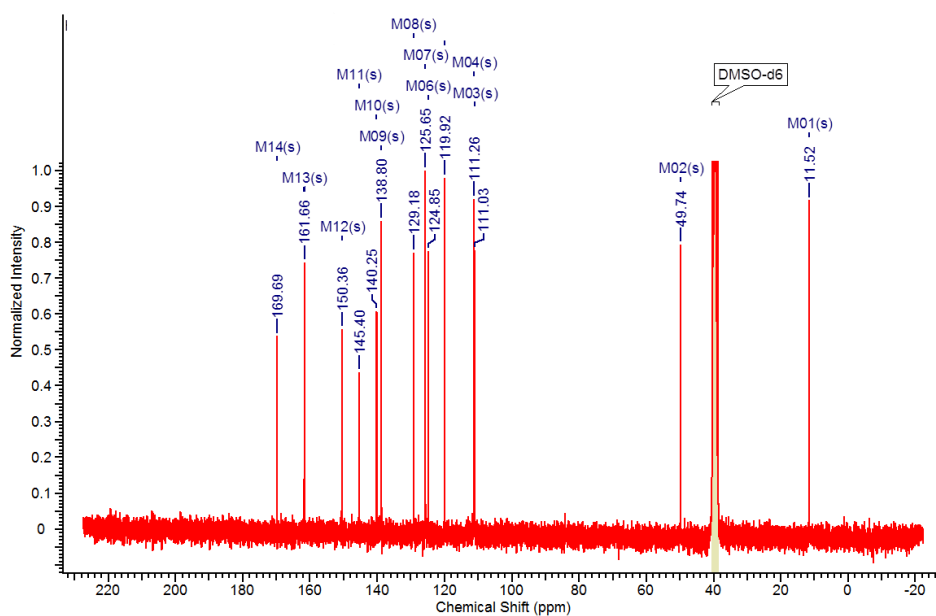


Figure A.3 ^{13}C NMR spectrum of Hmbo2p (75 MHz, 25 °C, DMSO-d_6). Figure reproduced by permission of The Royal Society of Chemistry.

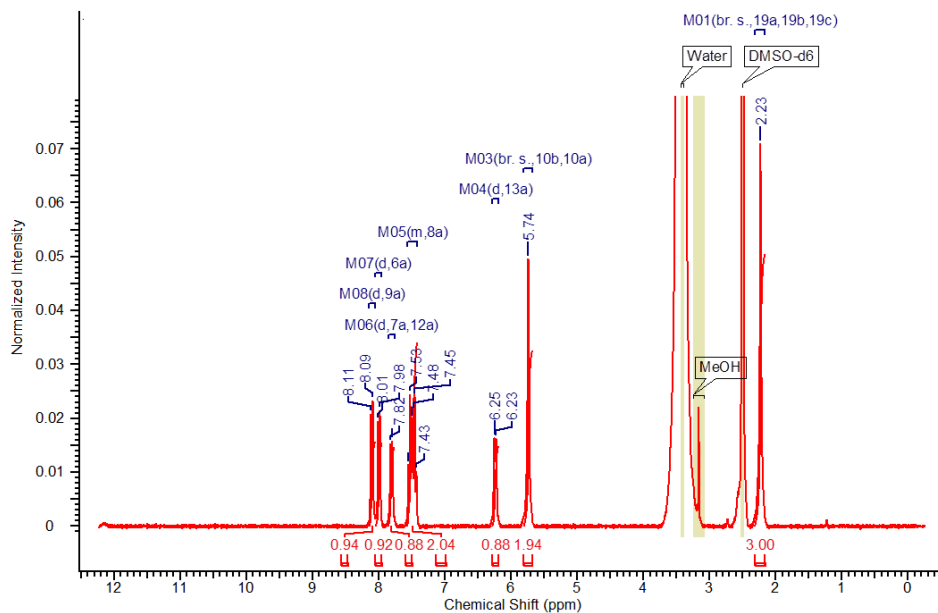


Figure A.4 ^1H NMR spectrum of Hmbt2p (300 MHz, 25 °C, DMSO- d_6). Figure reproduced by permission of The Royal Society of Chemistry.

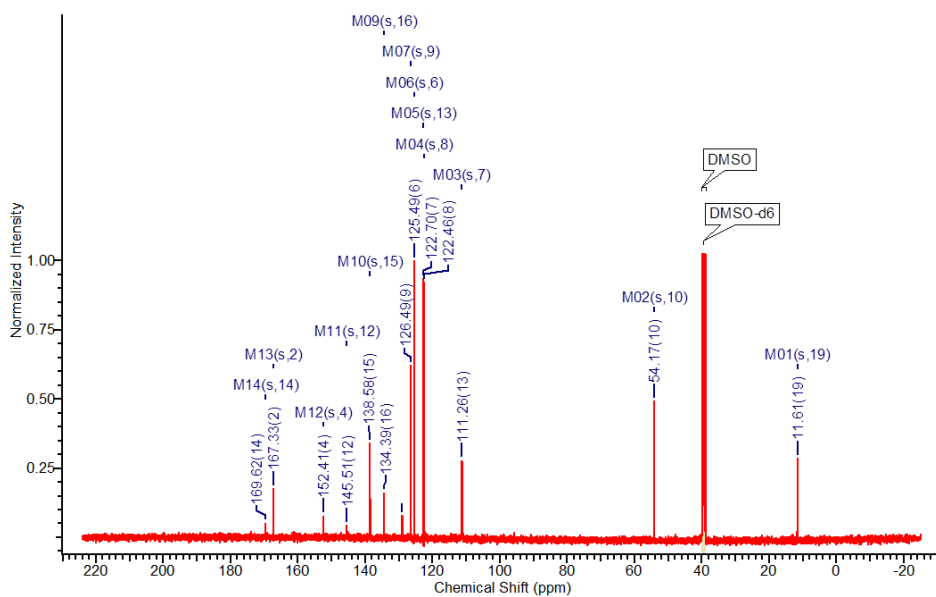


Figure A.5 ^{13}C NMR spectrum of Hmbt2p (151 MHz, 25 °C, DMSO- d_6). Figure reproduced by permission of The Royal Society of Chemistry.

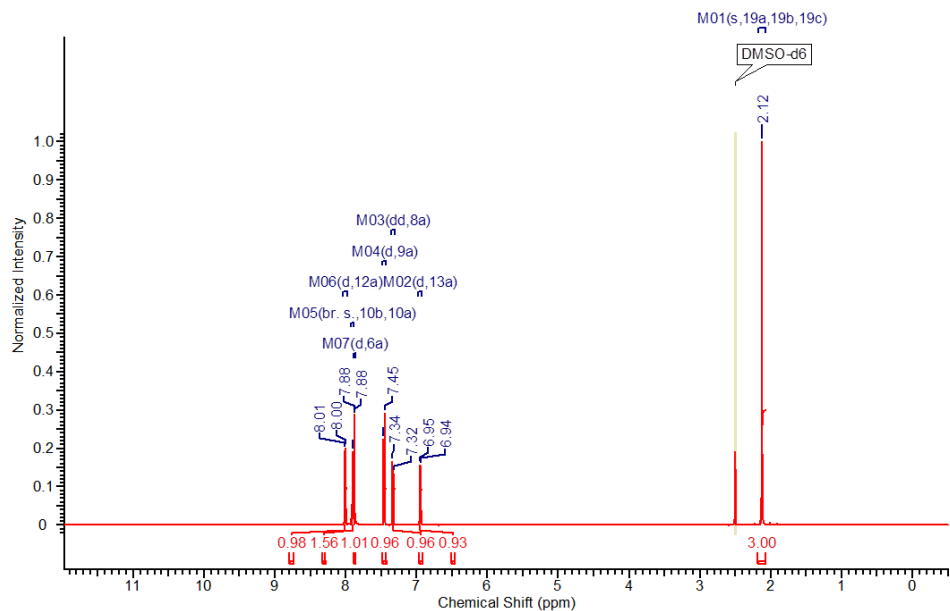


Figure A.6 ^1H NMR spectrum of Habt6p (600 MHz, 25 °C, DMSO- d_6). Figure reproduced by permission of The Royal Society of Chemistry.

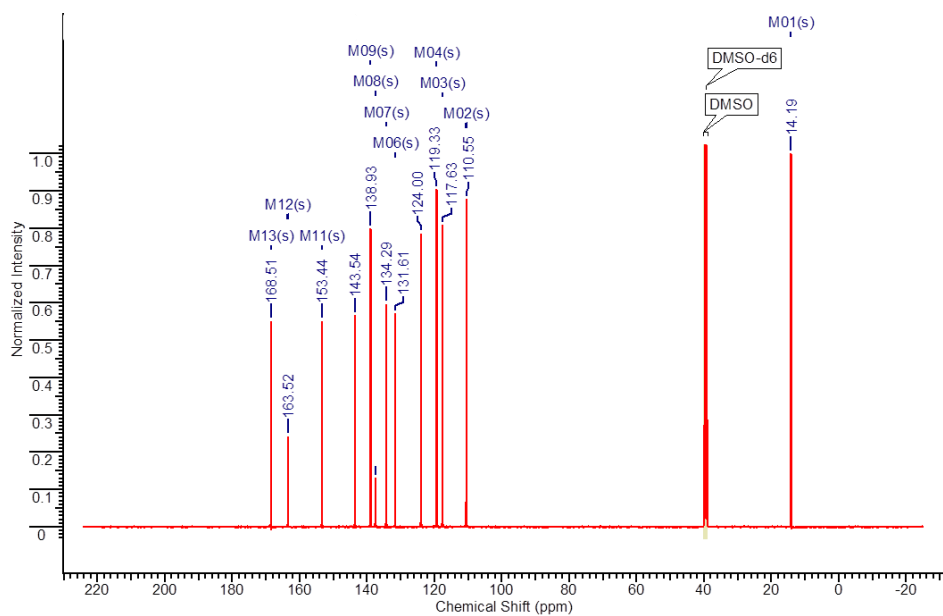


Figure A.7 ^{13}C NMR spectrum of Habt6p (151 MHz, 25 °C, DMSO- d_6). Figure reproduced by permission of The Royal Society of Chemistry.

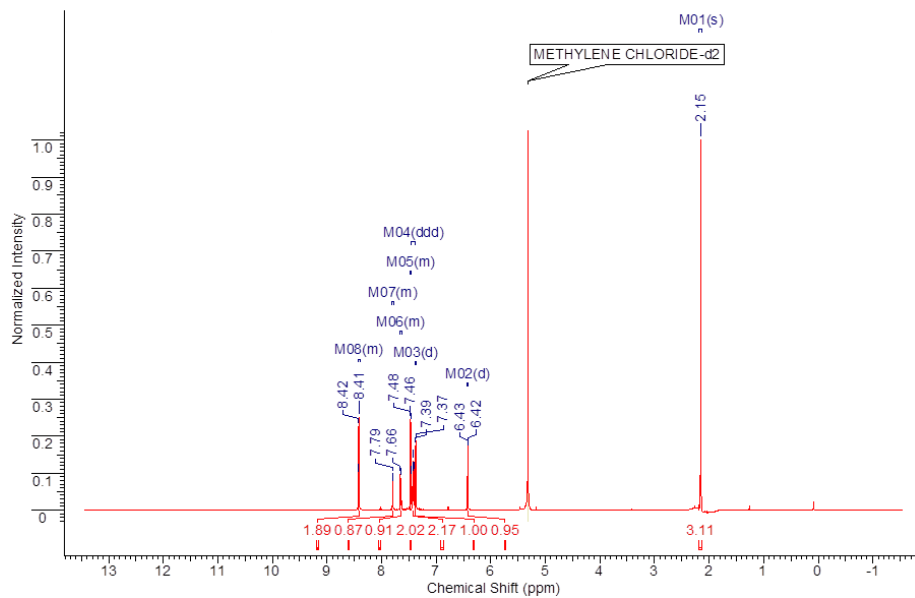


Figure A.8 ^1H NMR spectrum of Hpbo2p (600 MHz, 25 °C, DCM-d_2).

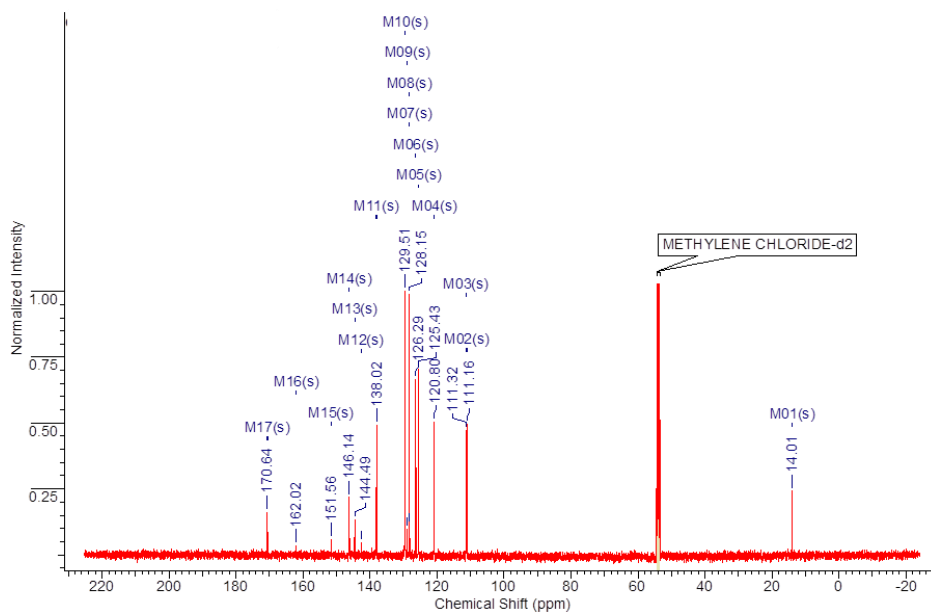


Figure A.9 ^{13}C NMR spectrum of Hpbo2p (151 MHz, 25 °C, DCM-d_2).

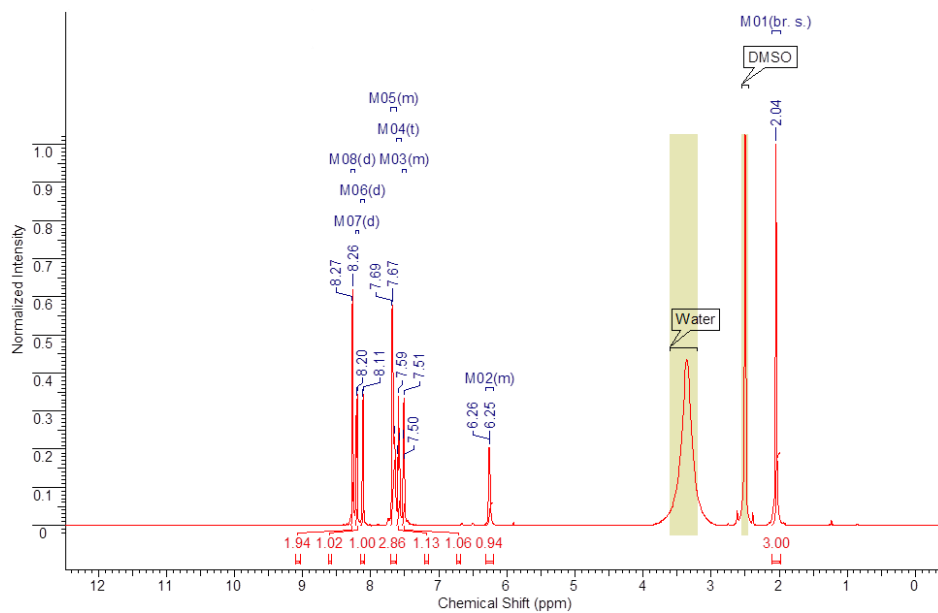


Figure A.10 ^1H NMR spectrum of Hpbt2p (600 MHz, 25 °C, DMSO-d_6).

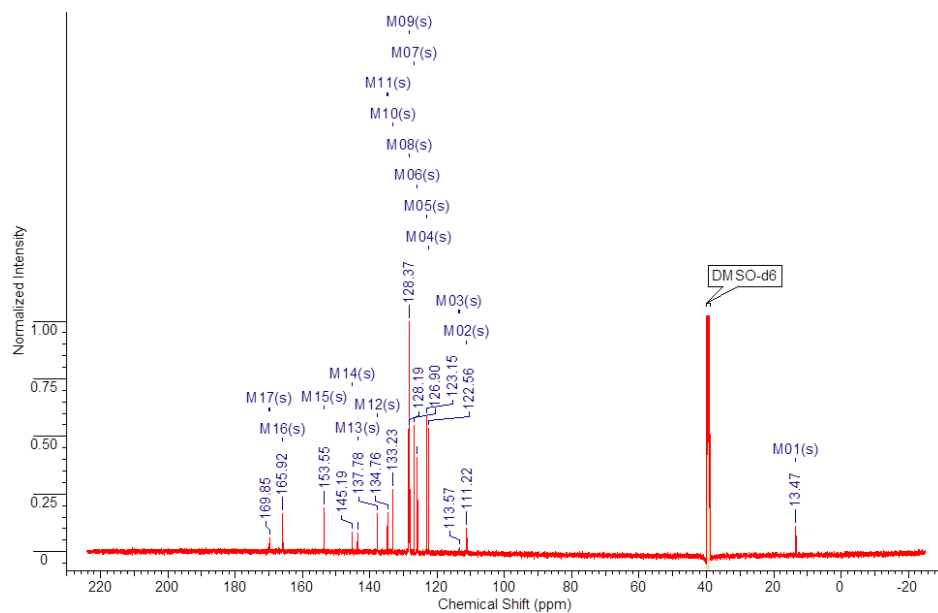


Figure A.11 ^{13}C NMR spectrum of Hpbt2p (151 MHz, 25 °C, DMSO-d_6).

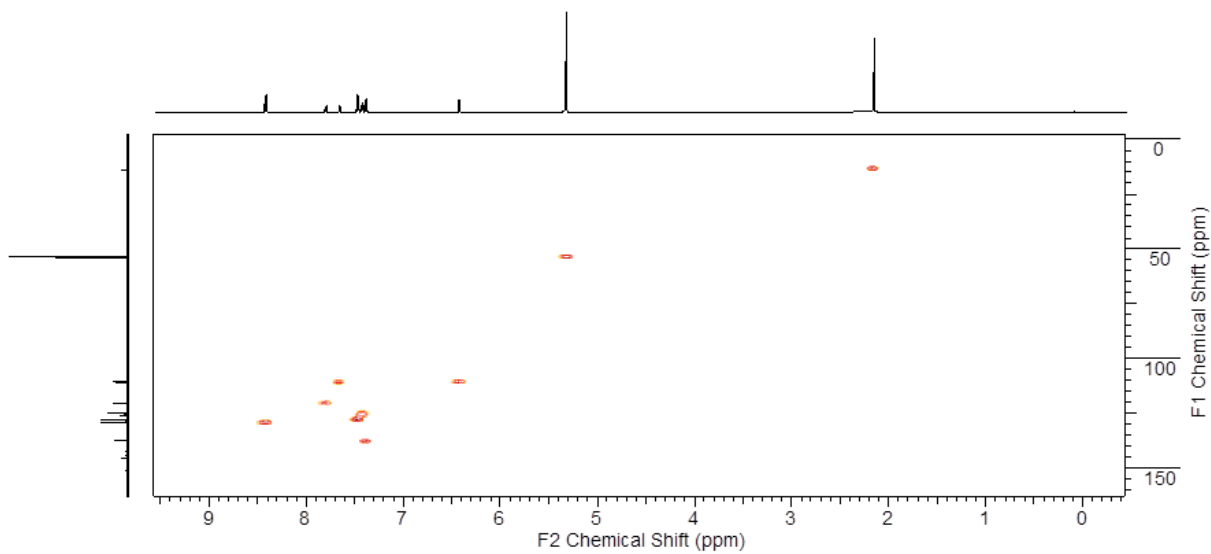


Figure A.12 ^1H - ^{13}C HSCQ spectrum of Hpbo2p (600 MHz, 25 °C, DCM- d_2).

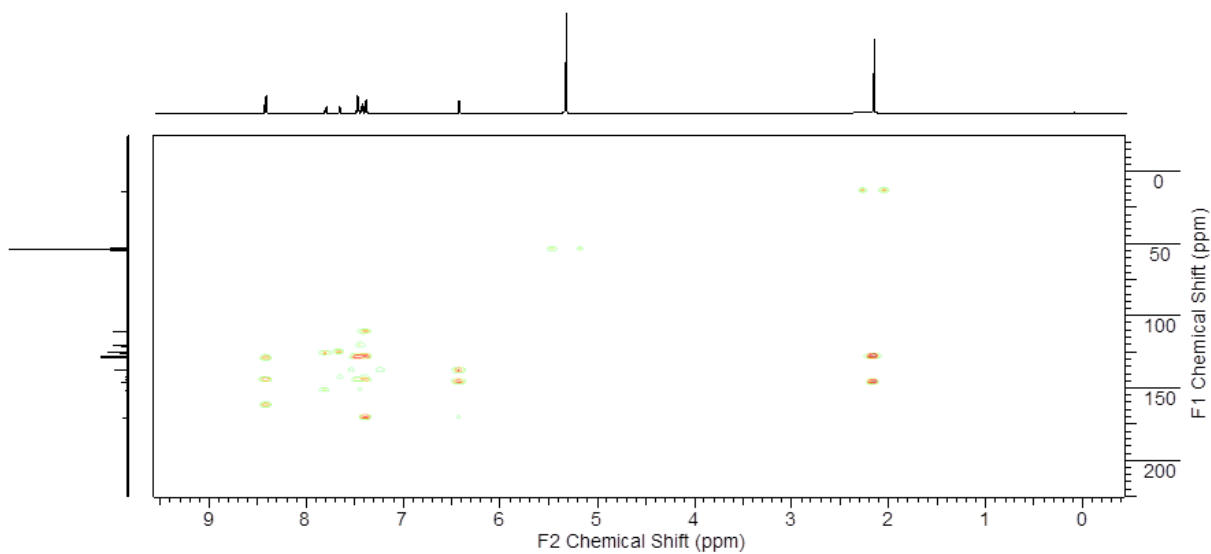


Figure A.13 ^1H - ^{13}C HMBC spectrum of Hpbo2p (600 MHz, 25 °C, DCM- d_2).

B.2 Metal complexes

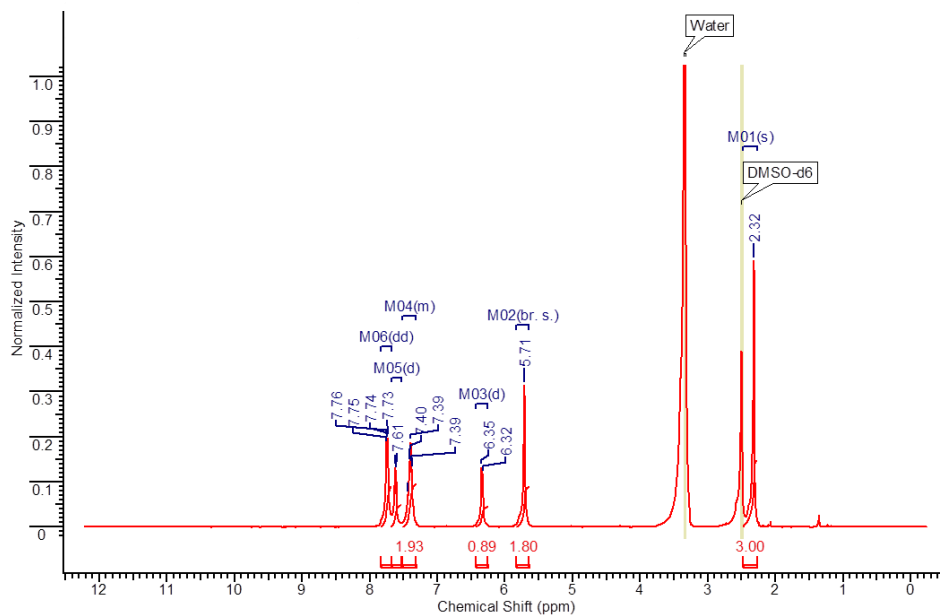


Figure A.14 ¹H NMR spectrum of Zn(mbo2p)₂ (300 MHz, 25 °C, DMSO-d₆). Figure reproduced by permission of The Royal Society of Chemistry.

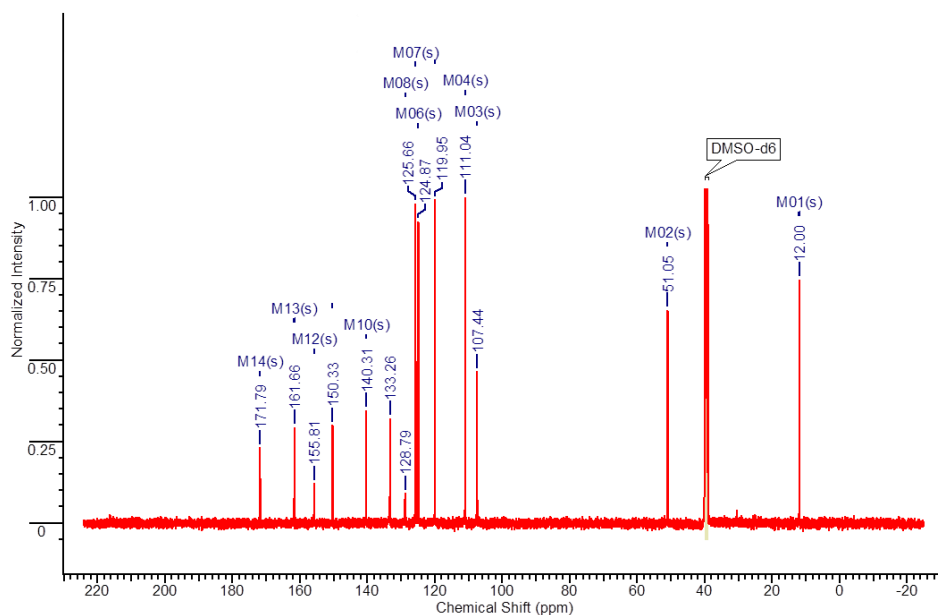


Figure A.15 ¹³C NMR spectrum of Zn(mbo2p)₂ (151 MHz, 25 °C, DMSO-d₆). Figure reproduced by permission of The Royal Society of Chemistry.

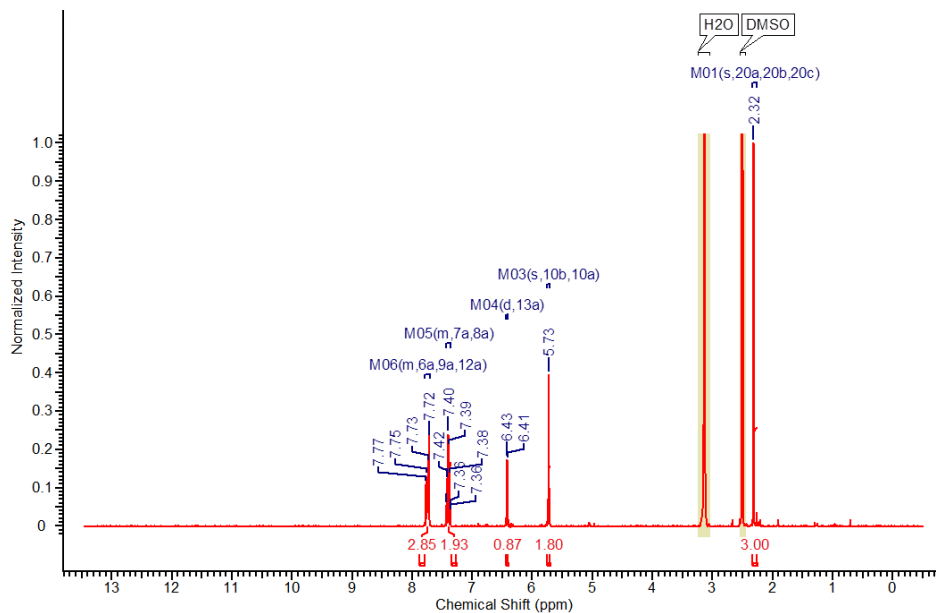


Figure A.16 ^1H NMR spectrum of $\text{Ga}(\text{mbo}2\text{p})_3$ (400 MHz, 65 °C, DMSO-d_6). Figure reproduced by permission of The Royal Society of Chemistry.

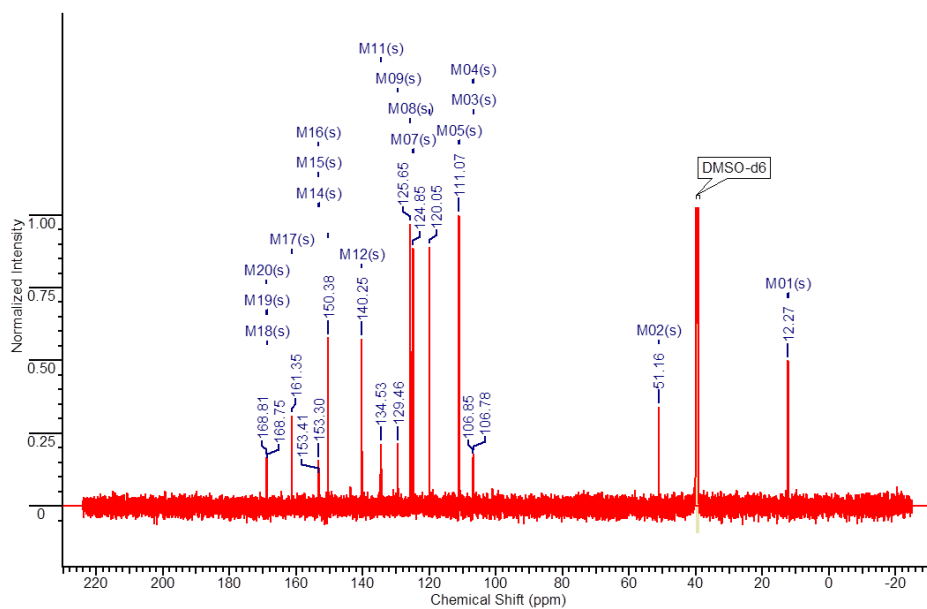


Figure A.17 ^{13}C NMR spectrum of $\text{Ga}(\text{mbo}2\text{p})_3$ (151 MHz, 25 °C, DMSO-d_6). Figure reproduced by permission of The Royal Society of Chemistry.

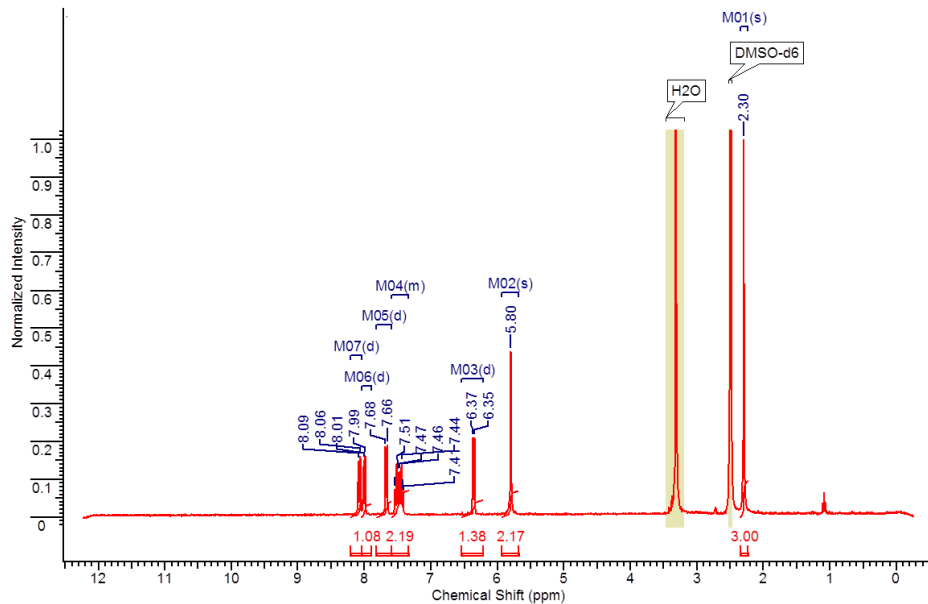


Figure A.18 ^1H NMR spectrum of $\text{Zn}(\text{mbt}2\text{p})_2$ (300 MHz, 25 °C, DMSO-d_6). Figure reproduced by permission of The Royal Society of Chemistry.

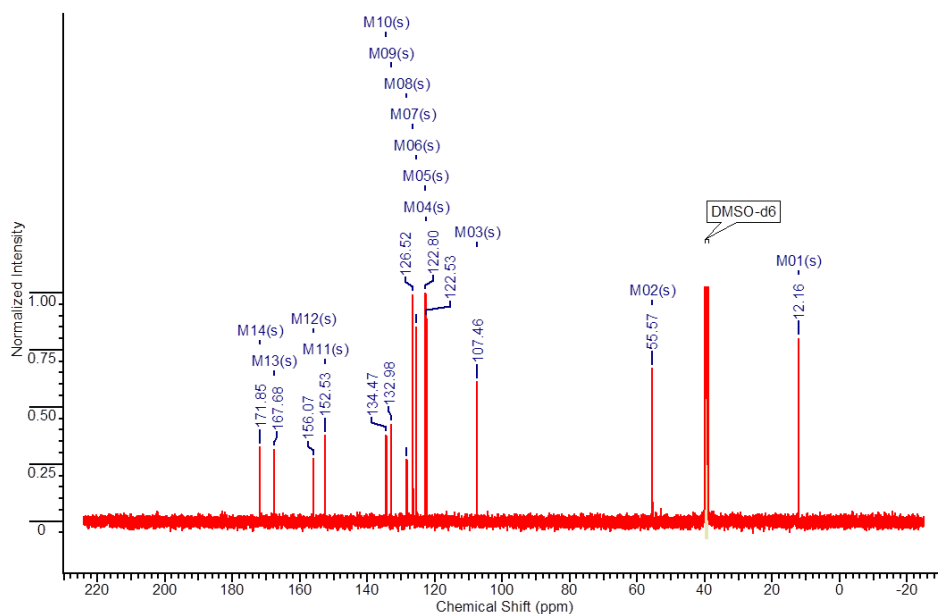


Figure A.19 ^{13}C NMR spectrum of $\text{Zn}(\text{mbt}2\text{p})_2$ (151 MHz, 25 °C, DMSO-d_6). Figure reproduced by permission of The Royal Society of Chemistry.

B.3 Carbamated compounds

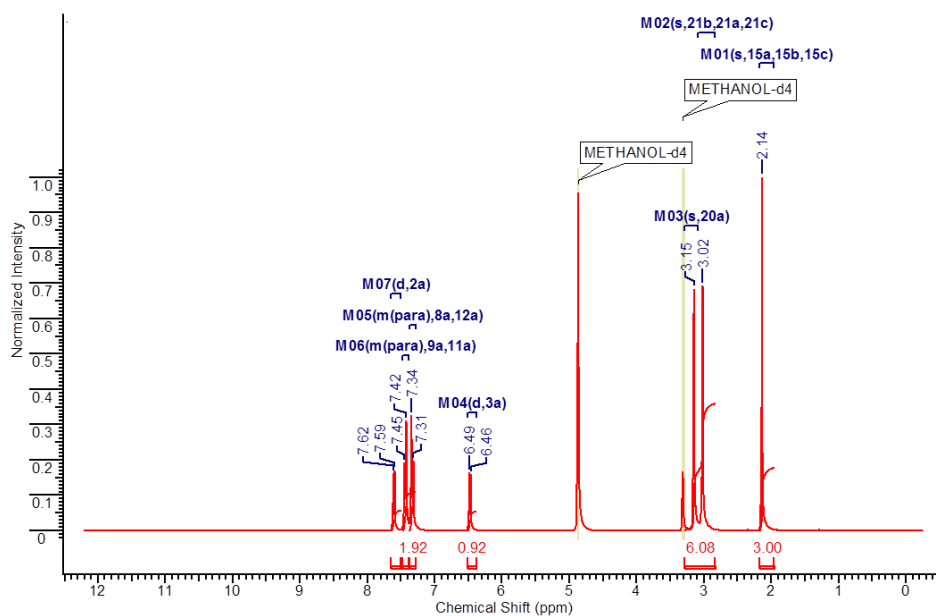


Figure A.20 ^1H NMR spectrum of Chpp (300 MHz, 25 °C, MeOD- d_4).

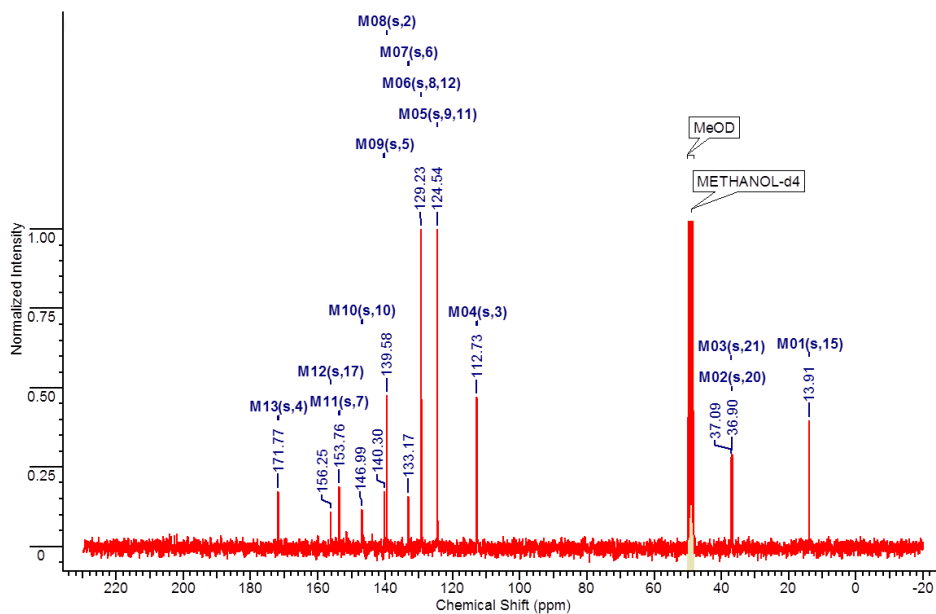


Figure A.21 ^{13}C NMR spectrum of Chpp (75 MHz, 25 °C, MeOD- d_4).

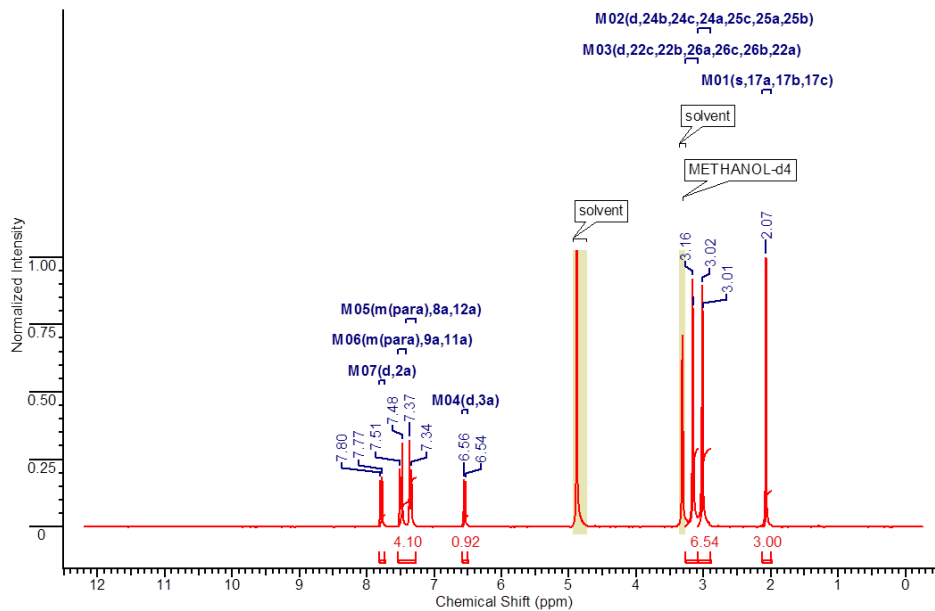


Figure A.22 ^1H NMR spectrum of Cchpp (300 MHz, 25 °C, MeOD- d_4).

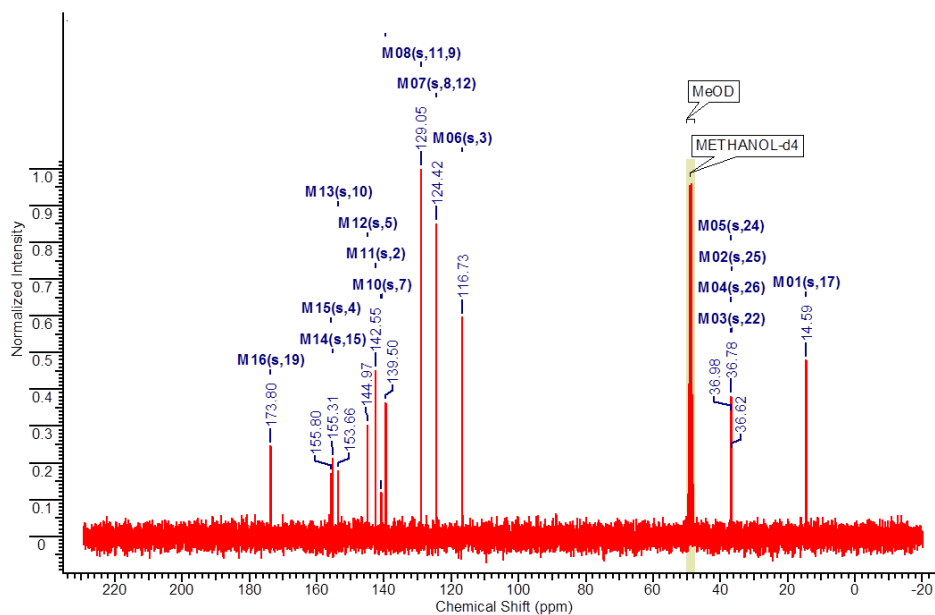


Figure A.23 ^{13}C NMR spectrum of Cchpp (75 MHz, 25 °C, MeOD- d_4).

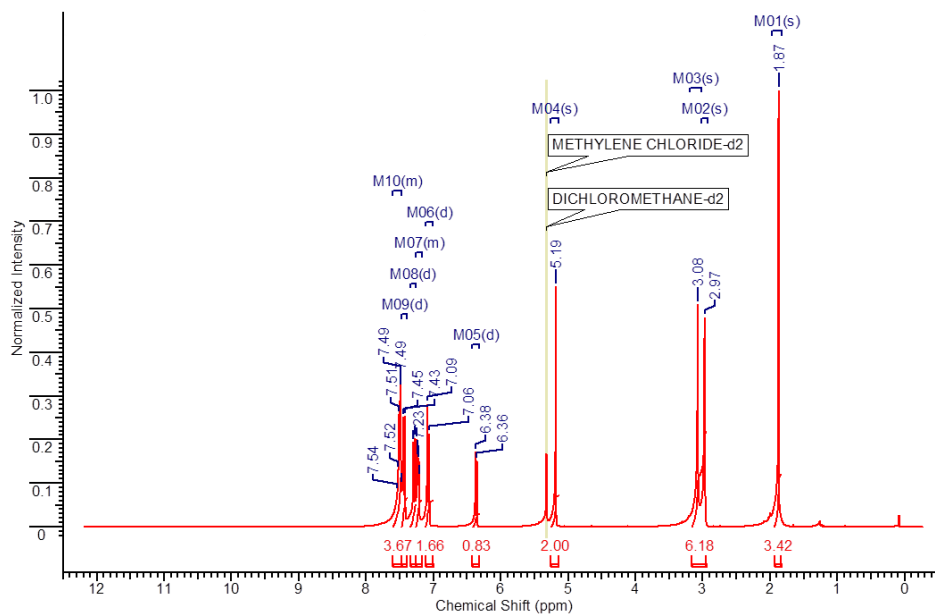


Figure A.24 ^1H NMR spectrum of Cbpp (300 MHz, 25 °C, DCM-d_2).

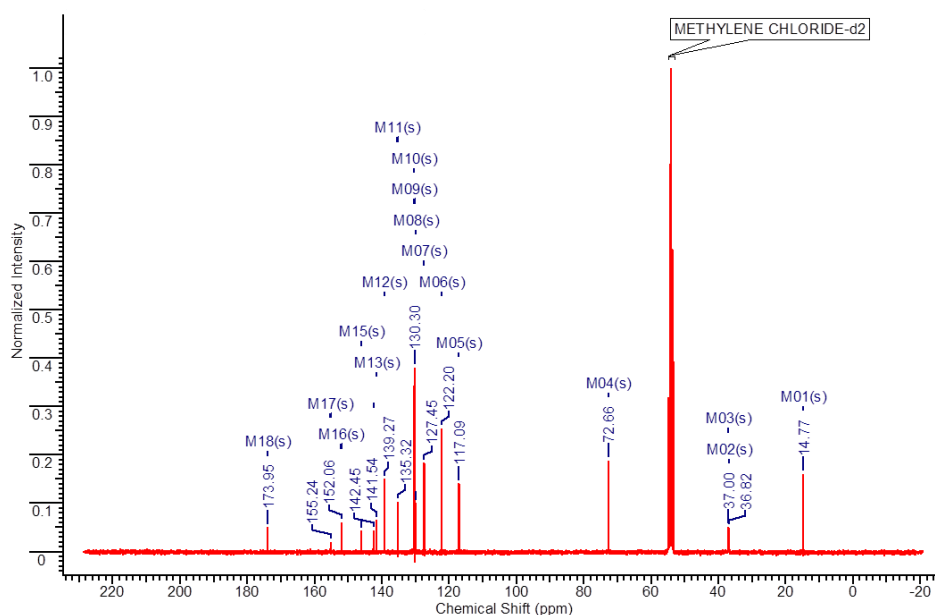


Figure A.25 ^{13}C NMR spectrum of Cbpp (75 MHz, 25 °C, DCM-d_2).

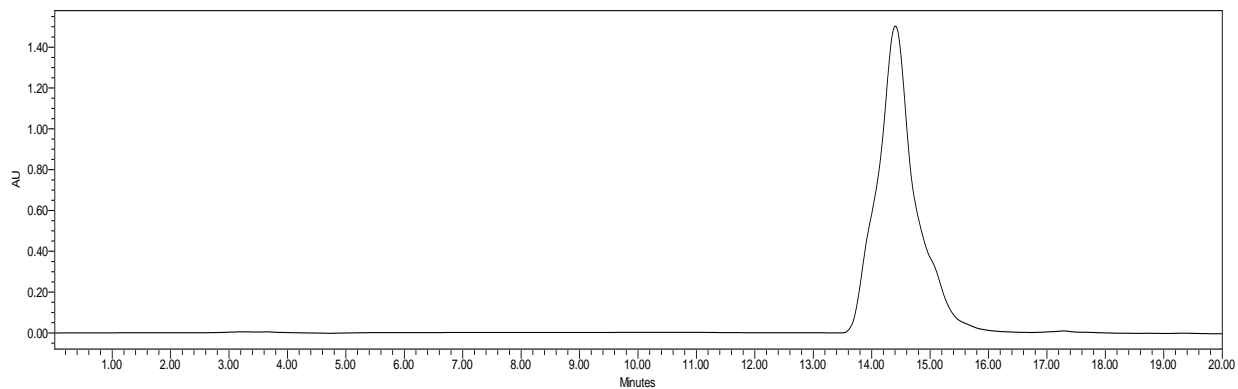


Figure A.26 HPLC chromatograph for the Cbppp after preparative TLC. HPLC gradient used was 50 to 100% of MeOH in H₂O for 10 minutes, followed by 10 minutes of 100% MeOH with 0.8 ml/min flow.

Appendix C – Additional data

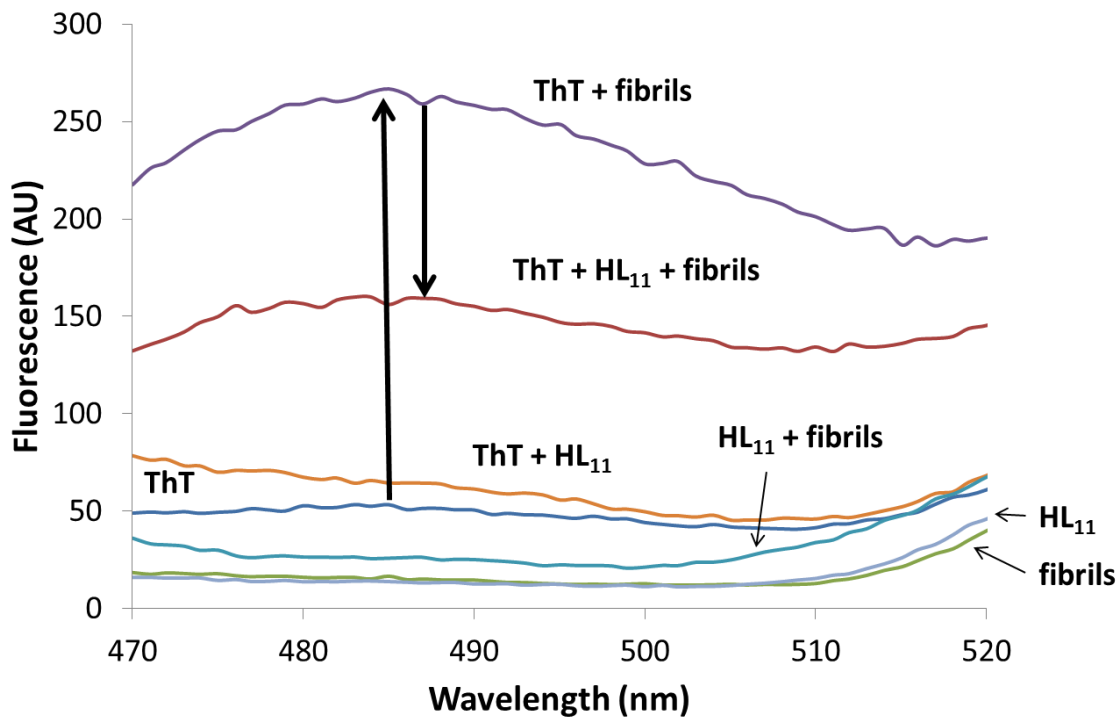


Figure A.27 Controls for the fibril binding experiment: fluorescence of fibrils, ThT, and Hmbo2p alone.

Fluorescence is additive when fibrils are added to Hmbo2p, and when ThT is added to Hmbo2p.

Enhancement of fluorescence is observed when ThT and fibrils are incubated together, and upon addition of ligand Hmbo2p, this fluorescence is partly quenched. Figure reproduced by permission of The Royal Society of Chemistry.

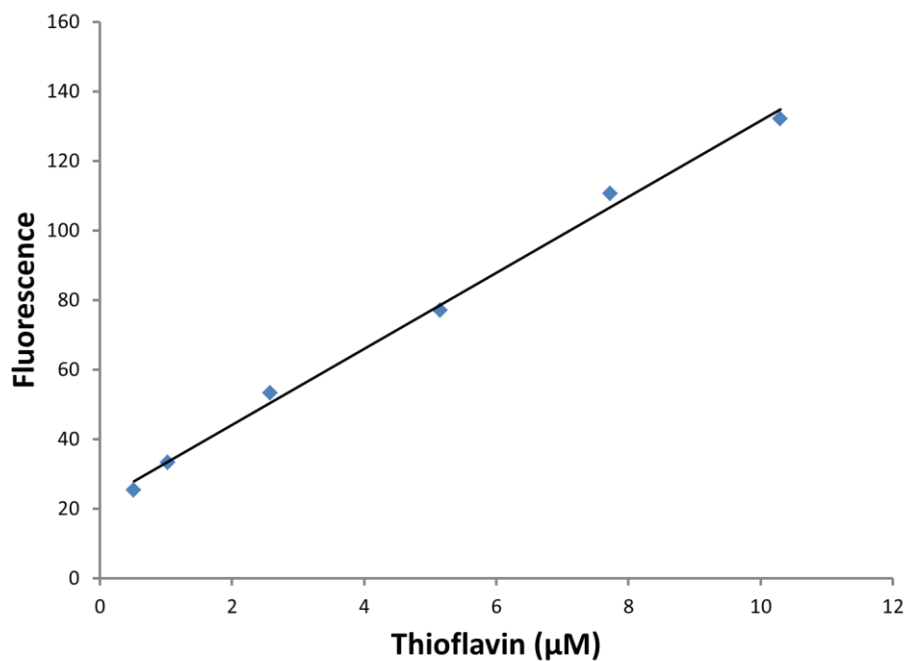


Figure A.28 Linearity of ThT under the study conditions. Figure reproduced by permission of The Royal Society of Chemistry.

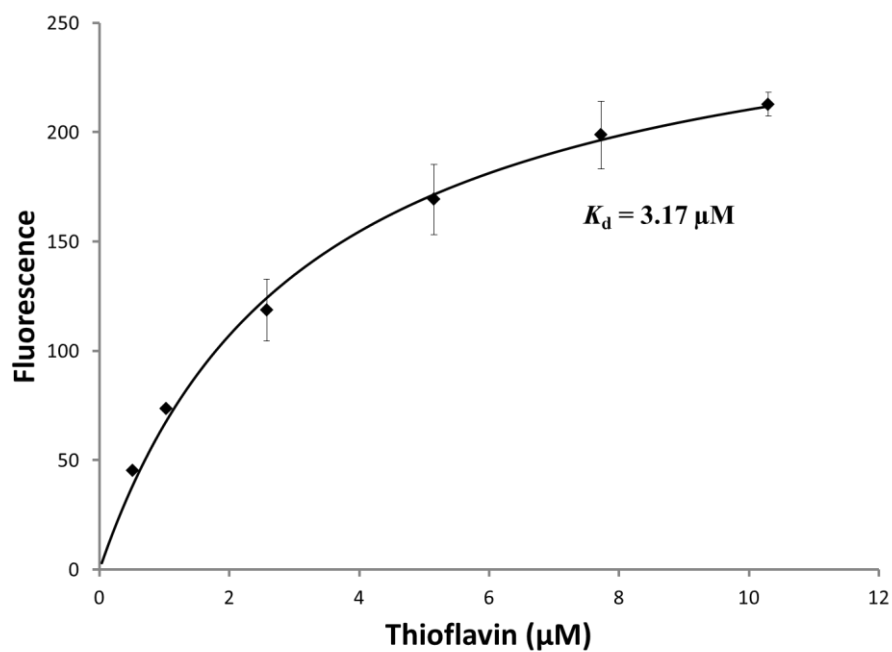


Figure A.29 Binding constant, K_d , for ThT (corrected for its intrinsic fluorescence) to $A\beta_{1-40}$ (~600 nM) under the study conditions. Data are an average of three trials, with relative standard deviation. Figure reproduced by permission of The Royal Society of Chemistry.

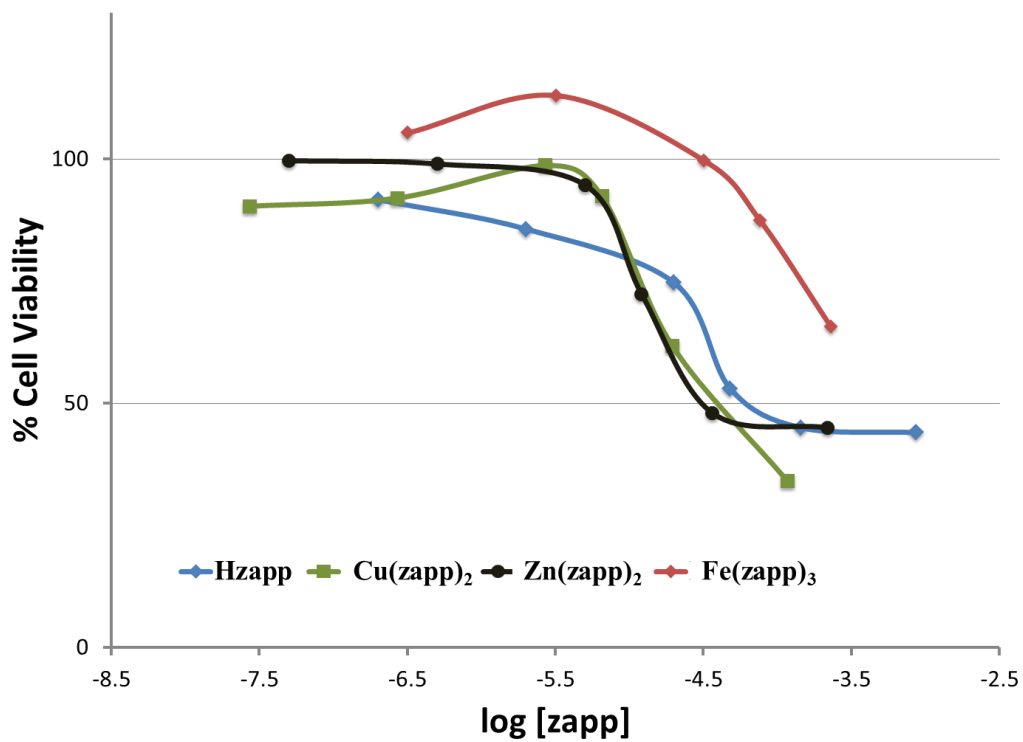


Figure A.30 BEnd.3 cell line viability in the presence of compounds Hzapp, Cu(zapp)₂, Zn(zapp)₂, and Fe(zapp)₃, with respect to the concentration of ligand Hzapp. Figure used with permission from Elsevier.

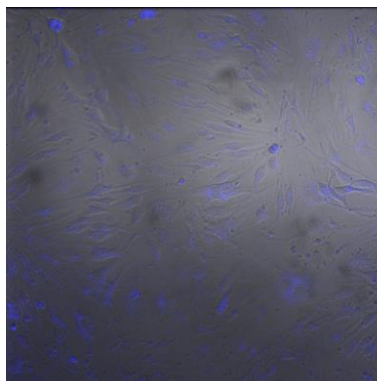


Figure A.31 Composite image with bEnd.3 cell line incubated with Hpbo2p; 20x magnification. Excitation 405 nm; emission 435-485 nm.